LAYERED TITANATE SODIUM-ION BATTERY NEGATIVE ELECTRODES

by

Ryan I. Fielden

Submitted in partial fulfilment of the requirements
for the degree of Doctor of Philosophy

at

Dalhousie University
Halifax, Nova Scotia
August 2017

DEDICATION PAGE

To my three children: Isaac, Lorelai and Lillian.

TABLE OF CONTENTS

LIST OF TABLES

LIST OF FIGURES

ABSTRACT

Sodium-ion batteries could offer an economical and environmentally friendly alternative to lithium-ion batteries, however, many challenges must be overcome first. The need for innovative negative electrode materials for sodium-ion batteries is of paramount importance as graphite, the most highly used negative electrode material in lithium-ion batteries, intercalates sodium to an insignificant degree and other current negative electrode materials do not perform satisfactorily. This work focuses on the investigation of layered sodium titanate phase systems as electrode materials in Na-ion batteries, specifically $Na_xM_xTi_{1-x}O_2$ where M = Cr or V.

The layered systems are of great importance for the development of not only traditional positive electrode materials, but novel negative electrode materials for sodium-ion batteries as well. The high capacity and ease of sodium intercalation of these layered systems make them prime candidates for implementation in sodium-ion batteries. The gravimetric capacity of these materials was found to directly relate to the number of vacancies within their layered structure. A vacancy limit of ~0.4 was determined for these sodium based layered oxides. To increase the capacity, the number of vacancies needs to be increased. Two methods were employed to increase vacancies in intercalation materials, namely the investigation of sulfide and potassium analogues, to varying degrees of success. The potassium analogues led to preliminary studies of materials for potassium-ion batteries, such as graphite and K_xCoO_2.

LIST OF ABBREVIATIONS USED

A	Alkali metal
a	lattice constant
b	lattice constant
BEV	Battery electric vehicle
BMF	Blown microfiber separator
c	lattice parameter or constant
CE	Coulombic efficiency
d	Spacing between planes in a crystal lattice
DMC	Dimethyl carbonate
DSC	Differential scanning calorimetry
$DW(hkl)$	Debye-Waller factor
EC	Ethylene carbonate
F	Faraday's constant
$F^2(hkl)$	Geometric structure factor
FTIR	Fourier transform infrared spectroscopy
hkl	Miller indices of a specific Bragg plane
I_0	Intensity of incident radiation
ICP-OES	Inductively coupled plasma optical emission spectroscopy
KIB	Potassium-ion battery
$L(\theta)$	Lorentz factor
LIB	Lithium-ion battery
M	Metal
$M(hkl)$	Multiplicity factor
MW	Molar mass per formula unit of a specified material
n	Integer that indicates the order of diffraction or the number of moles of Na
NCA	Nickel cobalt aluminum ($LiNi_xCo_yAl_zO_2$)
NIB	Sodium-ion battery
NMP	N-Methyl-2-Pyrrolidone
NPD	Neutron powder diffraction

O	Octahedral
P	Prismatic
$P(\theta)$	Polarization factor
PC	Propylene carbonate
PVdF	Polyvinylidene fluoride
Q_{charge}	Maesured capacity in mAh/g of a specific charge cycle
$Q_{discharge}$	Measured capacity in mAh/g of a specific discharge cycle
R-factor	Goodness of fit parameter
SEI	Solid electrolyte interphase
SEM	Scanning electron microscopy
SHE	Standard hydrogen electrode
T	Tetrahedral
TM	Transition metal
TMO	Transition metal oxide
V_{charge}	Average voltage during charge
$V_{discharge}$	Average voltage during discharge
VE	Voltage efficiency
XRD	X-Ray diffraction
α	Angle between the b and c lattice constants
β	Angle between the a and c lattice constants
γ	Angle between the a and b lattice constants
θ	Angle between incident X-rays and diffraction planes
λ	Wavelength

ACKNOWLEDGEMENTS

I would like to first and foremost acknowledge my supervisor Dr. Mark Obrovac for his guidance and ideas throughout this work. Dr. Tim Hatchard was an almost daily source of help and guidance in the lab, which was vital to my success. I would like to acknowledge financial support from NSERC and 3M for this work.

I would also like to mention past and present lab members for helpful discussions, namely John, Zack, Roy, Kalani, Lauren, Zilai, Annie, Simeng, Doug, Haonan, Yukun, Yidan, Wei, Ben, Lingjun, Phoebe, Bethany, Zhao and Justin. A specific mention goes to my desk neighbor, Lituo, for putting up with my constant interruptions. Summer students Victoria, Laura and Rommy showed great chemistry sense and patience while trying new synthesis routes, oftimes without much success.

Access to other facilities at Dalhousie were invaluable for the research done herein. These include the lab of Dr. Jeff Dahn (FTIR and pycnometry), Dr. John Gosse (ICP-OES), Dr, Mary Anne White (DSC) and Andy George (SEM). I would also like to acknowledge Dan MacDonald in the Electron Microprobe Lab and Patricia Scallion on the engineering campus.

I had a wonderful experience at the CINS in Chalk River, Ontario during my neutron diffraction experiments and acknowledge the support of Dr. Julien Lang.

Most importantly, I acknowledge my wife for her unwavering support as I made this journey.

CHAPTER 1 INTRODUCTION

1.1 Context

Secondary lithium-ion batteries (LIB) have been meeting the energy demands of portable electronics and been the dominant means to store energy in this industry for decades. They have more recently conquered energy storage for the electric vehicle industry. Battery electric vehicles (BEV) in Canada today that use lithium-ion batteries include, but may not be limited to, the BMW i3, Ford Focus, Mitsubishi i-MiEV, Nissan LEAF, Tesla Model S, Kia Soul and Chevrolet Spark [1]. Lithium-ion batteries are even being utilized in many grid energy battery storage projects [2]. This means that energy storage systems based on lithium-ion batteries have a very diverse range of sizes and usages. Lithium-ion secondary batteries provide the devices described above with energy densities ranging from just a few Watt hours to megaWatt hours. Typical laptop batteries have an energy density ranging from 30 Wh to 100 Wh. BEVs, on the other hand, have capacities in the range of tens of kWh (Nissan Leaf 24 kWh, Tesla model S as high as 85 kWh), while electrical grid applications using large lithium-ion battery systems have capacities on the scale of megawatt hours [1].

The amazing characteristics of lithium-ion batteries have led to this wide spread and varied use. They display high energy densities (~760 Wh/L) and long cycle life (>1000 cycles) [3]. There is another factor besides their superior characteristics that has driven the implementation of LIBs in certain applications. Governments have recognized the importance of limiting greenhouse gas emissions as global warming forecasts have become dire. Thus, many governments have set aggressive targets for carbon dioxide emission reduction. Road transport has been seen as a large contributor to emission volumes so development of electric mobility has been emphasized [4]. Electric mobility offers the possibility to substitute oil with a wide variety of renewable energy sources, with batteries providing a means to store this energy.

This unprecedented use of LIBs raises the question of whether future lithium resources and reserves availability can pose a threat to the BEV industry. Analyses thus far are unclear as to whether the availability of lithium will meet future requirements, even though several assessments have been performed over the past few years. Lithium resource estimates vary greatly, ranging from 19.2 Mt, to 71.3 Mt [5]. This thesis operates under the assumption that lithium mineral resources could possibly become an obstacle if lithium-ion batteries continue to be widely used in the BEV industry and most certainly lithium resources will be inadequate if lithium-ion batteries are widely used for grid energy storage [6]. If this is the case, then industry would just be replacing the depletion of fossil fuels by the depletion of another non-renewable and insufficient resource. The effect of the increased use of lithium in the BEV market has already been seen, where the price of battery grade lithium carbonate has increased by a factor of four since 2015 [7].

Since it is thought that lithium will simply be too rare an element for LIBs to be used for widespread large scale energy storage purposes, different high energy density battery chemistries which are derived from abundant elements are needed. Nowhere is this more important than in the intermittent nature of renewable energy sources, such as solar and wind power. Sustainable electrical energy storage technologies for stationary applications are required. Sodium is truly an earth abundant element, being ubiquitous around the globe as the 6th most abundant element in the earth's crust [8]. Sodium is found in high concentrations in the world's oceans as well as vast trona mineral deposits from which sodium carbonate is derived.

Sodium-ion batteries (NIBs) have shown promise as an alternate battery chemistry to lithium-ion, even though they remain relatively unproven [9,10]. NIBs operate upon the same rocking chair mechanism as lithium-ion batteries. Indeed, much like lithium, intercalation compounds exist where sodium can be electrochemically intercalated and deintercalated [11,12]. However, at this time their energy density and cyclability must be increased for practical use. Most studies have focused on half-cell cycling versus sodium metal. Future work needs to concentrate on constructing full-cells for testing, which more closely simulate commercial battery operation.

While still in its early stages sodium-ion battery research has the potential to yield solutions for large scale energy storage. Sodium compounds usually form crystal structures similar to their lithium analogues with small differences in lattice parameters. However, in some cases they form completely different structures [13]. This presents the opportunity for unique sodium intercalation electrode materials with innovative chemistries that could yield high energy densities.

A major cost advantage comes from the fact that sodium will not alloy with aluminum current collector foil at low voltages, whereas lithium does. Higher cost copper foil of the negative electrode, typical in lithium-ion cells, could be exchanged for lower cost aluminum foil. Further cost improvements could be made by substituting high cost transition metals in the metal layer of AMO_2 positive electrodes, such as cobalt, for a low cost metal like iron, which is appreciably electrochemically active in NIBs but not LIBs [14].

1.2 Objectives of this Research

Appropriate positive electrode materials for NIBs have been found that have sufficiently high capacity and energy density with good cycle life [12]. Unfortunately, the same cannot be said of negative electrode materials. The graphite that is commonly used as a negative electrode in LIBs, does not intercalate sodium to any appreciable extent [15,16]. For this reason, research on NIB negative electrode materials have focused on hard carbon and alloy type materials. Each of these has its challenges. Hard carbon has been shown to reversibly intercalate sodium, but has a relatively low volumetric capacity due to its low density. To make matters worse most of this capacity occurs at low voltages (<50 mV) where sodium plating could lead to safety issues if cells are over charged or discharged at high rates. Alloy-based negative electrodes have been reported and although they have large capacities they tend to have large volume expansion and contraction during cycling which leads to poor columbic efficiencies. Practical negative electrode materials are clearly needed for the implementation of NIBs [15].

For this reason, the primary goal of this work was to design, synthesize and characterize new high energy density negative electrode materials derived from earth abundant, low cost and sustainable elements to help accelerate the commercialization of NIB materials. Target applications include batteries for large format energy storage, such as BEV and grid storage. In addition to having high energy density these new materials need to display high Coulombic efficiencies and long calendar and cycle life (>1000). Low hysteresis even at high current rates is also desirable. These metrics will be explained later in the text.

Layered intercalation materials were the principal material type investigated in this thesis for these negative electrodes, as they traditionally meet the aforementioned requirements, due to their good ionic and electrical conduction. This project specifically investigated the $Na_xM_yTi_{1-y}O_2$ phase systems as they display appropriate voltages for negative electrodes in NIBs due to the presence of the Ti^{4+}/Ti^{3+} redox couple. A key goal was to increase the capacities of these materials so that they could compete with current LIB negative electrode energy densities. To achieve this the number of vacancies needed to be increased. To increase the number of vacancies in these materials various strategies were employed and they will be the subject of the latter half of this thesis.

CHAPTER 2 BACKGROUND

This chapter describes the fundamentals of both lithium-ion and sodium-ion batteries. Differences between the two are also highlighted as these differences can be exploited as a source of innovative material possibilities. This chapter also includes a description of the mechanisms of sodium electrochemical storage and a comprehensive literature review of negative electrode and positive electrode materials for NIBs. A great majority of electrode materials are layered structures, thus the end of this chapter contains an explanation of these structure types along with their particular nomenclature.

2.1 Lithium-ion Battery Properties

SIBs operate through a rocking chair mechanism, as do LIBs. LIB chemistry will be used to introduce the subject due to this similarity. LIBs consist of three main components: a positive electrode, a negative electrode and an electrolyte. Other major components include separators and current collectors. Figure 2.1 shows a schematic diagram of a LIB.

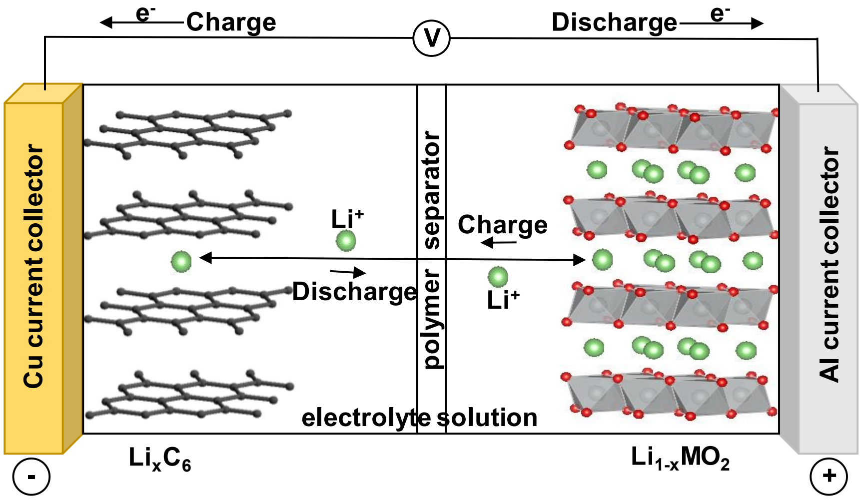

Figure 2.1: Schematic diagram of a Li-ion battery. A graphite negative electrode and a lithium metal oxide positive electrode are shown. Lithium, transition metal, oxygen and carbon are depicted by green, grey, red and black spheres, respectively.

The rocking chair mechanism refers to the way in which lithium ions are “rocked” back and forth between the positive and negative electrode during discharge and charge. The positive electrode is a material that contains lithium ions as made, which can then be removed electrochemically during charging. They also contain other elements with multiple oxidation states. When lithium is removed electrochemically from the positive electrode an electron is also removed while one of the other elements oxidizes to maintain charge neutrality. Most positive electrode materials in use today are lithium transition metal oxides, as they tend to have high voltages versus lithium metal. The negative electrode is usually graphite which can accept lithium ions into its layers and electrons into its band structure during charge. The electrolyte is usually an organic solvent with a lithium salt solute which provides lithium transport and diffusion between the positive and negative electrodes. There are additionally current collectors which act as a medium in supplying electrons to electrode active materials from the external circuit or conversely delivering electrons from electrode reactions to the external circuit. Metals, such as copper (negative electrode) or aluminum (positive electrode), are commonly used as current collectors due to their high electronic conductivity, electrochemical stability and ease of fabrication. Another integral component in LIBs is the separator which is typically a thin microporous polymer film (polyethylene or polypropylene) that allows the passage of ions while at the same time being electrically insulating to prevent short circuits from occurring between the positive and negative electrodes. The separator prevents physical contact between the negative electrode and positive electrode, effectively “separating” them from one another.

The most widely used lithium-ion positive electrode materials are those with layered oxide crystal structures. Layered lithium transition metal oxides typically adopt a hexagonal structure with the general chemical formula $\mathrm{Li}M\mathrm{O}_2$, where M stands for a single transition metal or a mixture of transition metals. These structure types are visualized in Section 2.3, Layered Structures for Sodium Intercalation. A distinct set of Bragg peaks is observed for these materials in X-ray diffraction (XRD) experiments. These peaks allow one to obtain lattice parameters and atomic positions that describe the unit cell, and hence, the material's structure. The chemical composition of the positive electrode has a significant effect on its functionality and properties, as different combinations of transition metals can change the capacity, voltage and thermal stability of constructed cells.

LIB technology actually includes a family of battery chemistries that employs various combinations of negative electrode and positive electrode materials, each with varying structures. Each of the combinations offer advantages and disadvantages in terms of cost, lifespan, performance, safety, specific power, and specific energy. Often a battery performs well in only some of these metrics, while performing poorly in the others. For example, a NCA positive electrode has a high specific power and is appropriately used in Tesla BEVs, while $NaFePO_4$ is has a lower cost and longer life span, thus it is being incorporated in batteries for grid energy storage.

2.2 Sodium-ion Battery Properties

Batteries could also be based on other metal-ion systems instead of lithium [17–19]. Other metals of interest today include sodium, magnesium, aluminum, potassium and calcium [20–23]. Considerable research is being done to find appropriate electrolytes and electrode materials for these alternate metal-ion chemistries. One of the advantages of changing the metal ion is that some of these metals have much more energy per unit volume than lithium metal [24]. Batteries based on these metals are predicted by theory to store significantly more energy than lithium-ion batteries. For these alternative metal-ion battery chemistries lithium ions are simply exchanged for another metal ion such as sodium ions. NIB research actually began alongside lithium-ion work in the early 1980's but vanished due the superior energy density of lithium-ion materials. In fact, an example of a sodium-ion full cell was published in early 1989, a couple of years before the first commercialized lithium-ion batteries of SONY appeared [25]. Sodium-ion batteries have since reemerged as fears of lithium sustainability have surfaced.

There are obvious differences between lithium and sodium ions, however, their chemistry is somewhat similar as they are in the same group of the periodic table. Perhaps the most significant differences are their atomic weight and ionic radii. The atomic masses of sodium and lithium are 22.99 g and 6.94 g, respectively. The radius of Na^+ is 1.02 Å and the radius of Li^+ is 0.76 Å, when their coordination number is six. These ionic radii values are taken from Shannon [26]. These are effective radii, which are a self-consistent set of radii used to predict ionic crystal structures by Pauling's rules. These radii indicate that Na^+ is larger than Li^+ in most ionic solids.

This size difference could pose challenges for sodium batteries in several ways. Theoretical gravimetric and volumetric capacities would be lower for sodium than lithium. This is exaggerated when the pure metals are analyzed. However, when comparing prototypical materials such as layered oxides the differences are manageable.

For example, $NaCoO_2$ and $LiCoO_2$ have theoretical gravimetric and volumetric capacities of 235/273 mAh/g and 1190/1390 Ah/L, respectively [9]. The differences here are both only <15 % because the alkali metal mass and volume only accounts for a small percentage of the total positive electrode mass/volume. Furthermore, the tolerance of alkali extraction amount is greater for sodium than lithium. The larger size of sodium enables more sodium to be extracted while maintaining structural stability. Perhaps the largest drawback is the inherent voltage difference that is observed for these types of layered positive electrode materials. Sodium containing layered oxides display an average voltage that is typically a 1 V lower than its lithium counterpart [13]. This is typically explained by the voltage difference between sodium and lithium electrodes versus the SHE in different electrolytes [27].

These differences could also be advantageous in a couple of ways. The larger size of sodium leads to increased flexibility for materials design. This is likely due to the fact that there is a large size difference between sodium and first row transition metal ions. This can cause sodium to separate more readily into its own layer in certain structures or adopt differing geometries compared to other smaller metal ions. Therefore, the sodium layered oxides are quite easily synthesized compared to the lithium ones, indeed it is common practice to ion exchange sodium for lithium during materials processing to obtain new lithium insertion materials that are otherwise unattainable. Furthermore, the structural chemistry of sodium compounds is much richer and complicated than lithium. There exist many polyanion compounds and natural occurring minerals based on sodium, with very few based on lithium.

The most striking advantage likely comes from sodium and lithium's Lewis acidity. As both share the same charge but lithium is drastically smaller, lithium has a relatively high charge density. This results in lithium tending to accept or share more electrons than sodium, in order to be energetically stabilized. The two main consequences of this are the larger energy of desolvation in electrolytes and higher activation energy for ion diffusion in layered oxides for lithium than sodium [20]. Both of these consequences could lead to enhanced battery performance for NIBs over LIBs.

2.2.1 Sodium Storage Mechanisms

There are three distinct ways to store sodium in sodium-ion battery materials, namely intercalation, alloy and conversion reactions. Each has its own advantages and disadvantages, as the dissimilar mechanisms lead to drastic differences in galvanostatic cycling curves and electrode characteristics.

An intercalation reaction mechanism is where sodium atoms are inserted and extracted or vice versa from lattice sites within the crystal structure of the electrode material. The specific lattice sites usually form tunnels or layers. This type of mechanism leaves the original structure relatively unchanged, with very little volume change. Intercalation mechanisms can further be separated into a solid solution or biphasic reactions. During a solid solution reaction, the sodiated and desodiated phase remain the same structure with minor changes in lattice constants. This results in a sloping potential profile due to the Gibbs phase rule. In a biphasic reaction sodiation or desodiation results in phase separation and a constant potential profile according to the Gibbs phase rule. The fact that sodium intercalates into vacant sites within these materials leads to little volume change, which in turn results in long cycle life with little polarization. A drawback to intercalation materials is that because they use specific sites within their crystal structure for Na insertion there is limited space for sodium and thus capacity is limited to no more than ~250 mAh/g or ~1250 Ah/L. Examples of these types of materials include Na_xMO_2 positive electrode materials, as well as titanate negative electrodes.

During an alloying reaction sodium is stored by forming an alloy with the host material. This leads to destruction and reconstruction of the framework structure [28]. Alloy reactions are of the type described by Equation 2.1,

$$xNa + M \rightarrow Na_xM \tag{2.1}$$

where M = Sn, Sb, Pb, or P and where many moles of sodium can be stored per mole of a host material, such as tin, which leads to capacities as high as ~2000 mAh/g or ~1500 Ah/L. However, because so much sodium is reacting volume changes as high as 500 % are possible. These changes in material structure lead to poor cyclability and high polarization of the electrode material. Examples of sodium alloy materials include Sn, Sb, Pb and P, all of which are negative electrode materials for sodium-ion batteries [29].

In conversion reactions sodium reacts with another material, where significant bond breaking occurs via displacement chemical reactions. Equation 2.2 shows an example conversion reaction of sodium with cobalt oxide.

$$2Na_{(s)} + CoO_{(s)} \rightarrow Na_2O_{(s)} + Co_{(s)} \tag{2.2}$$

As in alloy materials, many moles of sodium can potentially be stored per mole of host material. This gives materials with this type of mechanism capacities as high as 1000 mAh/g and ~4000 Ah/L. Once again, due to the significant bond breaking and reforming cyclability is poor and huge hysteresis is observed for these types of materials. Typical conversion materials are binary transition metal oxides that operate as negative electrode materials in NIBs [30].

2.2.2 Positive Electrode Materials for Sodium-ion Batteries

Positive electrode materials typically have a voltage greater than 2 V versus sodium metal. There are many material types that can function as positive electrodes in sodium-ion cells. However, the two most common groups under intense study include the polyanionic phosphate compounds and oxides. The first studies of sodium-ion electrodes concentrated on Na_xMO_2 materials, where M = transition metal. Much of this early work was performed by the Delmas lab in France during the early 1980s and has been revisited by in recent years by other researchers. One such example is Na_xTiO_2. In 1983 the Delmas group evaluated $NaTiO_2$ as a sodium-ion battery electrode material [31]. Their results showed that only a small amount of sodium, 0.3 mole percent, could be reversibly deintercalated from $NaTiO_2$ using 1M $NaClO_4$ in propylene carbonate as an electrolyte. The $NaTiO_2$ was studied again in 2014 by the Ceder group at MIT and they were able to reversibly deintercalate 0.5 of the sodium, which corresponds to a reversible capacity of 152 mAh/g or 740 Ah/L, using 1M $NaPF_6$ in ethylene carbonate:dimethyl carbonate (1:1 v/v) electrolyte [32]. Much improved cycling and good rate performance was achieved. The improved results of the Ceder group compared to the Delmas group were likely due to the difference in electrolytes used.

In the case of phosphates, the best known example is $NaFePO_4$. $NaFePO_4$ can be of two distinct structure types: maricite or triphylite. The maricite type works very poorly as an electrode material as sodium ions are isolated within the structure which leads to high energy diffusion barriers. The triphylite structure is obtained via ion exchange with $LiFePO_4$. Almost all of the sodium in this compound can be reversibly cycled with a gravimetric capacity of 125 mAh/g and an average voltage of 2.7 V. Unfortunately, because of its low density, triphylite $LiFePO_4$ has low volumetric capacity [33].

The most studied positive electrode material group for sodium-ion batteries consists of the layered oxides (Na_xMO_2). These oxides possess various crystal structures and display high voltages versus sodium metal. The first example was published in 1981 by the Delmas group. They demonstrated that sodium could be reversibly deintercalated from Na_xCoO_2 using sodium half-cells [34]. Since that time most of the Na_xMO_2 oxides of the first row transition metals have been studied and restudied electrochemically in sodium half-cells: $NaTiO_2$ [31,32], $NaVO_2$ [35–37], $NaCrO_2$ [38–41], $NaMnO_2$ [42,43], $NaFeO_2$ [14,44], $NaCoO_2$ [34], $NaNiO_2$ [38,45], and $NaCuO_2$ [46,47]. Most of these layered compounds allow only 0.5 of the sodium to be deintercalated from the structure with an average of 120 mAh/g or less capacity. Typically, the voltage curves for these materials slope or step severely and have lower average voltages (~0.5 V) than their lithium counterparts.

There is an interesting trend in the voltage versus sodium metal of these O3-type $NaMO_2$ materials (the different structure types are defined later in section 2.3, Layered Structures for Sodium Intercalation), where up to half of the sodium is removed. The average voltage versus sodium metal increases as one goes from left to right across the first row transition metals in the periodic table. Figure 2.2 shows this trend where the more d electrons the transition metal has the higher the average redox potential (voltage) for desodiation. This only holds true for the early first row transition metals, Ti, V and Cr. However, it is widely accepted as general rules that a later transition metal exhibits a higher voltage, Ti < V < Cr < Mn < Fe < Co < Ni, and that a higher valence transition metal exhibits a higher redox potential, $Ni^{2+}/Ni^{3+} < Ni^{3+}/Ni^{4+}$.

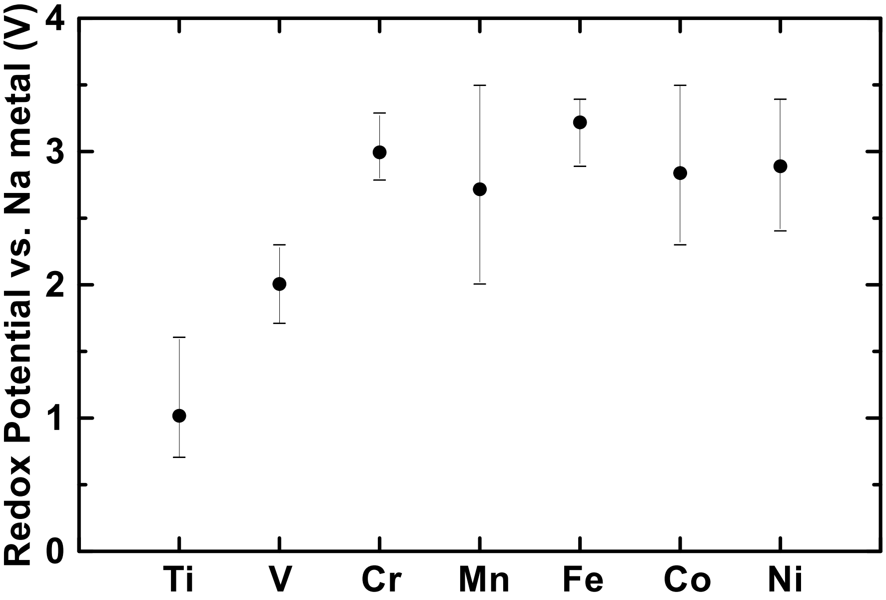

Figure 2.2: The average redox potential for desodiation of O3-Na_xMO_2 versus sodium metal. Error bars show the voltage range when $0.5 \le x \le 1$ [14,32,34,35,39,43,45]. Styled after Reference 48.

These general rules are thought to be due to the fact that the atomic radii of atoms decreases going from the left to the right of the periodic table. As the radius of the element becomes smaller, the electronegativity and ionization energies increase. Thus, the first row transition metals which possess the same charge have more oxidizing power from the left to the right of the periodic table, due to their decreasing atomic radius.

Due to the differences between sodium and lithium more layered first row transition metal oxides are electrochemically active versus sodium than lithium. For instance, layered LiMO$_2$ where M = Cr and Fe display very little to no capacity versus lithium metal. The sodium analogues of these materials can be cycled with stable capacity versus sodium metal. The fact that the lithium analogues cannot be cycled is thought to be due to transition metal migration. At higher voltages some transition metals can migrate from their layer to the alkali layer. This is an irreversible process and therefore on subsequent cycles significantly less alkali will be intercalated back into the host structure and capacity decreases rapidly. Due to the difference in size between lithium and sodium, they prefer different crystallographic sites. Both will adopt the octahedral geometry but sodium and lithium prefer prismatic and tetrahedral sites, respectively. Unfortunately, when lithium is in tetrahedral sites it can stabilize transition metals that migrate to the alkali layer, which is undesirable, as lithium ion diffusion is severely reduced as a result. The stabilization of transition metals by this mechanism is referred to as dumbbell stabilization [43,48]. This is another key difference between sodium and lithium chemistry in these layered oxide type materials where sodium has an advantage.

More recent studies have concentrated on sodium mixed transition metal oxide materials. This is where the occupants of the transition metal layer can be substituted while maintaining the total transition metal to oxygen stoichiometry and charge neutrality. This allows for cafeteria positive electrodes where one can pick and choose which transition metals to include so that electrode characteristics can be optimized. The most notable optimization for sodium-ion battery positive electrode materials has been for higher voltages, as the potentials of sodium-ion positive electrodes tends to be lower than their lithium counterparts. The first example of this was $Na_xNi_{0.6}Co_{0.4}O_2$ in 1996 [49]. In 2001 the Dahn group then reported $Na_{2/3}Mn_{2/3}Ni_{1/3}O_2$ [50]. It was not until 2010 that the number of reports accelerated and improved sodium layered positive electrode materials emerged. Some of these materials actually include up to four different transition metals in the transition metal layer, such as $NaMn_{1/4}Fe_{1/4}Co_{1/4}Ni_{1/4}O_2$ [51].

The reason positive electrode materials with more than one transition metal in the transition metal layer have received so much attention is that they tend have an increased average voltage and higher reversible capacities compared to the single $NaMO_2$ materials. Fewer phase transitions and less sodium ordering occurs upon cycling which can be observed in the voltage capacity profile of these materials, as they tend to have a single sloping plateau instead of a staircase profile. This means that the starting structure is maintained at higher charging voltages which allows more sodium to be deintercalated reversibly. These fewer transitions during cycling are indicative of greater structural stability and can lead to longer cycling life.

$Na_{2/3}Ni_{1/3}Mn_{1/2}Ti_{1/6}O_2$ and $Na_xMn_yFe_zO_2$ are both examples of mixed transition metal positive electrode materials with high energy densities that display good cyclability [52,53]. These types of positive electrode materials based on abundant, low cost raw materials could enable commercial sodium-ion batteries, if paired with a practical negative electrode material. However, practical high energy density negative electrode materials for sodium-ion batteries have been much more difficult to achieve thus far.

2.2.3 Negative Electrode Materials for Sodium-ion Batteries

Graphite is the most commonly used negative electrode material in lithium-ion batteries [3]. It has the near ideal electrode characteristics of a high volumetric capacity density (~700 Ah/L with lithium), a low average voltage versus Li metal (~150 mV), outstanding Coulombic efficiency when appropriate electrolyte additives are used (~99.997%) and it can easily be compressed to low porosity in electrode coatings [3]. Lithium-ion battery researchers have the daunting task of improving upon these already amazing negative electrode characteristics. Many are trying to accomplish this by adding increasing amounts of high capacity silicon alloy to the graphite electrode formulation to make higher capacity composite negative electrodes [54]. Unfortunately, graphite cannot be utilized as a negative electrode material for NIBs as it does not intercalate any substantial amount of sodium, with $C_{64}Na$ being the most highly sodiated phase [15,16]. There are examples of co-intercalation of solvated sodium ions in graphite but this would be impractical as only low energy densities are possible with this mechanism due to the added bulk of the solvent [55].

Just as using metallic lithium as a negative electrode material in lithium-ion batteries is deemed inappropriate due to safety concerns, so too would sodium metal. These concerns would be magnified for sodium because in group I of the periodic table the alkali metal reactivity increases down the group. The temperature could quickly rise to the melting point of metallic sodium (98 °C) during thermal runaway and cause a violent reaction. Sodium has also been shown to be more reactive with organic electrolyte solvents and displays more extreme dendritic formation during cycling than lithium [56]. In this work sodium half-cells were employed but additional separator in the form of blown micro fiber (BMF) was also used. Using BMF in addition to Celgard gives a greater and more even stack pressure and tends to limit dendrite growth [57].

The sodium storage mechanisms described earlier are most prevalent in negative electrode materials, as positive electrodes are almost exclusively intercalation materials. Indeed the earliest example of a sodium-ion battery negative electrode besides metallic sodium was an alloy type material [25]. Negative electrode materials are typically described as either carbonaceous or non-carbonaceous. In the realm of carbonaceous materials, the most highly studied material by far is hard carbon. Hard carbon has been shown to reversibly intercalate sodium with capacities as high as 300 mAh/g or 450 Ah/L. Hard carbon is thought to be composed of two domains that are highly dependent upon synthesis conditions, with one domain consisting of graphite like layers while the other consists of micropores formed between the disordered carbon layers. The first report of reversible intercalation of sodium in hard carbon was in 2000 by Stevens and Dahn [58]. Other, more recent, studies on hard carbon have focused on improving capacity and cycle life with varied electrolytes [58–60]. Even with optimization, hard carbon still has a relatively low volumetric capacity of only 510 Ah/L. Only a fraction of the gravimetric and volumetric capacity become usable when one considers that a large percentage of the capacity occurs at voltages less than 50 mV. Below 50 mV it is thought that there are safety concerns due to sodium plating during fast charging or overcharging in full cells. Due to these challenges in carbon based materials for sodium-ion batteries, non-carbonaceous materials have also been explored.

The main types of non-carbonaceous negative electrode materials for sodium ion batteries studied to date include: conversion compounds, sodium alloys, organic compounds, and titanium based compounds. The first reported sodium conversion reaction was that of $NiCo_2O_4$ in 2002 [61] and others have emerged since such as CuO, SbO_2 and Fe_3O_4 [30]. CuO shows a first discharge capacity of 600 mAh/g or 2400 Ah/L, most of which is realized below 0.6 V, however 250 mAh/g of this capacity is irreversible [29]. This conversion reaction and others need to be improved as they are accompanied by a large volume expansion and large hysteresis which leads to very poor cyclability.

Elements of group 14 and 15 in the periodic table that have shown to form binary compounds with sodium include silicon, germanium, tin, lead, phosphorus, arsenic, antimony and bismuth. These alloy materials display more than twice the volume change of lithium, due to the larger ionic radius of sodium [15]. This creates a huge challenge to incorporate alloy based negative electrodes for sodium-ion batteries. The enormous volume expansion would likely restrict long term continuous cycling, as high mechanical stress and repeated passivation often leads to cracking of the electrode material and loss of electrical contact and ultimately capacity loss. Although strategies have been employed to combat the volume expansion, such as nano-architecture, binders, and electrolyte additives, it is likely impractical to formulate an electrode with solely an alloy material. Perhaps the best example of an alloy material for sodium-ion batteries is SnSb/C [62]. The electrochemical behavior of the composite alloy is clearly different from the individual metals. It has a capacity of 540 mAh/g (volumetric capacity not determinable based on information given in Reference 63) with decent cyclability of 80 % capacity retention over 50 cycles. Phosphorus is also attractive as it displays anomalously low volume expansion, which is likely due to the covalent character of Na_3P [63].

Before 2010 only three titanium based compounds for sodium-ion batteries had been reported in the literature, namely TiS_2, $NaTiO_2$, and NASICON-type $NaTi_2(PO_4)_3$ [31,64–66]. NASICON stands for sodium super ionic conductor and as such was tested as a solid electrode material for obvious reasons. Since then numerous publications have appeared that are based on titanium oxides and titanium phosphates for low voltage sodium intercalation. The lowest intercalation potential for sodium reported to date is that of $Na_2Ti_3O_7$, which has a capacity of 175 mAh/g at 0.3 V [67]. Unfortunately, this material is white (as are most titanates) with poor electron conduction, and therefore large amounts of carbon black are typically added to the electrode formulation which adversely affects the reversible and irreversible capacity. Another sodium titanate that has been studied with similar properties is $Na_2Ti_6O_{13}$ [68]. Titanium is most commonly found in the earth's crust as TiO_2. Titania is attractive as a negative electrode material due to its low cost, nontoxicity, abundance, and exceptional stability. The nano sized anatase-TiO_2 polymorph is electrochemically active versus sodium metal. It displays a reversible capacity of over 150 mAh/g or 580 Ah/L when cycled between 0 – 2.0 V [69]. Due to its nanosize with a large surface area this material results in an extremely large irreversible capacity on the first cycle.

Titanium phosphates such as $NaTi_2(PO_4)_3$ have been proposed as electrode materials as well, however, this material has an intermediate voltage of 2.1 V [65,66]. This might make it more appropriate for an aqueous cell, where low positive electrode voltages remain in the water electrochemical voltage window. A reversible capacity of

130 mAh/g was obtained for this material which is close to the theoretical capacity where two equivalents of sodium can be intercalated giving a fully sodiated phase of $Na_3Ti_2(PO_4)_3$. Due to the bulky and heavy phosphate group these types of materials have low volumetric energy densities of < 400 Ah/L.

Most recently, a sodium lithium mixed titanate, $Na_{0.66}Li_{0.22}Ti_{0.78}O_2$, was studied for sodium insertion [70]. This material is layered like the Na_xMO_2 materials discussed earlier. In this case the lithium ions reside in the transition metal layer with the titanium atoms, as they have similar ionic radii, while sodium occupies its own layer and has vacancies within this sodium layer as well. A reversible capacity of 100 mAh/g or 480 Ah/L is achieved which is proximate to the theoretical capacity based on vacancies within the sodium layer. The average voltage was reported to be 0.75 V which is higher than that of $Na_2Ti_3O_7$. The advantage of this material lies in the fact that it has extremely good cyclability (over 1200 cycles with 75 % capacity retention) due to its zero-strain character, as the structure remains virtually unchanged during cycling. Another advantage is the increase of electrical conductivity by incorporating another metal within the relatively insulating titanium layer, thereby reducing the amount of carbon black in the electrode formulation.

The studies done thus far on positive electrode and negative electrode materials for sodium intercalation show that sodium-ion batteries are feasible and might have some distinct advantages over lithium-ion [11,48,71]. These advantages could include a sheer abundance of raw materials, lower cost, unique structure types and lower environmental impact. There are certainly more examples of applicable positive electrode materials than negative electrode materials and thus the focus in this work was to explore materials with a low redox potential versus sodium metal for application as negative electrode materials, specifically materials that incorporated Ti^{4+} metal. The goal herein is to find materials with long cycle life and volumetric energy density comparable to current LIB electrode materials. Graphite and lithium display an energy density of 700 Ah/L, while hard carbon and sodium yields 450 Ah/L. Current $Na_xM_yTi_{1-y}O_2$ materials can give energy densities near 500 Ah/L and the goal herein is to improve upon this number by increasing the number of stable vacancies.

NIBs have already begun being commercialized with prototypes introduced by several companies, such as Faradion and Alveo Energy [72]. An 18650 (cylindrical cell with an 18 mm diameter and 650 mm long) proof of concept or prototype cell has been made by researchers at the CNRS and CEA in France [73]. These cells have an energy density of 90Wh/kg, which is similar to those of LIB 18650 cells when they were introduced. The lifespan of these cells exceeded 2,000 cycles, with the capability of charging and discharging very rapidly, making these results very promising.

2.2.4 NIB Electrolytes and SEI

The electrolyte in a sodium-ion battery typically consists of a sodium salt ($NaPF_6$, NaTFSI or $NaClO_4$) dissolved in an organic solvent mixture (propylene carbonate, ethylene carbonate, dimethyl carbonate and/or ethylmethyl carbonate). The electrolyte must conduct sodium ions. As electrolyte is in intimate contact with the electrodes, there exists an interface between the electrolyte and both the negative electrode and positive electrode. As such, there are some properties needed for electrolytes to comply with in order to be incorporated in a sodium-ion battery. The electrolyte must be chemically stable where no reactions occur between itself, separator, electrodes, current collectors, and casing materials. It must also be electrochemically stable, so that within the potential window of the battery operation no decomposition due to oxidation or reduction occurs. The electrolyte should be ionically conductive and electrically insulating to allow easy sodium-ion transport and minimize self-discharge. It should be thermally stable with a wide range of its liquid phase so it remains liquid during cell operation temperatures. Ideally electrolytes should also have low toxicity, be made of sustainable materials, and be economical.

No cell is completely chemically stable. However chemical stability at the electrode/electrolyte interfaces can be maintained through the formation of passivation layers. These layers are referred to as the solid electrolyte interphase (SEI) and they are more dominant on the negative electrode [74]. The formation and physical properties of these passivation layers is highly dependent upon both the electrolyte (especially additives) and the electrodes. On the negative electrode, the organic solvents typically used are reduced at low voltage, while they are typically oxidized at the positive electrode during high voltage. The SEI is ideally non-porous and ionically conductive while being electronically insulating. Once the SEI has formed it prevents further decomposition of the electrolyte as it insulates the electrode surface from the electrolyte, however it still allows sodium ion diffusion. The higher the electrochemically active surface area of an electrode, the greater the amount of SEI that is formed.

When forming of the SEI some of the initial sodium content is consumed leaving less for subsequent cycles. This is the origin of the large irreversible capacity observed during the first cycle of many cells. Ideally, after the first few cycles, the SEI almost completely forms and the Coulombic efficiency approaches 100 % during later cycles. The sodium metal titanates studied herein exhibit large irreversible capacities during the first cycle due to SEI formation, but the majority is likely due to carbon black in the electrode formulation. This will be discussed later in the text.

At this time the SEI in lithium-ion batteries is just beginning to be understood in terms of its thickness and chemical composition [74]. There are still many things that remain relatively unknown regarding the SEI. The sodium-ion battery SEI is thought to be different from the lithium-ion SEI, even though there are relatively few reports of the sodium-ion SEI [75]. For example it is thought that the sodium-ion SEI is richer in inorganic species with a more homogeneous distribution of components [76].

Additives are used in traditional electrolyte formulations for lithium-ion batteries. This is where the liquid electrolytes contain small quantities of a compound which positively affect the battery performance and/or safety. Additives engage in different reactions with the electrodes and electrolyte. Perhaps the most important function of additives is that of SEI formation. Vinylene carbonate is a common additive in LIBs that is used to form and maintain a SEI at the negative electrode surface. However, studies have shown that this same additive, vinylene carbonate, does not efficiently passivate hard carbon in sodium-ion cells [75]. This once again highlights the difference between sodium and lithium based chemistries. Another additive, fluoroethylene carbonate, has been found that very efficiently forms a film and improves cycling for different negative electrode materials for sodium-ion batteries, including hard carbon [75].

2.2.5 Full Cell Results

There have been relatively few full cell results reported in the literature, and where they have been reported, the number of cycles is typically very limited (<50). This makes it hard to determine whether sodium-ion batteries would have a lifetime appropriate for commercialization. The first example of a sodium-ion full cell comprised a lead negative electrode and P2-$Na_{2/3}CoO_2$ positive electrode [25]. With a somewhat limited voltage range of 1.5-3.3 V, the cell demonstrated decent cyclability over the course of 300 cycles. After hard carbon was found to intercalate sodium at low voltage with a high capacity in 2000 it has become the standard negative electrode for sodium-ion battery full cell work [58]. One such example is the hard carbon and $NaNi_{1/2}Mn_{1/2}O_2$ full cell which had a voltage of approximately 3 V and capacity of over 200 mAh/g (per gram of positive electrode material) with 80 cycles demonstrated [60]. Voltages as high as 4.5 V have been reported for hard carbon and $Na_4Co_3(PO_4)_2P_2O_7$ cells with over 100 cycles shown [77]. Full cell results have recently been presented for a layered sodium titanate negative electrode ($Na_{0.66}Li_{0.22}Ti_{0.78}O_2$) with $Na_3V_2(PO_4)_3$ operating as the positive electrode that show decent rate and cycling performance [70].

2.3 Layered Structures for Sodium Intercalation

Layered structure materials are typically good ionic conductors. This is because there exists an entire two dimensional network for facile ion diffusion. For this reason, the work herein focused on layered materials, with rapid sodium conduction, for NIB negative electrodes. The layered structures under study are closely related to the common sodium chloride structure [78]. Figure 2.3 shows the relationship between the NaCl and α-NaFeO$_2$ structures.

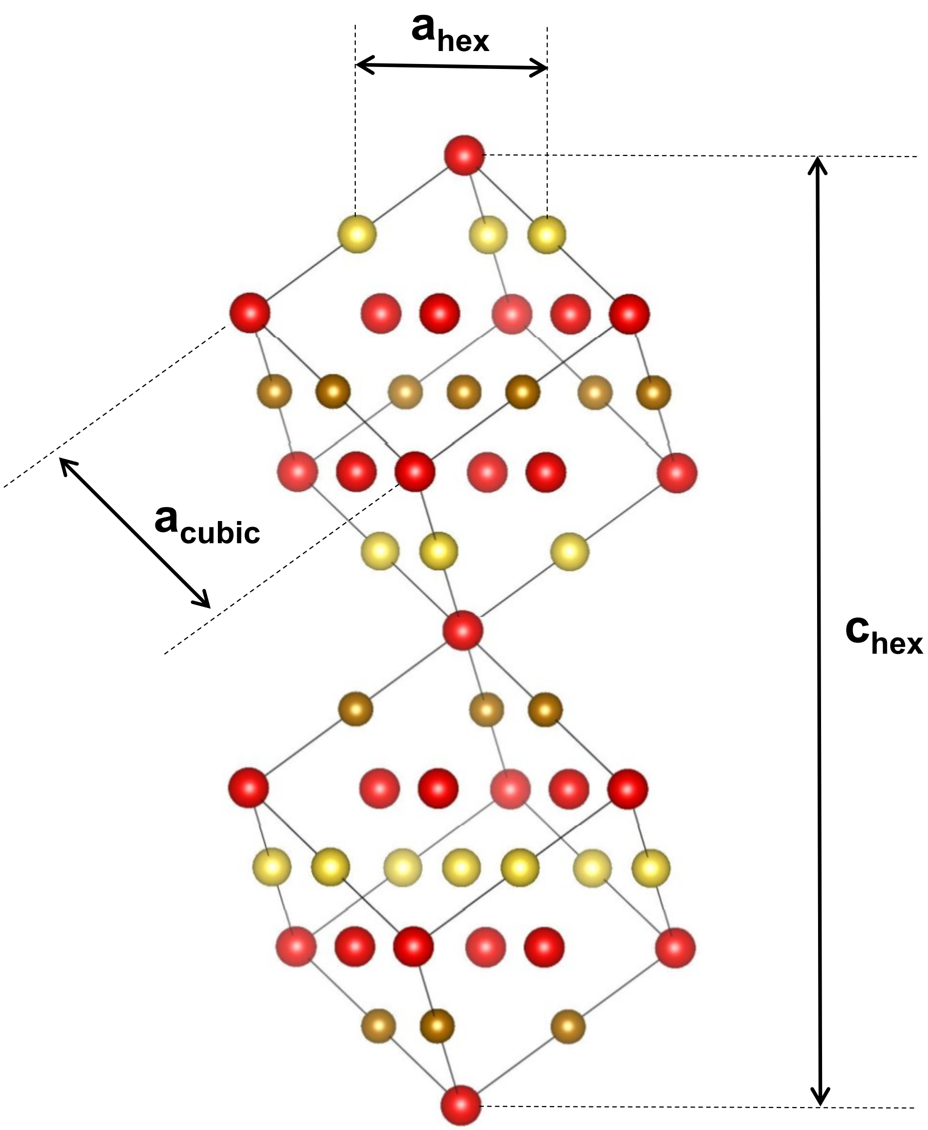

Figure 2.3: Two unit cells of the NaCl structure oriented so that they are sharing one vertex to show its layered nature and relation to hexagonal α-NaFeO$_2$. Sodium, iron and oxygen atoms are represented by yellow, orange and red spheres, respectively.

The α-NaFeO$_2$ structure has two cations and two anions according to its chemical formula and as such can be described according to two NaCl unit cells. The oxygen takes on the chloride sites while the sodium and iron occupy the sodium sites in the NaCl structure. The size difference between the two cations causes them to favour alternating layers, instead of mixing within the layers. This is depicted in Figure 2.3 where layers of sodium, iron and oxygen are shown as yellow, orange and red spheres, respectively. This is basically a face centered cubic network with metal cations occupying octahedral sites. The alternating of planes for the cations causes a rhombohedral distortion of the cubic lattice. This α-$NaFeO_2$ structure corresponds to the stacking in an O3 structure, according to the notation that will be explained below and utilized throughout this work. This notation is used to describe hexagonal layered oxides as it is easier to visualize the stacked layers. The relationship is further illustrated in Figure 2.3 where the lattice constant c_{hex} is the axis perpendicular to the (111) planes of the cubic lattice while the a_{hex} and b_{hex} lattice constants are parallel to these planes.

A specialized nomenclature to describe the AMO_2 (A = alkali metal and M = transition metal) materials with layered structures was introduced by Delmas, Fouassier, and Hagenmuller in 1980 [79]. These structures consist of alternating MO_2 sheets, consisting of MO_6 octahedra connected by their edges, with alkali metals sandwiched between those sheets at interstitial sites. This structure forms a foundation from which one can imagine different layered arrangements of the MO_2 sheets and geometry (coordination environment) of the interstitial sites that are occupied by the alkali metals. The nomenclature consists of a letter designating the coordination environment of the alkali metal and a number describing the number of MO_2 sheets in the hexagonal unit cell. Those two parameters are directly dependent upon the oxygen stacking sequence. The letter can be either a P (prismatic) or an O (octahedral) in the case where sodium is the alkali metal. For lithium T (tetrahedral) coordination is also possible, but prismatic coordination is not observed. The larger size of the sodium-ion prevents it from adopting tetrahedral geometry in layered transition metal oxides according to calculations reported in the literature [13]. However, there are instances where sodium occupies tetrahedral sites in oxides, *e.g.* Na_2O [80]. The larger size of sodium also makes it more prone to alkali metal ordering, but thus less prone to cation mixing with transition metals [13]. Figure 2.4 shows the common P2, O3, and O'3 monoclinic structures. Other possible layered structures include O6, O2, and P3. In the case of O3 and P2, the oxygen stacking sequences are ABCABC and ABBA, respectively.

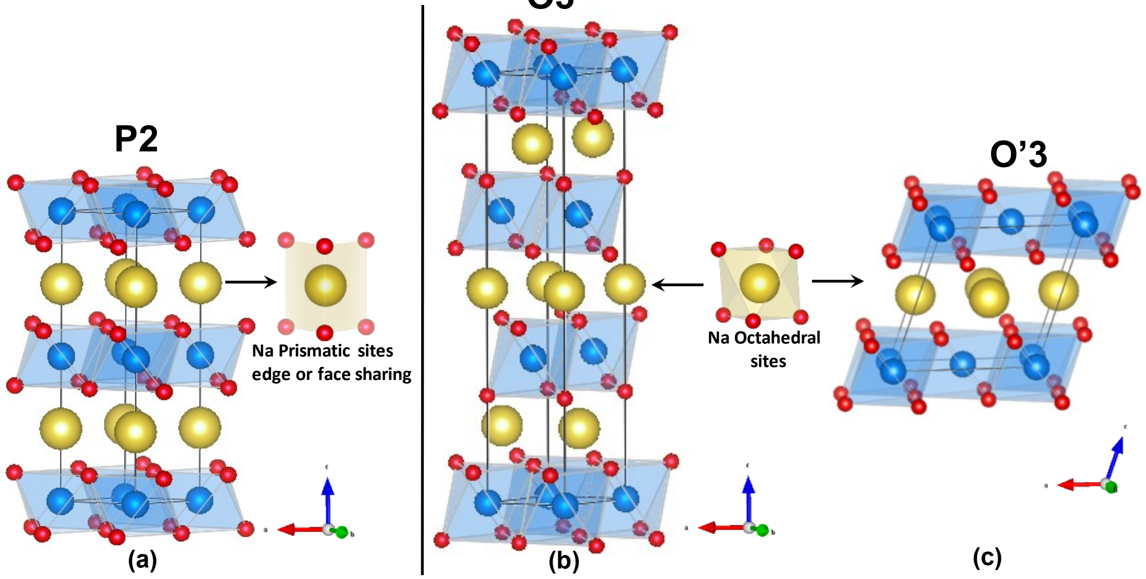

Figure 2.4: Common layered structures for sodium-ion batteries (a) P2, (b) O3 and (c) monoclinic or O'3. Red, yellow and blue spheres represent oxygen, sodium and metal atoms, respectively.

Monoclinic distortions commonly occur and are indicated by an apostrophe, as in O'3. The O3 structure can become distorted to O'3 by either a slight gliding of the slabs in the (a, c) plane which distorts the sodium sites or by a distortion of the MO_6 octahedra due to the Jahn-Teller effect [81]. Another common structural feature observed in these materials is cation ordering. This will be discussed later in Chapter 4.

CHAPTER 3 EXPERIMENTAL METHODS

In this chapter, synthesis methods of layered sodium-ion battery materials are described. A brief overview of X-ray diffraction (XRD), neutron diffraction, scanning electron microscopy (SEM), inductively coupled plasma optical emission spectroscopy (ICP-OES), pycnometery, Fourier transform infrared spectroscopy (FTIR) and differential scanning calorimetry (DSC) methods is also given as these were the main techniques employed to characterize the materials. This is followed by a description of how materials were incorporated into electrochemical cells. Further descriptions are given of various battery characteristics that were used to distinguish the materials, merit for use in sodium-ion batteries. These metrics of battery testing are included so that a reader who is not familiar with them will still be able to understand the results of the thesis. This will enable one to judge the merit of this work, compared to the work currently found in the literature.

3.1 Synthesis

Layered sodium mixed transition metal oxides were synthesized via solid state reactions. This so called solid state or ceramic synthesis method allows interdiffusion of the solid precursor materials on a reasonable timescale by using elevated temperatures to obtain the layered metal oxides. This type of reaction is diffusion controlled so the contact surface area was often maximized by pelletizing [82].

Roughly six grams total of precursors consisting of sodium carbonate and various transition metal oxides were weighed out, according to stoichiometry. The powders were then ball milled together in a SPEX 8000 high energy ball mill for thorough mixing. The high energy ball milling often causes the precursors to not only mix, but react chemically as well. Minimal iron contamination is present in these samples despite milling in a hardened steel vessel, as confirmed by inductively coupled plasma optical emission spectroscopy. Precursors were milled for a half hour in the ball mill. Generally, a 3:1 ball: sample mass ratio with a typical sample size of six grams and four stainless steel balls of half inch diameter were loaded into a milling vessel, under either inert argon atmosphere or air. At times the powders were pressed into two gram pellets after SPEX milling. Milled powders or pellets were then directly transferred to an alumina boat and placed in a tube furnace equipped with a quartz tube that had fittings on each end to allow control of the gas flow and pressure. The samples were then fired at high temperatures (as high as 1100 °C) in different atmospheres (ambient air, argon, H_2/argon mix) for differing amounts of time (6 – 48 hours) in a tube furnace. The effect of different atmospheres can lead to different phases forming, as some atmospheres are comparatively more oxidizing while others are more reducing. The exact synthesis methods are reported in the results section for each individual material tested. Synthesis of single phase layered materials was not trivial and oftimes many different precursor treatments, temperatures and atmospheres were tried in order to obtain the desired phase. All of the carbon and hydrogen in the samples leaves the samples as carbon dioxide and water during the heating process.

The precursors used in the series syntheses were: Na_2CO_3 (BioXtra, ≥ 99.0% Sigma Aldrich), Cr_2O_3 (50 µm, ≥ 98 % Sigma-Aldrich), V_2O_3 (99.7 %, metals basis, powder, Alfa Aesar), and anatase TiO_2 (puriss, 99 to 100.5 %, Sigma-Aldrich). An excess amount of the sodium carbonate precursor, usually 5 % by weight, was added to compensate for the loss of sodium due to the volatility of sodium containing precursors at the high reaction temperatures. For this reason, the elemental composition of the samples was determined by ICP-OES where possible. After heat treatment the samples were either slow cooled or quenched to room temperature under gas flow by removing the tube from the furnace to achieve the desired phase of the material. All samples were transferred directly to an argon filled glovebox while still in the furnace tube after the heating step to avoid air exposure, as many of the samples were found to be hygroscopic. Even those samples heated in air were removed at 200 °C and transferred directly to an argon glovebox, to avoid water contamination.

3.2 X-ray Crystallography

The main technique utilized in this work to characterize sample powders was XRD. XRD is a flexible, non-destructive technique that reveals detailed information about the chemical composition and crystallographic structure of materials [83]. A crystal structure can be defined by its unit cell as this is its simplest description at the atomic level. Therefore, the unit cell is a regularly repeating unit that can defines the entire bulk crystal structure. The unit cell dimensions can be described by three lattice constants and three lattice angles. These different lattice constants and angles lead to fourteen types of lattices, referred to as the Bravais lattice types. Atoms exist within this framework of a unit cell and are described by their atom positions in terms of the unit cell axes. XRD can be used to identify crystal structures and can reveal whether multiple lattice types or structures are present in a given sample.

3.2.1 X-ray Generation

For an XRD experiment to be performed X-rays must first be generated. The generation of X-rays is accomplished by electrons that are emitted from a heated filament and then accelerated in a vacuum by a high electric field, on the order of tens of kilovolts, towards a metal negative electrode, such as copper. These incident electrons are of such high energy that they interact with the electrons of the metal, knocking them out of the inner shells of the atomic electron energy levels. This allows higher energy electrons to “drop down” into a lower energy level and fill the void that was left. This dropping down in energy level results in an emission of energy in the form of X-radiation as shown in Figure 3.1.

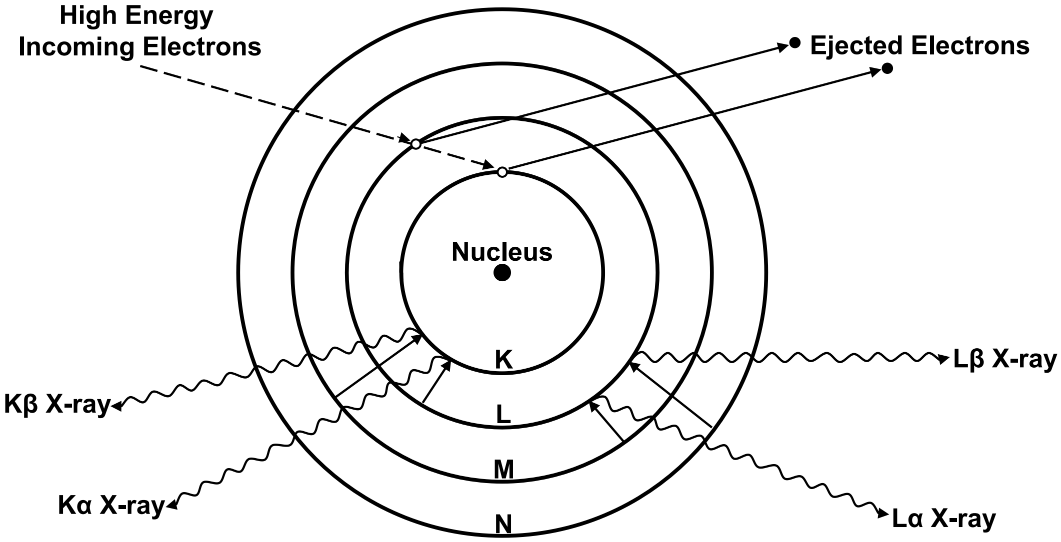

Figure 3.1: X-rays generated by incident electrons.

A particular wavelength emission is selected by a monochromator. For experiments described here Cu Kα radiation was used. It contains two wavelengths, a strong emission (Kα_1 at 1.54056 Å) and a weaker emission, by exactly two times from quantum mechanical effects (Kα_2 at 1.54439 Å) [83]. Peaks resulting from the diffraction of both of these wavelengths are present in well-resolved diffraction patterns.

3.2.2 Bragg Diffraction

Incident X-rays, once generated, is applied to a sample that typically possesses a crystal structure or lattice, however amorphous samples and liquids can also be studied. A crystal lattice is a regular three-dimensional distribution of atoms in space. The lattice of atoms can be thought of as residing in a series of parallel planes separated from one another by a distance *d*. This distance will vary according to the structure of the material. Planes can and do exist in a number of different orientations for any crystal, each with its own specific *d* spacing. These *d* spacings are on the same order of magnitude as the wavelength of incident X-rays, which causes these waves to diffract. The resulting diffraction pattern allows one to determine the exact structure of a sample. The structure determination is possible due to Bragg's Law, which is depicted in Figure 3.2.

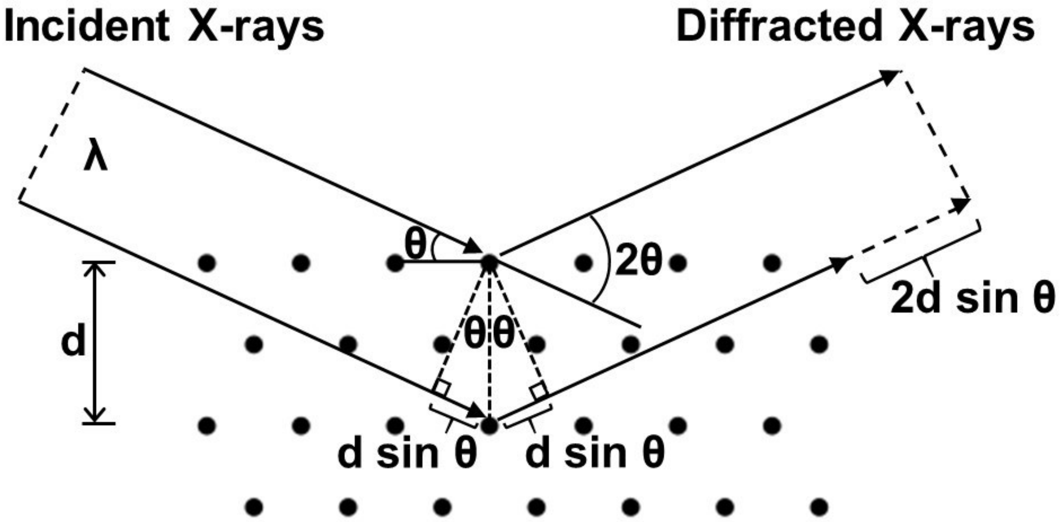

Figure 3.2: Bragg Diffraction from lattice planes in a crystal structure.

X-rays can be scattered from the top plane of a crystalline material or be transmitted through the sample to be scattered by planes that are deeper in the structure. This causes the beam reflected from the sample to have multiple phases that can interfere destructively or constructively with one another. The interference depends on the distance of the lattice spacing. This can be summed up using the equation for Braggs' law,

$$2\,d\sin\theta = n\,\lambda\,, \tag{3.1}$$

where n is an integer that indicates the order of diffraction, λ is the wavelength of the incident wave of X-rays, d is the spacing between the planes in the crystal lattice, and θ is the angle between the incident X-rays and the diffracting planes. A diffraction pattern is obtained by measuring the intensity of scattered X-ray waves as a function of scattering angle. Very strong intensities known as Bragg peaks are obtained at specific scattering angles in the diffraction pattern when scattered waves satisfy the Bragg condition. These Bragg peaks allow the plane spacing, d, to be determined. For example, Braggs' law can be used to obtain the lattice spacing of a particular simple cubic system through the following relation,

$$d = \frac{a}{\sqrt{h^2 + k^2 + l^2}} \tag{3.2}$$

where a is the lattice constant of the unit cell of the cubic crystal and h, k, and l are the Miller indices of the specific Bragg plane. Miller indices are a notation system in crystallography that consists of three integers which describe the group of planes in question. The h, k, and l values are actually the reciprocal of the fractional coordinates where the plane intercepts the x, y, and z axes. There are similar but much more complex relations for the other crystal structure types [83].

The obtained experimental XRD pattern can also be compared to a database for phase determination (qualitative analysis). Further characterization can be done using Rietveld refinement, which uses a least squares approach for quantitative analysis. This approach takes a theoretical line profile and changes it incrementally until it matches as closely as possible the measured or experimental profile. This allows for the determination of precise crystallographic structural information, such as atom positions, lattice constants, and site occupations. A powder XRD calculation of the total peak intensities, I, takes into account five factors as follows,

$$I(\theta) = I_0\, P(\theta)\, L(\theta)\, F^2(hkl)\, M(hkl) DW(hkl) \tag{3.3}$$

where I_o is the intensity of the incident radiation, $P(\theta)$ is the polarization factor, $L(\theta)$ is the Lorentz factor, $F^2(hkl)$ is the geometric structure factor, $M(hkl)$ is the multiplicity factor, and $DW(hkl)$ is the Debye-Waller factor [84]. These take into account the θ dependence of the peak intensity (both polarization and Lorentz factor), the interference between atoms within the unit cell, families of planes which have the same d-spacings, and the thermal vibration of atoms respectively [83]. All Rietveld refinement done in this work used the computer program Rietica to fit experimental data [85]. Structures were also visualized in another computer program called Vesta and all figures in this work depicting crystal structures were drawn using Vesta [86].

3.2.3 X-ray Diffraction Measurements

The crystallographic structures of the samples were determined by analysis with a Rigaku powder diffractometer X-ray system equipped with both a scintillation and linear detector. The scintillation detector with a diffracted beam monochromator was used to measure XRD patterns of some powder samples, while the D/TeX Ultra linear detector with a K-beta filter was typically used for *in situ* XRD measurements. This X-ray system is equipped with a Cu target X-ray tube. It uses a Bragg-Brentano θ:2θ geometry where the powder sample is stationary at the center of the focusing circle during measurements. The X-ray source and detector positions are varied at a constant distance from the sample with an equal angle θ. This is done using a computer controller, which also varies other parameters such as slit widths and scan rate. Figure 3.3 shows a general schematic of the Bragg-Brentano goniometer geometry.

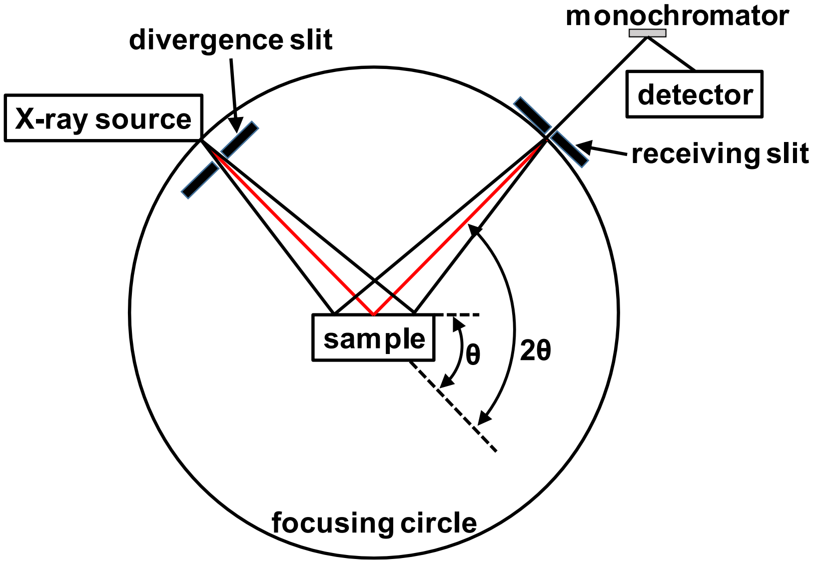

Figure 3.3: Schematic of the Bragg-Brentano geometry.

A filament current of 40 mA and an accelerating voltage of 45 kV were typically used to generate the X-rays. For XRD measurements, because most of the powder samples were hygroscopic they were loaded into a gas tight X-ray sample holder (DPM Solutions, Hebbville NS). The sample holder had an aluminized Mylar window mounted in an arc such that it was perpendicular to the incident and scattered X-ray beam and did not contribute to the measured XRD patterns. X-ray diffraction patterns were collected for each sample at a typical scattering angle range of 10 to 70 degrees 2θ with a step of 0.05 degrees and a scan rate of four degrees per minute. Specific experimental X-ray data collection conditions are specified for each material in later sections, particularly *in situ* and *ex situ* measurement set-up.

3.3 Neutron Crystallography

Neutron powder diffraction was carried out by the Neutron Scattering Branch at the Canadian Nuclear Laboratories' NRU reactor in Chalk River, Ontario, Canada. Using the C2 beamline with an 800 wire neutron detector several of the powder samples herein were loaded in a vanadium holder and studied with neutrons that had a wavelength of 1.328 Å.

Neutron diffraction is similar to X-ray diffraction as both display wave-particle duality with similar wavelengths (~2 and 1 Å, respectively) that can diffract from a crystal lattice. Thus, many of the principles discussed in section 3.2, X-ray diffraction, are also applicable here [87]. Although the same scattering theory can be utilized for both the major differences will now be emphasized in order to understand why neutron diffraction was employed in this work.

Neutrons, as the name implies, have no charge and can penetrate matter much better than charged particles. But perhaps the most contrasting difference between neutron and X-ray diffraction is how they interact with atoms in a crystal lattice. X-rays, as has been seen, interact with electrons, while neutrons are scattered by atomic nuclei. Due to this, neutron scattering from light elements is extremely dissimilar. The one electron on a hydrogen atom can be hard to see with X-rays but the hydrogen nucleus scatters neutrons strongly and is easily seen in a neutron diffraction experiment. This can be explained by the strength of the interaction between the X-ray and electron or neutron and nucleus, referred to as the scattering length. The scattering length for X-rays increases with atomic number, while neutrons follow no trend and vary erratically with atomic number. Isotopes of the same element can actually have very different neutron scattering properties.

As a result of the difference in scattering properties from element to element, neutrons are often utilized to discriminate between different atoms in crystal structures. This was done in this work as the first row transition metals in the layered structures of this thesis are typically indistinguishable in XRD experiments, as they have similar numbers of electrons and thus similar scattering power. However, the neutron scattering lengths of the natural isotope abundance of the first row transition metals are quite different. Neutron diffraction experiments are able to detect transition metal ordering within the metal layer of these types of materials.

When comparing diffraction patterns for the two techniques one will notice that the in XRD patterns the highest intensity peaks tend to be at low angles while intensity is quite uniform over the entire pattern for NPD. The scattering power has no angular dependence for neutrons while the scattering power falls off at higher angles for X-ray experiments. This is due to nuclei being considered point scattering centers while it is the large electron clouds of atoms that scatter X-rays.

Even though the neutron has no electric charge it has a magnetic dipole moment. This allows the magnetic structure of materials to be determined by neutron diffraction experiments as well. Neutrons are able to scatter from local magnetic fields within matter to provide a probe of electron spin fluctuations and ordered magnetic structures.

To summarize, neutron diffraction is a non-routine complimentary technique to X-ray diffraction based on the same principles. It allows further structural details, such as the detection of lighter elements, discrimination of neighboring elements (ordering), and recording of higher intensity Bragg reflections at higher angles, to be examined.

3.4 Scanning Electron Microscopy

A Phenom G2-pro scanning tabletop electron microscope (SEM, Nanoscience, Arizona) equipped with a backscatter detector was used to determine the microstructure of powder samples. A focused electron beam was rastered across the samples in a vacuum, where the electrons were scattered from the sample and detected. The intensity of electrons emitted from the sample was displayed as a brightness image (grayscale) on a computer monitor. This is made possible because as a rastered image the detector synchronizes the position in the image scan to that of the scan of the incident electron beam. Two types of electron detectors are common, namely secondary and backscattered.

Using the SEM posed several challenges for the powder samples in this work. Sample mounting had to be done using double sided carbon tape in order to get a flat sample and to avoid loose powder. Samples also had to be sufficiently conductive to avoid building up an electrical charge, which can cause images to become extremely distorted.

3.5 Inductively Coupled Plasma Optical Emission Spectroscopy

The elemental composition of powder samples was determined by inductively coupled plasma optical emission spectroscopy (ICP-OES). Powders were typically prepared for analysis by dissolving a small amount into nitric acid and then diluting to the appropriate volume. Standard solutions of each element were also prepared to obtain calibration curves. During an ICP measurement, the elements in the sample solutions were transformed into gaseous atoms and excited by the high temperature plasma torch. The excited atoms emit electromagnetic radiation of characteristic wavelengths for each particular element. The intensity of the emissions indicates the concentration of each element. The atomic ratio of sodium in these samples was of utmost importance as sodium can be lost during the high temperature synthesis and the capacity of the negative electrode materials was highly dependent upon the amount of sodium present. ICP data can be interpreted incorrectly, especially if more than one phase is present in samples. This complication will be discussed further in the text.

3.6 Helium Pycnometry

True density measurements of the as prepared powder samples were made using an AccuPyc II 1340 gas displacement pycnometer using He gas (ultrahigh purity, 99.999%). The pycnometer was calibrated with a given sample cup and a standard, for which the volume was known (given by the supplier). The calibration was repeated until the measured volume of the standard and the given volume agreed within the variance. The samples under investigation were stored in an argon filled glovebox and first transferred to accurately weigh (~1 g) and then transferred to the pycnometer chamber with minimal exposure to air. The measurement was initiated by purging the sample with helium gas five times. The purge-fill pressure and the cycle-fill pressure were set to 19.5 psig. Each run involved five cycles with an equilibration end time of 1 min. The average volume from the five cycles was calculated to deduce the density of the samples. The true density measurements were then compared to the density calculated from XRD measured lattice constants. If the two did not agree then typically more sodium vacancies were present in the sample than expected (as sodium is lost at high synthesis temperatures). This could then be checked by ICP measurements.

3.7 Fourier Transform Infrared Spectroscopy

Fourier transform infrared (FTIR) spectra were recorded using an Agilent Cary 630 FTIR spectrometer, which was located inside an inert atmosphere glove box. Infrared radiation of different wavelengths is passed through a sample and some of this radiation is absorbed by the sample and some passes through, being transmitted. The data are typically given as a percent transmittance versus wavenumber graph. The spectrum represents a molecular fingerprint of a sample. Different chemical structures produce different spectral patterns. These patterns are due to the fact that materials absorb frequencies of light that correspond to the different vibrational frequencies within their structure. This simple technique is more widely used for organic materials. In this work, FTIR was used to study inorganic materials and detect impurity sodium organic phases that may be present.

3.8 Differential Scanning Calorimetry

Differential scanning calorimetry (DSC) was used to probe the thermal stability of select materials in this work. Measurements were done using a TA Instruments Q-200 DSC up to temperatures of 500 ºC with a scanning rate of 10 ºC/min. Approximately 10 mg samples were loaded in hermetic aluminum pans in an argon glovebox. During a DSC measurement a sample of known mass is heated and the power is measured. The differential term in DSC comes from the fact that a sample and reference are both run simultaneously and the amount of power required to increase the temperature of both at the same rate is measured. The reference typically has no changes in heat capacity over the entire temperature range to be tested. This results in a heat flow versus temperature plot, for the sample under study, with peaks and valleys. These features arise from the physical transformations of the sample during heating, where more or less heat will need to flow in order keep the sample and reference at the same temperature. Whether more or less heat is needed to flow depends on if the process endothermic (melting) or exothermic (crystallization), respectively.

3.9 Electrode Fabrication

Once the synthesized powders were characterized via XRD analysis they were incorporated as active materials in composite electrodes for further testing. Electrodes were constructed in an argon atmosphere by combining the active material, a carbon black conductive diluent (C-NERGY SUPER C 65, Imerys Graphite & Carbon), and a PVdF binder (poly(vinylidene fluoride), average MW ~534,000 by GPC, powder, Sigma-Aldrich) in an 8:1:1 weight ratio. An adequate amount of N-methyl-2-pyrrolidone (Sigma Aldrich, anhydrous 99.5%) was added to the components until a desired viscosity was achieved. The mixture was then thoroughly mixed with two half inch diameter tungsten carbide balls in a Retsch PM200 rotary mill (100 rpm, 1 hour) to create a uniform black slurry. At this slow speed and short milling duration, the planetary mill effectively disperses particles in the electrode slurry, but does not reduce grain size. The slurry was then coated onto aluminum foil using a 0.006-inch (0.1524 mm) spreader bar and dried under vacuum at 120 °C for two hours. Circular electrodes, area 1.33 cm^2, were punched from the resulting coatings, which resulted in active material electrode loadings in the 1-2 mg/cm^2 range.

3.10 Electrochemical Studies

The performance of synthesized materials for application in sodium-ion batteries was analyzed using half-cell type 2325 coin cells with a Maccor cycler. Coin cell preparation was carried out in an argon filled glove box. For the negative reference electrode, thin sodium metal disks were used. These disks were punched from thin foil that was cold-rolled from a sodium ingot (Sigma Aldrich, ACS reagent grade), since sodium foil is not readily available. The surface of the sodium ingot was first scraped clean in an argon filled glovebox to remove the outer oxide coating. A small ingot was then placed in a plastic bag and passed through a PEPE Tools® foil roller multiple times, as the roller distance was decreased. This was repeated until the roller distance, as measured by a feeler gauge, corresponded to a foil thickness of approximately 0.016-inch (0.4 mm).

The electrolyte used was typically 1 M $NaPF_6$ (99+ %, crystalline, Alfa Aesar) dissolved in propylene carbonate (Selectilyte PC, BASF). A total of 120 μL of electrolyte solution was pipetted into each coin cell. Celgard 3501 and BMF (blown microfiber separator, 3M Company) were used as separators. BMF was used to improve cycling over Celgard® separator alone by simultaneously increasing the distance between electrodes, while providing a more even stack pressure and thus limiting sodium dendrite growth. Figure 3.4 shows the components of a sodium half-cell.

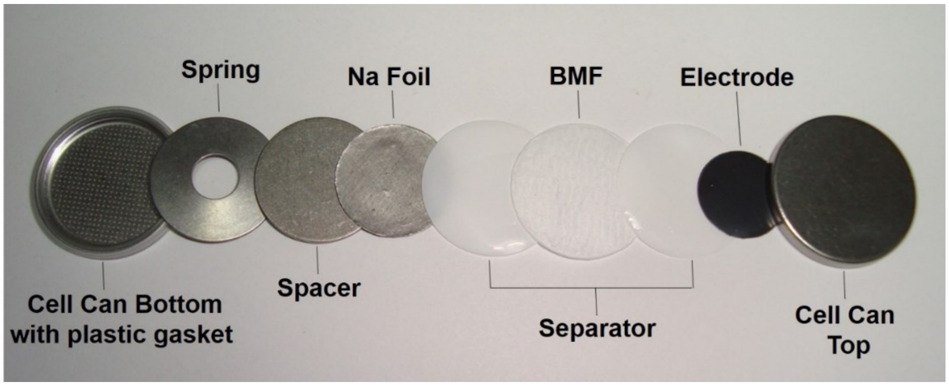

Figure 3.4: Sodium coin cell assembly.

Cells were tested using a Maccor Series 4000 automated cycler and were typically cycled at 30 °C at a constant current of C/10, calculated based on the capacity for each separate active material. Cycling was done for different voltage windows, depending on the electrode material. Low voltage cycling was typically done from 5 mV to 2 V. Again, specific experimental details will be emphasized for each material in their respective chapters.

In situ type coin cells were also constructed using the same procedure as described above for the 2325 type coin cells, except the cell can had a circular opening cut in it to receive a thin Be window. An electrode was then made directly on the Be window, using the coating procedure described above. The Be window was then affixed in the cell can using an acrylic adhesive (Super 77 Classic Spray Adhesive, 3M). After crimping shut, the *in situ* cell was cycled between specific voltages at a rate of C/10 calculated based on the capacity for each separate active material.

3.10.1 Full Cell versus Half-cell Studies

Sodium half-cells were used in this work to analyze the electrochemical properties of battery electrode materials. However, coin cells can be constructed as either a full cell, half-cell or symmetric cell. It is important to distinguish between the three types and understand why half-cells were utilized herein. Coin cells consisting of a working electrode comprising the active material of interest vs. a sodium metal reference/counter electrode are termed half-cells. These cells are most commonly used in the sodium-ion battery research community for active materials exploration. This is because as long as limited current and cycling times are used, the potential of sodium metal remains nearly constant during the operation of the cell, namely 0.00 V versus Na/Na^+ or -2.71 V versus SHE. Thus, sodium metal acts as both the reference and counter electrode and the potential is measured directly versus the Na/Na^+ potential. This allows important electrode characteristics, such as potential vs. Na content, to be easily studied vs. a constant voltage reference. Figure 3.5 shows a schematic of sodium-ion half-cells during both charge and discharge operation.

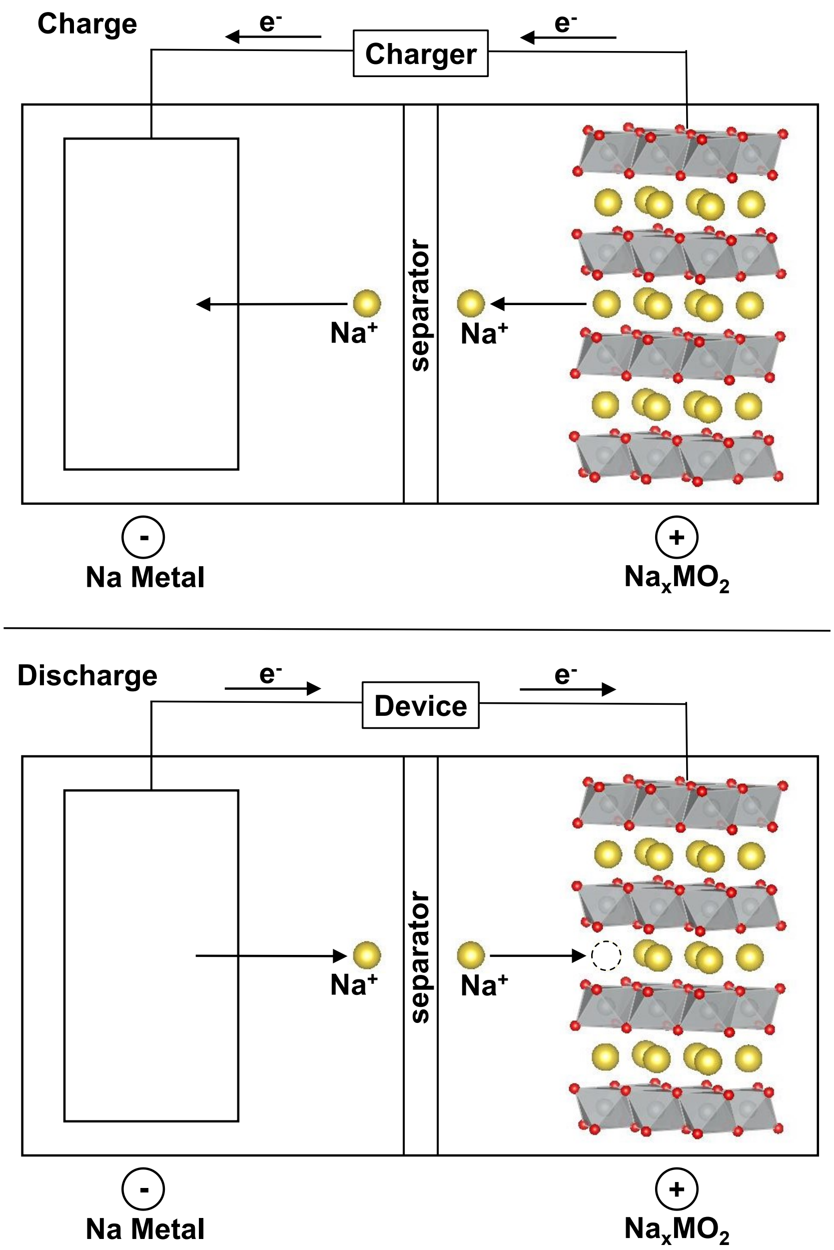

Figure 3.5: Schematic diagram of Na-ion half-cells during charge and discharge operation. The yellow, red, and grey spheres of the positive electrodes are sodium, oxygen, and transition metal ions respectively.

Understanding each electrode material in terms of potential, polarizability and cyclability is necessary before putting them into a full cell battery. This allows one know what cut-off voltages to use. This why initial or exploratory studies on electrode materials typically begins with half-cells. However, the half-cells have the disadvantage of using a somewhat unstable alkali metal reference/counter electrode which can react with common non-aqueous electrolytes, causing high cell impedance. In the extreme case this is expressed as dendrite formation which can short the cell. Due to this reactivity, half cells cannot be used for long term studies.

After half-cell evaluation, full cells are often used to evaluate electrodes in an environment that is more similar to their ultimate use in a commercial battery. Full coin cells use insertion active materials for both the positive and negative electrodes, often without a reference electrode. Another common coin cell configuration is symmetric cells. Symmetric cells use the same insertion material for both of the electrodes, with one containing the alkali metal while the other does not. A symmetric cell displays an average voltage of zero, however, it can provide information about reactions between the electrode materials, as well as reactions between electrode materials and electrolytes. Symmetric cells are particularly useful because their fade rate is an accurate measure of electrode Coulombic efficiency.

3.10.2 Galvanic Cycling and Capacities

Galvanic cycling is also termed constant current cycling. As such, the current applied to the battery during the charge and discharge cycles is held at a constant value. In cycling this way one controls the amount of current or charge that is supplied to the battery and measures the voltage at which the charge is stored. From this data, potential versus capacity can be plotted. Galvanic cycling is the type of cycling employed in this work. This is in sharp contrast to cyclic voltammetry that is most common in electrochemistry. It is opposite of galvanic cycling in that during cyclic voltammetry the voltage is controlled and the current is measured, which gives a potential versus current plot.

Electrode materials have a characteristic amount of sodium and charge that they can store. A performance metric of a sodium-ion battery that accounts for the sodium-ion storage ability of the material is termed the "specific capacity". This is the amount of charge that a material can store per unit mass. This is shown in Equation 3.4,

$$\text{Specific Theoretical Capacity} = \frac{nF}{MW} \times 1000 \tag{3.4}$$

where n is the number of moles of sodium that can be stored per mole of the material, F is Faraday's constant (26.802 Ah/mol) and MW is the material's molar mass per formula unit(g/mol). This gives mAh/g as units for specific capacity. This indicates how many moles of sodium can be stored in the crystal structure of an electrode material, per mole of that material. Therefore, the greater the number of moles of sodium a material can store and the lighter it is, the higher its theoretical specific capacity.

In a full cell battery, the greater the potential difference in the redox voltages of the negative electrode and positive electrode the greater the voltage of the cell. Thus, it is desirable to have as low a voltage as possible for a negative electrode and as high as possible voltage for a positive electrode, as a greater voltage will translate to higher energy stored for a specific capacity. The importance of a material's voltage is demonstrated by the following equation for specific energy density,

$$\text{Specific Energy Density} = \text{Specific Capacity } (mAh/g) \times \text{Voltage } (V) \tag{3.5}$$

which gives the amount of energy that a battery can store in typical units of Wh/kg. Both the specific capacity and specific energy density can be converted to volumetric capacity and volumetric energy density, respectively, by multiplying by the density of the material yielding units of mAh/L and Wh/L, respectively. These are very meaningful metrics as for nearly all applications the energy stored per unit volume is of greater importance than the energy stored per weight.

3.10.3 Differential Capacity

Another common way to show cell performance data, besides a voltage versus capacity plot, is a differential capacity (dQ/dV) plot. This represents the amount of charge that is stored per change in voltage. Often, when presented this way features in the voltage versus capacity plot are much easier to distinguish. For example, whenever there is a plateau in the voltage versus capacity plot there is a sharp peak in the corresponding differential capacity plot. This is indicative of a large amount of sodium being transferred with a very small change in the voltage of the cell. This typically occurs during a phase transition.

3.10.4 C-rate

During the constant current (galvanostatic) cycling of a half-cell there is a specific way to define the magnitude of the current delivered to and from the cell. The current is not specified in units of just amps, but by relative units which are scaled to a material's capacity. This is what is termed the C-rate. C-rate refers to the total current that would result in the complete charge or discharge of an electrode material in one hour. A common C-rate used throughout this thesis is C/10. This means that a cell is charged or discharged in 10 hours. On the other hand, a C-rate of 5 C means a cell is charged or discharged in 12 minutes (1/5 hour).

The ideal battery would deliver the same capacity irrespective of the C-rate it was subjected to. Oft times, this is not the case and most batteries lose capacity with increased rate. How well a battery copes with changes to the C-rate is designated as its rate performance. This is measured by testing the cell with different C-rates in succession (lowest to highest) to gauge how much capacity is lost with increased rate.

3.10.5 Voltage Hysteresis

The charge and discharge profiles of an electrochemical cell are always separated by a certain voltage during galvanic cycling. The difference between the charge and discharge voltages is termed voltage hysteresis. The voltage hysteresis can be decreased by decreasing the rate of cycling, particle size or the electrode thickness [88]. All of these strategies involve decreasing the current density or impedance due to charge transport. However, even at extremely small currents there exists a voltage gap or hysteresis [89]. This type of hysteresis is only observed in materials where cycling is described by a single reaction, such as intercalation reactions. Certain conversion reactions display large voltage hysteresis which is predominantly due to different reaction pathways upon charge and discharge.

A large voltage hysteresis is undesirable as it makes a battery inefficient due to energy lost as heat during cycling. This is one of the main reasons that layered intercalation materials were studied herein. They typically have low hysteresis, which is inherent to their structure, and they display long cycle life. A large portion of the hysteresis seen in this work is expected to result from large current densities used, as discussed above. However, the current densities were kept constant from material to material so that meaningful comparisons could be made. The average voltage hysteresis was often calculated based on the second charge and discharge cycle. This was done by performing a Riemann sum of the voltage versus time data.

Another way to express the hysteresis is the voltage efficiency, which is defined as the ratio of the discharge voltage to the charge voltage as seen in Equation 3.6,

$$VE = \frac{V_{discharge}}{V_{charge}} \tag{3.6}$$

where $V_{discharge}$ and V_{charge} are the average voltage during discharge and charge. Voltage efficiency would be equal to 1.0000 if there was no polarization whatsoever and the cell was operating at equilibrium conditions. Thus, voltage efficiency can be a good indicator of cycle life.

3.10.6 Coulombic Efficiency

Due to reactions that occur within any electrochemical cell, the charge and discharge capacities of any given cycle will not be equal. This asymmetry is captured in the metric of Coulombic efficiency. It is defined as the ratio of the discharge capacity of a cycle to the charge capacity of the cycle that immediately follows it, as seen in Equation 3.7,

$$\mathrm{CE} = \frac{Q_{charge}}{Q_{discharge}} \tag{3.7}$$

where $Q_{discharge}$ and Q_{charge} are measured capacities (mAh/g) of the corresponding cycle. The ideal cell would have a Coulombic efficiency of 1.0000 and cycle indefinitely, owing to the fact that no parasitic reactions are taking place and the charge transferred on both the charge and discharge of the cell are equal. This is never the case for sodium-ion half-cells and typical Coulombic efficiencies on the order of 0.990 or less are observed.

CHAPTER 4 $Na_xCr_xTi_{1-x}O_2$ (0.6 ≤ x ≤ 1)

4.1 Introduction

Titanium oxides and phosphates display a low average voltage versus sodium. Examples include TiO_2, $NaTi_2(PO_4)_3$, and $Na_2Ti_3O_7$ [66,67,90]. More recently, layered sodium titanium oxides substituted with another transition metal, such as $Na_xNi_{x/2}Ti_{1-x/2}O_2$ ($0.5 \leq x \leq 1.0$), $Na_{2/3}Ni_{1/3}Ti_{2/3}O_2$, $Na_{2/3}Co_{1/3}Ti_{2/3}O_2$ have been reported [91–93]. When cycled to low voltages in sodium cells, these $Na_xM^{2+}{}_{x/2}Ti^{4+}{}_{1-x/2}O_2$ materials have a single sloping plateau at ~0.7 V due to the Ti^{4+}/Ti^{3+} redox couple [91–93]. *In situ* XRD studies of $Na_{0.6}Ni_{0.3}Ti_{0.6}O_2$ indicate that this is an intercalation process, with the material's P2 structure being maintained during cycling and only 2% volume expansion occurring during sodiation [91]. The capacity is directly related to the number of sodium vacancies in $Na_xNi_{x/2}Ti_{1-x/2}O_2$. The sodium can intercalate into the vacant lattice sites which is likely the cause of low volume expansion during cycling [91]. Due to these small changes of the crystal lattice during charge and discharge, good cycling stability is observed in these materials. Over 3000 cycles has been demonstrated for $Na_{2/3}Co_{1/3}Ti_{2/3}O_2$, with ~85 % capacity retention [93]. All of these type of materials reported can be cycled using bulk powders, without large amounts of carbon black, which is not common for pure titanates [91–93]. This may be due to enhanced electronic conductivity imparted by the presence of late first row transition metals in the samples.

Previous reported layered sodium transition metal titanium oxide negative electrode materials employed transition metals in a +2 oxidation state, resulting in a stoichiometry of $Na_xM_{x/2}Ti_{1-x/2}O_2$. The sodium chromium titanate series was the first report of a transition metal in its +3 state resulting in a layered sodium transition metal titanium oxide negative electrode material of the formula $Na_xM_xTi_{1-x}O_2$. Specifically, P2-$Na_{0.6}Cr_{0.6}Ti_{0.4}O_2$ was found to be an excellent negative electrode material with low hysteresis (0.11 V) during cycling, good reversibility and low voltage. Due to the presence of chromium +3 in this material it can also be used as a positive electrode material, enabling a battery to be made out of a single material. Thus $Na_{0.6}Cr_{0.6}Ti_{0.4}O_2$ is referred to as a bi-functional or dual electrode.

This is the first study of the $Na_xCr_xTi_{1-x}O_2$ series and the compositions therein. A patent was filed on the $Na_{0.6}Cr_{0.6}Ti_{0.4}O_2$ composition in 2014. Others have published in this area since that time. Wang *et al*. reported an approach to prevent Na^+/vacancy ordering by breaking charge ordering in the transition metal layer [94]. This allows the design of disordered electrode materials with long cycle life. $Na_{0.6}Cr_{0.6}Ti_{0.4}O_2$ was used as an example to demonstrate this approach and cycled as a negative electrode in sodium cells. More recently the entire $Na_xCr_xTi_{1-x}O_2$ series was examined by Tsuchiya *et al*. as possible bi-functional electrode materials and the electrode performance was tested in sodium cells [95].

4.2 Experimental

The $Na_xCr_xTi_{1-x}O_2$ series where $0.6 \leq x \leq 1$ was synthesized via a solid state reaction on the scale of about 6 g using stoichiometric amounts of Na_2CO_3 (BioXtra, ≥ 99.0% Sigma Aldrich), Cr_2O_3 (50 μm, ≥ 98 % Sigma-Aldrich), and TiO_2 (puriss, 99 – 100.5 %, Sigma-Aldrich). The precursors were SPEX ball milled under ambient air with three half inch steel balls for a half hour and the resultant powder was pressed into ~2 g pellets at 2.55×10^8 Pascals prior to heating at high temperature. An argon atmosphere was used for synthesis and two separate heating protocols were employed depending on the value of x in order to achieve pure layered phases. When $0.6 \leq x \leq 0.7$ heating was done at 1000 ºC for three hours and when $0.75 \leq x \leq 1$ heating was done at 950 ºC for five hours.

4.3 Results and Discussion

Figure 4.1 shows an SEM image of the $x = 0.6$ as prepared powder. It comprises 2 μm hexagonal plate-like primary particles that are aggregated into secondary particles of about 20 μm in size.

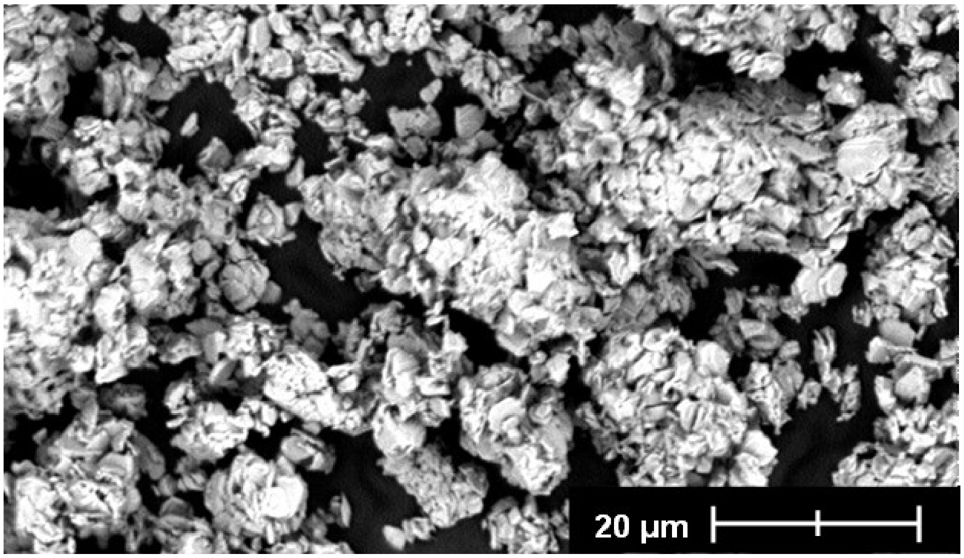

Figure 4.1: SEM image of the as prepared $Na_{0.6}Cr_{0.6}Ti_{0.4}O_2$ powder.

The XRD patterns for the as prepared sample powders is shown in Figure 4.2. Samples from $0.75 \leq x \leq 1$ are O3 type while samples with a large amount of sodium vacancies ranging from $0.6 \leq x \leq 0.66$ are P2 type. At these lower sodium concentrations, the sodium tends to be energetically stabilized at the larger prismatic sites. There is a O3/P2 coexistance region around $x = 0.7$. Below $x = 0.6$ there is an unidentified electrochemically inactive second phase that appears. The crystallinity of the materials tends to decrease with increasing *x*.

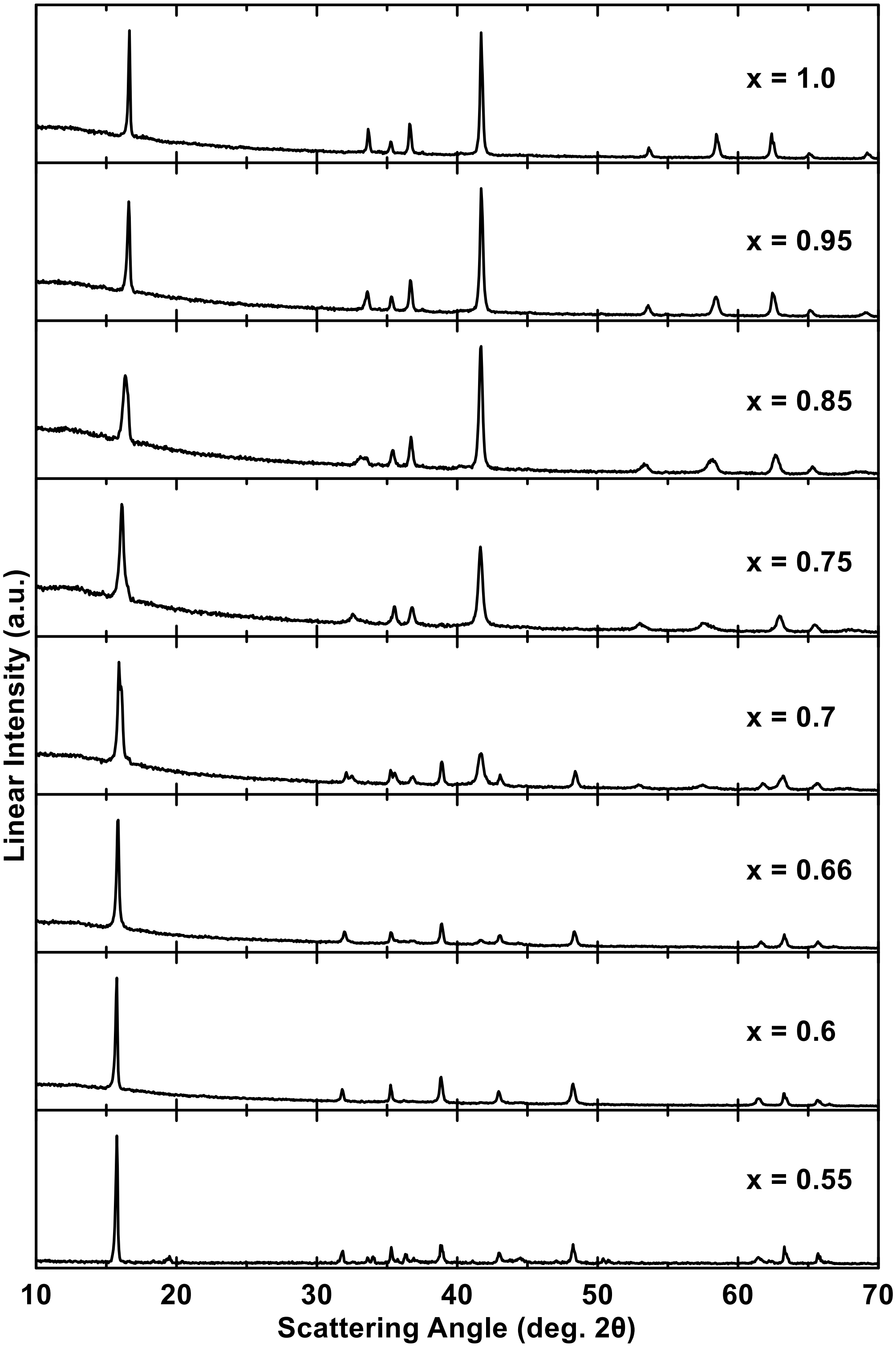

Figure 4.2: XRD patterns of the $Na_xCr_xTi_{1-x}O_2$ synthesized powders from $0.55 \leq x \leq 1.0$.

Rietveld refinement was performed for the single phase materials. An example of such a refinement is shown in Figure 4.3 for the $x = 0.6$ sample. The refinement resulted in a good fit and the crystallographic parameters used for the refinement are listed in Table 4.1. These are in good agreement with previous reports by Yu *et al.* who also prepared non-stoichiometric hexagonal sodium titanate chromites [96]. The large number of significant figures in the powder diffraction refinement results are a reflection of the uncertainty in the refinements. They are not the uncertainty in the occupancy, atomic positions or lattice constant values.

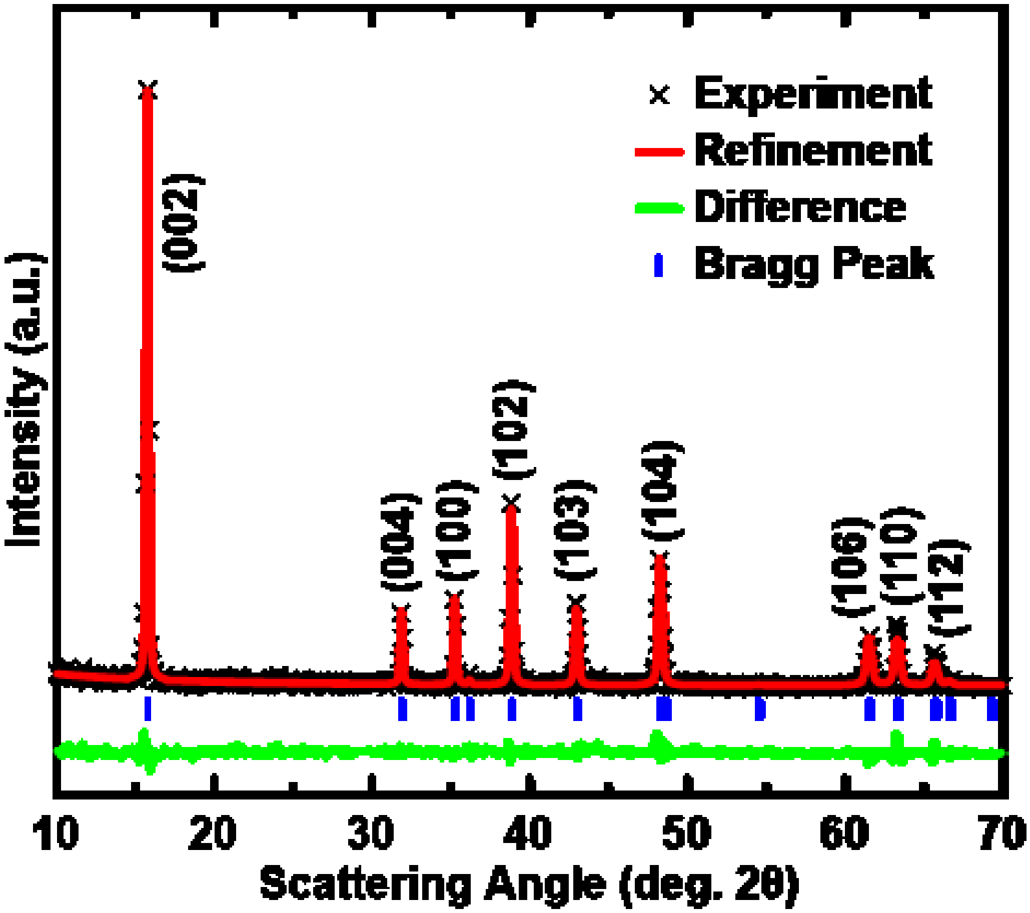

Figure 4.3: Experimental XRD pattern and refinement of P2-$Na_{0.6}Cr_{0.6}Ti_{0.4}O_2$.

Table 4.1: Structural parameters obtained from Rietveld refinement of $Na_{0.6}Cr_{0.6}Ti_{0.4}O_2$ XRD data.

$Na_{0.6}Cr_{0.6}Ti_{0.4}O_2$ (space group: $P6_3/mmc$)					
atom	site	x	y	z	occupancy
Na_f	2b	0	0	0.25	0.1946(1)
Na_e	2c	0.33	0.67	0.25	0.3778(7)
Cr	2a	0	0	0	0.60
Ti	2a	0	0	0	0.40
O	4f	0.33	0.67	0.0829(5)	1.00
Cell parameters		a (Å)	b (Å)	c (Å)	R-factor
		2.936(4)	2.936(4)	11.223(1)	
		α (°)	β (°)	γ (°)	2.97
		90	90	120	

The ordered layered structure of the sodium deficient P2 structure of $Na_xCr_xTi_{1-x}O_2$ is illustrated in Figure 4.4. The transition metals and sodium occupy alternating layers of octahedral and prismatic sites, respectively, with vacancies occurring in the sodium layer. Two separate sodium sites are present in the sodium layer, namely 2b and 2c, which are face and edge sharing with the octahedra of the transition metal layer, respectively. The edge sharing prisms tend to be of higher occupancy as they are lower energy in comparison to the face sharing sites [9]. This is likely due to the increased distance from the transition metals and results in less electrostatic repulsion.

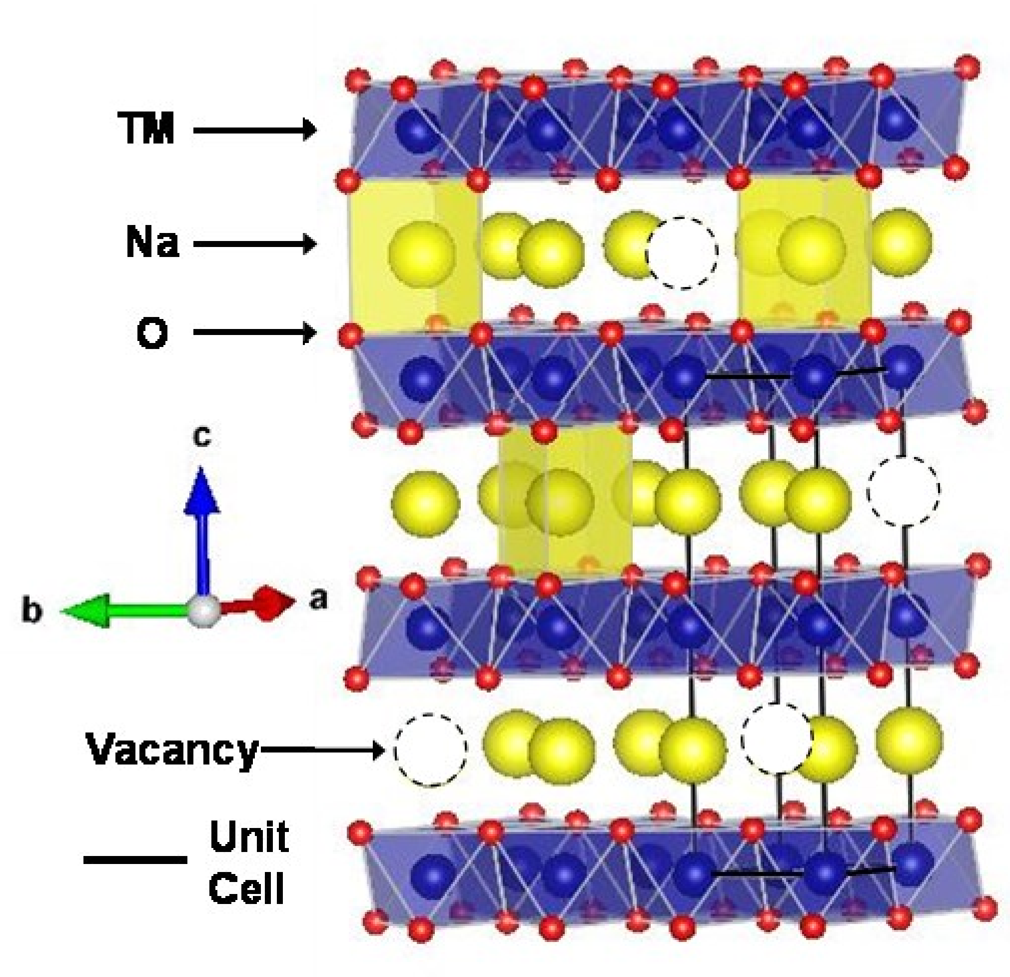

Figure 4.4: Representation of the P2-$Na_xCr_xTi_{1-x}O_2$ structure, with vacancies and local sodium environments highlighted. The P2 unit cell is indicated by the solid black lines.

Figure 4.5 shows how the lattice constants *a* and *c* of the $Na_xCr_xTi_{1-x}O_2$ series change with respect to *x*. To directly compare the *c* lattice constants of the P2 and O3 structures, the *c* lattice constants of the P2 structures were multiplied by a factor of 3/2. As *x* is increased the lattice constant *a* increases, while *c* decreases. Also, there is a slight discontinuity for the lattice constants in the transition from P2 to O3. The increase in *a* with *x* can be attributed to the smaller ionic radius of Ti^{4+} compared to Cr^{3+} [26], while the decrease in the *c* lattice constant with *x* is likely due to the decrease in electrostatic repulsion between oxygen layers as vacancies in the Na layers are filled. Since the *a* lattice constant increases, while the c lattice constant decreases with *x*, the unit cell volume changes very little over the entire series. The lower panel in Figure 4.5 shows that the calculated density increases linearly with *x*, due to the unit cell mass increasing with increasing sodium content. Also displayed in Figure 4.5 is the true density as measured by a helium gas pycnometer. The measured densities are consistently slightly lower than the calculated densities. This is likely due to a very minor loss of sodium from these materials during the high synthesis temperatures.

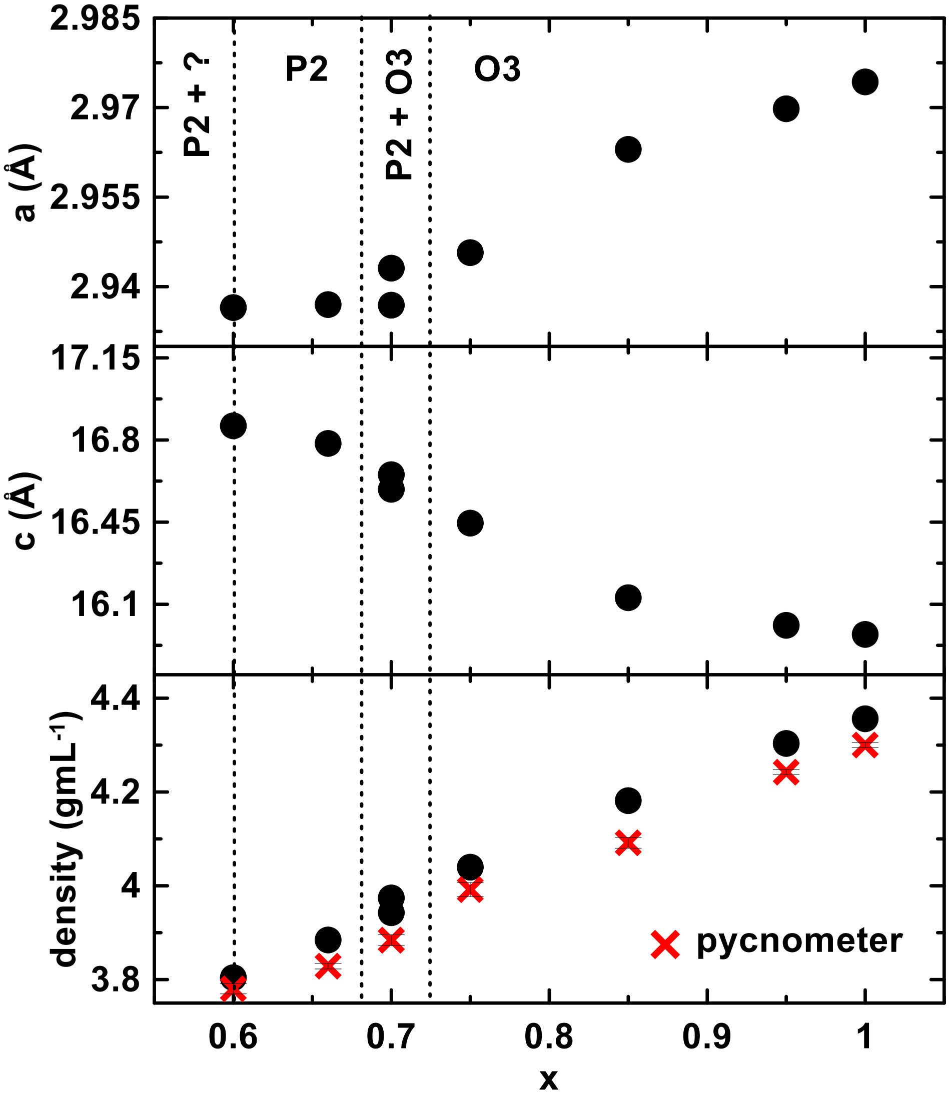

Figure 4.5: Lattice constants *a* and *c* and calculated/true density versus *x*.

These results show that a solid-solution exists over a large composition range, $0.6 \leq x \leq 1.0$, for this series. This is further evidenced by the neutron diffraction patterns and refinements for the $x = 0.6$ and 0.75 samples shown in Figure 4.6, Table 4.2, Figure 4.7 and Table 4.3. In plane chromium/titanium ordering is not apparent in the NPD data as new peaks do not appear in either the P2 or O3 structures. This is expected as the ionic radii of chromium (III) and titanium (IV) are extremely close at 0.755 and 0.745 Å, respectively [26].

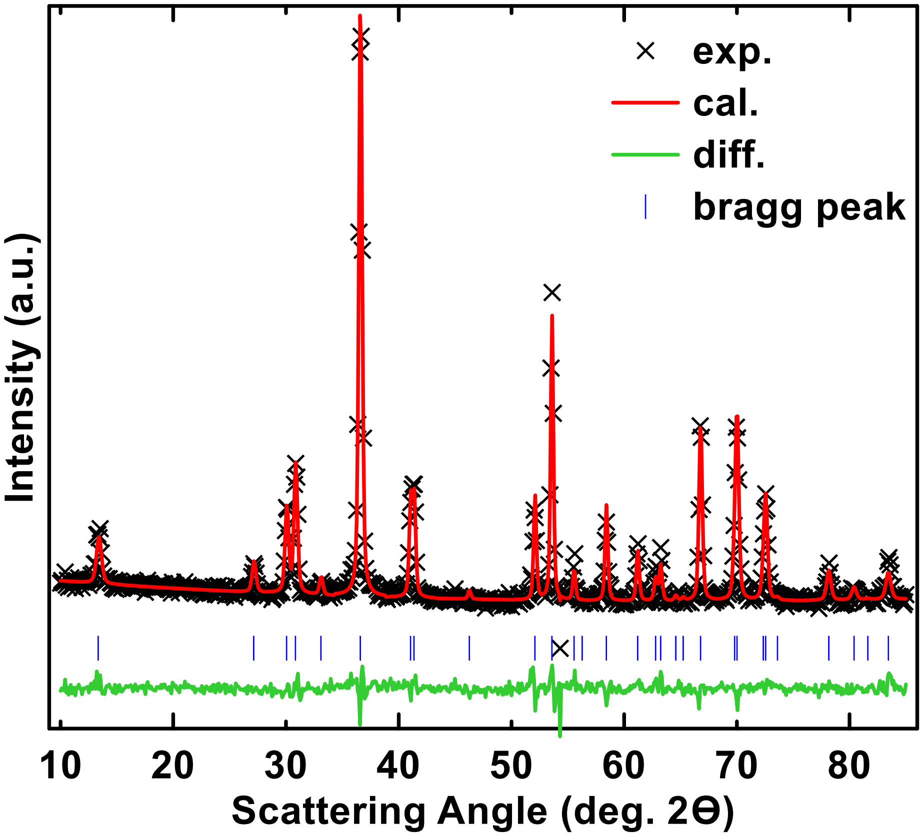

Figure 4.6: Experimental NPD pattern and refinement of P2-$Na_{0.6}Cr_{0.6}Ti_{0.4}O_2$.

Table 4.2: Structural parameters obtained from Rietveld refinement of $Na_{0.6}Cr_{0.6}Ti_{0.4}O_2$ NPD data.

$Na_{0.6}Cr_{0.6}Ti_{0.4}O_2$ (space group: $P6_3/mmc$)					
atom	site	x	y	z	occupancy
Na_f	2b	0	0	0.25	0.2201(6)
Na_e	2c	0.33	0.66	0.25	0.3765(1)
Cr	2a	0	0	0	0.60
Ti	2a	0	0	0	0.40
O	4f	0.33	0.66	0.0915(8)	1.00
Cell parameters		a (Å)	b (Å)	c (Å)	R-factor
		2.933(0)	2.933(0)	11.216(8)	2.18
		α (˚)	β (˚)	γ (˚)	
		90	90	120	

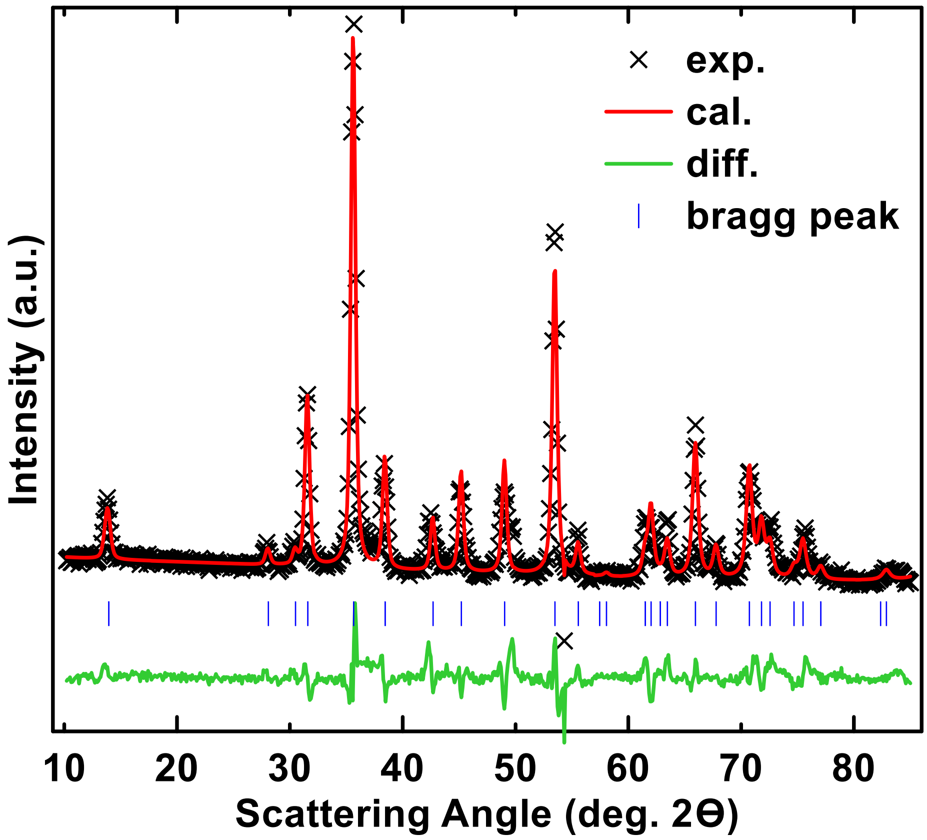

Figure 4.7: Experimental NPD pattern and refinement of O3-$Na_{0.75}Cr_{0.75}Ti_{0.25}O_2$.

Table 4.3: Structural parameters obtained from Rietveld refinement of $Na_{0.75}Cr_{0.75}Ti_{0.25}O_2$ NPD data.

<table>
<tr><td colspan="7">$Na_{0.75}Cr_{0.75}Ti_{0.25}O_2$ (space group: $R\bar{3}m$)</td></tr>
<tr><td>atom</td><td>site</td><td>x</td><td>y</td><td>z</td><td colspan="2">occupancy</td></tr>
<tr><td>Na</td><td>3b</td><td>0</td><td>0</td><td>0.5</td><td colspan="2">0.7384(6)</td></tr>
<tr><td>Cr</td><td>3a</td><td>0</td><td>0</td><td>0</td><td colspan="2">0.75</td></tr>
<tr><td>Ti</td><td>3a</td><td>0</td><td>0</td><td>0</td><td colspan="2">0.25</td></tr>
<tr><td>O</td><td>6c</td><td>0</td><td>0</td><td>0.2705(1)</td><td colspan="2">1.00</td></tr>
<tr><td colspan="2">Cell parameters</td><td>a (Å)</td><td>b (Å)</td><td>c (Å)</td><td colspan="2">R-factor</td></tr>
<tr><td colspan="2"></td><td>2.9516(0)</td><td>2.9516(0)</td><td>16.4240(0)</td><td colspan="2"></td></tr>
<tr><td colspan="2"></td><td>α (˚)</td><td>β (˚)</td><td>γ (˚)</td><td colspan="2">2.57</td></tr>
<tr><td colspan="2"></td><td>90</td><td>90</td><td>120</td><td colspan="2"></td></tr>
</table>

It appears that ordering, or lack thereof, is extremely important in these $Na_xM_yTi_{1-y}O_2$ materials. Each and every composition reported thus far in the literature has been disordered, implying that this is a prerequisite for these materials to cycle reversibly in sodium cells. In general, there are three types of ordering that can occur in these type of layered oxides and they can all influence one another [94]. The most widely observed ordering is that of sodium-ion vacancy ordering within the sodium layer, with the classic example being Na_xCoO_2 [97]. Much of the step-like profiles observed in sodium-ion battery voltage versus capacities plots is due to sodium ordering during intercalation and deintercalation of sodium. Transition metal ordering can also occur within its layer. This typically occurs when two metals have a large difference in their ionic radii. Disorder is observed when there is only a small difference in the ionic radii. According to crystal chemistry the typical boundary for the transition from disordered to ordered is a radii difference greater than 15% [80]. The final type of ordering is charge ordering where charges can be localized on specific sites due to strong interactions between electrons. Each of these types of ordering can be coupled to each other.

Figure 4.8 illustrates that these samples are hygroscopic as the XRD pattern has additional peaks appearing when samples at left in ambient atmosphere. These peaks disappear and the sample is effectively "heat healed" when the sample is placed in a furnace at 120 ºC overnight. These results indicate that water molecules are intercalating into the layered structure. Water and carbonate anion uptake has been observed for other layered sodium metal oxides where there are a large number of sodium vacancies [98,99].

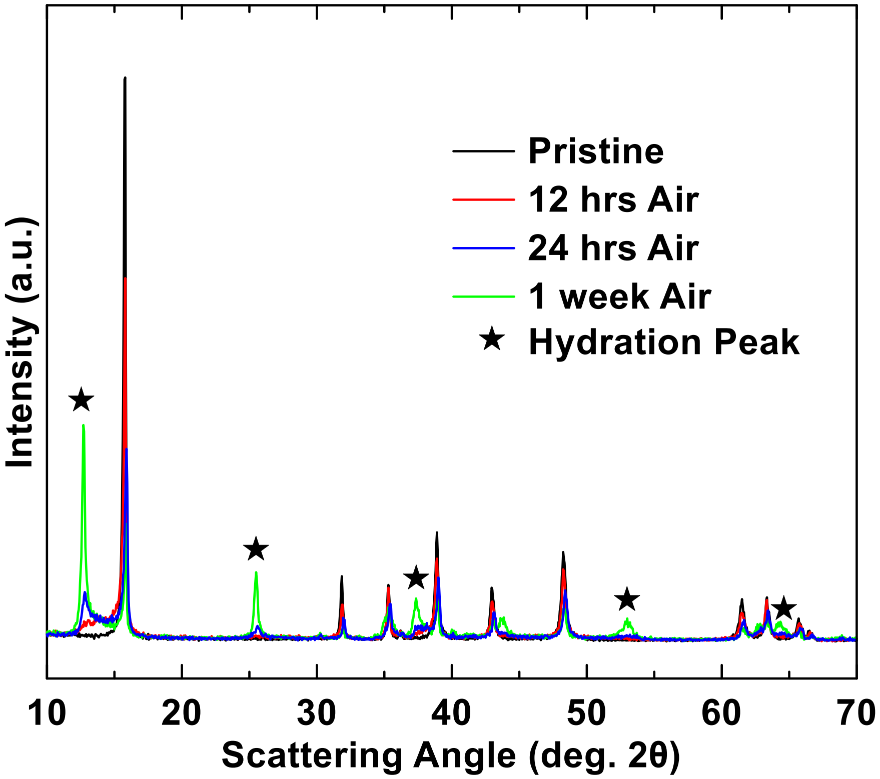

Figure 4.8: XRD patterns of the pristine $Na_{0.6}Cr_{0.6}Ti_{0.4}O_2$ material (black) and after the sample has been exposed to ambient air 12 hours, 24 hours and 1 week shown by the red, green and blue lines, respectively.

Figure 4.9 shows the voltage versus capacity curves of three compositions in the $Na_xCr_xTi_{1-x}O_2$ series, namely x = 0.6, 0.75 and 1.0 versus sodium metal. Here positive capacity is defined as when sodium is added in excess of the material's initial sodium composition. Negative capacity occurs when sodium has been removed so that the material's sodium composition is less than it was originally. This can easily be seen from the upper x-axis in Figure 4.9 where the sodium composition change, y, in $Na_{x+y}Cr_xTi_{1-x}O_2$, is labelled. Sodium was initially intercalated into the materials vacancies by discharging (sodiation) to 5 mV, followed by charging (desodiation) to 3.5 V. Two sloping plateaus with significant capacity are observed at two very distinct potentials, namely less than 1.0 and greater than 3.0 V. The low voltage plateau occurs at positive capacities while the high voltage plateau predominately occurs at negative capacities. The voltage curves were found to be highly reversible and have low hysteresis.

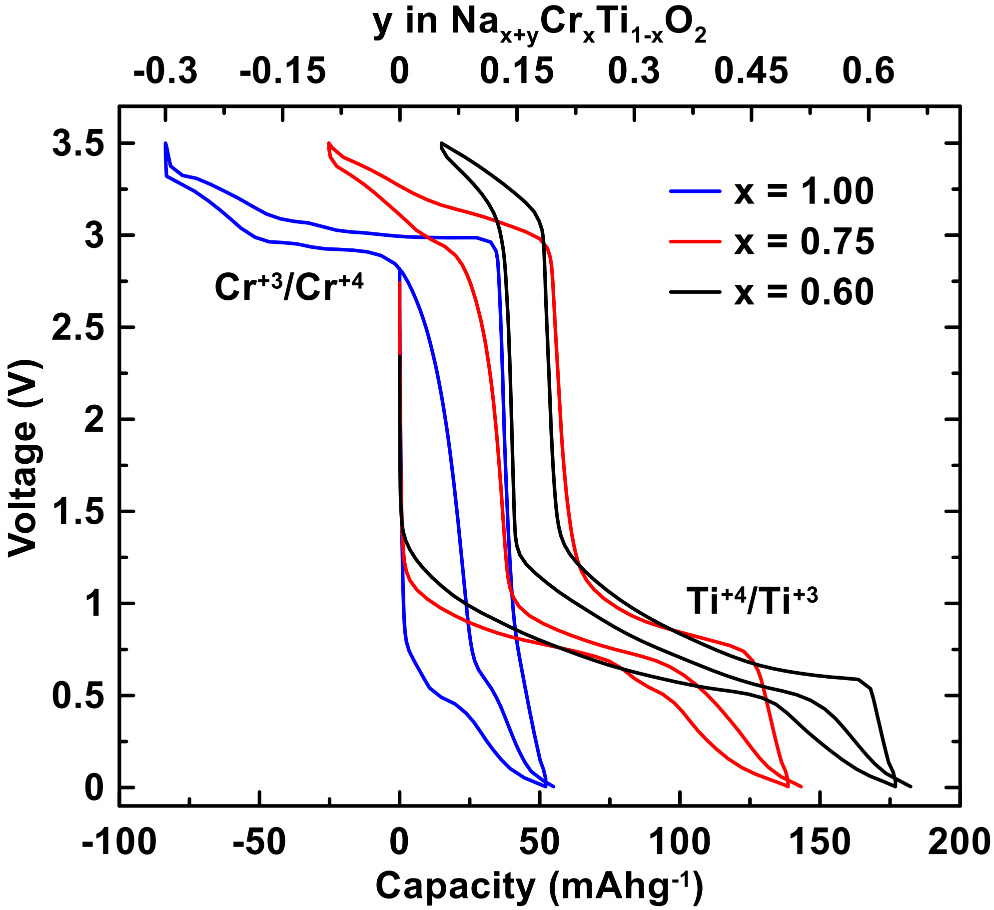

Figure 4.9: Voltage versus capacity curves for $x = 0.60$ (black), 0.75 (red) and 1.00 (blue) cycled in the voltage window of 0.005 – 3.5 V. The upper x-axis shows the variation in sodium content (y) from the original material, with positive and negative values corresponding to sodium addition and removal, respectively.

As *x* is decreased the high voltage plateau during charge decreases in capacity. This is consistent with there being less sodium available for desodiation in $Na_xCr_xTi_{1-x}O_2$ as *x* is decreased. At the same time, the low voltage plateau increases in capacity as *x* is decreased. This plateau is associated with providing the material with more sodium than it had initially. During discharge on this plateau sodium is being accommodated into the vacancies of the $Na_xCr_xTi_{1-x}O_2$ sodium layer. Therefore, the increasing capacity of this plateau with decreasing *x* is consistent with the number of sodium vacancies in $Na_xCr_xTi_{1-x}O_2$ increasing with decreasing *x*. This is confirmed in Figure 4.10 where the capacity of the lower voltage plateau during discharge from 2.0 – 0.3 V versus the number of vacancies (1-*x*) is plotted for the entire $Na_xCr_xTi_{1-x}O_2$ series. Also shown is the theoretical capacity based on each inserted sodium occupying one vacancy in the lattice. The experimental results are in good agreement with the theoretical capacities.

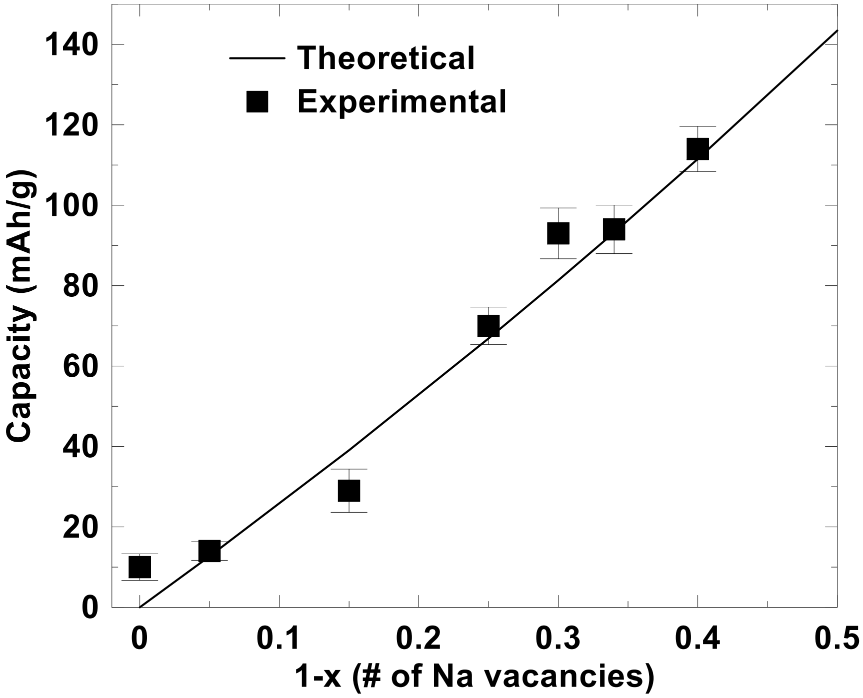

Figure 4.10: Capacity versus the number of sodium vacancies for the $Na_xCr_xTi_{1-x}O_2$ materials when charged to 1.5 V (low voltage plateau). Theoretical capacities that were calculated (solid black line) and experimental capacities (square black symbols) are shown.

The low voltage and low hysteresis of both plateaus in these materials is interesting for application in sodium cells. Of particular interest are materials with low values of *x* for negative electrode materials and high values of *x* for positive electrode materials. Therefore, the cycling characteristics of both plateaus were investigated in narrower voltage ranges.

Figure 4.11 shows the voltage versus capacity curve of $Na_{0.6}Cr_{0.6}Ti_{0.4}O_2$ versus Na metal cycled in two separate voltage ranges. A single sloping plateau is observed at an average potential of 0.7 V. The voltage curve was found to be highly reversible and has very low hysteresis (~ 0.1 V) and an initial capacity of 124 mAh/g. This is indicative of intercalation, which is significant, because conversion-type reactions typically occur in transition metal oxides with sodium below 1 V [30,100]. It has been found that this is also the case for other layered sodium transition metal oxides that contain titanium and another transition metal, such as $Na_{2/3}Mn_{1/3}Ti_{2/3}O_2$, $Na_{0.75}Fe_{0.75}Ti_{0.25}O_2$, $Na_{2/3}Co_{1/3}Ti_{2/3}O_2$, and $Na_{0.6}Ni_{0.3}Ti_{0.7}O_2$.

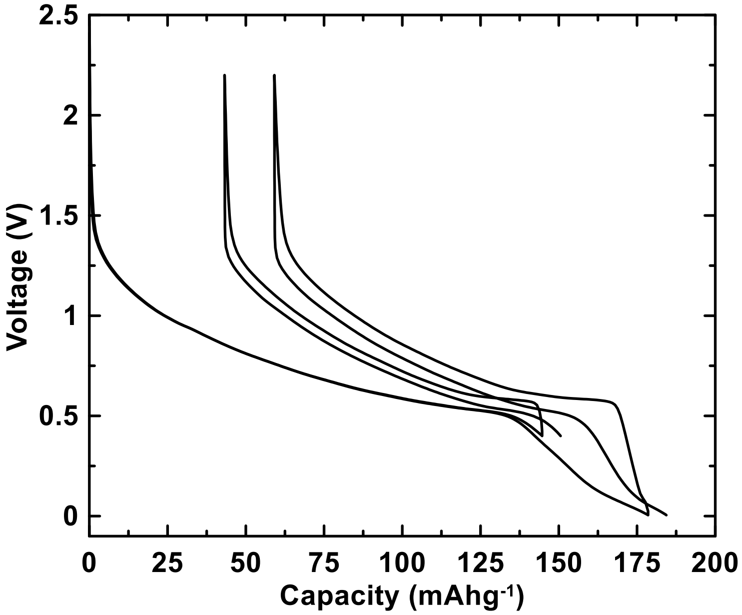

Figure 4.11: Voltage versus gravimetric capacity curve of $Na_{0.6}Cr_{0.6}Ti_{0.4}O_2$ versus Na metal for two separate voltage ranges, 0.5 – 2.2 V and 0.005 – 2.2 V.

After the large sloping plateau, two small plateaus are present at about 0.5 V and 0.1 V. A large irreversible capacity is present in the voltage curve of $Na_{0.6}Cr_{0.6}Ti_{0.4}O_2$ on the first cycle in Figure 4.13. This is believed to be attributable mostly to carbon black in the electrode formulation. Carbon black has a large irreversible capacity at virtually the same voltage as the $Na_xM_yTi_{1-y}O_2$ type materials. The irreversible capacity of sodium with carbon black has been measured as ~500 mAh/g in Figure 4.12. This corresponds to ~50 mAh/g irreversible capacity contribution to the electrodes studied herein, which have 10 % carbon black in their electrode formulation.

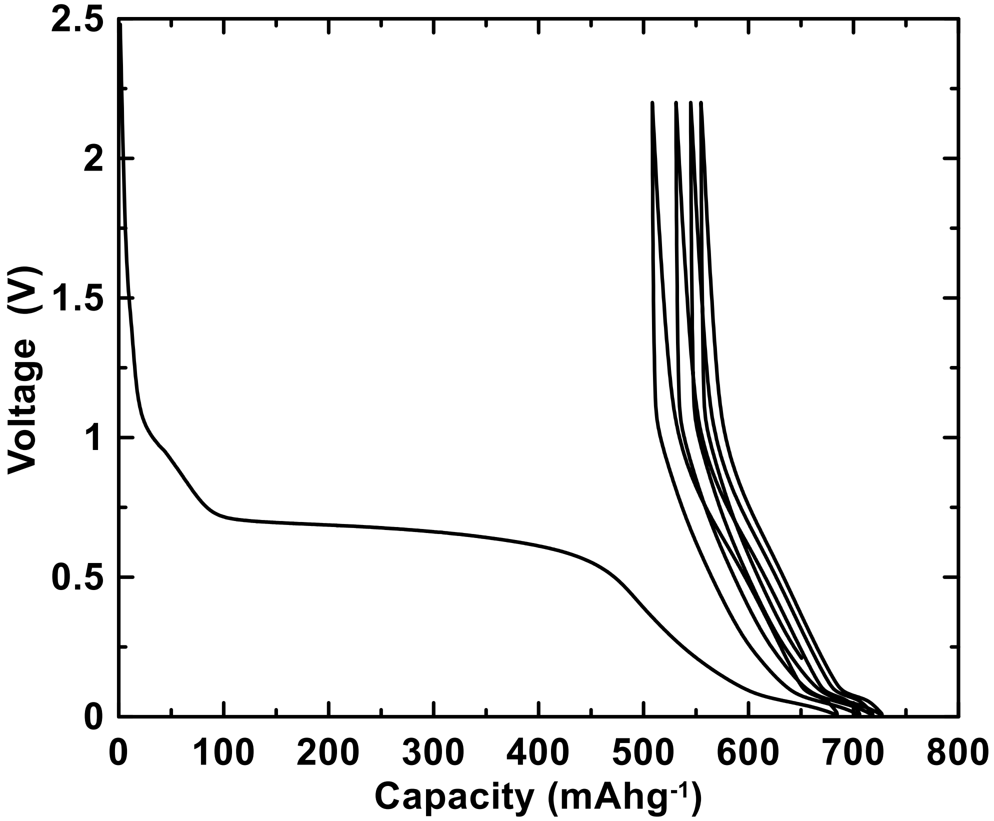

Figure 4.12: Voltage versus capacity curve of a carbon black electrode with only 10 % PVDF binder versus Na metal.

Reducing the amount of carbon black can lead to a corresponding reduction in irreversible capacity, as shown in Figure 4.13 and Figure 4.14 where 1, 2.5, 5 and 10%

carbon black were used in the electrode formulation. These figures highlight the danger of not having enough carbon black to enhance the electronic conduction. 5% carbon black reduces the irreversible capacity but below this value the reversible capacity is greatly reduced while hysteresis is greatly increased. However, the electrode with 5 % carbon black cycles poorly over 50 cycles and therefore 10 % carbon black is required in these titanate based electrodes.

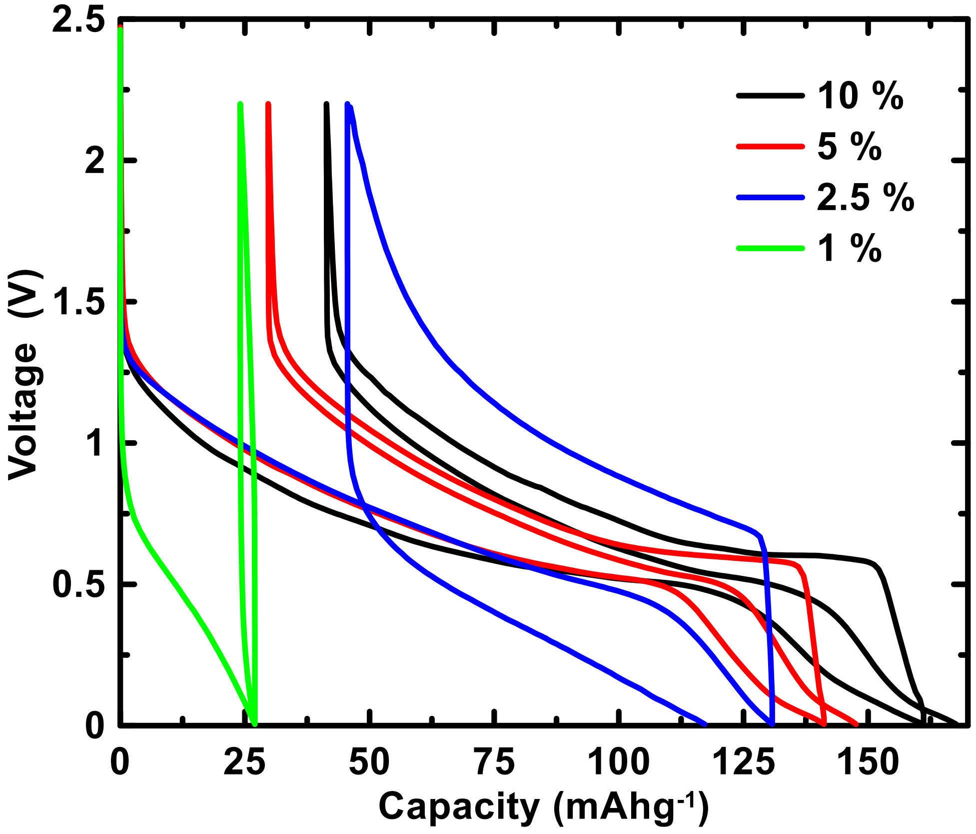

Figure 4.13: Voltage versus capacity curve of $Na_{0.6}Cr_{0.6}Ti_{0.4}O_2$ versus Na metal for different amounts of carbon black in the electrode formulation, 10 % (black), 5 % (red), 2.5 % (blue) and 1 % (green).

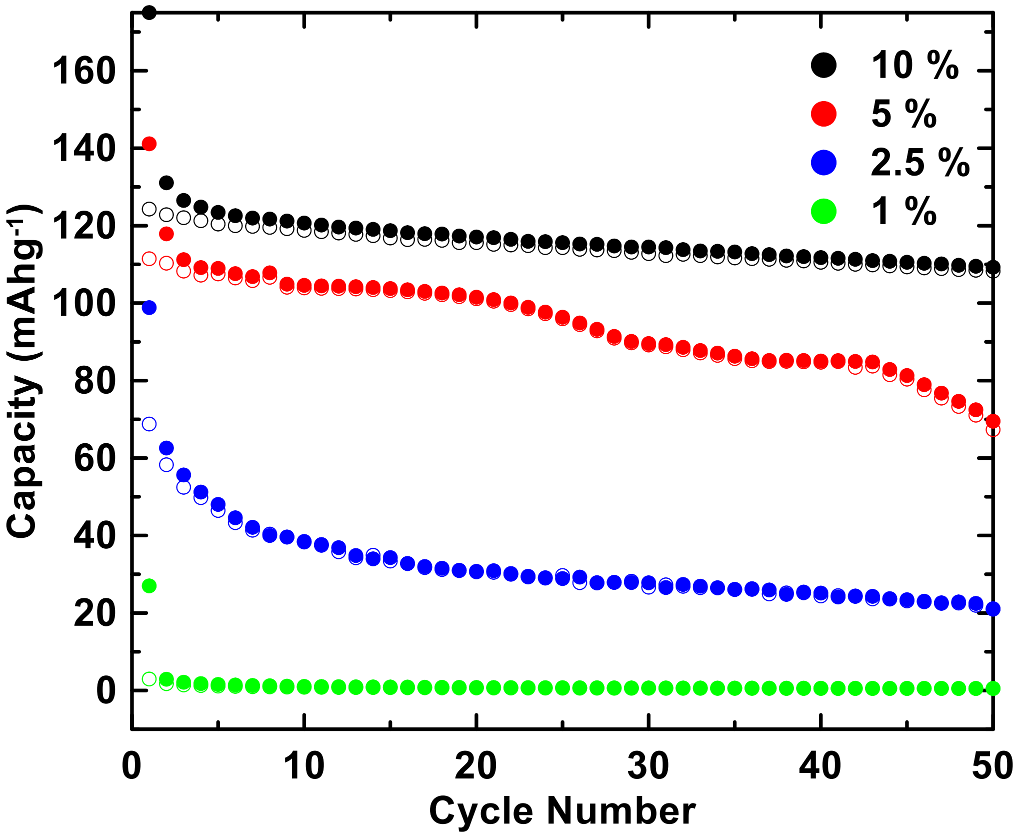

Figure 4.14: Capacity versus cycle number of $Na_{0.6}Cr_{0.6}Ti_{0.4}O_2$ versus Na metal for different amounts of carbon black in the electrode formulation, 10 % (black), 5 % (red), 2.5 % (blue) and 1 % (green). Solid and open symbols represent discharge and charge capacities, respectively.

The differential capacity curve of $Na_{0.6}Cr_{0.6}Ti_{0.4}O_2$ is shown in Figure 4.15. The first discharge has excess capacity below 0.85 V disappearing after the first cycle. This is due to irreversible capacity during the formation of the initial SEI layer on the active material and further irreversible reactions involving carbon black. After the first cycle, the differential capacity becomes reversible, and comprises a broad peak extending from about 0.7 V to 1.5 V, a very sharp peak near about 0.5 V and a small peak at about 0.1 V. These peaks correspond to the initial sloping voltage curve, and two small plateaus noted above in the voltage curve, respectively.

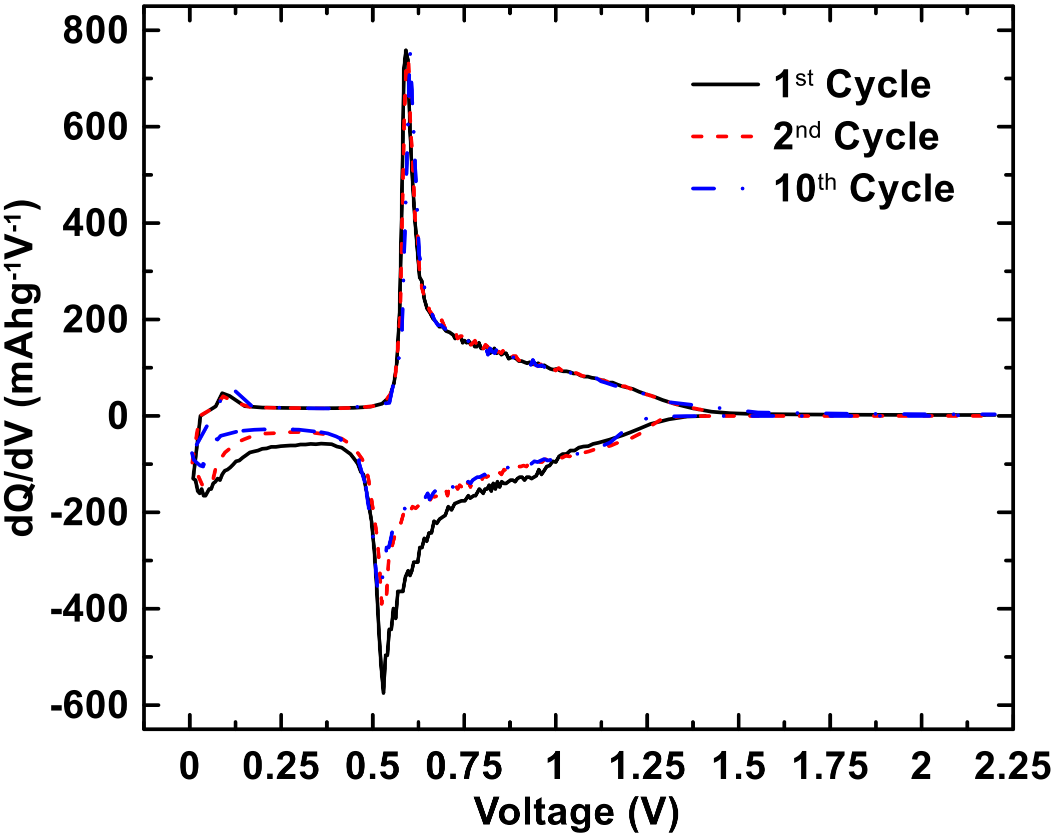

Figure 4.15: The differential capacity curve, dQ/dV vs. V, of $Na_{0.6}Cr_{0.6}Ti_{0.4}O_2$ versus Na metal, with the first, second and tenth cycles shown in black, red and blue lines, respectively.

Figure 4.16 shows the cycling performance of the same cells shown in Figure 4.11. The cells exhibit a linear fade over 120 cycles, with the 0.4 V cut-off cell displaying less fade than the 0.005 V cut-off cell. Both show a similar maximum Coulombic efficiency of only < 99.5 %. These characteristics need to be improved for such materials to be used in practical applications.

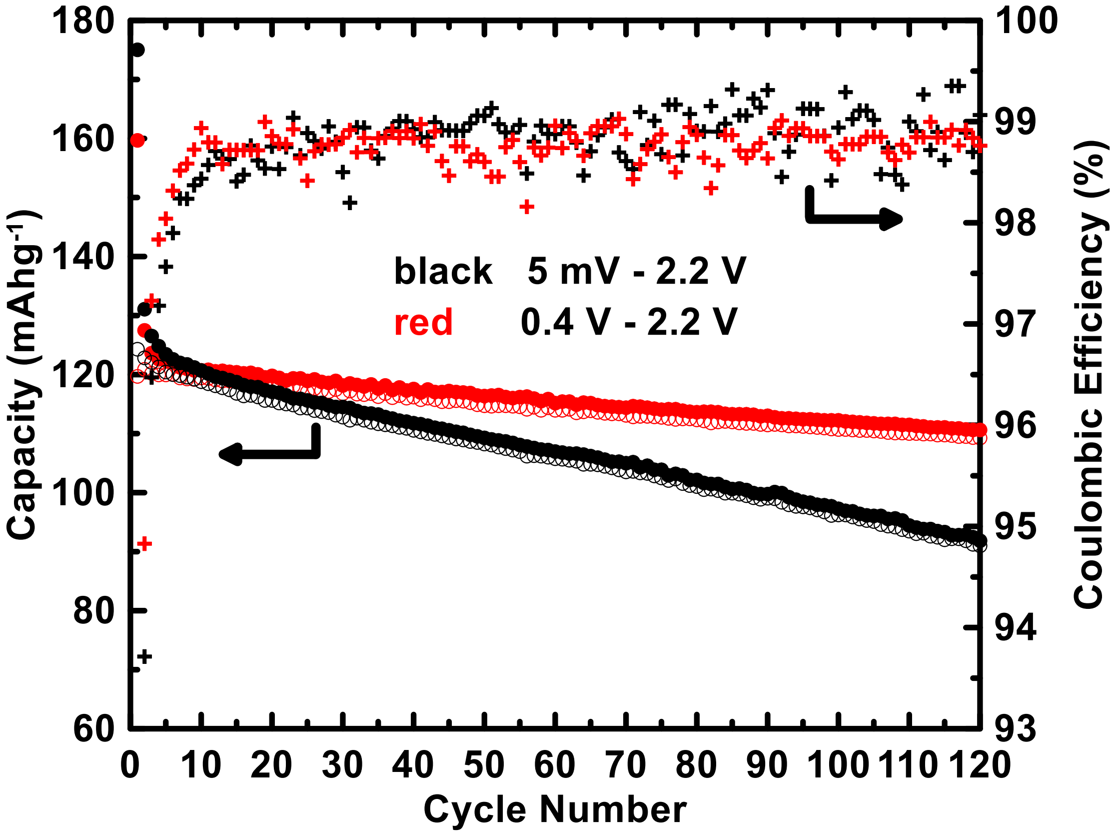

Figure 4.16: Capacity and Coulombic efficiency versus cycle number of the $Na_{0.6}Cr_{0.6}Ti_{0.4}O_2$ cells cycled between 0.005 – 2.2 V (black) and 0.4 – 2.2 V (red) over 120 cycles.

Figure 4.17 shows *in situ* XRD patterns of a $Na_{0.6}Cr_{0.6}Ti_{0.4}O_2$ cell with the corresponding voltage-time curve. *In situ* cycling was performed between 0.15 and 2 V over two cycles. Most peaks correspond to the P2-$Na_{0.6}Cr_{0.6}Ti_{0.4}O_2$ phase, as indicated in Figure 4.17. Other peaks in the XRD patterns are caused by the Be window, with BeO on its surface, and stainless steel cell parts. These peaks do not shift during the charge and discharge processes. The initial XRD pattern is that of the phase pure P2-$Na_{0.6}Cr_{0.6}Ti_{0.4}O_2$. During cycling only shifts in peak positions were observed and the electrode material remains in the P2 structure throughout the entire charging and discharging process. This is indicative of a reversible intercalation process. This has also been observed for $Na_{0.6}Ni_{0.3}Ti_{0.7}O_2$ and is reflective of the stability of the P2 phase [91,101].

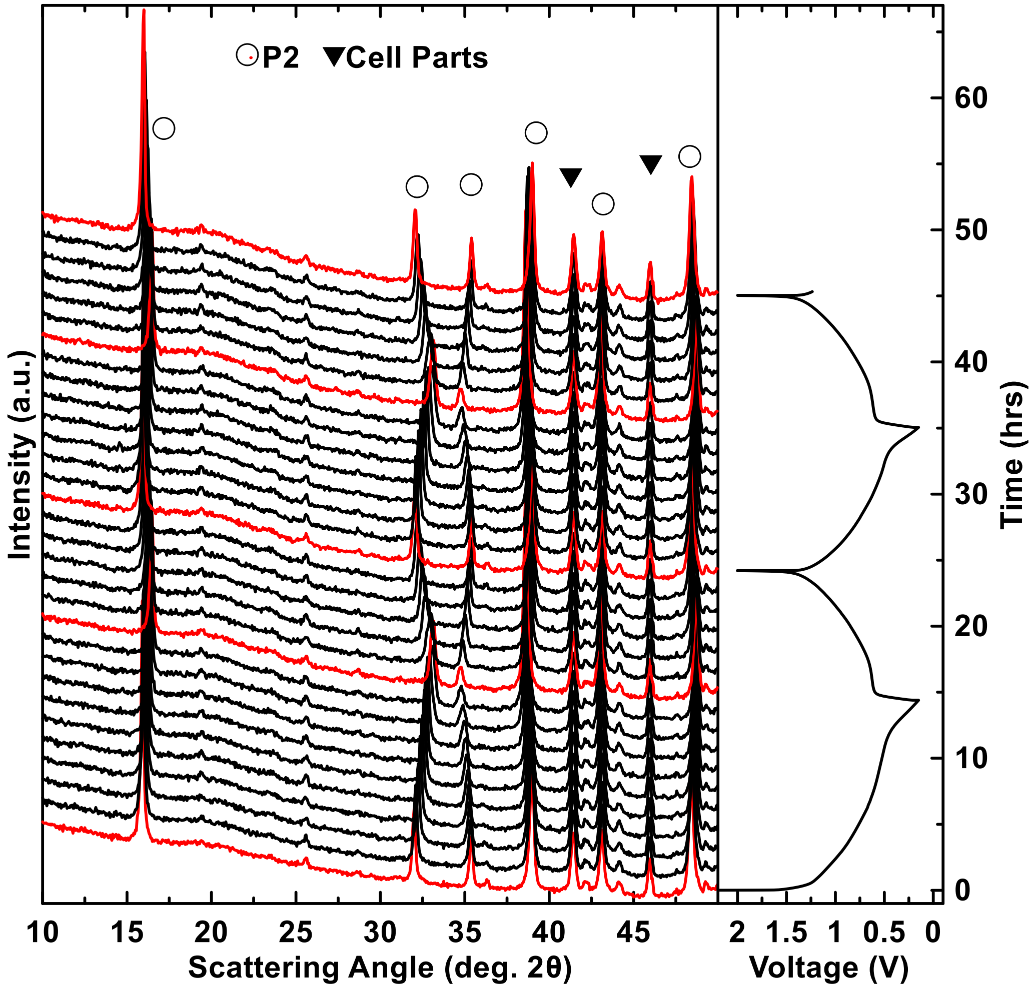

Figure 4.17: XRD patterns measured during charge and discharge of a $Na_{0.6}Cr_{0.6}Ti_{0.4}O_2$ *in situ* cell with the corresponding voltage-time curve. Most peaks correspond to the P2-$Na_{0.6}Cr_{0.6}Ti_{0.4}O_2$ electrode marked by (○), with other peaks resulting from cell parts such as Be or steel denoted by (▼).

During the first discharge, the (00*l*) peaks shift to higher angle while the (10*l*) peaks shift to lower angle. This indicates that the *a*-axis is expanding and the *c*-axis is contracting while sodium is being inserted. During discharge, the opposite occurs and the peaks shift to their original positions. Figure 4.18 shows the lattice parameters, voltage, and unit cell volume plotted versus time. The expansion of the a-axis is almost completely compensated by the contraction of the c-axis, resulting in a small overall volume expansion of only 1.0 % at full sodiation. This is advantageous, since materials with low volume change tend to maintain structural integrity and retain contact with the current collector over many charge and discharge cycles. The expansion and contraction of the lattice constants is highly anisotropic, even thought the overall volume change is almost negligible. This anisotropy is common for layered intercalation compounds when an alkali is inserted and removed. This is because the *c* lattice constant is highly dependent upon the alkali concentration in the van der Waal's gap from oxide sheet repulsion, while the *a* lattice constant is more dependant upon the *M*O bond lengths.

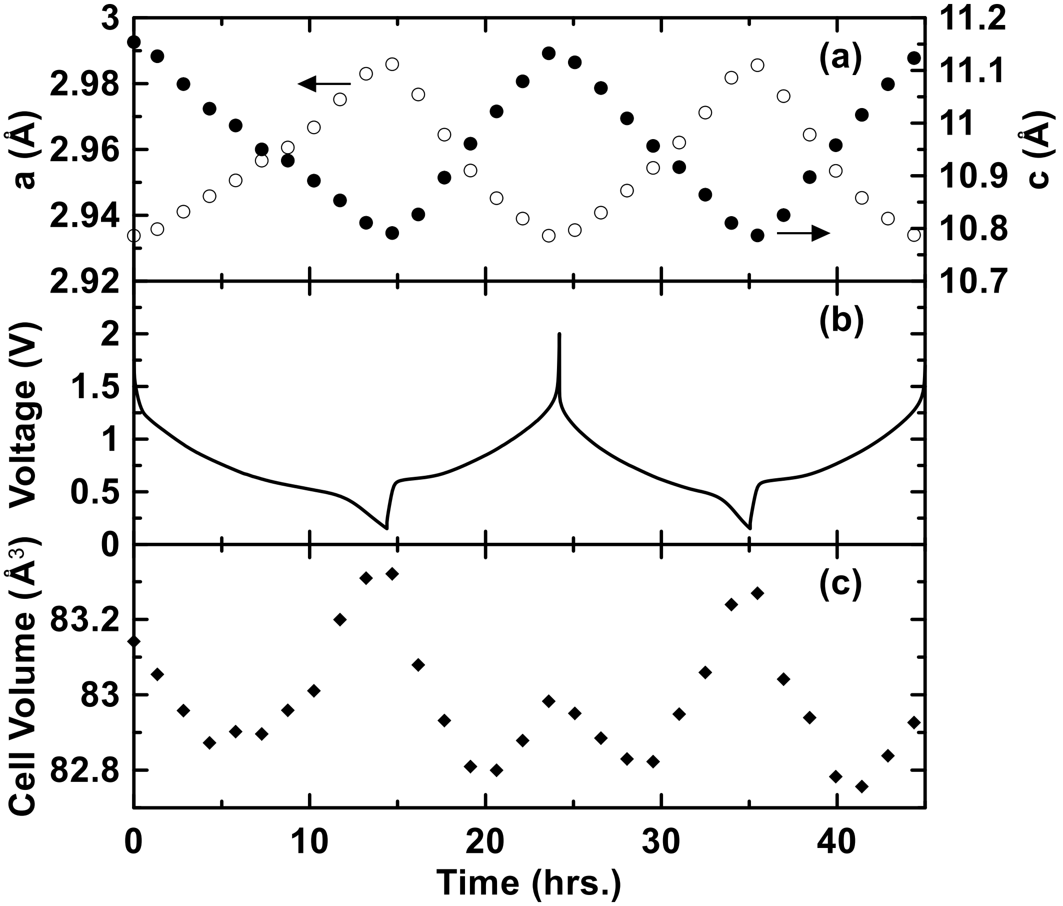

Figure 4.18: The variation in the lattice parameters *a* (open circles) and *c* (closed circles) vs. time (a) corresponding to the $Na_{0.6}Cr_{0.6}Ti_{0.4}O_2$ *in situ* X-ray cell voltage curve (b). Unit cell volume vs. time is also shown in panel (c) corresponding to the voltage curve in (b).

Figure 4.19 shows voltage versus capacity curves of $Na_{0.6}Cr_{0.6}Ti_{0.4}O_2$ cycled at rates ranging from C/10 to (11 mA/g) to 5 C (550 mA/g). C-rate was defined based on a theoretical capacity of 110 mAh/g, which is based on the number of sodium vacancies in the structure. The rate capability was poor. This can be more easily seen in Figure 4.20 where cycle number versus capacity is plotted. Cycling at 2 C resulted in a capacity that was 52% of the C/10 capacity with a dramatic increase in hysteresis. Further improvements in rate capability are desirable if these materials are to be used in practical applications.

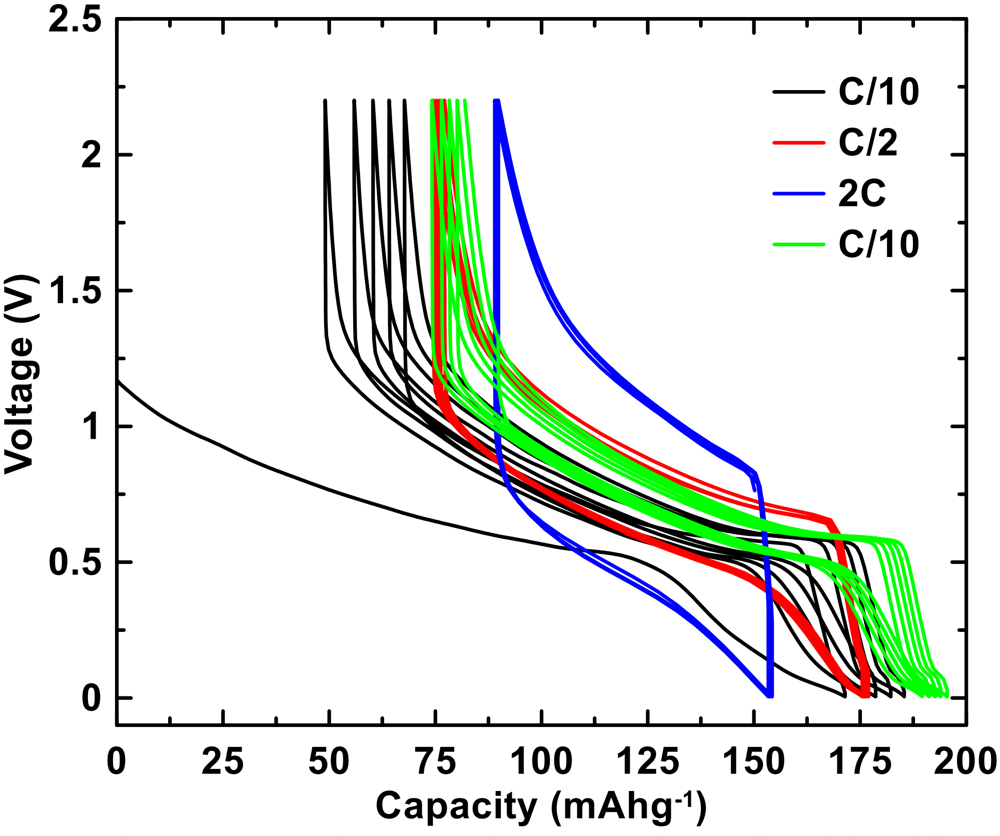

Figure 4.19: Voltage versus capacity curves of a $Na_{0.6}Cr_{0.6}Ti_{0.4}O_2$ cell cycled at different rates. The cell was discharged to 0.005 V and charged to 2.2 V for five cycles each at rates of C/10 (black), C/2 (red), 2C (blue), and C/10 (green).

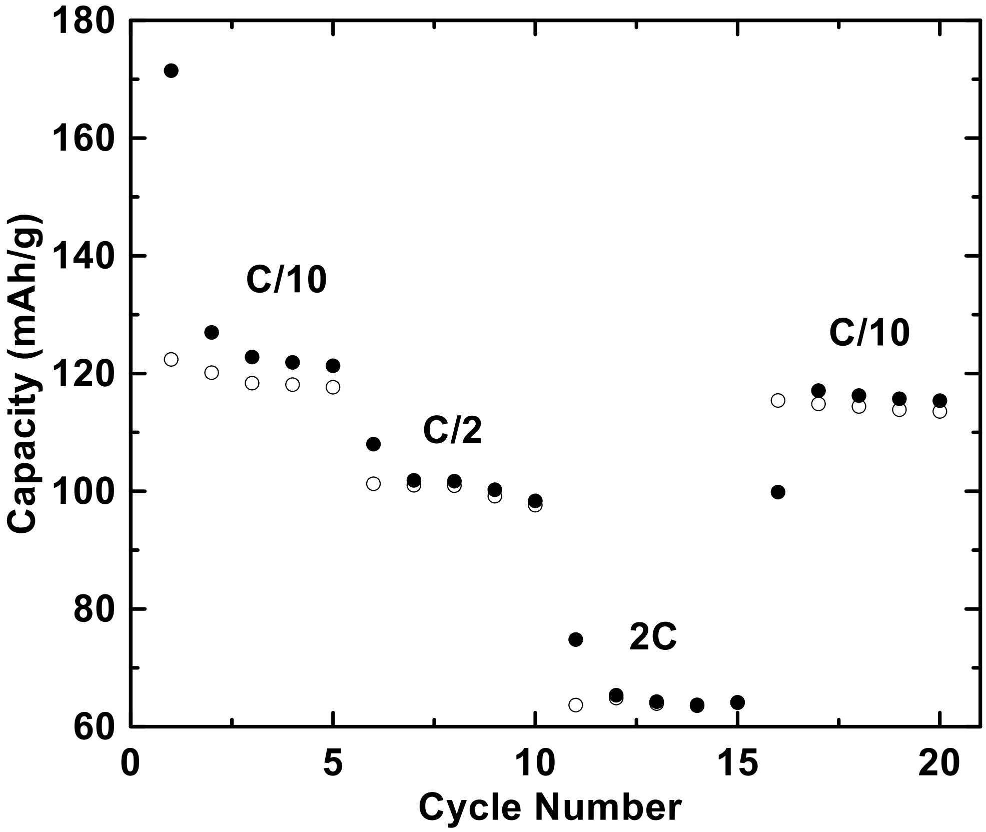

Figure 4.20: Capacity versus cycle number of a $Na_{0.6}Cr_{0.6}Ti_{0.4}O_2$ cell cycled at different rates. The cell was charged to 0.005 V and discharged to 2.2 V for five cycles each at rates of C/10, C/2, 2C, and C/10. Open and closed circles represent discharge and charge cycles, respectively.

The performance of $Na_{0.6}Cr_{0.6}Ti_{0.4}O_2$ was also evaluated in Li cells. Figure 4.21 shows the voltage versus capacity curve of $Na_{0.6}Cr_{0.6}Ti_{0.4}O_2$ versus Li metal. It has a first discharge capacity of 122 mAh/g (or 400 Ah/L) and a large irreversible capacity with Li. This irreversible capacity is primarily due to the carbon black in the electrode formulation, as in the case of sodium. Figure 4.22 shows the cycling performance of the same cell in Figure 4.21. After 10 cycles, the capacity slowly fades linearly, with about 100 mAh/g capacity retention after 30 cycles. The electrochemical behavior of $Na_{0.6}Cr_{0.6}Ti_{0.4}O_2$ versus lithium is very similar to its performance versus sodium, however the average voltage in lithium cells (1.44 V) is much higher than that in sodium cells

(0.70 V vs. Na, which corresponds to 1.03 V vs Li). This is typical of transition metal oxides where intercalation or conversion reactions with lithium occur at higher voltages than with sodium.[30]

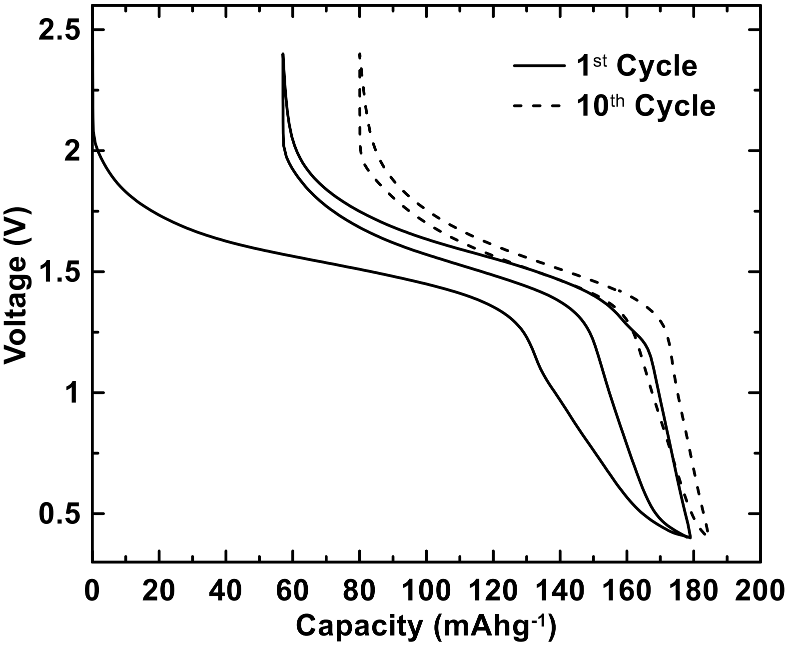

Figure 4.21: Voltage versus gravimetric capacity curve of $Na_{0.6}Cr_{0.6}Ti_{0.4}O_2$ versus Li metal between 0.4 – 2.4 V, with the first and tenth cycles represented by solid and dashed lines, respectively.

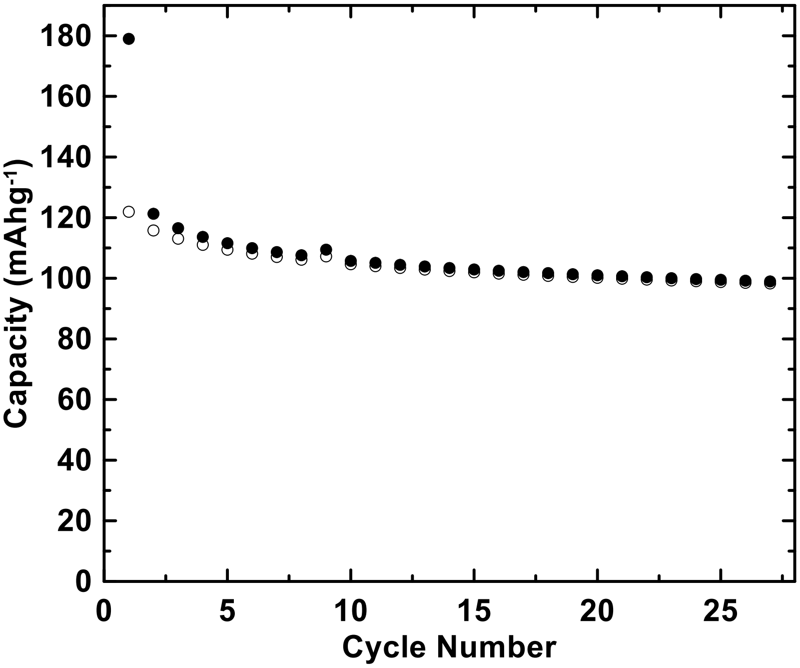

Figure 4.22: Capacity versus cycle number for $Na_{0.6}Cr_{0.6}Ti_{0.4}O_2$ cycled with lithium metal. Open and closed circles represent discharge and charge cycles, respectively.

Due to the presence of chromium (III) in these layered oxides, upon sodium deintercalation chromium could be oxidized to chromium (IV). This would enable it as a possible positive electrode material. Figure 4.23 shows the first couple of charge and discharge curves of $Na_xCr_xTi_{1-x}O_2$ where $x = 0.6$, 0.75 and 1.0 in the upper voltage range with varying upper voltage cut-offs.

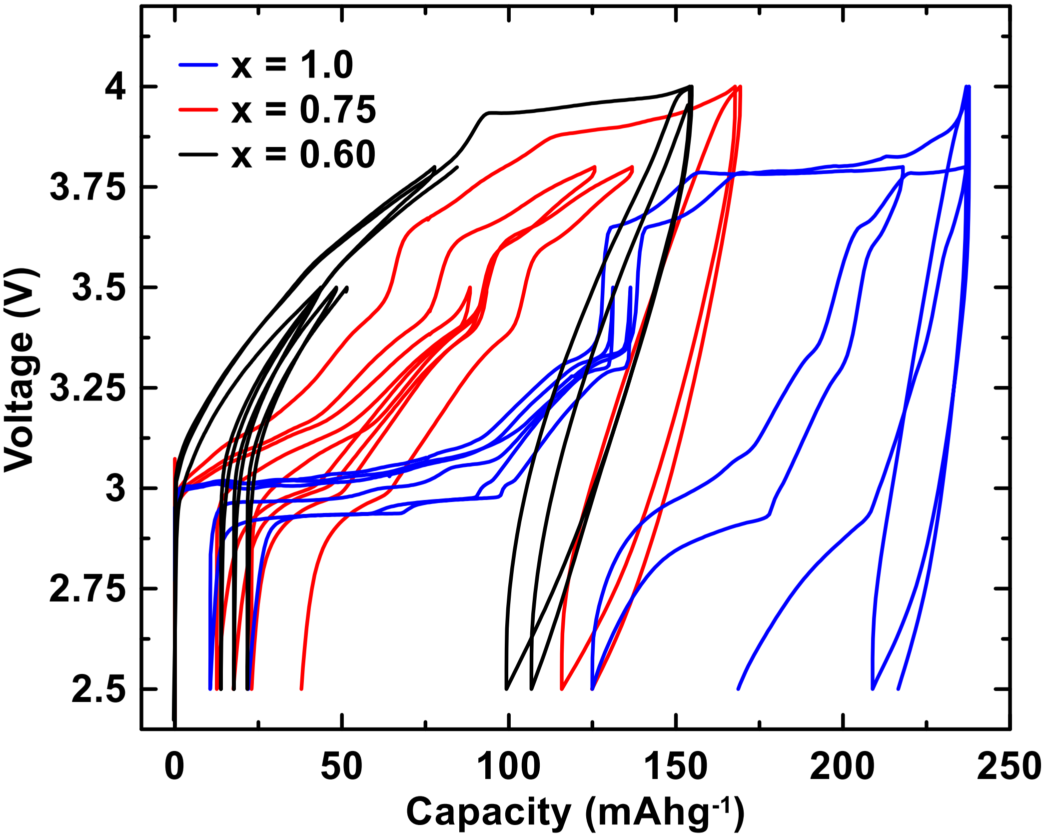

Figure 4.23: Voltage versus capacity curves for $x = 0.60$ (black), 0.75 (red) and 1.00 (blue) cycled using a lower voltage cut-off of 2.5 and varying upper voltage cut-offs, 3.5, 3.8 and 4.0 V.

As x is increased the upper voltage capacity also increases, regardless of the upper voltage cut-off. The $x = 0.6$ composition shows voltage curves with smooth slopes without plateaus up to 3.8 V. This is indicative of a single phase reaction during sodium deintercalation and intercalation. All other voltage curves show plateaus or step like voltage behavior. The average sodium storage voltage for the materials appears to increase with decreasing *x*, even with the same chromium redox couple. Ti^{4+} substitution has been shown in the literature to cause complex voltage behavior and the average voltage is highly dependent upon whether higher voltage plateaus are accessed [102].

Based on the cycling reversibility results of the high and low voltage plateaus for $Na_{0.6}Cr_{0.6}Ti_{0.4}O_2$, a sodium-ion full cell was constructed where it was used as both the negative and positive electrode. This strategy of using a single material for both electrodes in a single battery offers obvious advantages in terms of material's processing costs. Figure 4.24 shows the voltage versus capacity profile for the $Na_{0.6}Cr_{0.6}Ti_{0.4}O_2$ full cell in the voltage range of 3.1 – 1.7 V.

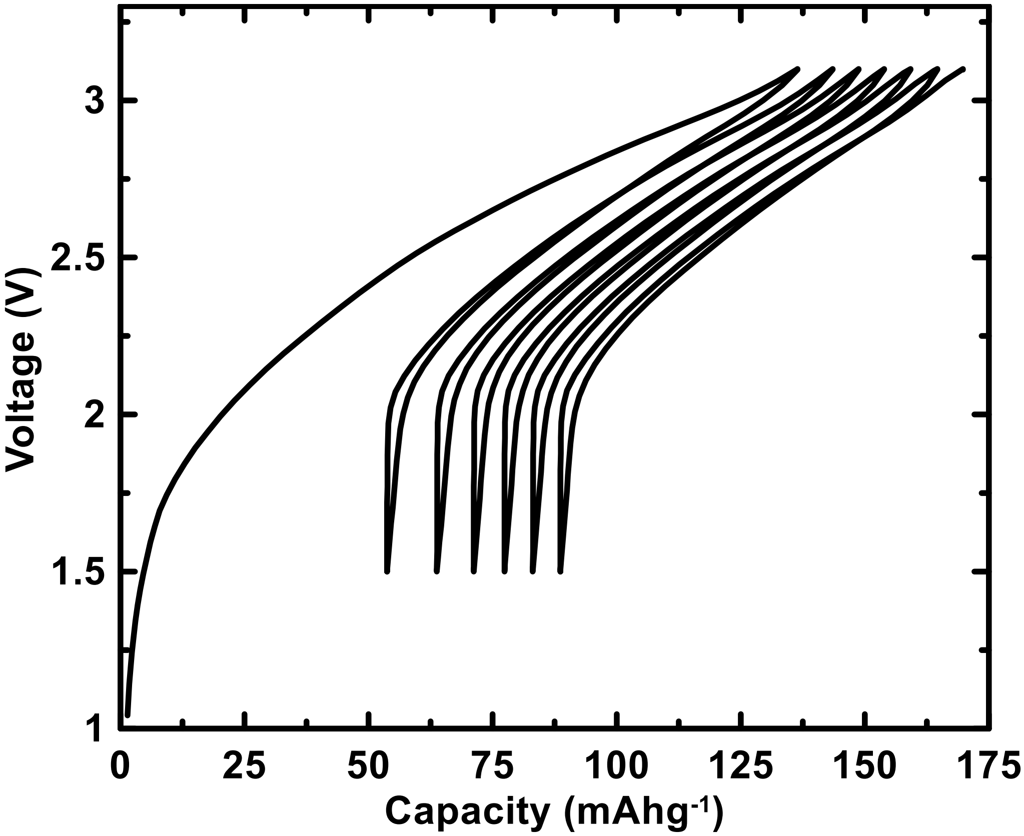

Figure 4.24: Voltage versus capacity of a full cell using a negative electrode and positive electrode material that are both $Na_{0.6}Cr_{0.6}Ti_{0.4}O_2$. Cycled from 3.1 – 1.7 V using 1 M $NaPF_6$ in PC at a rate of C/10.

Figure 4.25 shows the capacity versus cycle number of the $Na_{0.6}Cr_{0.6}Ti_{0.4}O_2$ full cell. This full cell delivers a modest capacity of 80 mAh/g with an average operating voltage plateau of ~2.5 V. This type of cell where the positive and negative electrode are constructed using the same material has been dubbed a symmetric cell, with the single material referred to as a bifunctional or dual electrode.

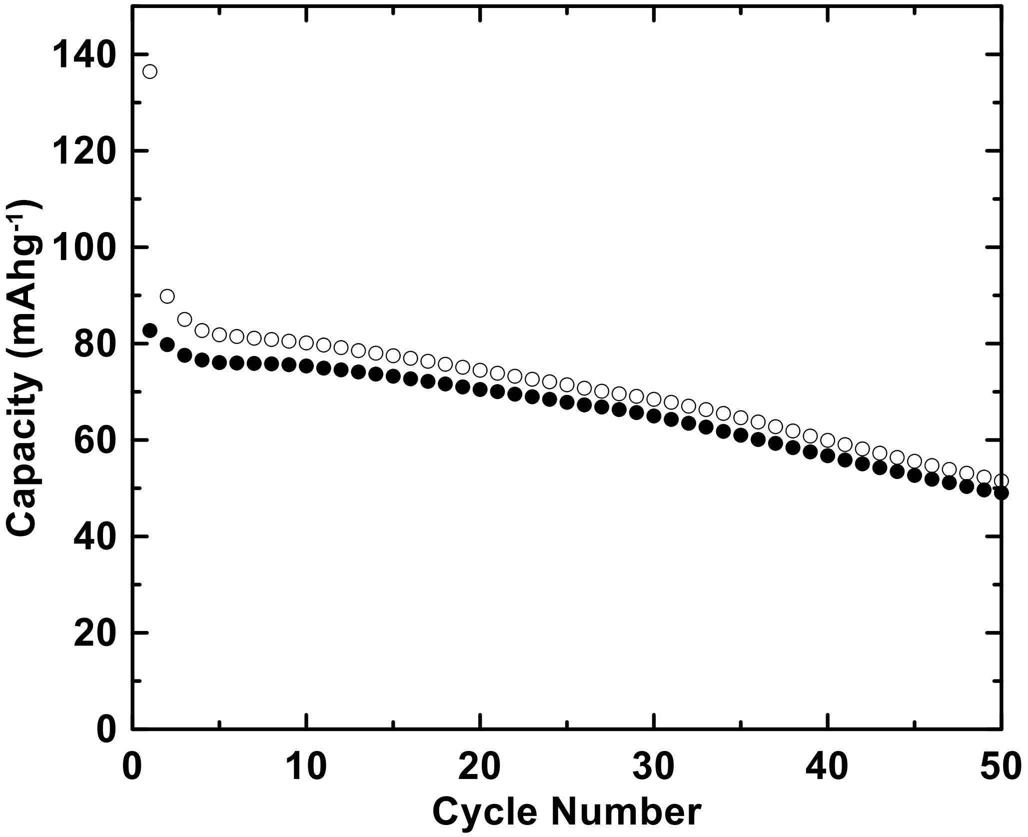

Figure 4.25: Capacity versus cycle number of a full cell using a negative electrode and positive electrode material that are both $Na_{0.6}Cr_{0.6}Ti_{0.4}O_2$. Cycled from 3.1 – 1.7 V using 1 M $NaPF_6$ in PC at a rate of C/10. Open and closed circles represent charge and discharge cycles, respectively.

This type of symmetric full cell is interesting due to the slightly smaller and larger cell volume of the $Na_xCr_{0.6}Ti_{0.4}O_2$ sodium rich and poor compositions, respectively. This was highlighted for the *in-situ* results found in Figure 4.18 where volume changes were less than 2%. This means that changes to the total volume of the dual electrode battery using $Na_{0.6}Cr_{0.6}Ti_{0.4}O_2$ would be negligible, as the volume changes would be complimentary. This situation is very different in a traditional lithium-ion battery composed of a graphite negative electrode and a $LiCoO_2$ positive electrode where both expand during charging.

The $x = 0.75$ composition of this series showed interesting electrochemical behavior upon cycling from 5 mV to 3.5 V, as shown in Figure 4.26. At this specific composition the high and low voltage plateau have capacities that are very similar and low hysteresis is observed.

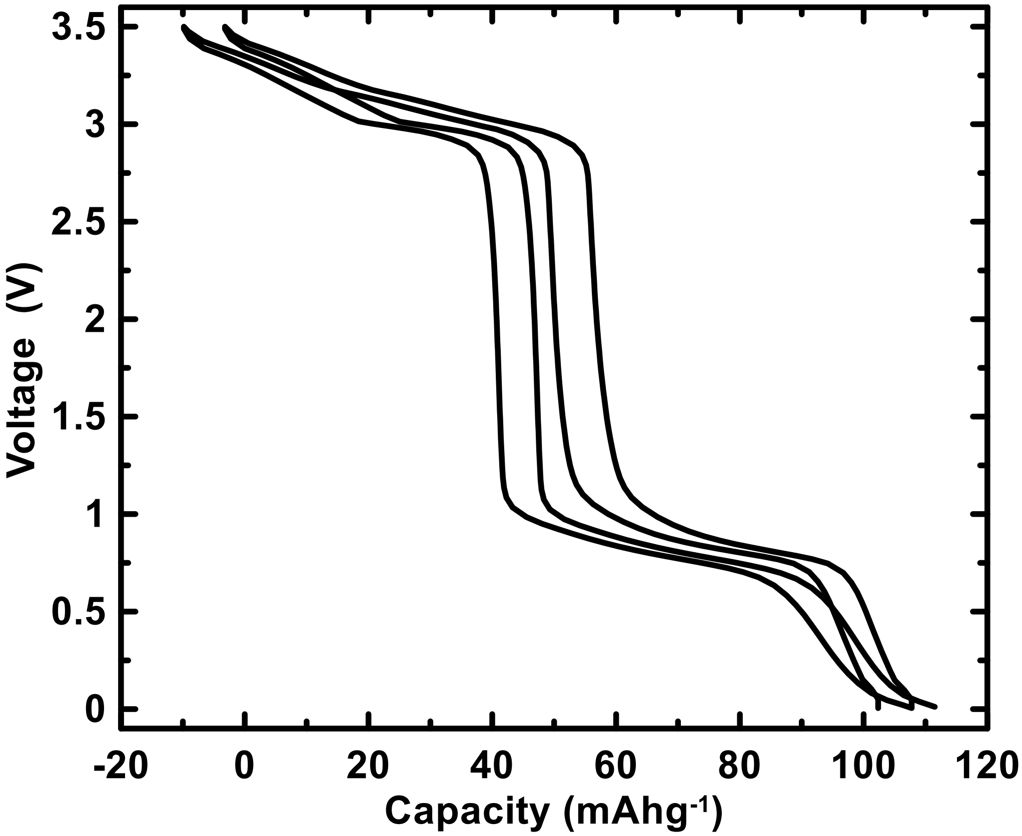

Figure 4.26: Voltage versus capacity profile of $Na_{0.75}Cr_{0.75}Ti_{0.25}O_2$ material cycled from 0.005 – 3.5 V.

A second $x = 0.75$ composition was made using the same synthesis conditions where the sodium content was close to 1.0, while at the same time the chromium titanium transition metal ratio was kept the same. This gave a chemical formula of $NaCr_{0.75}Ti_{0.25}O_2$, which will be abbreviated as $x = 1$. Figure 4.27 shows the voltage versus capacity profile of both of the $x = 0.75$ and 1 samples cycled between 0.005 and 3.5 V starting with either a charge or discharge cycle.

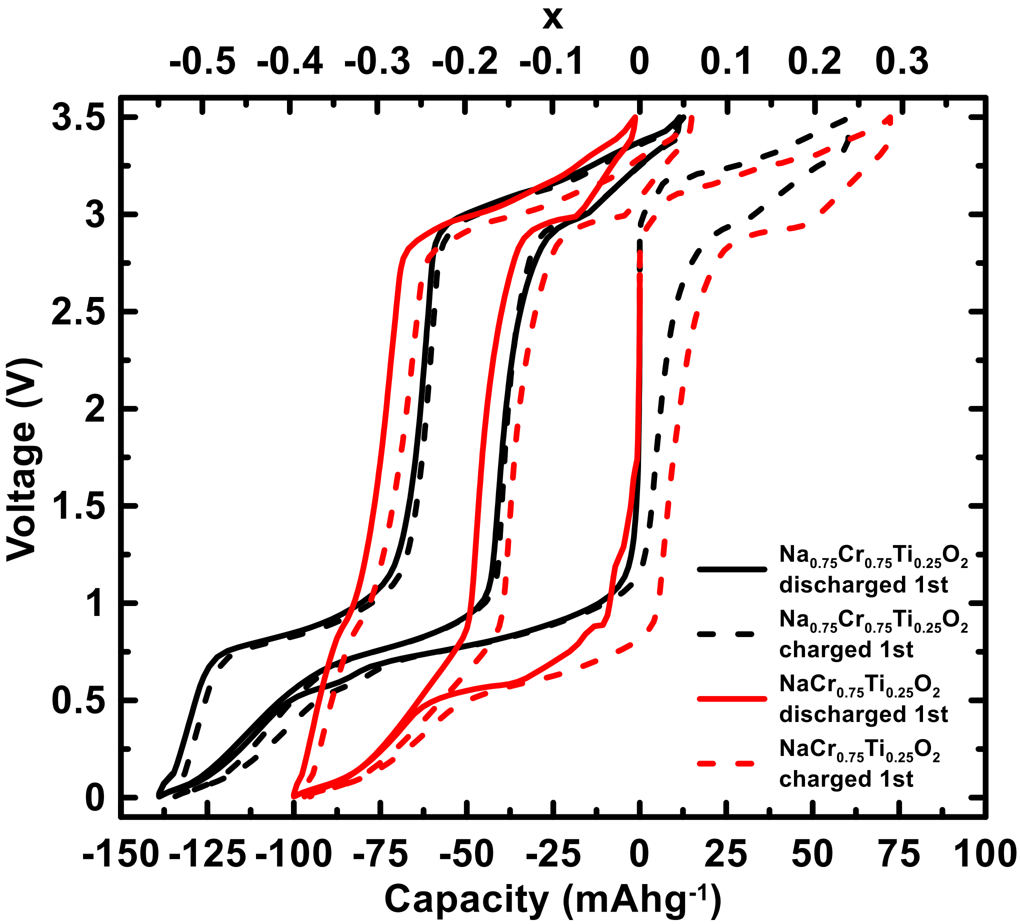

Figure 4.27: Voltage versus capacity profile of the $Na_{0.75}Cr_{0.75}Ti_{0.25}O_2$ (black) and $NaCr_{0.75}Ti_{0.25}O_2$ (red) cycled between 0.005 and 3.5 V. The solid and dashed curved were started on discharge and charge cycles, respectively.

The difference in sodium content can readily be seen from the lower voltage plateau capacity. The higher sodium content composition shows almost no capacity at low voltage while the lower sodium content composition that has vacancies in the sodium layer gives a capacity of approximately 70 mAh/g. What makes this result interesting is the fact that both of these compositions adopt the O3 structure and if the $Na_{0.75}Cr_{0.75}Ti_{0.25}O_2$ material is discharged to 0.005 V it becomes fully sodiated. This means that the $Na_{0.75}Cr_{0.75}Ti_{0.25}O_2$ material has now become $NaCr_{0.75}Ti_{0.25}O_2$. The reverse is also true of the $NaCr_{0.75}Ti_{0.25}O_2$ material charged to 3.5 V. It becomes desodiated and its composition is now $Na_{0.75}Cr_{0.75}Ti_{0.25}O_2$. *Ex-situ* XRD was done on all of these compositions to see what structural changes were occurring as each pristine material was either charged or discharged. Figure 4.28 and Figure 4.29 show that all of the compositions remain in the O3 structure.

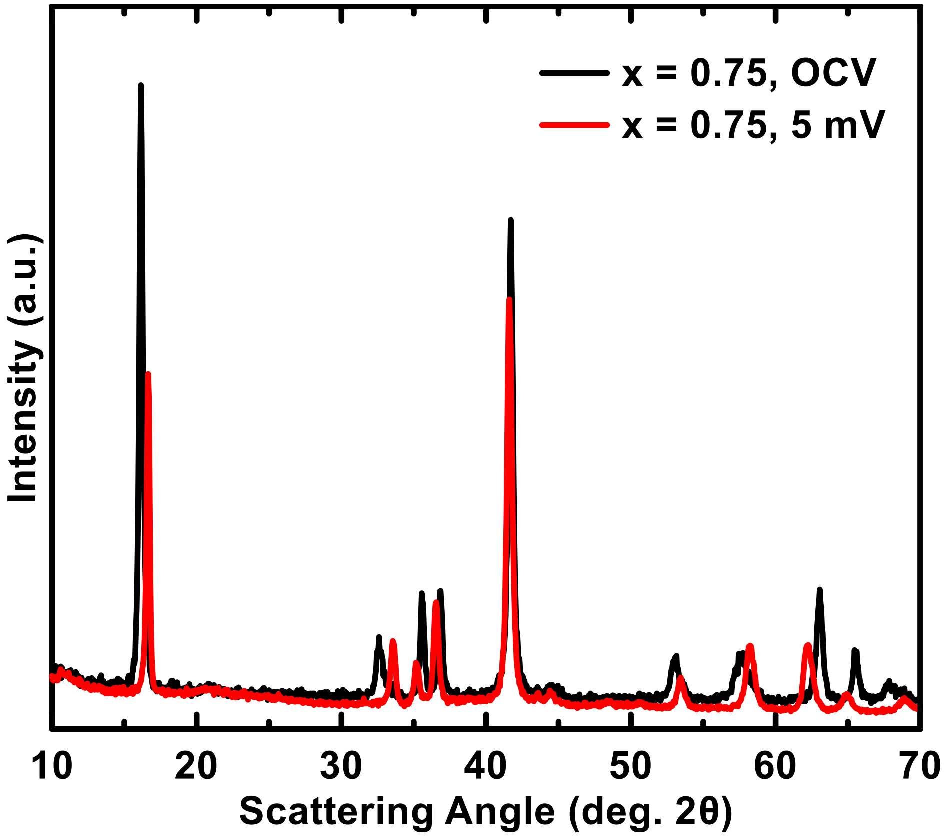

Figure 4.28: XRD patterns of the OCV, open circuit voltage, pristine (black) and discharged (red) $Na_{0.75}Cr_{0.75}Ti_{0.25}O_2$ material.

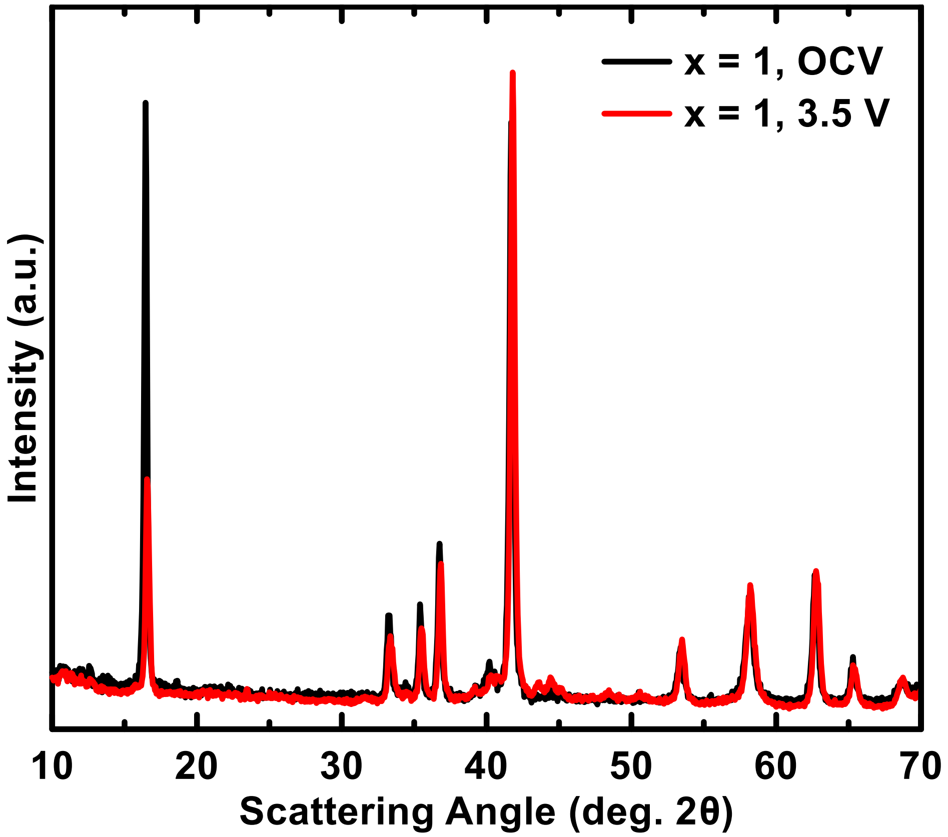

Figure 4.29: XRD patterns of the OCV, open circuit voltage, pristine (black) and charged (red) $NaCr_{0.75}Ti_{0.25}O_2$ material.

This means that identical structures may coexist at very different voltages. This is impressive as the voltage difference is about 1.5 V. It was originally thought that this phenomenon could be due to differences in transition metal ordering within the layered structure. However, NPD experiment results shown in Figure 4.7, Figure 4.30, Table 4.3 and Table 4.4 revealed that no chromium titanium ordering was present in either the x = 0.75 or 1 samples.

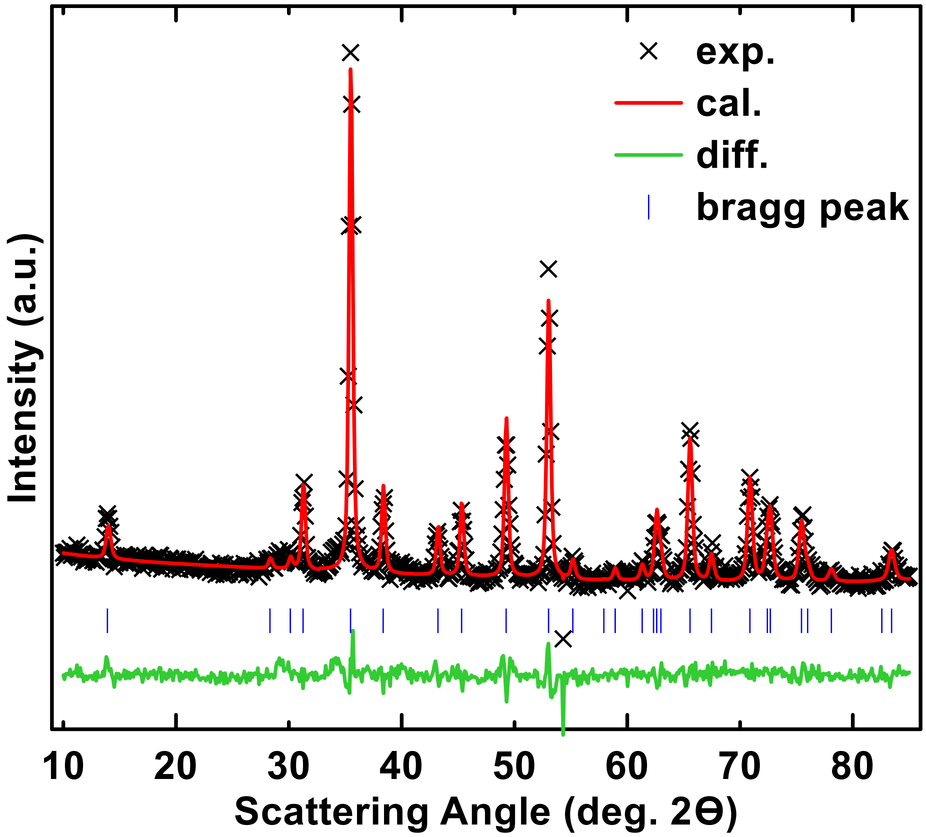

Figure 4.30: Experimental NPD pattern and refinement of O3-NaCr$_{0.75}$Ti$_{0.25}$O$_2$.

Table 4.4: Structural parameters obtained from Rietveld refinement of NaCr$_{0.75}$Ti$_{0.25}$O$_2$ NPD data.

NaCr$_{0.75}$Ti$_{0.25}$O$_2$ (space group: R$\bar{3}$m)					
atom	site	x	y	z	occupancy
Na	3b	0	0	0.5	0.9811(0)
Cr	3a	0	0	0	0.75
Ti	3a	0	0	0	0.25
O	6c	0	0	0.2314(2)	1.00
Cell parameters		a (Å)	b (Å)	c (Å)	R-factor
		2.9610(0)	2.9610(0)	16.1307(0)	
		α (°)	β (°)	γ (°)	1.44
		90	90	120	

More careful *ex-situ* or *in-situ* XRD experiments need to be carried out in order to confirm the existence of identical structures at different voltages. At this time the x = 0.75 *ex-situ* results show a decrease in the c lattice constant as sodium is inserted at low voltage as expected, however, the x = 1 *ex-situ* results do not show a substantial change in the c lattice constant as sodium is removed.

4.4 Conclusions

The $Na_xCr_xTi_{1-x}O_2$ series was synthesized via a facile solid state reaction. These materials display two major plateaus during cycling in sodium cells, one at high voltage and one at low voltage. The high voltage plateau is associated with the chromium +3 to +4 redox couple while the low voltage plateau is associated with the titanium +4 to +3 redox couple. The capacity of the high voltage plateau increases with increases x while the low voltage plateau decreases in capacity with increasing x. Of all the materials in the $Na_xCr_xTi_{1-x}O_2$ series, $Na_{0.6}Cr_{0.6}Ti_{0.4}O_2$ is of most interest as a potential negative electrode material due to its low voltage and low hysteresis in sodium cells. It can reversibly intercalate sodium at an average potential of 0.7 V with as low as 0.1 V hysteresis. This low voltage capacity comes from the existence of sodium ion vacancies in the layered P2 lattice structure and the previously mentioned Ti^{4+}/Ti^{3+} redox couple. $Na_{0.6}Cr_{0.6}Ti_{0.4}O_2$ has good cyclability and a first charge capacity of 120 mAh/g (or 457 Ah/L) during cycling between 0.005 and 2.2 V versus sodium, which corresponds to a 1500 Wh/L volumetric energy density in a cell vs. a 4 V positive electrode. Cycling P2-$Na_{0.6}Cr_{0.6}Ti_{0.4}O_2$ versus Li yields a similar capacity, however the average intercalation potential is much higher, at 1.44 V vs Li.

Compared to the other known layered $Na_xM_yTi_{1-y}O_2$ materials, such as $M = Li^+$, Ni^{2+} and Co^{2+}, $Na_{0.6}Cr_{0.6}Ti_{0.4}O_2$ has higher reversible capacity (120 versus ≤100 mAh/g) and lower hysteresis (0.1 versus 0.2 V) on the low voltage plateau [70,92,93]. $Na_{0.6}Cr_{0.6}Ti_{0.4}O_2$ can also behave as both a positive and negative electrode making it a dual purpose material. Full cells can be made from this single material for reduced cost and they display good cyclability. The only other example of a bi-functional material of this type is $Na_{2/3}Ni_{1/3}T_{12/3}O_2$. While $Na_{2/3}Ni_{1/3}T_{12/3}O_2$ falls short on the low voltage plateau compared to $Na_{0.6}Cr_{0.6}Ti_{0.4}O_2$, as outlined above, it displays a higher average voltage (3.7 versus 3.5 V) and higher capacity (90 versus 80 mAh/g) on the high voltage plateau, however full-cell data has yet to be presented.

Finally, a fascinating composition in this series, namely $Na_xCr_{0.75}Ti_{0.25}O_2$ where $x = 0.75$ or 1, interestingly shows structurally identical materials when cycled in sodium cells but with vastly different voltages. Further work is needed to fully understand this phenomenon.

CHAPTER 5 $Na_xV_xTi_{1-x}O_2$ ($0.66 \leq x \leq 1.0$)*

5.1 Introduction

Na_xVO_2 has been studied as an electrode material for sodium-ion batteries. The electrochemistry and structure of Na_xVO_2 pure phases having either octahedral or prismatic symmetry have been demonstrated [35–37]. Both P2 or O3 phases of Na_xVO_2 can tolerate the reversible removal/re-insertion of 0.5 Na, corresponding to a capacity of 120 mAh/g. Approximately 50 % of this capacity is centered near 1.6 V, with multiple voltage steps, which can be associated with sodium ion ordering within layers. The P2 phase has less hysteresis than its O3 counterpart along with superior rate capability. This is likely due to the higher sodium diffusion barrier for O3 Na migration from edge shared octahedra to tetrahedra sites versus the more facile P2 Na diffusion between face shared prismatic sites. The mechanism for sodium deintercalation/intercalation also appears to be dissimilar for the P2 and O3 phases as the differential capacity curves are significantly different. During sodium deintercalation, both $NaTiO_2$ and $NaVO_2$ have high average voltages of 1 V or greater, which would result in lower energy density, if they were employed as negative electrode materials in Na-ion cells. Although reversible Na removal from $NaTiO_2$ or $NaVO_2$ has been discussed, the low voltage Na insertion in these materials has not. In this study, the low voltage Na insertion into the $Na_xV_xTi_{1-x}O_2$ series was investigated. These materials were found to have high reversibility for low voltage Na insertion with little hysteresis.

---

*This chapter was adapted with permission from Fielden, R.; Cole, L.; Obrovac, M.N., Low Voltage Sodium Intercalation in $Na_xV_xTi_{1-x}O_2$ ($2/3 \leq x \leq 1$). *J. Electrochem. Soc.*, **2017**, *164*, A490–A497. Copyright 2017 Electrochemical Society. The author performed all of experimental work and writing contained in this paper.

5.2 Experimental

To prepare $Na_xV_xTi_{1-x}O_2$ ($2/3 \leq x \leq 1$), approximately 6 g of a stoichiometric ratio of Na_2CO_3 (BioXtra, ≥ 99.0 % Sigma Aldrich), V_2O_3 (99.7 %, metals basis, powder, Alfa Aesar), and anatase TiO_2 (puriss, 99 – 100.5 %, Sigma-Aldrich) were SPEX ball milled under argon with two half inch steel balls for a half hour and the resultant powder was pressed into ~2 g pellets at 2.55×10^8 Pa. The pellets were then heated at 950 °C in a 5 % H_2 in Ar atmosphere for 6 hours. A 5 % excess by weight of Na_2CO_3 was used to compensate for the loss of sodium due to its volatility at the high reaction temperature. After synthesis, the samples were transferred directly to an argon filled glove box without air exposure, to avoid reactivity with water, as the products were found to be hygroscopic.

5.3 Results and Discussion

Figure 5.1 shows SEM images of the $Na_{2/3}V_{2/3}Ti_{1/3}O_2$ material. The as prepared powder $Na_{2/3}V_{2/3}Ti_{1/3}O_2$ sample in panel (a) of Figure 5.1 has a particle size ranging from 2 - 10 μm with a smooth hexagonal shape morphology. Panel (b) of Figure 5.1 shows the powder with a roughened surface after air exposure for 30 days, highlighting the hygroscopic nature of these samples.

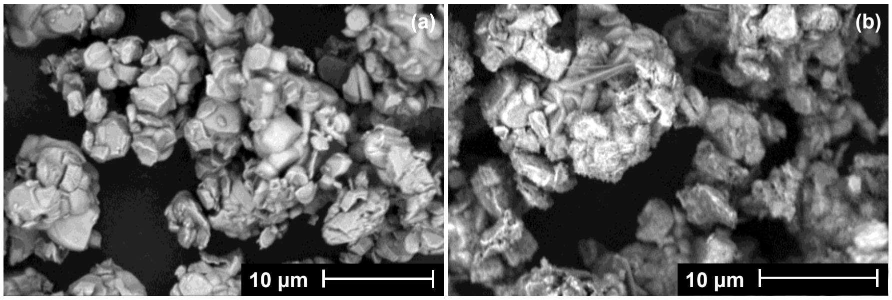

Figure 5.1: SEM image showing $Na_{2/3}V_{2/3}Ti_{1/3}O_2$ particles as prepared by solid state synthesis. A pristine powder and a powder exposed to air for 30 days are shown in panel (a) and (b), respectively. Adapted with permission from Reference 108.

Figure 5.2 shows the XRD patterns of the $Na_xV_xTi_{1-x}O_2$ series where $0.6 \leq x \leq 1.0$. Using the notation by Delmas [79], samples with $0.66 \leq x \leq 0.7$ are phase pure with the P2 structure while samples with $0.8 \leq x \leq 1.0$ are phase pure with the O3 structure. The transition metals and sodium ions occupy alternating layers of octahedral and prismatic site symmetry, respectively. Vacancies are present in the sodium layer as discussed in a previous report [91]. For compositions with $x < 0.66$, multiple unidentified phases are present. It was found that this causes the observed capacity to be much lower than the theoretical capacity for these compositions, suggesting that the additional phases are electrochemically inactive. It is thought that at such low x values there are not enough sodium ions present in the Na layer to maintain the layered framework.

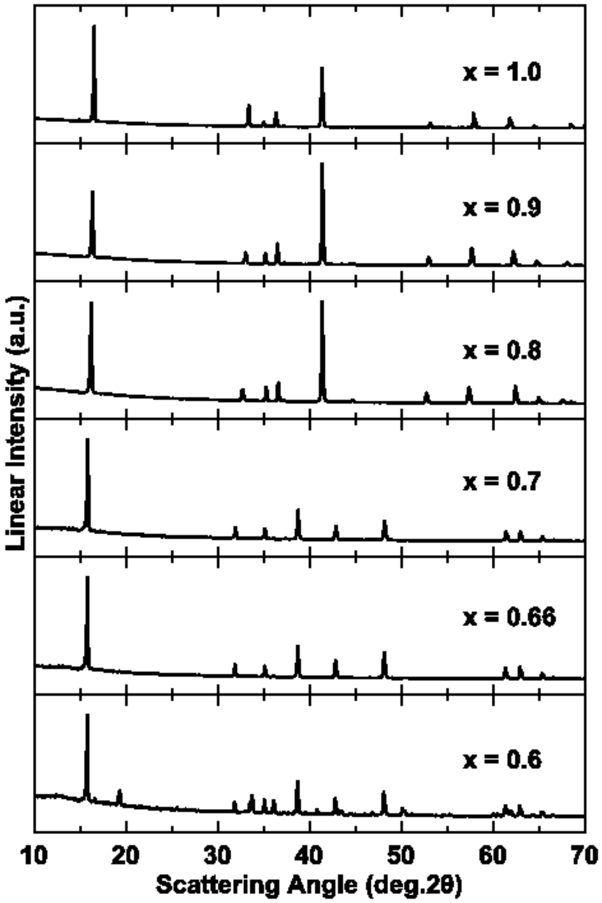

Figure 5.2: XRD patterns for the $Na_xV_xTi_{1-x}O_2$ series from $0.6 \leq x \leq 1.0$. Reproduced with permission from Reference 108.

Rietveld refinement of the XRD patterns was conducted for all the single phase samples. The Bragg R factors of all the refinements were less than 5 %. As an example, Figure 5.3 shows the measured XRD pattern of $Na_{2/3}V_{2/3}Ti_{1/3}O_2$, the XRD pattern calculated by Rietveld refinement of the P2 structure, a difference plot, and Bragg reflections. The crystallographic parameters obtained from the refinement are listed in Table 5.1.

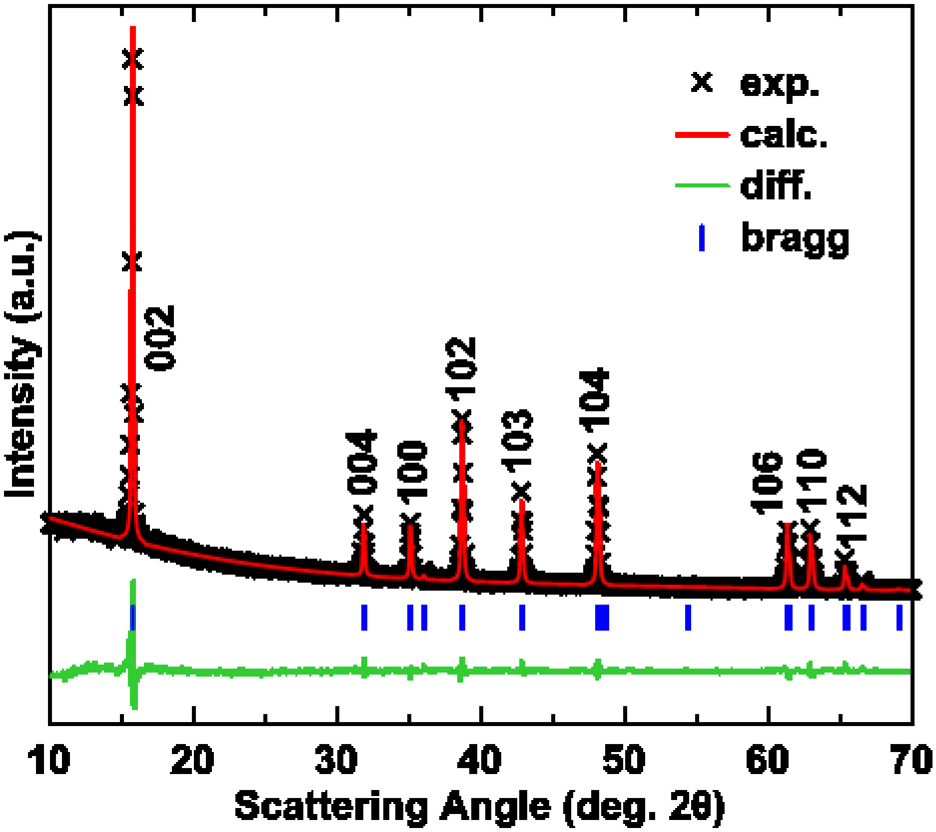

Figure 5.3: XRD pattern and Rietveld refinement of $Na_{2/3}V_{2/3}Ti_{1/3}O_2$, with Bragg peaks indicated. Reproduced with permission from Reference 108.

Table 5.1: Structural parameters obtained from Rietveld refinement of $Na_{2/3}V_{2/3}Ti_{1/3}O_2$ XRD data.

$Na_{0.66}V_{0.66}Ti_{0.33}O_2$ (space group: $P6_3/mmc$)					
atom	site	x	y	z	occupancy
Na_f	2b	0	0	0.25	0.2100(2)
Na_e	2c	0.33	0.66	0.25	0.4223(8)
V	2a	0	0	0	0.66
Ti	2a	0	0	0	0.33
O	4f	0.66	0.33	0.0911(4)	1.0043(6)
Cell parameters		a (Å)	b (Å)	c (Å)	R-factor
		2.951(8)	2.951(8)	11.239(1)	
		α (˚)	β (˚)	γ (˚)	2.55
		90	90	120	

Neutron diffraction studies were also done on the x = 0.66 and 0.8 samples and determined that no in plane ordering was occurring in the sodium or transition metal layer. The NPD patterns and fit parameters can be seen in Figure 5.4, Figure 5.5, Table 5.2, and Table 5.3.

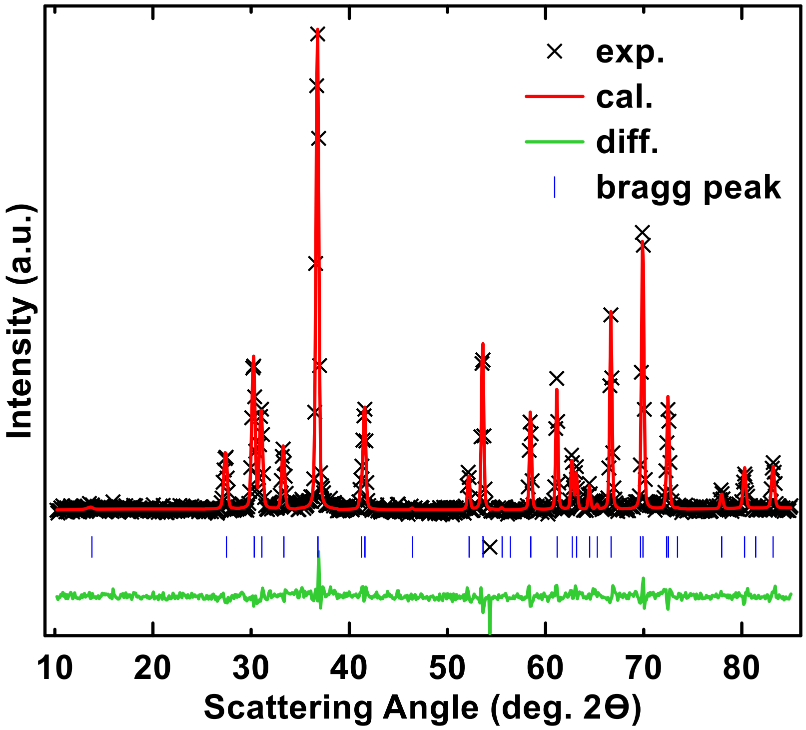

Figure 5.4: Experimental NPD pattern and refinement of P2-$Na_{0.66}V_{0.66}Ti_{0.33}O_2$.

Table 5.2: Structural parameters obtained from Rietveld refinement of $Na_{0.66}V_{0.66}Ti_{0.33}O_2$ NPD data.

$Na_{0.66}V_{0.66}Ti_{0.33}O_2$ (space group: $P6_3/mmc$)					
atom	site	x	y	z	occupancy
Na_f	2b	0	0	0.25	0.2294(5)
Na_e	2c	0.33	0.66	0.25	0.4226(6)
V	2a	0	0	0	0.66
Ti	2a	0	0	0	0.34
O	4f	0.33	0.66	0.0937(7)	1.00
Cell parameters		a (Å)	b (Å)	c (Å)	R-factor
		2.958(0)	2.958(0)	11.287(6)	2.18
		α (°)	β (°)	γ (°)	
		90	90	120	

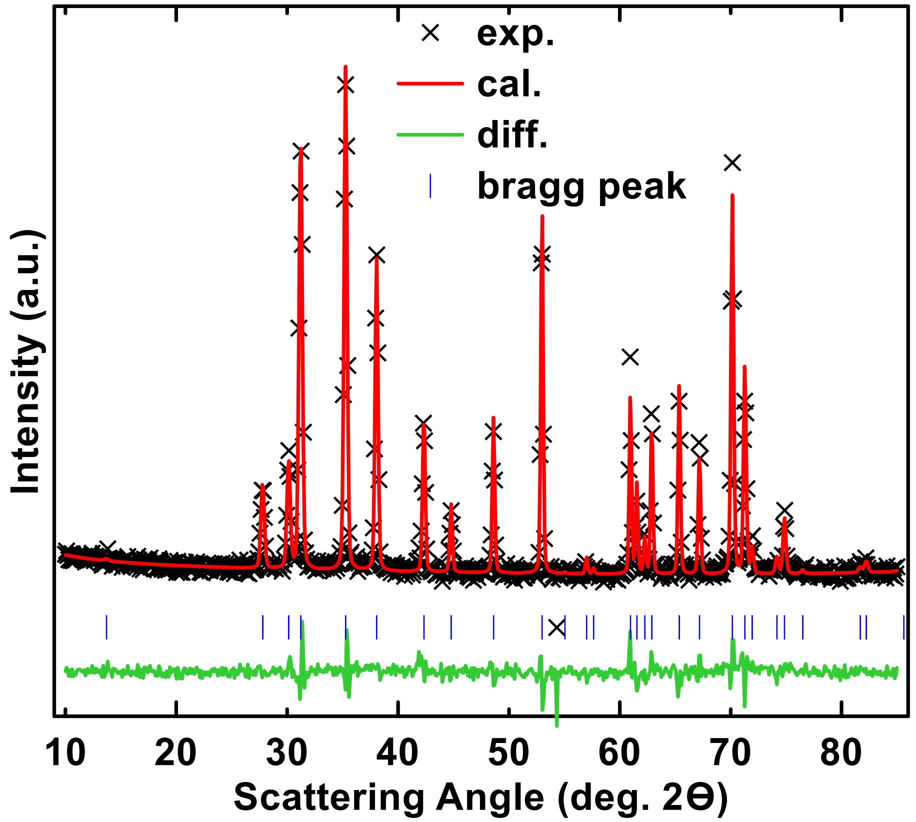

Figure 5.5: Experimental NPD pattern and refinement of O3-$Na_{0.8}V_{0.8}Ti_{0.2}O_2$.

Table 5.3: Structural parameters obtained from Rietveld refinement of $Na_{0.8}V_{0.8}Ti_{0.2}O_2$ NPD data.

<table>
<tr><td colspan="6">$Na_{0.8}V_{0.8}Ti_{0.2}O_2$ (space group: $R\bar{3}m$)</td></tr>
<tr><td>atom</td><td>site</td><td>x</td><td>y</td><td>z</td><td>occupancy</td></tr>
<tr><td>Na</td><td>3b</td><td>0</td><td>0</td><td>0.5</td><td>0.6515(5)</td></tr>
<tr><td>V</td><td>3a</td><td>0</td><td>0</td><td>0</td><td>0.8</td></tr>
<tr><td>Ti</td><td>3a</td><td>0</td><td>0</td><td>0</td><td>0.2</td></tr>
<tr><td>O</td><td>6c</td><td>0</td><td>0</td><td>0.2687(2)</td><td>1.00</td></tr>
<tr><td colspan="2">Cell parameters</td><td>a (Å)</td><td>b (Å)</td><td>c (Å)</td><td rowspan="2">R-factor</td></tr>
<tr><td colspan="2"></td><td>2.9682(0)</td><td>2.9682(0)</td><td>16.4859(0)</td></tr>
<tr><td colspan="2"></td><td>α (˚)</td><td>β (˚)</td><td>γ (˚)</td><td rowspan="2">2.73</td></tr>
<tr><td colspan="2"></td><td>90</td><td>90</td><td>120</td></tr>
</table>

Figure 5.6 demonstrates the air stability of these materials. It shows XRD patterns of the $Na_{2/3}V_{2/3}Ti_{1/3}O_2$ material after being exposed to ambient air for differing amounts of time. $NaVO_2$ is known for its poor air stability [35,36], however as titanium is substituted for vanadium and sodium vacancies are created in these layered compounds their air stability is markedly increased. After 30 days the air exposed P2 sample shows only slight changes in the peak positions and peak intensity in its XRD pattern, with no new peaks appearing. This is also in stark contrast to the P2 chromium titanate samples in the previous chapter where only a few hours produced new peaks in the XRD pattern.

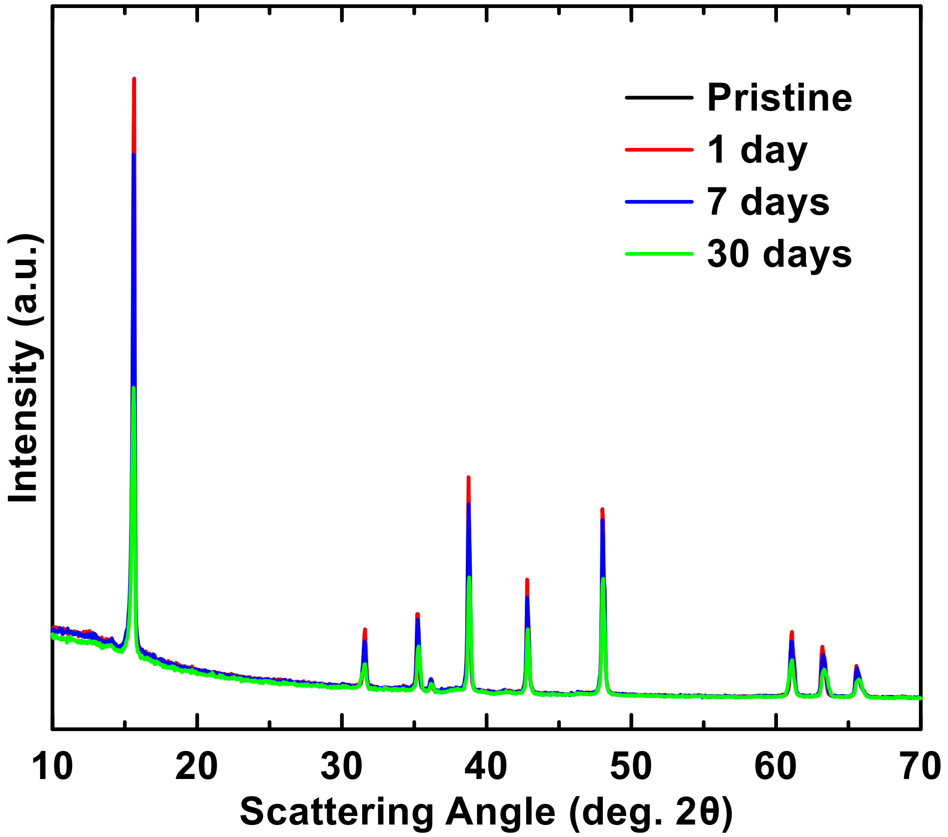

Figure 5.6: XRD patterns of the $Na_{2/3}V_{2/3}Ti_{1/3}O_2$ sample after exposure to ambient air at all, 1 day, 7 days, and 30 days shown in black, red, blue, and green, respectively.

Figure 5.7 shows how the lattice constants *a* and *c* of the $Na_xV_xTi_{1-x}O_2$ series change with respect to *x*. To directly compare the *c* lattice constants of the P2 and O3 structures, the *c* lattice constants of the P2 structures were multiplied by a factor of 3/2. As *x* is increased the lattice constant *a* increases, while *c* decreases, and, furthermore, there is a slight discontinuity for the lattice constants in the transition from P2 to O3. The increase in *a* with *x* can be attributed to the smaller ionic radius of Ti^{4+} compared to V^{3+} [26], while the decrease in the *c* lattice constant with *x* is likely due to the decrease in electrostatic repulsion between oxygen layers as vacancies in the Na layers are filled. Since the *a* lattice constant increases, while the c lattice constant decreases with *x*, the unit cell volume changes very little over the entire series. The lower panel in Figure 5.7

shows that the calculated density increases linearly with x, due to the unit cell mass increasing with increasing sodium content. Also displayed in Figure 5.7 is the true density as measured by a helium gas pycnometer. The large differences observed for the two density values at high x values will be discussed below.

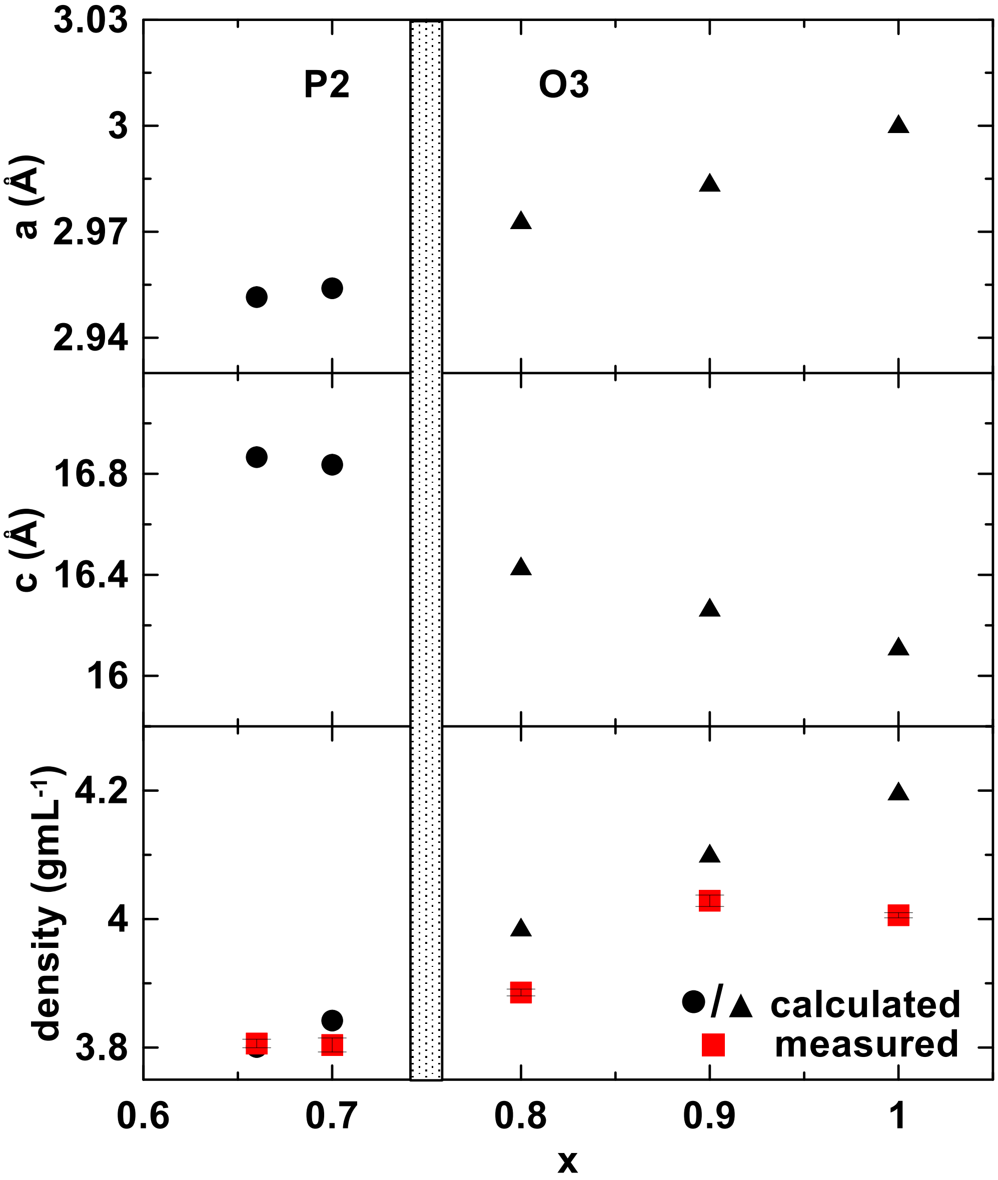

Figure 5.7: Lattice constants and the density of the $Na_xV_xTi_{1-x}O_2$ $0.66 \leq x \leq 1.0$ series where layered phases were observed. The lattice constants a and c are shown in top and middle panels, respectively, and the density is shown in the lower panel. P2: circles, O3: triangles. The lower panel also shows true density pycnometer measurements with red squares and black error bars. The dotted box is to illustrate the transition region from P2 to O3 structure types. Reproduced with permission from Reference 108.

Figure 5.8 shows the sodium content (*x*) from ICP measurements versus the target sodium composition, *x*. The solid black line is the where they should be in exact agreement. The ICP measurements tend to be lower than the target sodium composition, suggesting sodium has been lost during the high temperature synthesis. Although the ICP measurements are an accurate measure of the total sample composition, they do not necessarily reflect the stoichiometry of the phases formed. Indeed, the ICP results will be shown below to be inconsistent with electrochemical, XRD and density measurements, which is indicative that other phases are formed during synthesis.

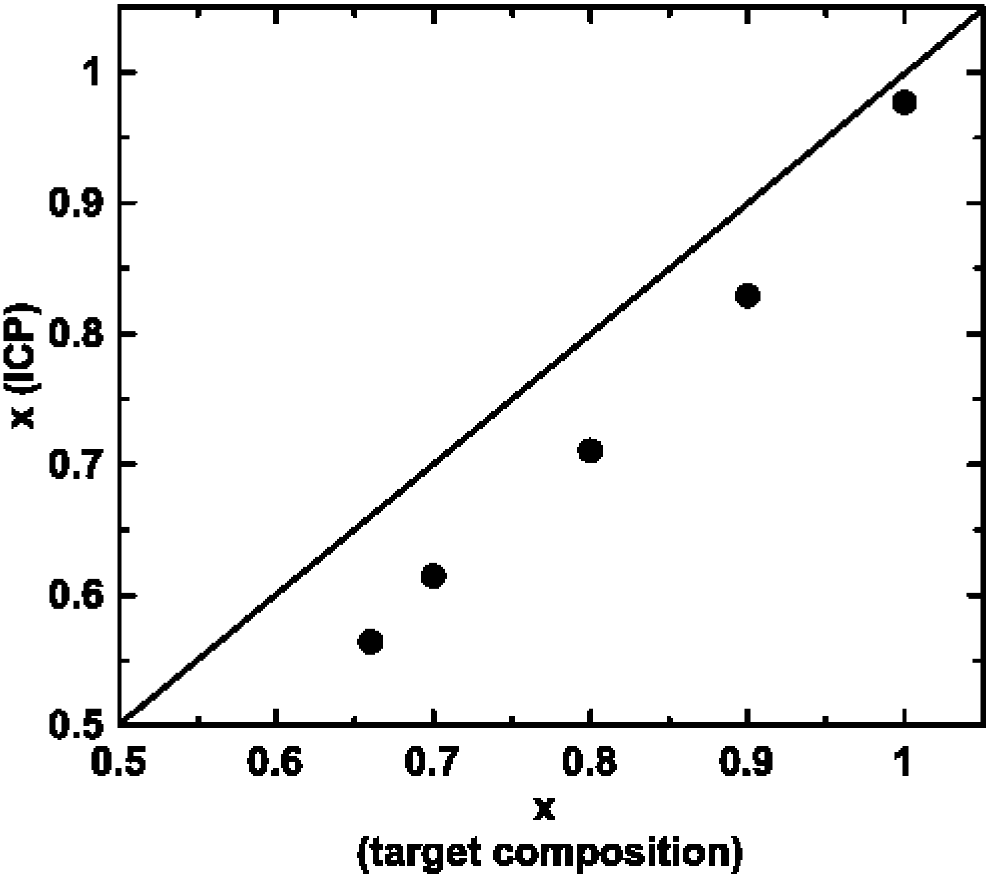

Figure 5.8: Sodium content (*x*) from ICP versus the experimental target of *x*. The solid black line shows where they would be in exact agreement. Reproduced with permission from Reference 108.

Figure 5.9 shows voltage curves of the $Na_xV_xTi_{1-x}O_2$ ($0.66 \leq x \leq 1.0$) series cycled in Na half-cells. The cells were initially discharged (sodiation) to 0.005 V, and then charged. Here positive capacity is defined as when sodium is added in excess of the initial sodium composition. Some negative capacity occurs when sodium has been removed, so that the materials' sodium composition is less than it was initially. Over half of the first discharge capacity can be attributed to the carbon black used in the electrode formulation. The type of carbon black used here was measured to have 500 mAh/g irreversible capacity versus Na. This corresponds to about 50 mAh/g irreversible capacity in all of the $Na_xV_xTi_{1-x}O_2$ cells. For all materials, during the initial discharge to 0.005 V, three sloping plateaus occur at about 1.8, 0.7, and 0.1 V. During the subsequent charge, four sloping plateaus can be observed at about 0.1, 0.7, 1.8 and 2.7 V. Part of the highest plateau occurs at negative capacities, while all the other plateaus occur at positive capacities. None of the plateaus were found to be very reversible in this voltage range and all plateaus faded during subsequent cycles. The 0.7 V plateau has been demonstrated by XAS to be due to the Ti^{4+}/Ti^{3+} redox couple in $Na_{0.6}[Cr_{0.6}Ti_{0.4}]O_2$ [94], however in $Na_xV_xTi_{1-x}O_2$ the V^{3+}/V^{2+} redox couple may also be contributing. The large voltage window used is thought to be the reason for the poor cyclability of these materials. If smaller strategic voltage windows are employed, depending upon the composition, very stable cycling with low voltage polarization can be achieved, as will be demonstrated below.

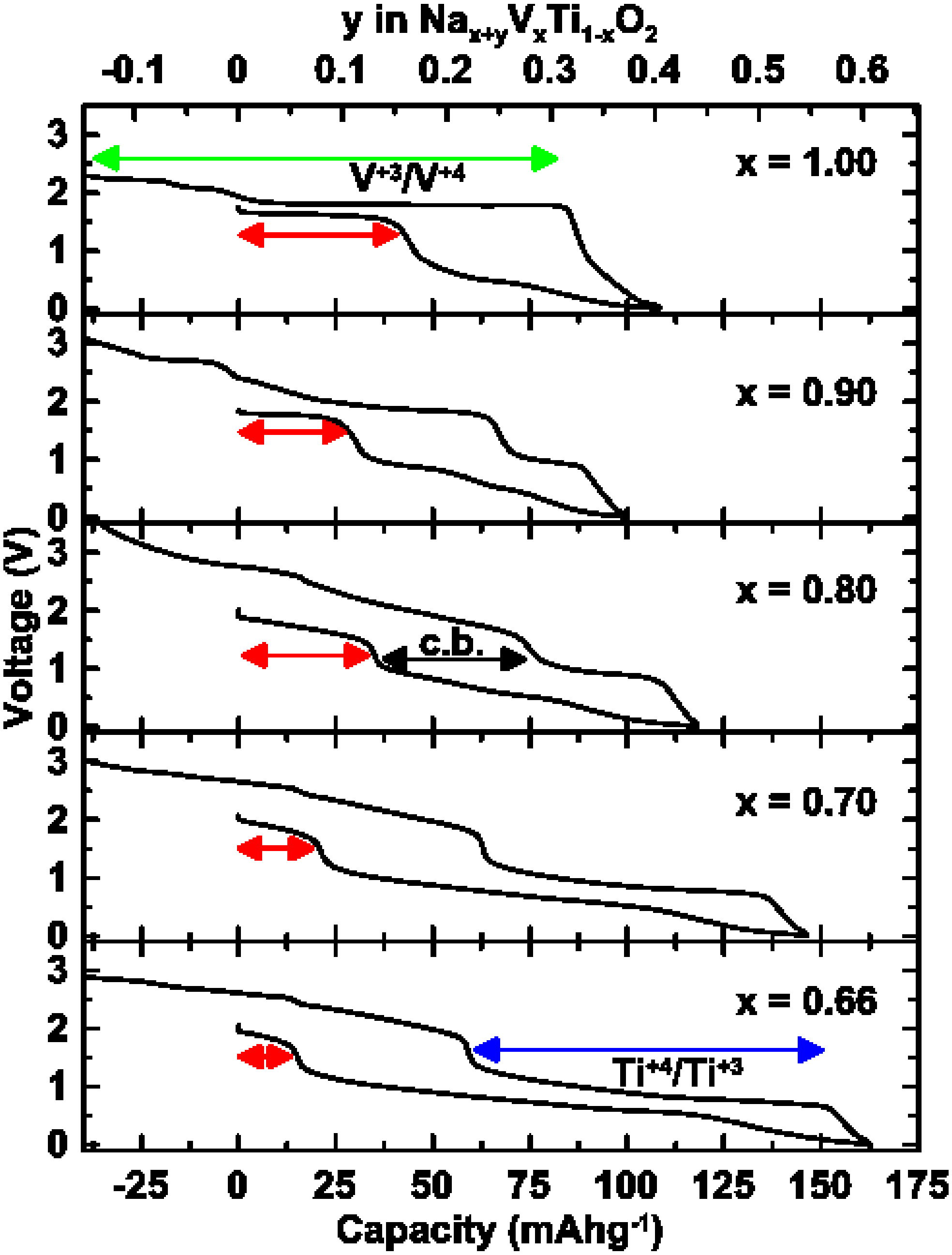

Figure 5.9: Voltage curves of $Na_xV_xTi_{1-x}O_2$ $0.66 \leq x \leq 1.0$ phases. The sodium content during cycling is indicated on the top axis as y in $Na_{x+y}V_xTi_{1-x}O_2$. Arrowed lines indicate the capacity at certain voltages due to sodium loss (red), carbon black (black), titanium redox (blue) and vanadium redox (green). Reproduced with permission from Reference 108.

The voltage curve of the $x = 1$ $NaVO_2$ sample consists of an initial plateau at about 1.7 V that corresponds to the V^{3+}/V^{4+} redox couple [35], followed by a sloping voltage curve that can be attributed to carbon black. The presence of the 1.7 V plateau is unexpected. $NaVO_2$ should not contain any V^{4+} and should not have vacancies in the sodium layer. Therefore, $NaVO_2$ should not be able to accommodate excess sodium and its initial discharge capacity should be zero. However, if Na is lost from the structure during synthesis, resulting in Na vacancies, there would be added capacity during the initial discharge. This should also result in lower measured densities than what is expected from the crystallographic densities, which is in fact what is observed in Figure 5.7. By comparing the lattice parameters from XRD measurements to the true density measurement, the actual sodium content of the $NaVO_2$ sample was determined to be 0.8 or about 0.2 Na vacancies exist in the structure. This corresponds well with the electrochemical results, in which about 0.18 formula units of Na could be inserted into this material above 1 V. Indeed, this is observed in previous reports of $NaVO_2$ synthesized with non-stoichiometric amounts of sodium in the layered structure [35–37].

The voltage curves of other $Na_yV_xTi_{1-x}O_2$ compositions also show an initial plateau at 1.7 V. The capacity of this plateau decreases with decreasing values of x. This suggests that less Na loss occurs as the V content is decreased and the Ti content is increased. The amount of Na loss can be calculated from the capacity of the 1.7 V plateau. Figure 5.10 shows a plot of the sodium loss, z, versus the target sodium content, x, in $Na_{x-z}V_xTi_{1-x}O_2$ as measured with a pycnometer and as calculated from the capacity of the 1.7 V plateau. There is a clear correlation between the two measurements, indicating that the more the pycnometry density measurements deviate from the calculated density, the greater the sodium loss in the samples, which is manifest as added capacity at 1.7 V. Therefore, according to Figure 5.7, the samples with the greatest Na loss are the $x = 0.8$ and $x = 1$ compositions, since the x-ray density and pycnometry density deviate the most for these samples.

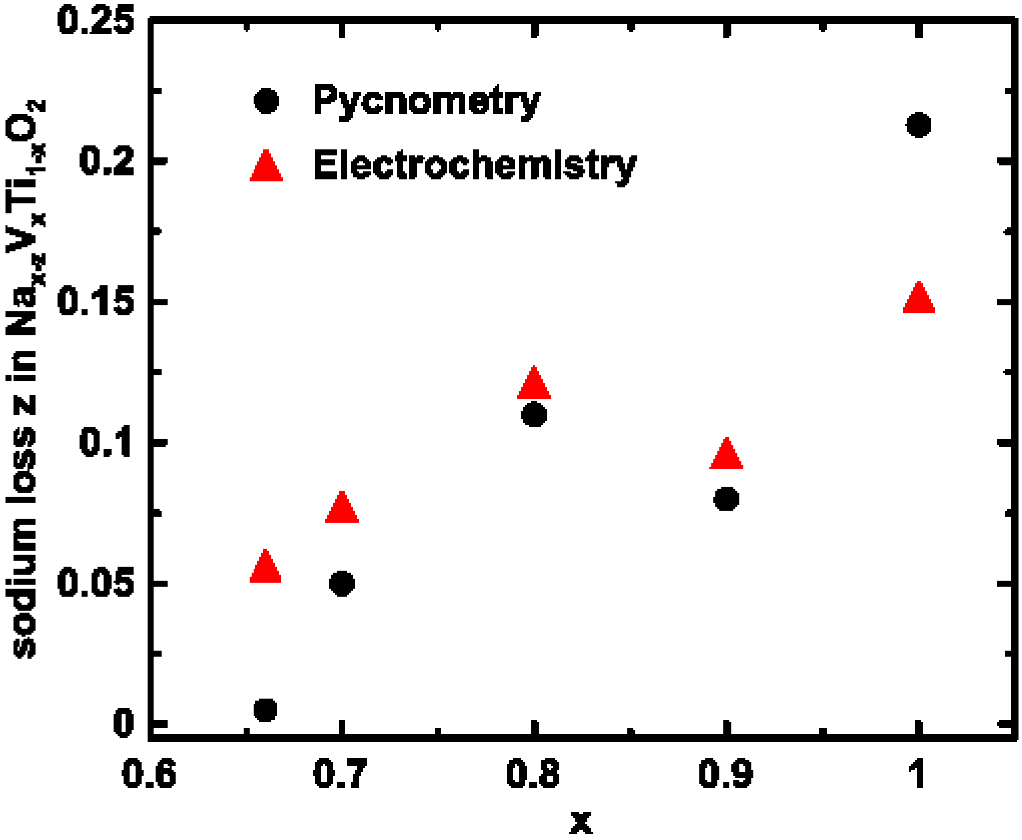

Figure 5.10: Sodium loss (z in $Na_{x-z}V_xTi_{1-x}O_2$) versus sodium target composition x. Black circles denote the sodium loss calculated from pycnometry, while red triangles show sodium loss from the electrochemistry. Reproduced with permission from Reference 108.

Interestingly, although the pycnometry, XRD and electrochemical results are in excellent agreement with respect to sodium loss at high x values, the ICP results are not. Although the ICP results shown in Figure 5.8 are indicative of some Na loss during synthesis, they do not reflect the trend shown by pycnometry or electrochemistry that the loss becomes more severe as the vanadium content is increased. This is an indication that sodium is likely lost from the structure to form solids that remain in the sample, but are not detectable by XRD, such as amorphous Na_2CO_3 or other sodium containing compounds. A simple way to probe the existence of Na_2CO_3 or other sodium containing phases is by FTIR [103]. Figure 5.11 shows the FTIR spectra of the $Na_xV_xTi_{1-x}O_2$ materials. All the samples have strong absorption peaks at ~400 cm^{-1} (labeled as peak 'A' in Figure 5.11), which can be attributed to TM-O vibrations [104]. Another peak at ~880 cm^{-1} (labeled as peak 'B' in Figure 5.11), which can be attributed to CO_3 vibrations in Na_2CO_3, sodium oxide or sodium hydroxide [103] is observed only for the $x = 0.80$ and 1.0 samples. The $x = 0.8$ and 1.0 samples have the largest disagreement between the ICP results and XRD and pycnometry results, and are those that display strong peaks at 880 cm^{-1} in their FTIR spectra. This result corroborates the hypothesis that sodium loss during synthesis results in the formation of an inactive sodium-containing phase.

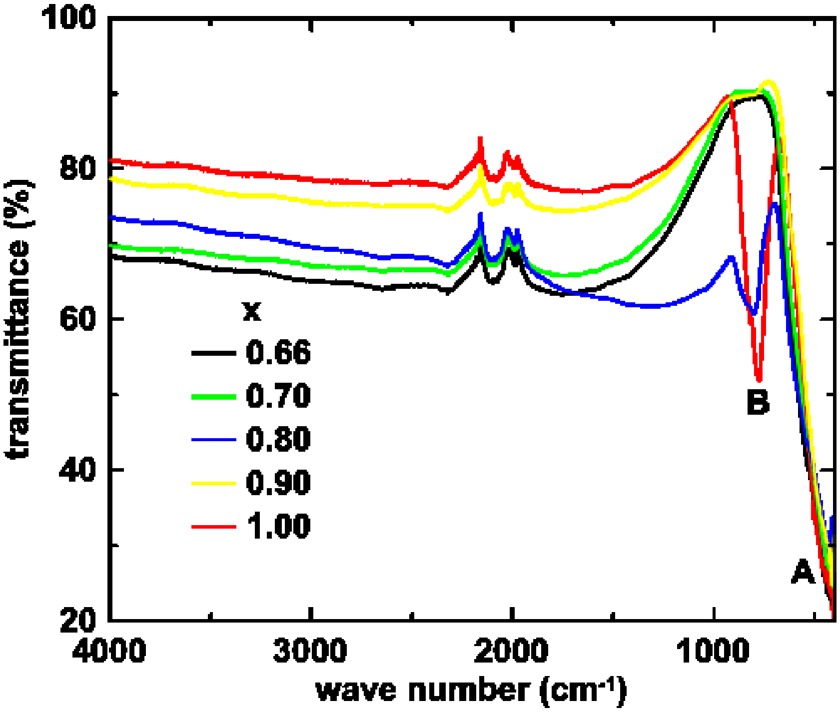

Figure 5.11: FTIR spectra of the $Na_xV_xTi_{1-x}O_2$ $0.66 \leq x \leq 1.0$ samples. As discussed in the text, peak A is attributed to metal-oxygen bonding in the layered oxides, while peak B is attributed to sodium carbonate or sodium oxide surface species. Reproduced with permission from Reference 108.

The above demonstrates an inherent danger in interpreting ICP results, namely that ICP results only indicate the overall sample composition, but they do not necessarily imply that a phase with this stoichiometry has been synthesized. Because of the possibility of the formation of sodium carbonates and hydroxides that may not be observable by XRD, ICP results may not accurately reflect Na-stoichiometries. This problem has also been reported for determining Li-stoichiometries in the case of Li-containing positive electrode materials (see for example Reference [105]). However, the presence of large amounts of transition metal containing species that cannot be observed by XRD is unlikely, because of the high scattering power of these elements. Therefore, the ICP reported transition metal contents of these samples are likely accurate. Accurate initial Na-stoichiometries are easily determinable from the size of the 1.7 V plateau. Using these results, the overall initial sample stoichiometries were determined and are listed in Table 5.4. Apart from deviations in the Na-content due to the formation of sodium containing surface species, the sample compositions agree well with target compositions. The largest deviation observed for any transition metal stoichiometry was only 4 atomic %.

Table 5.4: Comparison of the desired and actual stoichiometries of the $Na_xV_xTi_{1-x}O_2$ $0.66 \leq x \leq 1.0$ series as determined by ICP (transition metal content) and electrochemical analysis (Na content).

Desired Stoichiometry	**Actual Stoichiometry**
$Na_{0.66}V_{0.66}Ti_{0.34}O_2$	$Na_{0.61}V_{0.62}Ti_{0.38}O_2$
$Na_{0.70}V_{0.70}Ti_{0.30}O_2$	$Na_{0.63}V_{0.66}Ti_{0.34}O_2$
$Na_{0.80}V_{0.80}Ti_{0.20}O_2$	$Na_{0.68}V_{0.77}Ti_{0.23}O_2$
$Na_{0.90}V_{0.90}Ti_{0.10}O_2$	$Na_{0.81}V_{0.87}Ti_{0.13}O_2$
$NaVO_2$	$Na_{0.85}VO_2$

The amount of sodium loss during the synthesis of $Na_yV_xTi_{1-x}O_2$ has not previously been observed for other sodium transition metal titanates. The sodium titanates that are substituted with vanadium are unique when compared to those substituted by other first row transition metals such as chromium, cobalt and nickel. Figure 5.12 shows the first charge voltage curve of $Na_{0.6}Co_{0.6}Ti_{0.4}O_2$, $Na_{2/3}V_{2/3}Ti_{1/3}O_2$, $Na_{0.6}Cr_{0.6}Ti_{0.4}O_2$ and $Na_{0.6}Ni_{0.3}Ti_{0.7}O_2$. The differences in the voltage curve are a reflection of the sodium binding energy differences in these $Na_xM_yTi_{1-y}O_2$ materials. Sodium is uniquely weakly bound in the sodium vanadium titanates, with the onset of the high voltage plateau corresponding to transition metal ion oxidation occurring at a much lower voltage than for the other first row transition metals. For the other $Na_xM_yTi_{1-y}O_2$ materials, sodium deintercalation occurs at a much higher voltage and therefore Na is more tightly bound. This could explain why a significant amount of Na is lost from $Na_yV_xTi_{1-x}O_2$ during synthesis compared to other $Na_xM_yTi_{1-y}O_2$ materials.

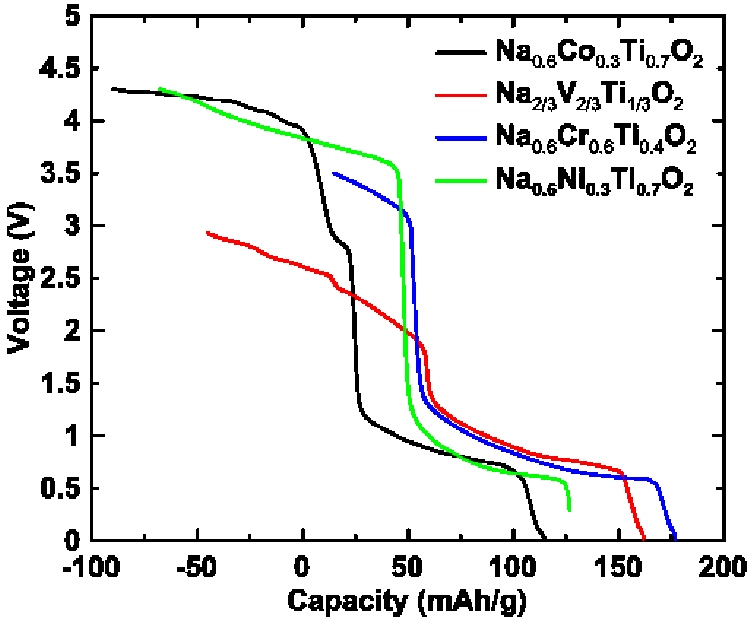

Figure 5.12: First charge voltage curve of $Na_{0.6}Co_{0.6}Ti_{0.4}O_2$ (black), $Na_{2/3}V_{2/3}Ti_{1/3}O_2$ (red), $Na_{0.6}Cr_{0.6}Ti_{0.4}O_2$ (blue) and $Na_{0.6}Ni_{0.3}Ti_{0.7}O_2$ (green), illustrating the sodium binding energy differences between the $Na_xM_yTi_{1-y}O_2$ materials. Reproduced with permission from Reference 108.

Figure 5.13 shows the gravimetric capacity of the 0.7 V plateau versus the number of vacancies (1-x) in $Na_xV_xTi_{1-x}O_2$. As x is decreased the lowest voltage plateau (0.7 V) increases in capacity. During discharge on this plateau sodium is being accommodated into the vacancies in the $Na_xV_xTi_{1-x}O_2$ sodium layer (as is confirmed by *in situ* XRD below). Therefore, the increasing capacity of this plateau with decreasing x is consistent with the number of sodium vacancies increasing in $Na_xV_xTi_{1-x}O_2$ with decreasing x. The low voltage and low hysteresis of the lower plateau is interesting for negative electrode material applications in sodium cells, especially for those materials with low values of x. Therefore, the cycling characteristics of the low voltage plateau were investigated.

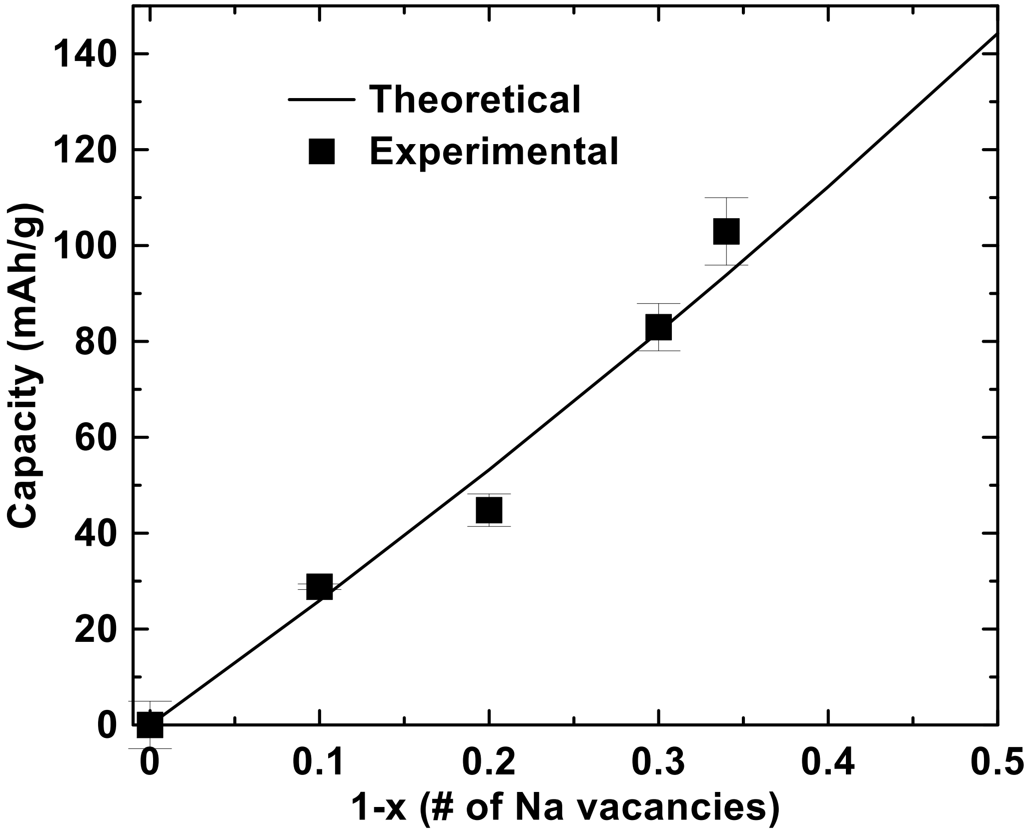

Figure 5.13: Theoretical (black line) and experimental (symbols) capacity versus the number of vacancies (1-x) in $Na_xM_yTi_{1-y}O_2$. Reproduced with permission from Reference 108.

Figure 5.14 shows the voltage curve of a $Na_{2/3}V_{2/3}Ti_{1/3}O_2$ vs. sodium cell that was initially discharged and cycled between 5 mV and 1.6 V and 0.4 V and 1.6 V. These voltage ranges restrict cycling to the low voltage plateau. The 5 mV - 1.6 V and 0.4 V - 1.6 V voltage curves exhibit a large first cycle irreversible capacity and a reversible capacity of about 103 mAh/g (or 391 Ah/L) and 94 mAh/g (or 357 Ah/L), respectively. This is proximate to the theoretical gravimetric capacity value of 92 mAh/g that can be accommodated by the Na vacancies in $Na_{2/3}V_{2/3}Ti_{1/3}O_2$. The average voltage during desodiation for the cells discharged to 5 mV and 0.4 V were 0.76 V and 0.86 V, respectively. Very little hysteresis was observed for the cells discharged to both 5 mV and 0.4 V, namely 0.13 V and 0.06 V, respectively.

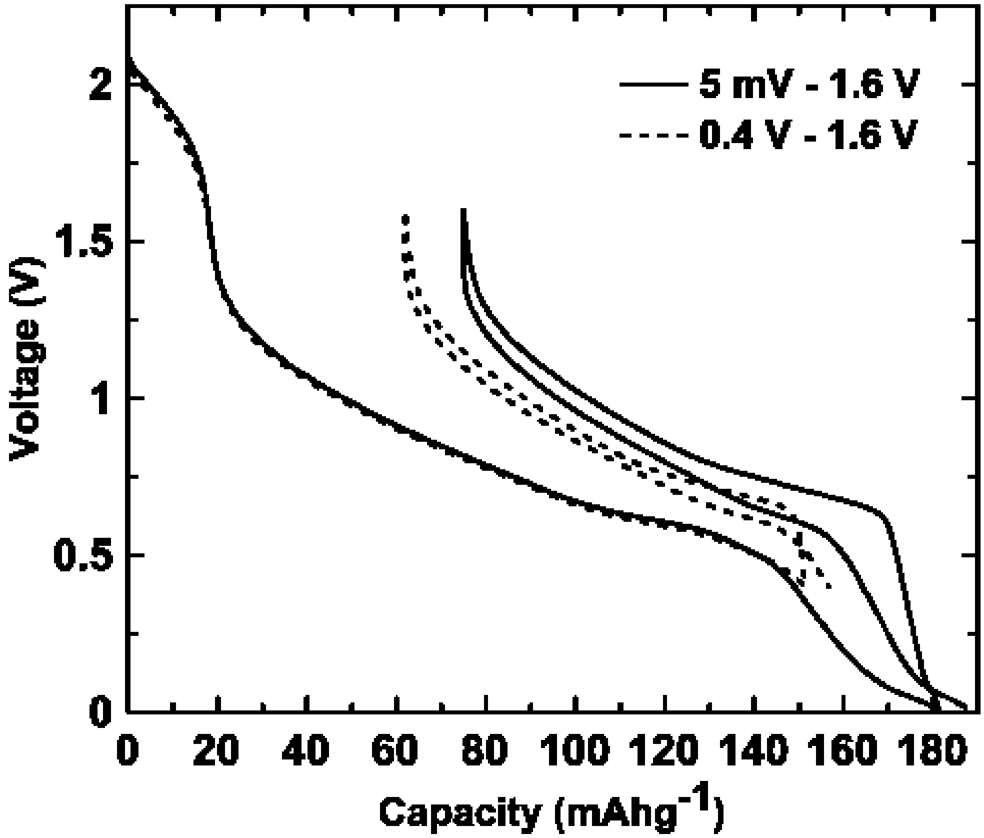

Figure 5.14: The voltage curve of $Na_{2/3}V_{2/3}Ti_{1/3}O_2$, cycled between 0.005 – 1.6 V (solid) and 0.4 – 1.6 V (dashed). Reproduced with permission from Reference 108.

The features in the $Na_{2/3}V_{2/3}Ti_{1/3}O_2$ voltage curve can be more readily seen in the differential capacity plot shown in Figure 5.15. Features in the differential capacity plot appear to evolve during cycling. The discharge differential capacity consists of a broad peak between 1.3 V and 0.7 V, typical of single phase Na^+ insertion. This is followed by two sharper peaks at about 0.6 V and 0.1 V. The peaks observed during the first discharge in Figure 5.15 at about 0.6 V and 0.1 V and the reversible oxidation peak at about 0.6 V are consistent with the same features in the differential capacity of a carbon black electrode, shown in Figure 5.16. Therefore, these features are attributed to the carbon black additive in the electrode formulation and to the formation of the initial SEI layer. Most of this capacity is irreversible. This irreversible change is likely the reason for the sharp drop in capacity in early cycles. Other peaks evolve slightly during cycling until there are two peaks during charge and two during discharge. In order to correlate the features in the differential capacity with structural changes, an *in situ* XRD experiment was performed.

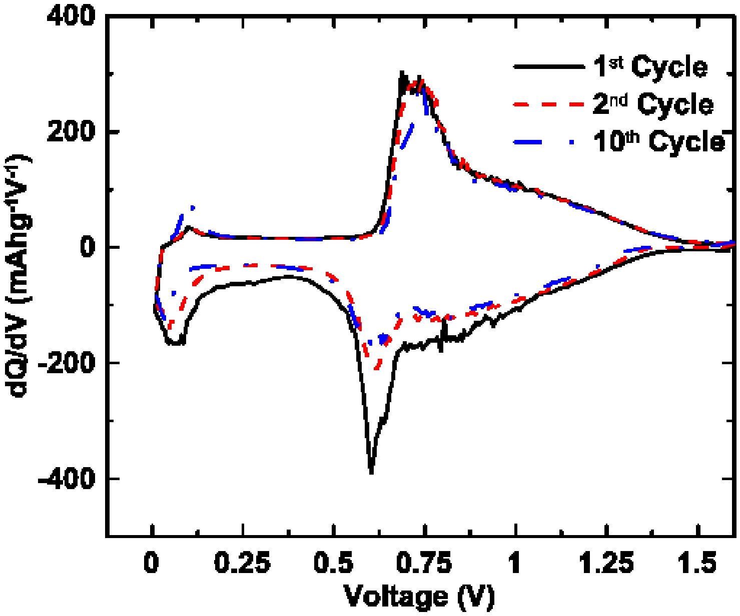

Figure 5.15: Differential capacity curves of $Na_{2/3}V_{2/3}Ti_{1/3}O_2$ cycled between 0.005 – 1.6 V. Reproduced with permission from Reference 108.

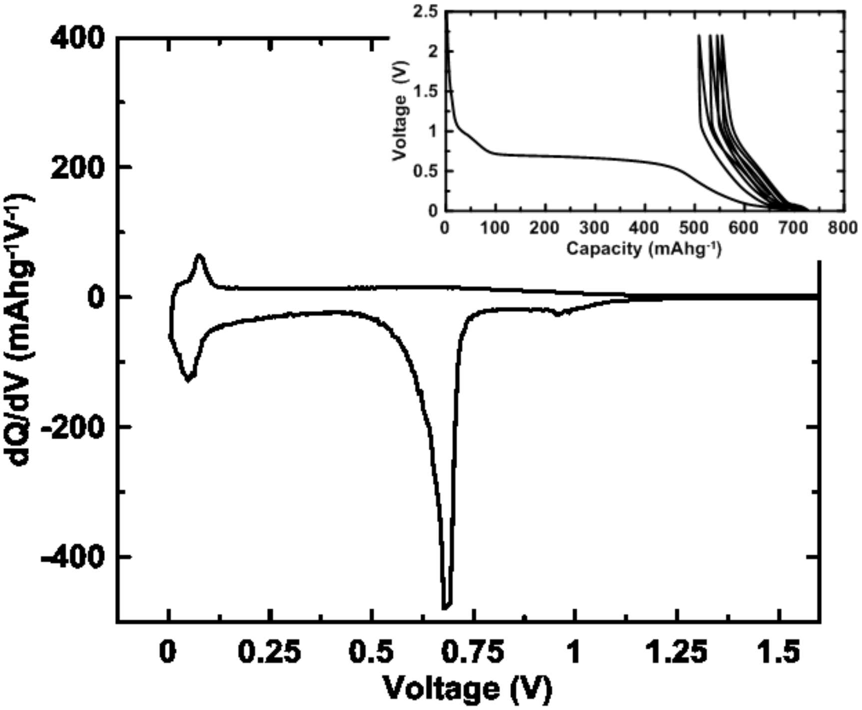

Figure 5.16: The differential capacity curve of carbon black cycled between 0.005 – 1.6 V with the inset showing the accompanying voltage curve. Reproduced with permission from Reference 108.

Figure 5.17 shows the XRD patterns of a $Na_{2/3}V_{2/3}Ti_{1/3}O_2$ *in situ* XRD cell during the first cycle between 5 mV and 4.0 V. Some of the peaks in the XRD patterns are caused by the Be window, and the *in-situ* cell parts. These peaks do not change during the charge and discharge process and are indicated in Figure 5.17. The initial XRD pattern is that of the phase pure $Na_{2/3}V_{2/3}Ti_{1/3}O_2$. During the first discharge only shifts in peak positions were observed and the electrode material remains in the P2 structure. During charge the material remains in the P2 structure until the voltage reaches 2.0 V. During the first discharge the (00*l*) peaks shift to higher angle while the (10*l*) peaks shift to lower angle. This indicates that the *a*-axis is expanding and the *c*-axis is contracting while sodium is being inserted. During the charge process up to 2.0 V, the opposite occurs and the peaks shift to their original position. Figure 5.18 shows the cell voltage, lattice constants, and unit cell volume plotted versus time. Overall, the changes in the lattice constants are small and correspond to a volume expansion of only 1.1 % at full sodiation. This is advantageous, since materials with low volume change during cycling are expected to maintain good structural integrity during cycling.

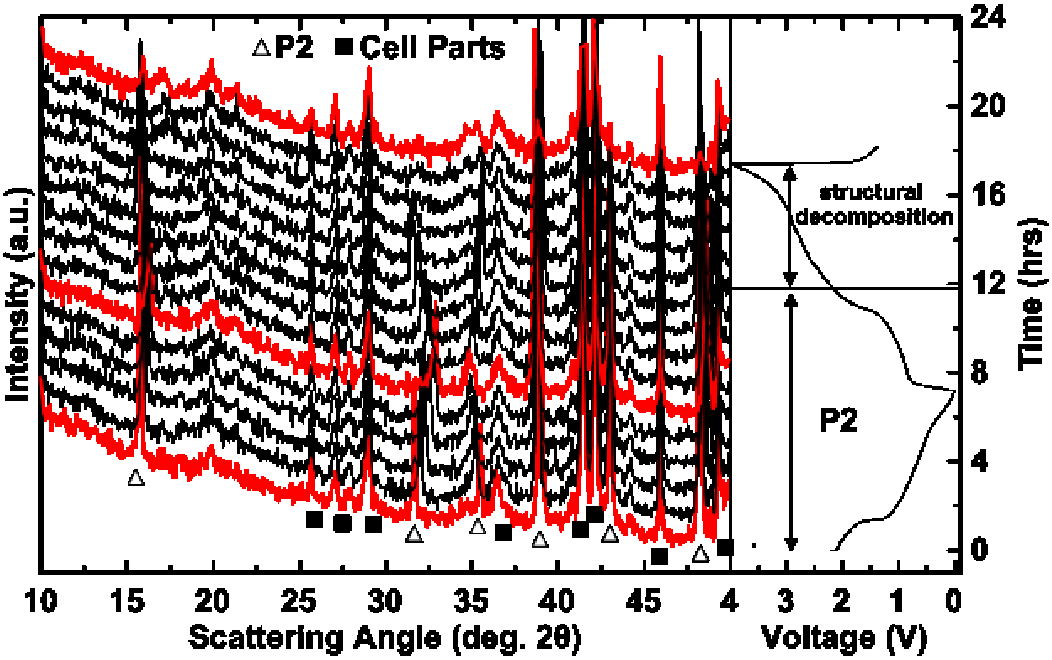

Figure 5.17: XRD patterns measured during the charge and discharge of a $Na_{2/3}V_{2/3}Ti_{1/3}O_2$ *in situ* cell with the corresponding voltage-time curve. Reproduced with permission from Reference 108.

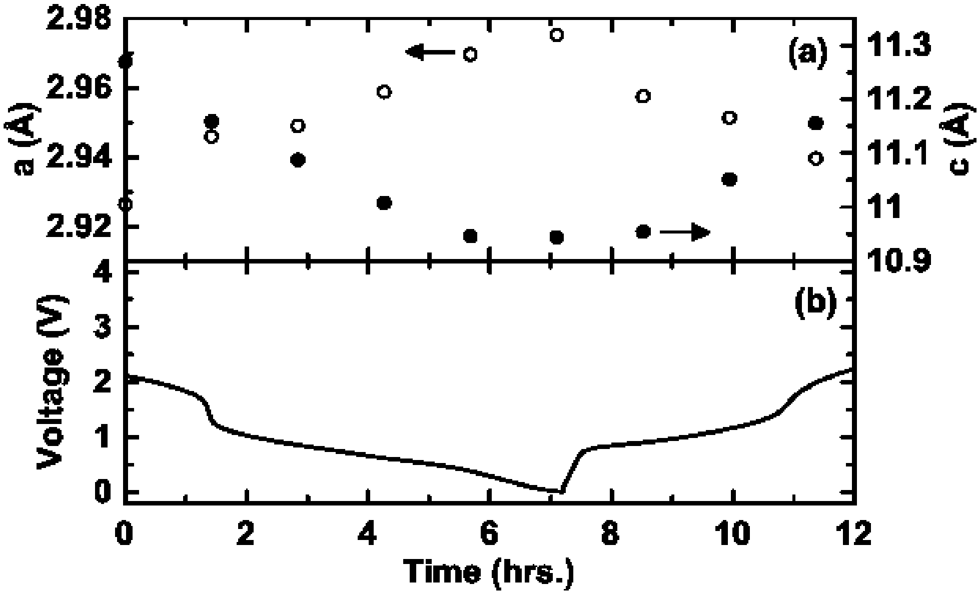

Figure 5.18: (a) The variation in the lattice parameters *a* (open circles) and *c* (closed circles) vs. time corresponding to the voltage curve of the $Na_{2/3}V_{2/3}Ti_{1/3}O_2$ *in situ* X-ray cell in panel (b). Reproduced with permission from Reference 108.

Above 2.0 V the structure begins to change and once the voltage surpasses 2.5 V the P2 Bragg peaks all but disappear. After charging to 4 V the *in situ* cell was discharged a second time. During this second discharge the voltage drops extremely rapidly, indicating a large cell polarization and the cell capacity is drastically decreased. Other P2-$Na_xM_yTi_{1-y}O_2$ negative electrodes, such as M = Ni or Fe, have large polarization after cycling at high voltages that access the M ion redox couple [91,106]. In each of these instances the authors do not elaborate as to what causes this irreversible change. Different behavior is observed for $Na_{0.6}Cr_{0.6}Ti_{0.4}O_2$, where stable cycling with little polarization can be achieved when the voltage window is kept below 3.8 V [94]. Above 3.8 polarization is increased, a phenomenon that is also observed for O3-$NaCrO_2$, which has been attributed to Cr^{3+} migration in the sodium layer [95]. However, transition metal migration is not expected for these P2-type materials, as their migration to prismatic sites would be energetically unfavorable. Another explanation for this behavior could be from the collapse of the layered structure due to the emptying of the Na layer. Since total structural decomposition occurs during this process, it is not possible to determine its mechanism by XRD. It should be noted that if the upper cut-off voltage is restricted to 1.6 V the structure remains phase pure P2 throughout the cycling process, resulting in stable cycling performance.

Figure 5.19 shows the capacity versus cycle number of the cells shown in Figure 5.14. The cells discharged to 5 mV and 0.4 V exhibit a linear fade over 100 cycles. A maximum Coulombic efficiency of only 99.1 % and 99.4 %, respectively and a 74 % and 78 % capacity retention over 100 cycles was achieved for the cells discharged to 5 mV and 0.4 V, respectively. These characteristics need to be improved for such materials to be used in practical application. Unfortunately, it is often difficult to make meaningful assessments of Na half-cell cycle life as the Na metal reference electrode stability and reactivity is an issue [107]. Both cells demonstrated large irreversible capacities during their first cycle, which lead to an initial Coulombic efficiency of only 0.59 for each. This is typical of the Na transition metal titanates, where 10 % by weight carbon black in the electrode formulation leads to large first cycle irreversible capacities of ~50 mAh/g.

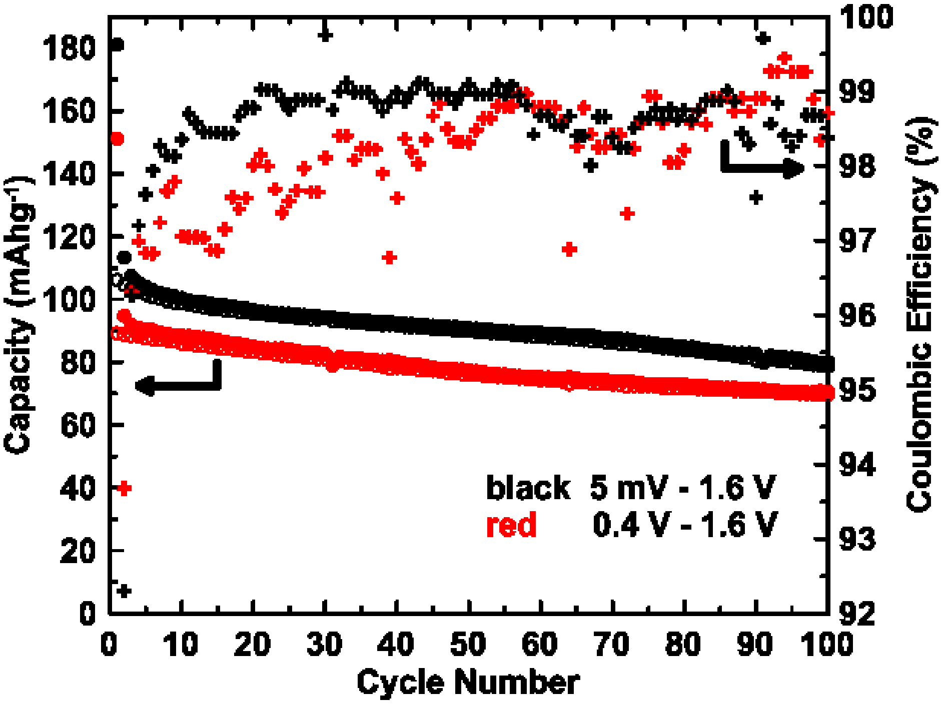

Figure 5.19: Capacity and Coulombic efficiency versus cycle number of the $Na_{2/3}V_{2/3}Ti_{1/3}O_2$ cells cycled between 0.005 – 1.6 V (black) and 0.4 – 1.6 V (red). Reproduced with permission from Reference 108.

Figure 5.20 shows voltage curve of $Na_{2/3}V_{2/3}Ti_{1/3}O_2$ cycled at rates ranging from C/10 (11 mA/g) to 5C (550 mA/g). C-rate was defined based on a theoretical capacity of 92 mAh/g, which is based on the number of sodium vacancies in the structure. The rate capability was poor. This can be more easily seen in Figure 5.21 where cycle number versus capacity is plotted. Cycling at 2C resulted in a capacity that was 66% of the C/10 capacity. This performance is typical for $Na_xM_yTi_{1-y}O_2$ type materials, where M = Cr, Co, Ni and Li [70,91–94,106]. Further improvements in rate capability are desirable if these materials are to be used in practical applications.

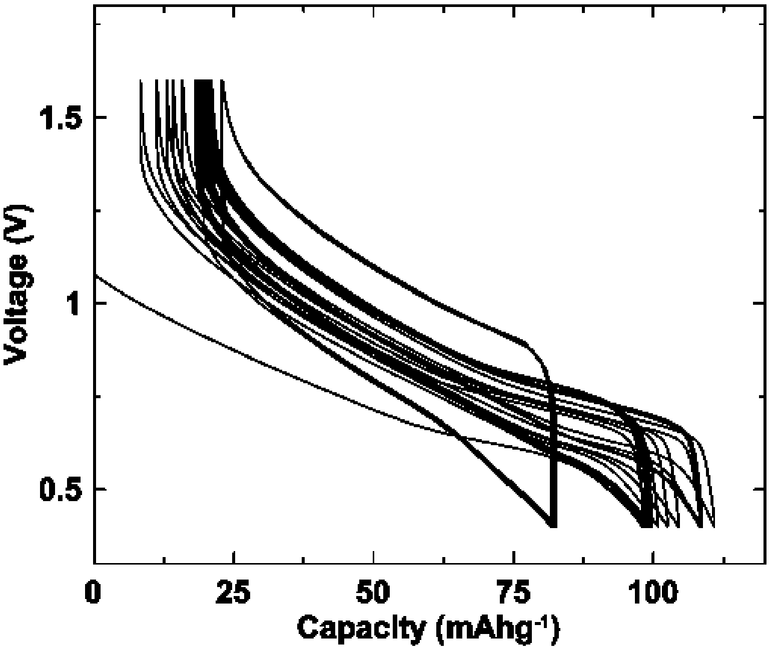

Figure 5.20: Voltage curves of a $Na_{2/3}V_{2/3}Ti_{1/3}O_2$ cell cycled at different rates. The cell was discharged to 0.4 V and charged to 1.6 V for five cycles each at rates of C/10, C/2, 2C, and C/10. Reproduced with permission from Reference 108.

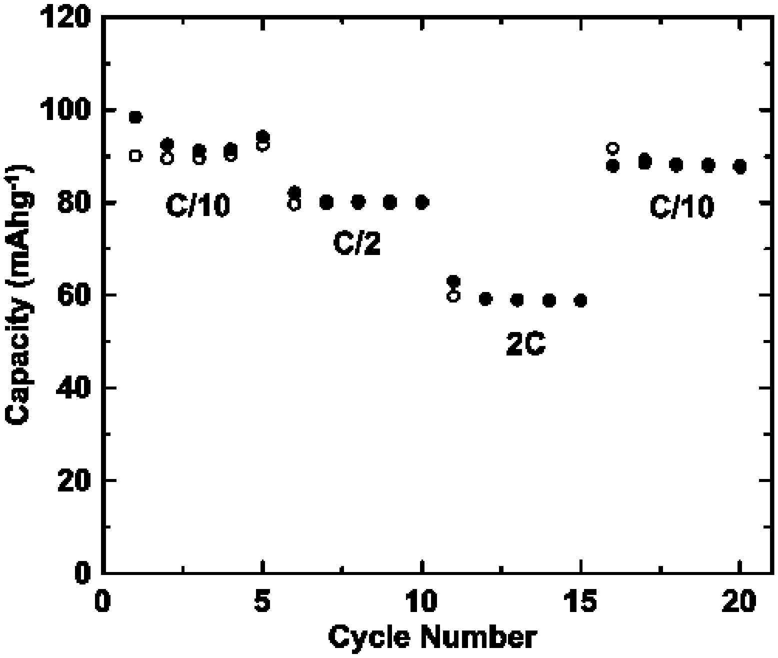

Figure 5.21: Capacity versus cycle number of a $Na_{2/3}V_{2/3}Ti_{1/3}O_2$ cell cycled at different rates. The cell was discharged to 0.4 V and charged to 1.6 V for five cycles each at rates of C/10, C/2, 2C, and C/10. Open and closed circles represent charge and discharge capacity, respectively. Reproduced with permission from Reference 108.

5.4 Conclusions

The $Na_xV_xTi_{1-x}O_2$ ($0.66 \leq x \leq 1.0$) series of oxides was synthesized via a facile solid state reaction. These materials can reversibly intercalate sodium at an average potential of 0.7 V with exceptional voltage efficiency. This average potential is similar across $Na_xM_yTi_{1-y}O_2$ type materials independent of *M*, as the same Ti^{4+}/Ti^{3+} redox couple is employed during electrochemical cycling. The lowest known average voltage for an oxide insertion material for NIBs is $Na_2Ti_3O_7$, with an average voltage of 0.3 V from the same Ti^{4+}/Ti^{3+} redox couple [67]. $Na_2Ti_3O_7$ has zig zag layers in which sodium atoms can be reversibly inserted. This structural difference leads to the lower sodium insertion voltage. However, poor conductivity is observed with titanium only containing sodium metal oxides, such as $Na_2Ti_3O_7$, and thus large amounts of carbon black are utilized in the electrode formulation (typically 30 versus 10 %). This is unfavorable as a threefold increase in carbon black greatly reduces the energy density.

The low voltage capacity of the $Na_xV_xTi_{1-x}O_2$ series increases with increasing sodium vacancies in the structure ($1-x$). The $x = 0.66$ composition, namely, $Na_{2/3}V_{2/3}Ti_{1/3}O_2$ has good cyclability (100 cycles) and delivered a first charge capacity of 100 mAh/g during cycling between 0.005 and 1.6 V, which correlates to a volumetric energy density of about 400 Ah/L. This capacity is similar to all other $Na_xM_yTi_{1-y}O_2$ materials except $M = Cr^{3+}$, to which it is inferior by only 20 mAh/g [94,108].

The P2 structure is maintained throughout cycling when the upper voltage cut-off is restricted to 1.6 V, as confirmed by i*n situ* XRD. For this reason, this is considered an intercalation process instead of a conversion reaction, which is typical of many metal oxides at low voltages. One important difference when vanadium (III) is substituted for titanium (IV) compared to other $Na_xM_yTi_{1-y}O_2$ materials is that it is less structurally stable. Structural decomposition occurs above 1.6 V, which is possibly due to transition metal migration. This voltage is much lower than other $Na_xM_yTi_{1-y}O_2$ materials where voltages of 3.5 V or higher are needed in order for structural decomposition to take place [109]. This is interesting as P2 structure type materials are generally thought to be more stable than the O3 types. However, in the V-Ti series extremely low structural stability is observed for not only for the O3 phases, but the P2 phases as well, such as P2-$Na_{2/3}V_{2/3}Ti_{1/3}O_2$.

During the high synthesis temperatures sodium loss was extreme with vanadium (III) in the transition metal layer compared to other metals [94,108]. Discrepancies between the calculated and measured densities were observed, where other $Na_xM_yTi_{1-y}O_2$ materials show good agreement. This led to a better understanding of the inherent dangers of ICP data interpretation, namely ICP results may not accurately reflect Na-stoichiometries when multiple unknown or undetectable phases are present.

Good cyclability and low hysteresis make this material a promising negative electrode material for NIBs. This adds another member to the already diverse sodium transition metal titanate family of layered negative electrode materials for NIBs.

CHAPTER 6 OTHER SODIUM TRANSITION METAL TITANATES

The two preceding chapters showed results for entire series of materials in order to illustrate trends in material properties. It is useful to substitute titanium with other transition metals in order to tune these properties. Many other layered sodium transition metal titanates were studied in this work. This chapter highlights two specific examples, namely $Na_{2/3}Mn_{1/3}Ti_{2/3}O_2$ and $Na_{2/3}Ni_{1/3}Mn_{1/3}Ti_{1/3}O_2$, where interesting properties emerged.

6.1 Experimental

$Na_{2/3}Mn_{1/3}Ti_{2/3}O_2$ was synthesized via a solid state reaction using stoichiometric amounts of Na_2O (80%, Sigma Aldrich), MnO (powder, −60 mesh, 99%, Sigma-Aldrich), and TiO_2 (puriss, 99 – 100.5 %, Sigma-Aldrich). Approximately six grams of the precursors were SPEX ball milled under ambient air with three half inch steel balls for a half hour and the resultant powders was pressed into ~2 g pellets at $2.55x10^8$ Pascals prior to heating at high temperature in an alumina boat. The pellets were heated in an argon atmosphere at 950 ºC for 12 hours.

$Na_{2/3}Ni_{1/3}Mn_{1/3}Ti_{1/3}O_2$ was synthesized similarly to $Na_{2/3}Mn_{1/3}Ti_{2/3}O_2$ using stoichiometric amounts of Na_2CO_3 (BioXtra, ≥ 99.0 %, Sigma Aldrich), NiO (green, −325 mesh, 99%, Sigma-Aldrich), Mn_2O_3 (−325 mesh, 99%, Sigma-Aldrich), and TiO_2 (puriss, 99 – 100.5 %, Sigma-Aldrich), however heat treatment was done in a box furnace of ambient air at 900 ºC for 12 hours. This method yields a single layered phase, where others, such as the one above, lead to multiple undesirable phases.

6.2 $Na_{2/3}Mn_{1/3}Ti_{2/3}O_2$

The most sustainable sodium metal titanate composition synthesized in this study was $Na_{2/3}Mn_{1/3}Ti_{2/3}O_2$. It contains the abundant and low cost elements of manganese and titanium in its transition metal layer, where traditionally this layer has toxic and/or high cost metals such as cobalt. Figure 6.1 shows the XRD pattern and Rietveld refinement of the $Na_{2/3}Mn_{1/3}Ti_{2/3}O_2$. The structure is pure P2 and the refined crystallographic parameters are given in Table 6.1.

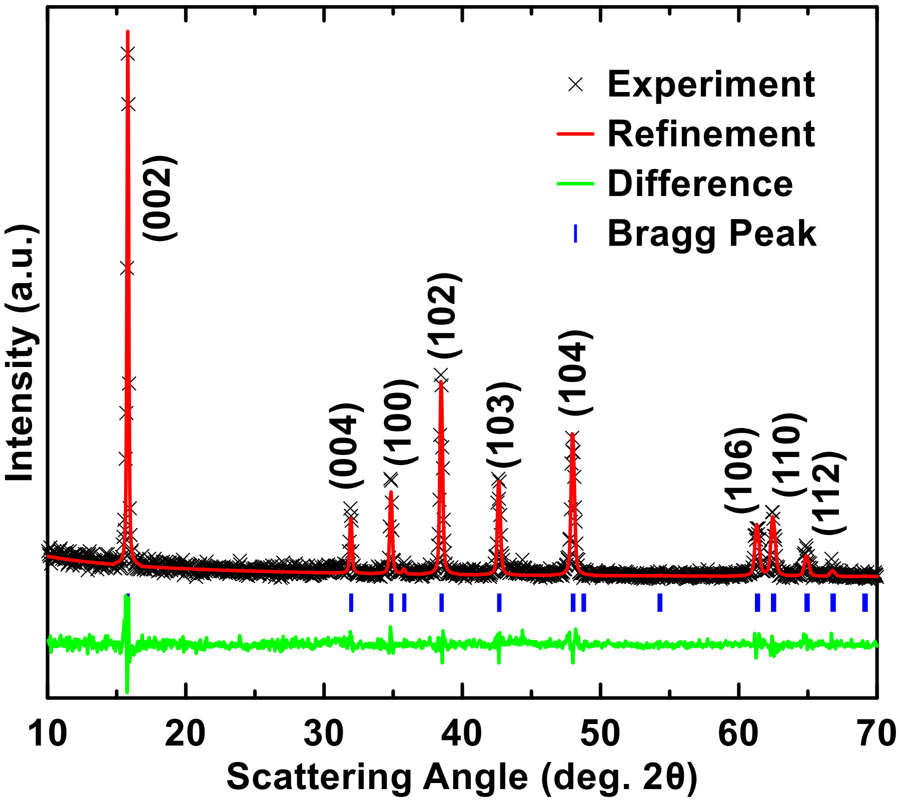

Figure 6.1: XRD pattern and Rietveld refinement of $Na_{0.66}Mn_{0.33}Ti_{0.66}O_2$, with Bragg peaks indicated.

Table 6.1: Structural parameters obtained from Rietveld refinement of $Na_{2/3}Mn_{1/3}Ti_{2/3}O_2$ XRD data.

$Na_{0.66}Mn_{0.33}Ti_{0.66}O_2$ (space group: $P6_3/mmc$)					
atom	site	x	y	z	occupancy
Na_f	2b	0	0	0.25	0.2294(2)
Na_e	2c	0.33	0.66	0.25	0.4754(7)
Mn	2a	0	0	0	0.33
Ti	2a	0	0	0	0.66
O	4f	0.66	0.33	0.0927(5)	1.0212(0)
Cell parameters		a (Å)	b (Å)	c (Å)	R-factor
		2.972(5)	2.972(5)	11.204(4)	
		α (˚)	β (˚)	γ (˚)	4.29
		90	90	120	

Figure 6.2 shows the voltage versus capacity profile of $Na_{2/3}Mn_{1/3}Ti_{2/3}O_2$ cycled from 0.005 – 2.2 V in a sodium half-cell. The cell was cycled at C/10 based on a capacity of 100 mAh/g wherein all of the vacancies in the sodium layer are filled. The electrolyte used was 1 M $NaPF_6$ in EC:DEC with a 1:2 volume ratio.

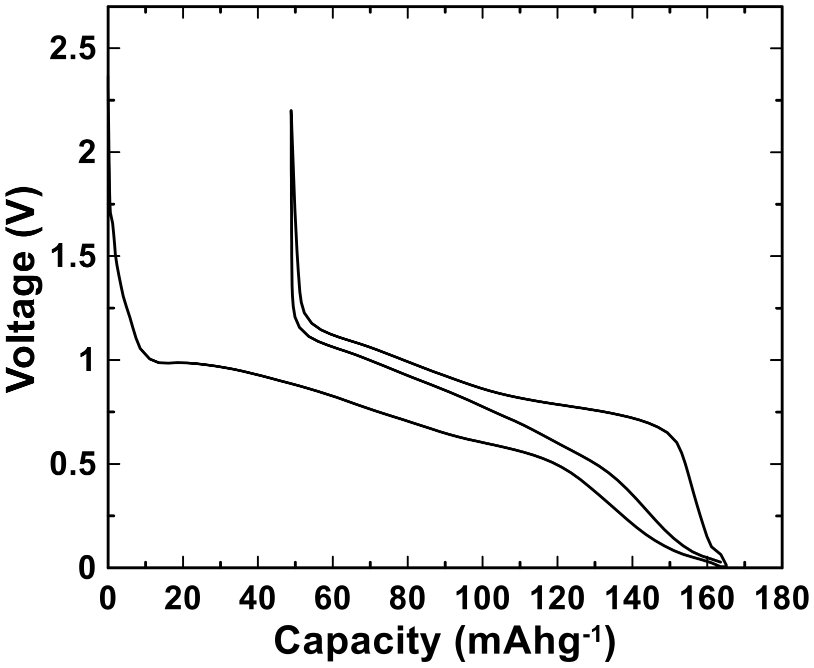

Figure 6.2: Voltage versus capacity profile of the $Na_{2/3}Mn_{1/3}Ti_{2/3}O_2$ material cycled from 0.005 – 2.2 V.

The cell displayed a reversible capacity of 118 mAh/g with an average voltage of 0.84 V, which is slightly higher than the ~0.7 V average voltage for most of the other $Na_xM_yTi_{1-y}O_2$ materials. Figure 6.3 shows the capacity versus cycle number for the cell in Figure 6.3. It shows good capacity retention with linear fade over 50 cycles.

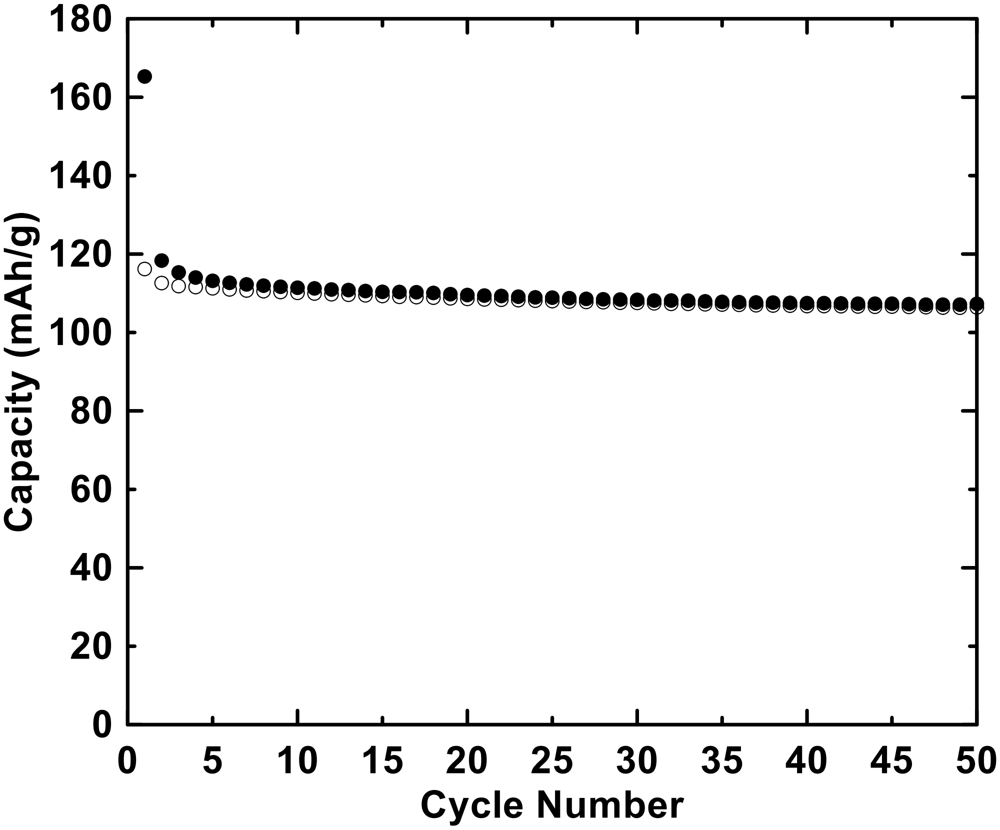

Figure 6.3: Capacity versus cycle number of the $Na_{2/3}Mn_{1/3}Ti_{2/3}O_2$ material cycled from 0.005 – 2.2 V. Open and closed circles represent discharge and charge capacities, respectively.

The presence of manganese +2 makes it possible for this material to be a positive electrode material as well, as manganese can go to higher oxidation states. Figure 6.4 shows $Na_{2/3}Mn_{1/3}Ti_{2/3}O_2$ cycled to 4.5 V. A high voltage plateau is observed at voltages above 4 V with over 200 mAh/g. There is likely some electrolyte decomposition going on at these high voltages. Unfortunately, this plateau is not very reversible as capacity decreases rapidly with cycle number. This plateau displays a huge hysteresis and cycling on this plateau cannot occur unless the cell is discharged to voltages below 1 V. This would be very impractical in a commercial cell.

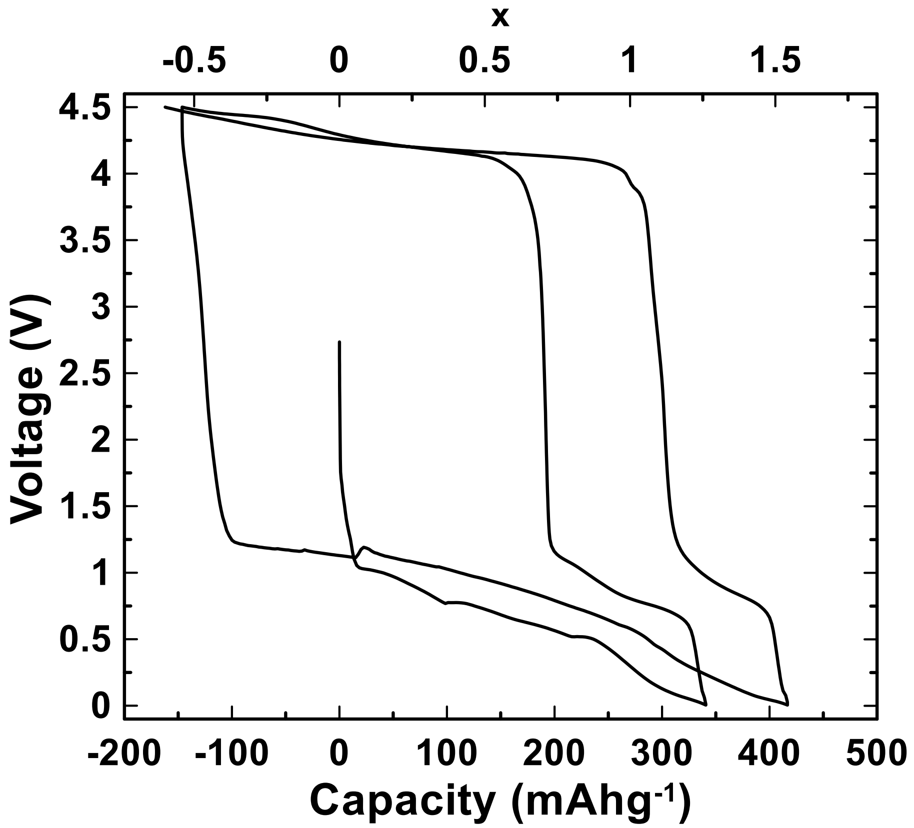

Figure 6.4: Voltage versus capacity profile of the $Na_{2/3}Mn_{1/3}Ti_{2/3}O_2$ material cycled from 0.005 – 4.5 V.

$Na_{2/3}Mn_{1/3}Ti_{2/3}O_2$ is another example of a $Na_xM_yTi_{1-y}O_2$ composition. It displays similar negative electrode electrochemical properties as the other transition metal substituted sodium titanates. However, it has the distinct advantage of being composed of highly abundant, non-toxic and low cost elements.

6.3 Ordered $Na_{2/3}Ni_{1/3}Mn_{1/3}Ti_{1/3}O_2$

Another $Na_xM_yTi_{1-y}O_2$ composition of interest is $Na_{2/3}Ni_{1/3}Mn_{1/3}Ti_{1/3}O_2$. Instead of substituting titanium for a single transition metal, two transition metals are used for charge balance, namely Ni^{2+} and Mn^{4+}.

Figure 6.5 shows the XRD pattern and Rietveld refinement of $Na_{2/3}Ni_{1/3}Mn_{1/3}Ti_{1/3}O_2$. The structure is pure P2 and the refined XRD crystallographic parameters are given in Table 6.2.

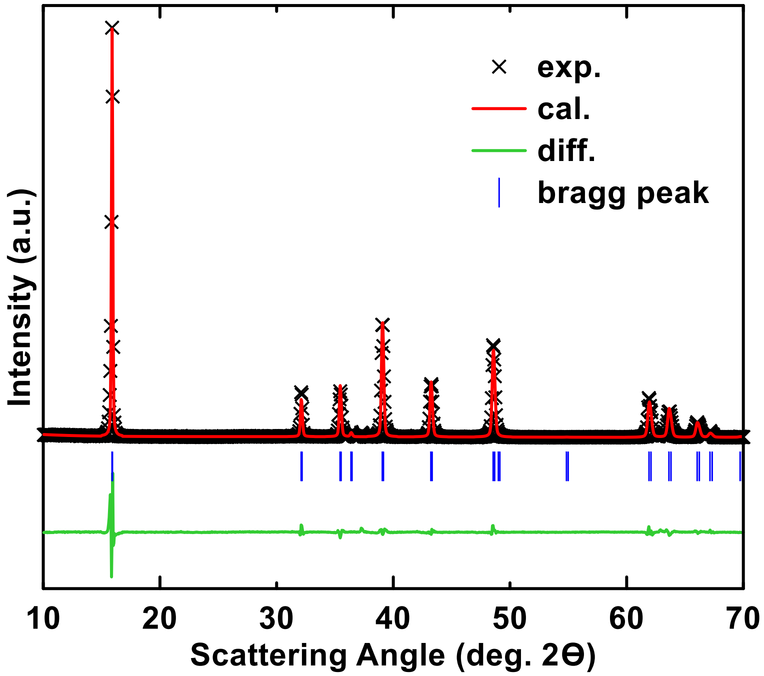

Figure 6.5: XRD pattern and Rietveld refinement of $Na_{0.66}Ni_{0.33}Mn_{0.33}Ti_{0.33}O_2$, with Bragg peaks indicated.

Table 6.2: Structural parameters obtained from Rietveld refinement of $Na_{0.66}Ni_{0.33}Mn_{0.33}Ti_{0.33}O_2$ XRD data.

$Na_{0.66}Ni_{0.33}Mn_{0.33}Ti_{0.33}O_2$ (space group: $P6_3/mmc$)					
atom	site	x	y	z	occupancy
Na_f	2b	0	0	0.25	0.2070(2)
Na_e	2c	0.33	0.66	0.25	0.4348(9)
Ni	2a	0	0	0	0.33
Mn	2a	0	0	0	0.33
Ti	2a	0	0	0	0.33
O	4f	0.33	0.66	0.0920(1)	1.00
Cell parameters	a (Å)	b (Å)	c (Å)	R-factor	
	2.922(5)	2.922(5)	11.143(7)	3.42	
	α (˚)	β (˚)	γ (˚)		
	90	90	120		

This material was first studied as a positive electrode material for sodium-ion batteries [52]. It shows good cyclability at high voltage and a reversible capacity of greater than 125 mAh/g as seen in Figure 6.6.

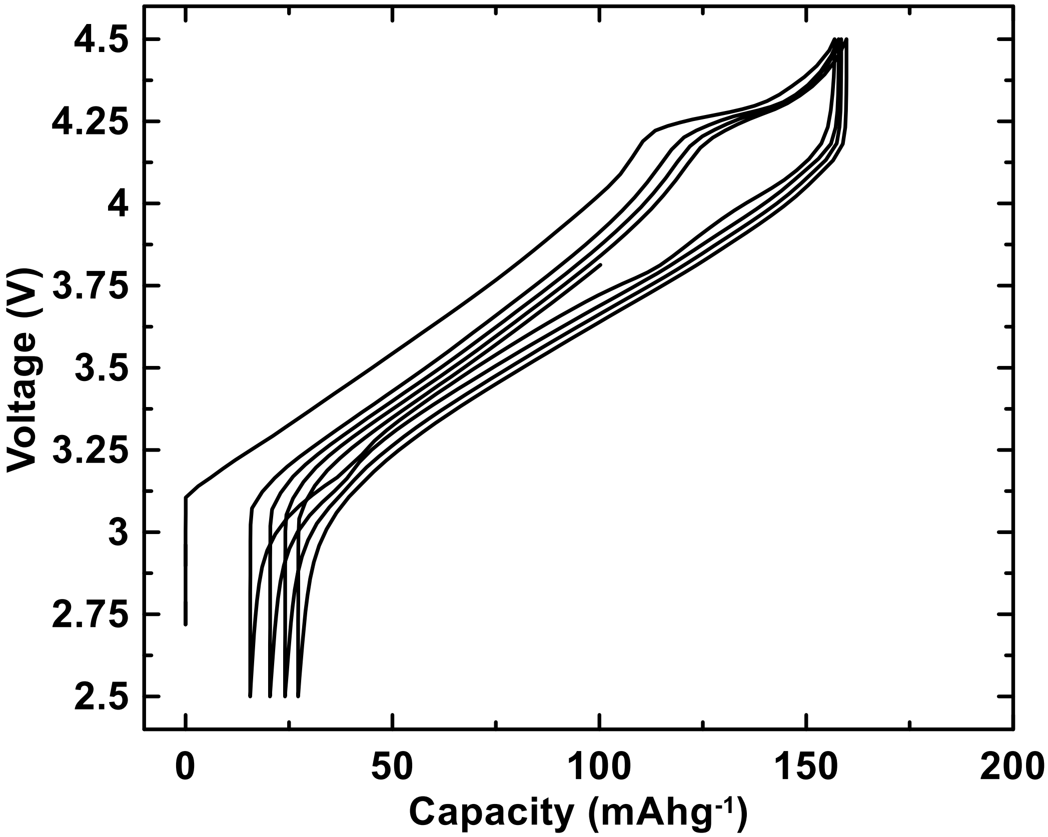

Figure 6.6: Voltage versus capacity profile for $Na_{0.66}Ni_{0.33}Mn_{0.33}Ti_{0.33}O_2$ at high voltage.

This material has 0.33 vacancies within the sodium layer and 0.33 Ti^{4+} atoms in the transition metal layer. According to other $Na_xM_yTi_{1-y}O_2$ studies this would indicate that sodium insertion is possible for this material at a voltage of about 0.7 V and a reversible capacity of greater than 90 mAh/g. However, Figure 6.7 shows that this is not the case. The voltage versus capacity profile for $Na_{2/3}Ni_{1/3}Mn_{1/3}Ti_{1/3}O_2$ shows several plateaus during the first discharge. Carbon black is responsible for the features below 1 V during the first discharge, while it is unclear what is occurring at voltages above 1.5. The plateaus all but disappear upon further cycling which means that almost no reversible capacity is achieved.

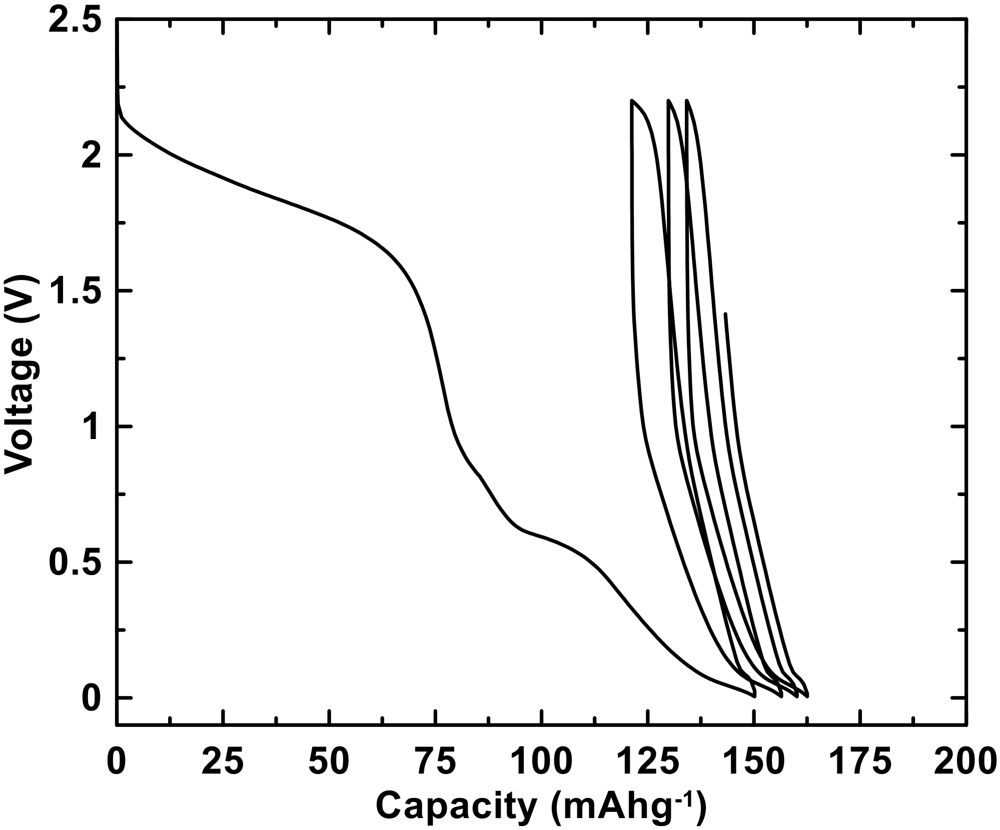

Figure 6.7: Voltage versus capacity profile for $Na_{0.66}Ni_{0.33}Mn_{0.33}Ti_{0.33}O_2$ at low voltage.

To investigate further what was going on here neutron powder diffraction measurements of the pristine $Na_{2/3}Ni_{1/3}Mn_{1/3}Ti_{1/3}O_2$ powder were undertaken. Figure 6.8 shows the experimental neutron diffraction pattern and refinement of the $Na_{2/3}Ni_{1/3}Mn_{1/3}Ti_{1/3}O_2$ material, with fit parameters shown in Table 6.3.

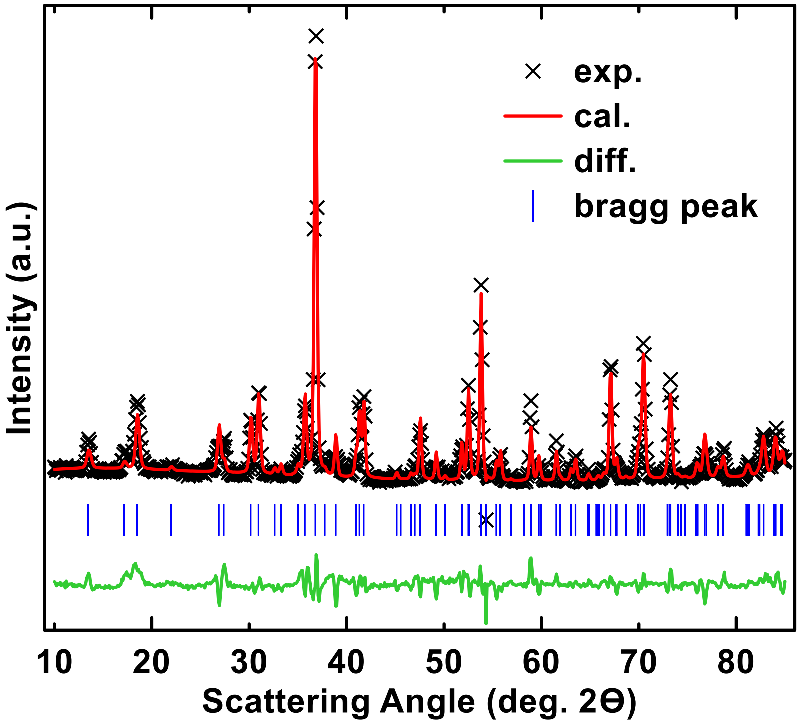

Figure 6.8: Experimental NPD pattern and refinement of ordered P2-$Na_{0.66}Ni_{0.33}Mn_{0.33}Ti_{0.33}O_2$.

Table 6.3: Structural parameters obtained from Rietveld refinement of $Na_{0.66}Ni_{0.33}Mn_{0.33}Ti_{0.33}O_2$ NPD data.

$Na_{0.66}Ni_{0.33}Mn_{0.33}Ti_{0.33}O_2$ (space group: $P6_3$)					
atom	site	x	y	z	occupancy
Na_1	2a	0	0	0.25	0.5214(6)
Na_2	6c	0.33	0	0.25	1.5001(1)
Na_3	2b	0.33	0.66	0.25	0.4965(0)
Na_4	2b	0.66	0.33	0.25	0.5092(5)
Ni	2a	0	0	0	3
Mn	2b	0.33	0.66	0	3
Ti	2b	0.33	0.66	0.5	3
O_1	6c	0.66	0	-0.4168(3)	3
O_2	6c	0	0	0.3908(0)	3
Cell parameters	a (Å)	b (Å)	c (Å)	R-factor	
	5.060(6)	5.060(6)	11.110(0)	4.12	
	α (˚)	β (˚)	γ (˚)		
	90	90	120		

From the XRD refinement the structure is P2. When attempting to fit the NPD data with the P2 parameters and $P6_3/mmc$ space group there are many peaks that are unaccounted for in the pattern. The extra peaks are indicative of a superlattice that exists within the original P2 structure. X-rays cannot distinguish between nickel, manganese and titanium as they have similar numbers of electrons and thus similar scattering power. For this reason, superlattice ordering is difficult to detect by XRD. However, the neutron scattering lengths of the natural isotope abundance of these elements are quite different. Neutron diffraction experiments are able to detect transition metal ordering.

Figure 6.9 shows the transition metal layer in $Na_{2/3}Ni_{1/3}Mn_{1/3}Ti_{1/3}O_2$ with three different atom types illustrated to represent the three distinct transition metals. Both small and large hexagonal unit cells are highlighted in this layer. When XRD experiments are performed the transition metals are indistinguishable and the small hexagonal unit cell can be used to describe the transition metal layer of the P2 structure. When NPD experiments are done the small hexagonal unit cell will no longer suffice due to the different scattering lengths of the transition metals. The ordered state of the transition metal layer must now be described using the large hexagonal unit cell shown in Figure 6.9. In this unit cell there are three distinct positions for the transition metals. Due to this difference, space group $P6_3$ was used to refine the structure. The best fit is achieved when the transition metals fully occupy a single distinct position in the transition metal layer. This ordering results in new peaks in the NPD pattern, with the strongest peaks occurring at ~18 and 19 °2θ. A similar superlattice ordering result is observed in $Na_{2/3}Ni_{1/3}Mn_{2/3}O_2$, where nickel and manganese transition metal cations occupy distinct sites on the transition metal layer [110].

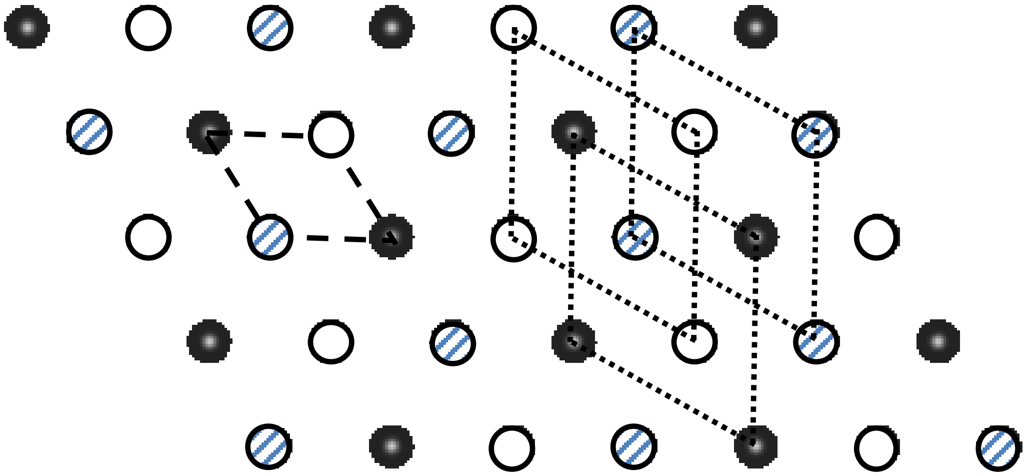

Figure 6.9: The transition metal layer in the P2-$Na_{0.66}Ni_{0.33}Mn_{0.33}Ti_{0.33}O_2$ material which shows the ordered cation arrangement with small and large hexagonal unit cells indicated by long and short dashed lines, respectively.

The impact of ordering of this material on cycling is dramatic. At low voltage virtually no sodium is able to reversibly insert into the ordered host structure. A possible theory as to why no low voltage capacity is observed here is that the diffusion of sodium ions is hindered due to the lack of di-vacancies in the sodium layer. This could result from a specific sodium ion ordering scheme that is coupled to the transition metal ordering. However, when either nickel or manganese is substituted as *M* (without the other) in $Na_xM_xTi_{1-x}O_2$ a reversible low voltage capacity is observed [91,92]. Neither of these two active materials or other $Na_xM_yTi_{1-y}O_2$ display ordering and they are considered cation disordered structures. The three types of ordering, that were discussed in section, 4.3 Results and Discussion, can cause superstructures that can in turn display distinct plateaus in potential profiles during galvanostatic cycling, lower sodium ion diffusion (up to two orders of magnitude) and reduce ion transport dimensionality [94,111]. Rapid capacity fade during electrochemical cycling is often observed for these ordered materials [112–114]. Prevention of ordered structures is important for electrode development. Different strategies were employed, such as ball milling and low temperature synthesis, to prevent the ordering in this material without success. A hot topic in the lithium-ion battery community today, that is similar to this, is that of lithium rich disordered rock salt structures. To further demonstrate the utility of intercalation metal oxides with disordered structures, high reversible capacities at high voltages have been observed for disordered Li_2MO_3 layered structures in lithium-ion batteries where M is a first row transition metal [115].

6.4 Conclusions

A plethora of metals can be substituted for titanium in layered sodium titanates. When substitution takes place distinct properties are observable, which are dependent upon the metal or metals utilized. The two properties highlighted in this chapter were resource sustainability and ordering in the transition metal layer. Resource sustainability is a positive characteristic of these materials, since high abundant elements are used, while transition metal ordering is thought of as a negative characteristic.

$Na_{2/3}Mn_{1/3}Ti_{2/3}O_2$, where manganese (II) is substituted for titanium in the metal layer, was shown to have good reversibility of sodium insertion at low voltage when cycled in a sodium half-cell. It showed similar characteristics to the other $Na_xM_yTi_{1-y}O_2$ materials, with an average voltage of 0.84 V and a reversible capacity of 118 mAh/g. Manganese is considered a sustainable metal due to its abundance and low cost. Thus, $Na_{2/3}Mn_{1/3}Ti_{2/3}O_2$, is thought to be the most sustainable composition to date compared to those found in the literature that have been made and tested in sodium half-cells.

$Na_{2/3}Ni_{1/3}Mn_{1/3}Ti_{1/3}O_2$ was shown as an example in which ordering occurs within the transition metal layer. Suppression of this ordering was not achieved. This ordering is believed to result in very little reversible capacity for $Na_{2/3}Ni_{1/3}Mn_{1/3}Ti_{1/3}O_2$ at low voltage in sodium half-cells. However, at high voltage $Na_{2/3}Ni_{1/3}Mn_{1/3}Ti_{1/3}O_2$ displays good cyclability with over 120 mAh/g of capacity in sodium cells. To the author's knowledge no other materials exist in the literature where a direct comparison between ordering and low voltage capacity is shown. All of the layered materials to date that show low voltage capacity with the Ti^{4+}/Ti^{3+} redox display no transition metal ordering. Theoretically, other properties could also be tuned negatively or positively depending on the substituents in the transition metal layer.

CHAPTER 7 INCREASING VACANCIES

7.1 Layered $Na_xM_yTi_{1-y}O_2$ Materials Outlook

Layered $Na_xM_yTi_{1-y}O_2$ materials show promise as negative electrode materials for NIBs. Compositions investigated thus far are shown in Figure 7.1 and include $M = Li^+$, Mg^{2+}, V^{3+}, Cr^{3+}, Mn^{2+}, Fe^{3+}, Co^{2+}, Ni^{2+} [70,91–95,106,108]. Materials have now been reported in the literature where two metals are substituted, such as $Na_{2/3}Ni_{1/6}Co_{1/6}Ti_{2/3}O_2$ [116,117].

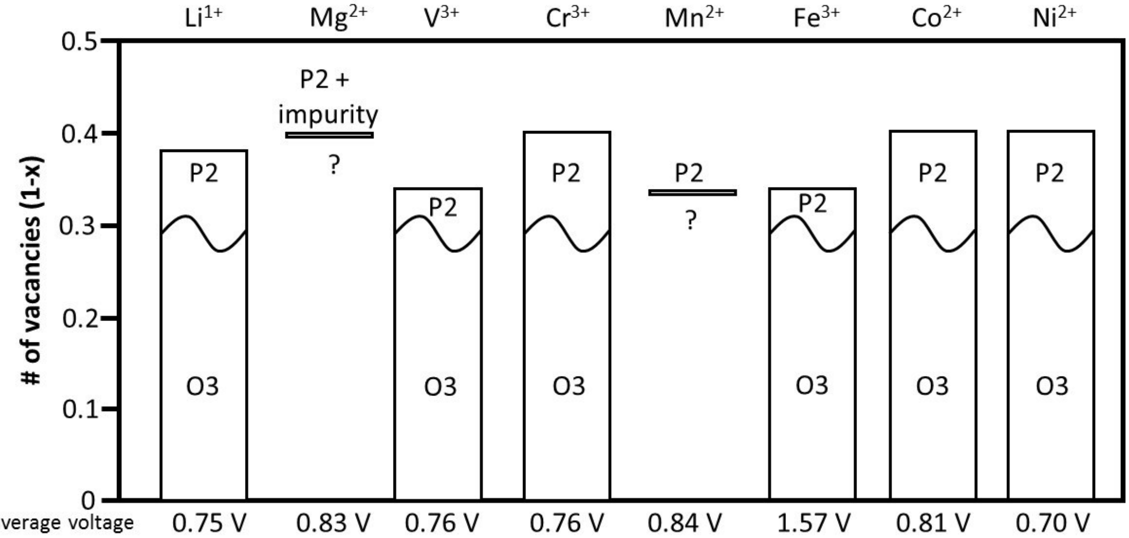

Figure 7.1: Summary of the vacancy limit versus different $Na_xM_yTi_{1-y}O_2$ materials, with M shown on the top x-axis. The bottom x-axis shows the average voltage of each of the different M series.

These materials all incorporate the low redox couple of Ti^{4+}/Ti^{3+} which yields appropriate negative electrode potentials of ~0.7 V versus sodium metal. The hysteresis can be somewhat tuned depending on the metal substituted for titanium. These properties are summarized by the voltage curves in Figure 7.2 and the differential capacity curves in Figure 7.3.

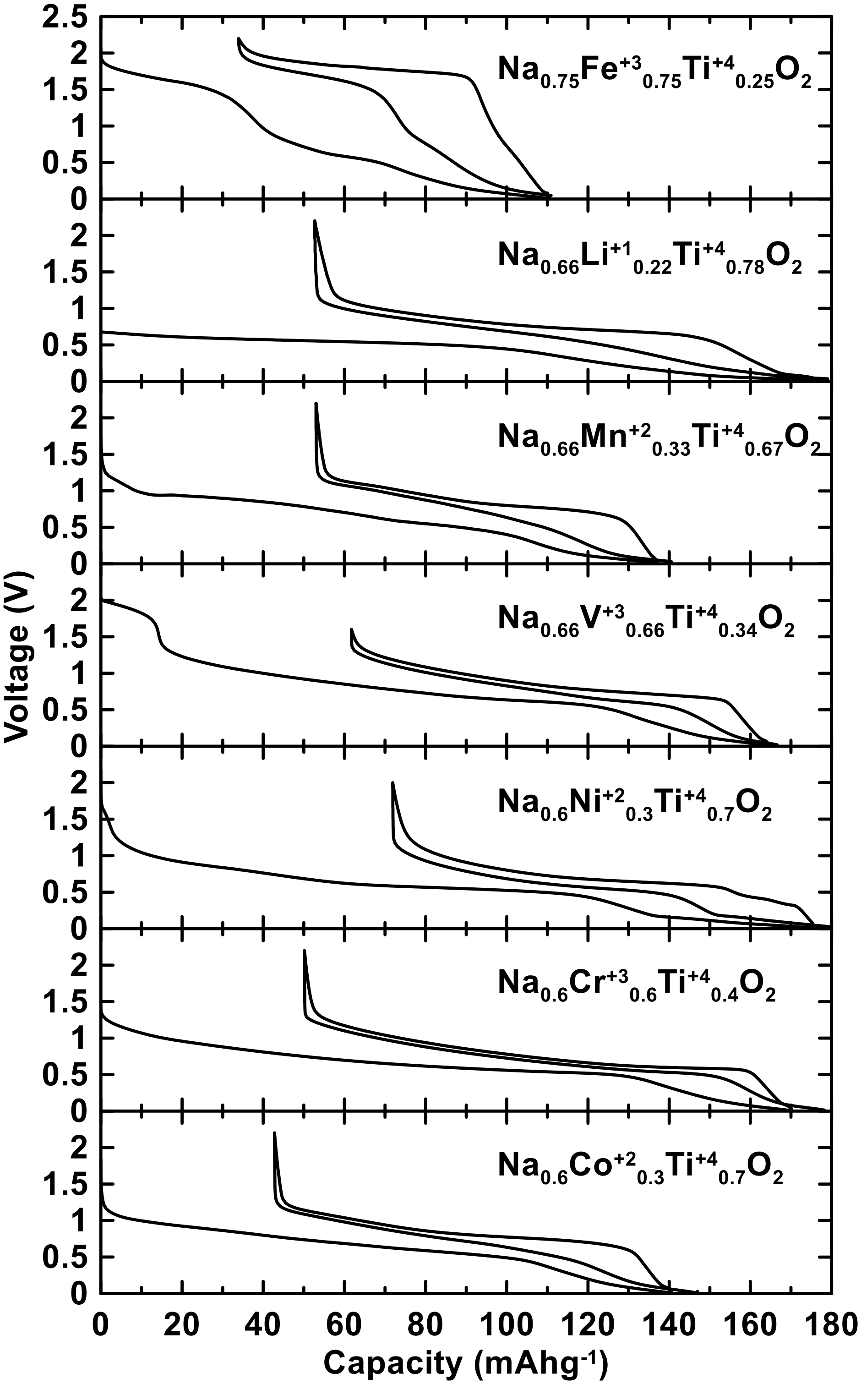

Figure 7.2: Voltage versus capacity profiles for all of the highest vacancy $Na_xM_yTi_{1-y}O_2$ materials.

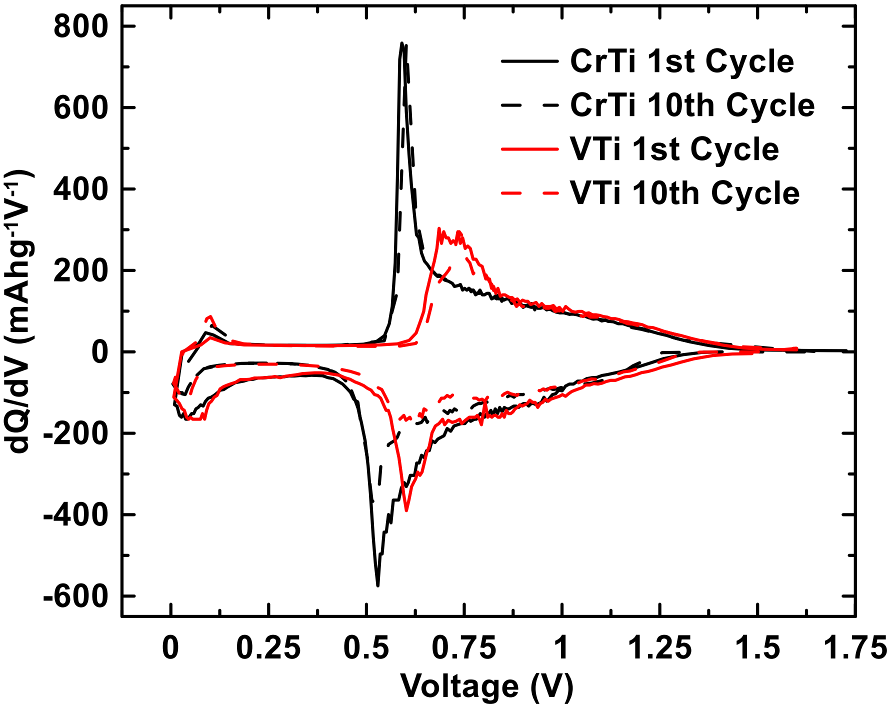

Figure 7.3: Comparison between differential capacity curves of $Na_{0.6}Cr_{0.6}Ti_{0.4}O_2$ (black) and $Na_{2/3}V_{2/3}Ti_{1/3}O_2$ (red).

Due to the presence of the metals substituted for titanium less conductive diluent is required than for pure titanates. These materials also display smooth voltage profiles which are typically indicative of a lack of sodium and charge ordering [94]. Perhaps the most important characteristic of these negative electrode materials is their stability while cycling in a cell. They have been described as zero-strain and ultra-stable as they remain in the P2 structure during charge and discharge with very little change in their lattice constants. There is a broad solid-solution range for most of the metal titanium series when titanium is substituted (sodium can typically range from $0.6 \leq x \leq 1.0$). Another advantage of these materials over conventional electrode materials is their bi-functionality. Due to the presence of a second metal substituting for titanium, which can be electrochemically active at higher voltages, these materials can function as not only a negative electrode but as a positive electrode as well. This means that a ~3 V battery can be constructed from a single material which would reduce cost as only one coating needs to be processed. Also, when these types of materials function as positive electrodes, the presence of titanium might increase the average voltage than if there was no titanium. The volume change is not significant when sodium is added or removed, owing to the fact that this is an intercalation reaction. Thus, when acting simultaneously as negative electrode and positive electrode material in a battery the two electrodes expand and contract complimentarily. During charge the negative electrode contracts while the positive electrode expands at virtually the same rate. This means that total changes to the volume of the battery will be negligible. This sharply contrasts a typical LIB where during charging both the $LiCoO_2$ and graphite electrodes expand.

The layered sodium metal titanates exploit differences between lithium and sodium chemistry. Different materials properties emerge in terms of voltage, vacancies and stability when sodium is used instead of lithium. Sodium metal oxides yield lower voltages, tolerate more vacancies and are more stable at low voltages than their lithium counterparts. New high energy density electrodes can be made by taking advantage of these differences. Research is reaching beyond simple LIB analogues, which have dominated NIB research, to innovative materials such as these oxides with vacancies for NIB negative electrodes. Unfortunately, there are also disadvantages to these types of materials. Large irreversible capacities are observed during the first cycles which are due to the carbon black additive in the electrode formulation. These materials are hygroscopic to differing degrees as well. This air sensitivity would increase synthesis and processing costs of electrodes. Perhaps the largest disadvantage is the capacity limit. It is unlikely that a capacity over 250 mAh/g will be achieved with these layered intercalation materials, as there are only so many vacancies which are possible within the sodium layers. At this time 120 mAh/g is the highest capacity corresponding to a sodium atomic ratio (x in Na_xMO_2) of 0.6, resulting in 0.4 vacancies. This corresponds to a theoretical energy density of 1500 Wh/L (crystallographic density of 3.81 g/cc) for $Na_{0.6}Cr_{0.6}Ti_{0.4}O_2$ in a cell vs. a 4 V positive electrode. This is comparable to the total theoretical energy density of hard carbon vs. a 4 V positive electrode (~1700 Wh/L) [60]. However, the energy density of $Na_{0.6}Cr_{0.6}Ti_{0.4}O_2$ is much superior to hard carbon if one supposes that the useable capacity of a negative electrode must be restricted to > 50 mV. Under these conditions the energy density of hard carbon is reduced to only about 620 Wh/L [32,60]. Nevertheless, the energy density of $Na_{0.6}Cr_{0.6}Ti_{0.4}O_2$ is significantly less than the energy density of graphite vs. a 4 V positive electrode in a Li-ion cell (~2800 Wh/L) [3]. A comparison of these volumetric energy densities is summarized in Table 7.1. To increase the capacity (and energy density) of $Na_{0.6}Cr_{0.6}Ti_{0.4}O_2$ further would require the inclusion of more vacancies (lower amount of Na in $Na_{0.6}Cr_{0.6}Ti_{0.4}O_2$). However, when $x < 0.6$, phase pure samples could not be obtained and the capacity of the resulting phases decreases. This has been the case for all other metals substituted as well. A limit to the number of vacancies could result from an increase in the bond ionicity within these structures. This phenomenon leads to definite Na coordination boundaries (P2 or O3) when x is varied and only certain stoichiometric ranges are possible as a result [96,118].

Table 7.1: Comparison of volumetric energy densities of typical negative electrode materials versus a 4 V positive electrode.

Material	**Volumetric Energy Denisty (Wh/L)**	**Cell Type**
Graphite	2800[3]	Li-ion
Hard Carbon	1700[60]	Na-ion
Hard Carbon (>50 mV)	620[60]	Na-ion
P2-$Na_{0.6}Cr_{0.6}T_{0.4}O_2$	1500 (this thesis)	Na-ion

DSC experiments were performed in order to further explore the thermal stability of the de-sodiated $Na_xM_yTi_{1-y}O_2$ materials. The thermal behavior of pristine $Na_{0.6}Cr_{0.6}Ti_{0.4}O_2$ powder, along with sodiated and de-sodiated variants was measured in a DSC. $Na_{0.6}Cr_{0.6}Ti_{0.4}O_2$ sodiated and de-sodiated at different levels, where sodium content equalled 1.0 and 0.33, respectively, were made electrochemically. This means that $Na_{0.6}Cr_{0.6}Ti_{0.4}O_2$ cells were either charged or discharged to a desired voltage and then disassembled in a glovebox to recover the electrode material.

Figure 7.4 shows XRD patterns of $Na_{0.6}Cr_{0.6}Ti_{0.4}O_2$, sodiated $NaCr_{0.6}Ti_{0.4}O_2$ and de-sodiated $Na_{0.33}Cr_{0.6}Ti_{0.4}O_2$. They remain predominantly in the P2 phase regardless of the sodium content.

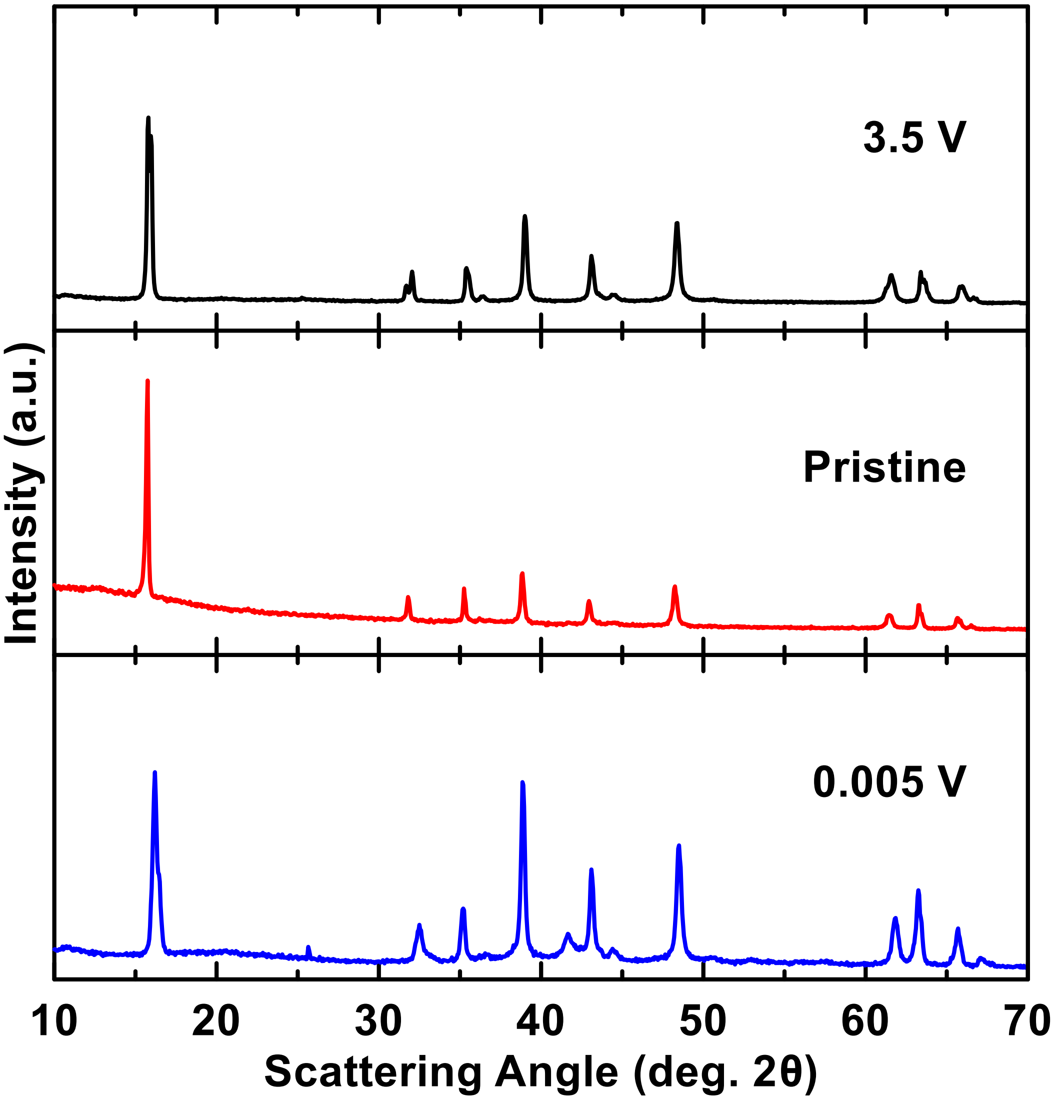

Figure 7.4: XRD of the pristine $Na_{0.6}Cr_{0.6}Ti_{0.4}O_2$ (middle) and ex-situ XRD of the sodiated $NaCr_{0.6}Ti_{0.4}O_2$ (bottom) and de-sodiated $Na_{0.33}Cr_{0.6}Ti_{0.4}O_2$ (top).

Figure 7.5 shows the DSC curves of $Na_{0.6}Cr_{0.6}Ti_{0.4}O_2$, sodiated $NaCr_{0.6}Ti_{0.4}O_2$ and de-sodiated $Na_{0.33}Cr_{0.6}Ti_{0.4}O_2$. DSC was done herein instead of TGA due to the hygroscopic nature of the samples. DSC samples were sealed in aluminum pans in an inert argon filled glovebox.

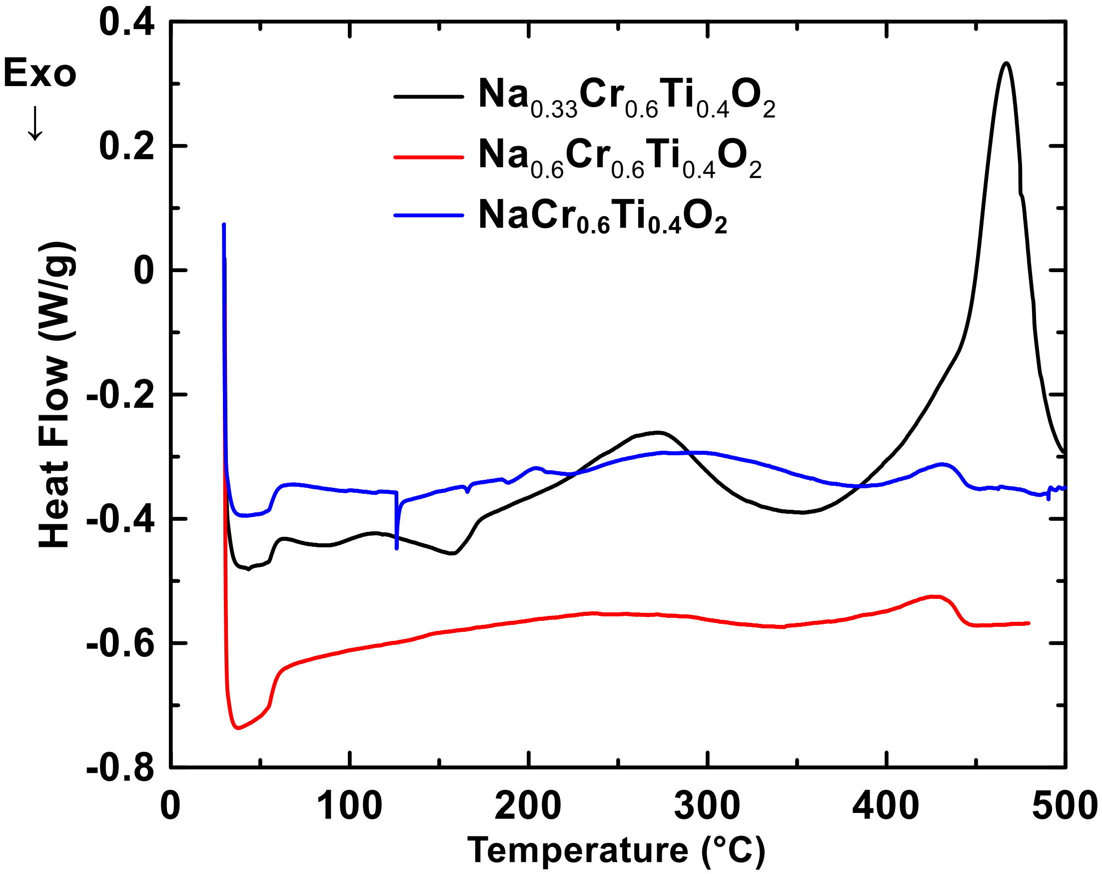

Figure 7.5: DSC curve of $Na_{0.6}Cr_{0.6}Ti_{0.4}O_2$ (red), along with sodiated $NaCr_{0.6}Ti_{0.4}O_2$ (blue) and de-sodiated $Na_{0.33}Cr_{0.6}Ti_{0.4}O_2$ (black) variants.

$Na_{0.6}Cr_{0.6}Ti_{0.4}O_2$ and $NaCr_{0.6}Ti_{0.4}O_2$ display a relatively featureless DSC curve. This means that there are no thermal transitions within the temperature range of the experiment. The highly de-sodiated $Na_{0.33}Cr_{0.6}Ti_{0.4}O_2$, however, shows a large endothermic peak between 400 and 500 ºC. This is likely due to thermal decomposition. This has been observed for other highly de-sodiated layered sodium metal oxides [44,119]. This result indicates that highly de-sodiated materials of this type are not as thermally or structurally stable as their highly sodiated counterparts. Furthermore, it is unlikely that synthesis of highly de-sodiated phases at high temperatures via solid state reactions is possible. For this reason, the vacancy limit for these layered sodium metal titanates is thought to be 0.4 regardless of transition metal substitution.

The advantages and disadvantages to these types of materials have been highlighted. Where disadvantages are found there is opportunity for improvement. The most promising opportunity comes from increasing the capacities of these materials by increasing the number of vacancies within the layered framework. A relevant sodium occupancy or ratio would be $x = 0.33$ (Na_xMO_2) which means 0.66 vacancies. This would yield capacities and energy densities near that of graphite in lithium cells. To achieve this end two separate pathways were tried, namely, sulfide and potassium analogues.

7.2 Sulfide Analogues

The first strategy employed for increasing the number of vacancies was to make sulfides instead of oxides. This just meant swapping the oxygen for sulfur in the $Na_xM_yTi_{1-y}O_2$ formula, yielding $Na_xM_yTi_{1-y}S_2$. The reasoning for this was that sulfur, lying just below oxygen in the periodic table, would be able to make many of the same compounds while at the same time decrease the iconicity, or vice versa increase the covalency, of the sheets within the layered structure. It is already well known that TiS_2 forms a layered structure without needing any alkali metals within the van der Waals gap to stabilize the structure [120]. In other words, the number of vacancies was already maximized. Titanium disulfide can also form intercalation compounds with alkali metals and this has been demonstrated in electrochemical cells [121,122]. More recently, the electrochemical activity of layered Na_xTiS_2 and Na_xVS_2 versus Na metal was shown using more mature battery technologies [123]. These materials showed very similar behavior in terms of capacity and voltage, with the titanium containing compound displaying a more complicated voltage profile instead of well developed flat voltage plateaus as in the case of vanadium. One other main difference was the presence of conversion reactions for Na_xVS_2 when cycled at voltages lower than 0.5 V. No such reactions were observed for Na_xTiS_2.

The best performing sodium transition metal oxide material, $Na_xCr_xTi_{1-x}O_2$, was imitated by synthesizing $Na_xCr_xTi_{1-x}S_2$, where $x = 2/3$ and 1/3. In the literature there is a report on the structural, electrical, magnetic and NMR properties of $Na_xCr_xTi_{1-x}S_2$, with no electrochemical measurements reported [124].

7.2.1 Experimental

This series of materials was made via heating $NaCrS_2$ mixed with TiS_2 in a sealed silica tube at 800 ºC for a week. $NaCrS_2$ was obtained by heating a mixture of Cr_2S_3 and Na_2CO_3 at 700 ºC for six hours under a flow of carbon disulfide diluted in nitrogen [124]. A simpler and less time intensive synthesis was designed where approximately five grams of precursors of Na_2S, Cr, Ti and S were ball milled for four hours with 180 g of 1/16" balls. The resultant powder was pelletized and then heated in argon at 1000 ºC for 15 hrs followed by quenching in liquid nitrogen.

7.2.2 Results and Discussion

Figure 7.6 shows the XRD patterns of the $x = 2.3$ and 1/3 samples along with a TiS_2 reference pattern from the ICSD database. $Na_{2/3}Cr_{2/3}Ti_{1/3}S_2$ has a P3 structure with space group $R\bar{3}m$ and lattice constants, $a = 3.4840$ and $c = 20.4601$. A small amount of

O3 and TiS_2 impurity phases are also present. These results are in good agreement with the crystallographic results in the literature [124]. The *x* = 1/3 sample was found to predominantly contain TiS_2 and thus electrochemical testing was not performed on it as there are ample electrochemical results shown for this material in the literature.

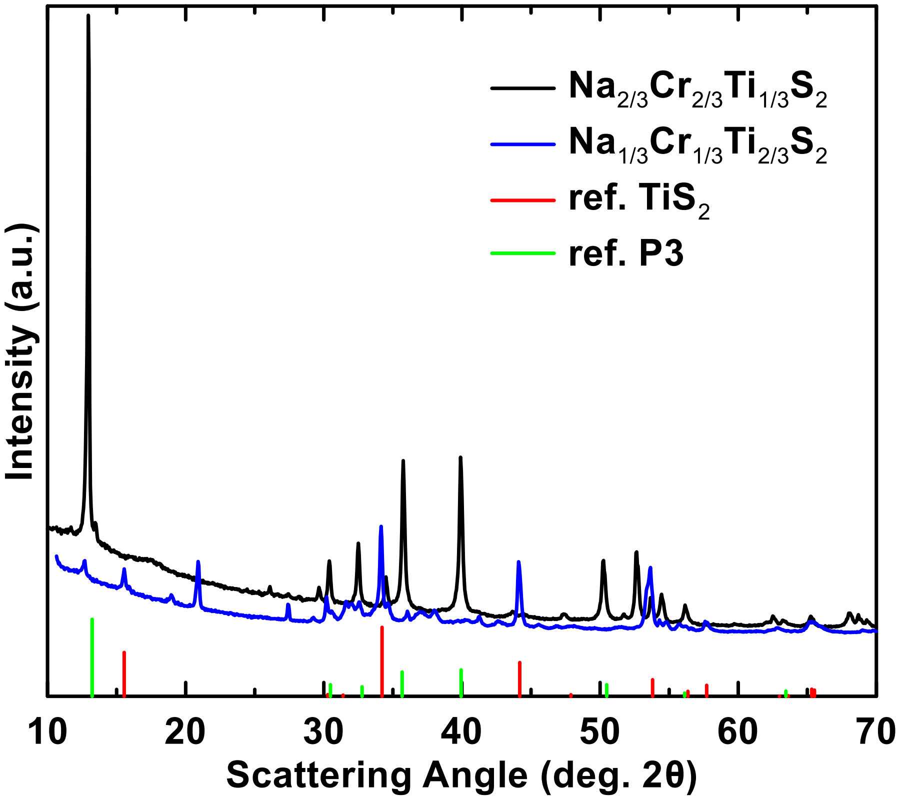

Figure 7.6: XRD patterns of $Na_xCr_xTi_{1-x}S_2$ where *x* = 1/3 (blue) and 2/3 (black), with a TiS_2 and P3 reference pattern shown in red and green, respectively.

Figure 7.7 shows the electrochemistry of $Na_{2/3}Cr_{2/3}Ti_{1/3}S_2$ versus sodium in the voltage range of 1.0 – 3.2 V. Since the material is sodium deficient, like the oxides, the cell was initially discharged. The voltage profile shows a plateau at ~1.7 V where sodium intercalates into the vacancies within the layered structure. Upon charging, another plateau appears at ~2.8 V, although this plateau has increased voltage hysteresis than the lower voltage plateau. The two voltage plateaus are not completely flat and actually include multiple steps. This complicated voltage profile actually evolves during further charge and discharge cycles, with the capacity of the upper voltage plateau decreasing on each subsequent cycle rendering it essentially non-reversible.

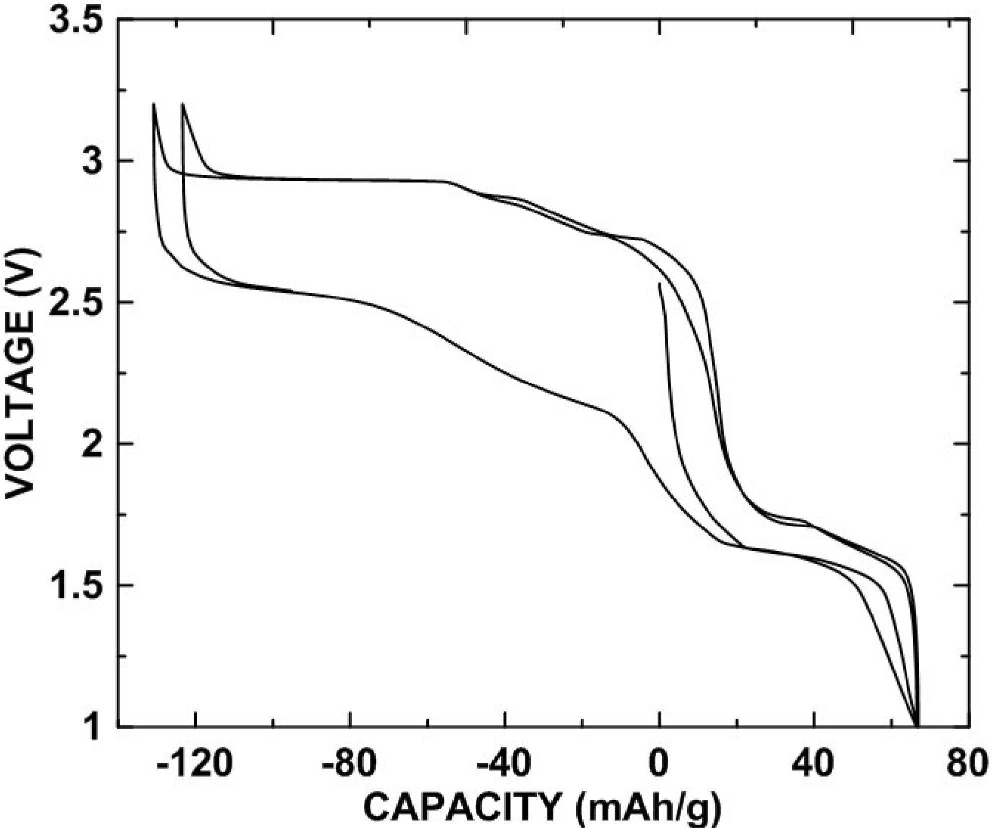

Figure 7.7: Voltage versus capacity profile of $Na_{2/3}Cr_{2/3}Ti_{1/3}S_2$ from 1.0 to 3.2 V.

Figure 7.8 shows the reversibility of the lower ~1.7 voltage plateau for $Na_{2/3}Cr_{2/3}Ti_{1/3}S_2$ by cycling in the voltage range of 1.0 – 2.4 V. This reversible region has a capacity of ~60 mAh/g, which is approximately the theoretical gravimetric capacity of 68 mAh/g. The theoretical volumetric capacity is ~205 Ah/L. For comparison, the oxide analogue of this material theoretically has 91 mAh/g and 350 Ah/L of gravimetric and volumetric capacity, respectively.

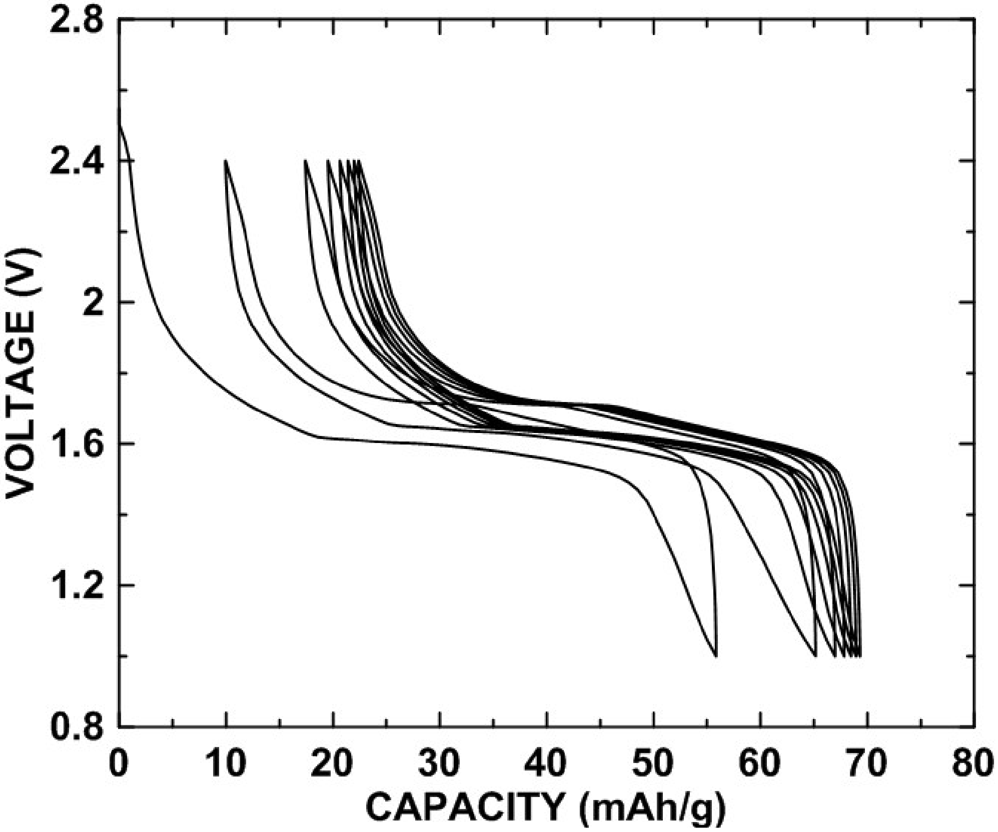

Figure 7.8: Voltage versus capacity profile of $Na_{2/3}Cr_{2/3}Ti_{1/3}S_2$ from 1.0 to 2.4 V.

These results are somewhat discouraging if the aim was to increase the number of vacancies while maintaining the good cyclability and low voltage nature of $Na_xM_yTi_{1-y}O_2$. It appears that this $Na_{2/3}Cr_{2/3}Ti_{1/3}S_2$ analogue behaves very similar to other sodium transition metal sulfides. The substitution of titanium for chromium in the structure actually increased the voltage of the upper plateau from 2.3 V to 2.8 V, while the lower voltage plateau remained virtually unchanged. The similarity of the voltage profile in the layered sulfide family can be attributed to sulfur redox chemistry. Instead of transition metals, it is the sulfur, being oxidized and reduced during alkali intercalation and deintercalation. This is also the mechanism for sodium or lithium sulfur batteries [71]. A similar thing occurs when the oxygen 2p orbital is of the correct energy in disordered lithium excess materials and oxygen can participate in the electrochemistry [125]. The high voltage and poor reversibility of these materials led to the abandonment of sulfide analogues and search for other ways to increase vacancies in the $Na_xM_yTi_{1-y}O_2$ materials while preserving performance.

7.3 Potassium Analogues

The second strategy employed for increasing the number of vacancies was to use potassium analogues. Making potassium analogues of the $Na_xM_yTi_{1-y}O_2$ type materials could be suitable due to elemental trends found in the periodic table. Table 7.2 shows that as one goes down group I in the periodic table there is a trend of increasing ionic radii from lithium to sodium to potassium and so on [26].

Table 7.2: Ionic radius of the first four group I elements. Values were taken from Reference 26.

Element	**Ionic Radius (Å)**
Li	0.76
Na	1.02
K	1.38
Rb	1.52

This increase in size could allow the layered framework to be maintained even at higher vacancy levels. It has been demonstrated that sodium can tolerate more vacancies than lithium [13,91]. This is possibly due to sodium's ability to stabilize the electrostatic repulsion of the oxygen layers in the structure, even with vacancies, because of its larger size. The larger still potassium ions might be able to further stabilize the oxide sheets in the layered structure. So this trend likely continues as one moves from sodium to potassium and so on down the periodic table. Indeed, there exist examples where alkali occupancies in layered potassium metal oxides are as low as 0.3 and 0.14 [126,127]. Perhaps the low occupancy potassium layered metal oxides could serve as the framework for sodium insertion. The limited examples of potassium layered oxides with a high number of vacancies do not include titanium in the metal layer. Thus, there was a need to modify the synthesis conditions for layered potassium compounds in order to obtain potassium transition metal titanates. These materials could then be cycled versus sodium metal to understand their electrochemical behavior, specifically voltage of sodium intercalation and attainable capacities. $K_xM_yTi_{1-y}O_2$ with $x = 0.3$ could likely allow enough sodium to be inserted to achieve a capacity of ~250 mAh/g (~925 Ah/L).

7.3.1 Experimental

$K_{0.3}MnO_2$ was made by following the method of Vaalma *et al.*[126]. To summarize, $KMnO_4$ was ground (>99%, Sigma Aldrich) into a fine powder and dispersed (approximately two grams) as a thin film in an alumina boat. It was then heated in air at 1000 ºC for five hours, using slow ramp rates of 1 ºC/min. The resultant powder was then rinsed several times with distilled water to remove any remaining permanganate and then vacuum dried. It was further dried in a drying oven at 120 ºC overnight.

P2-$K_{2/3}Cr_{2/3}Ti_{1/3}O_2$ was synthesized by ball milling approximately five grams of K_2CO_3 (BioXtra, ≥ 99.0 %), Cr_2O_3 (50 µm, ≥ 98 % Sigma-Aldrich), and TiO_2 (puriss, 99

– 100.5 %, Sigma-Aldrich) together in air with approximately 15 grams of half inch steel balls for a half hour. The resultant powder was pelletized and the pellets were packed in its own powder in an alumina crucible. Then heat treatment was done at 750 ºC in argon for 12 hours followed by grinding the pellets. This heating and grinding step was performed three times before a final heating step at 1100 ºC for 12 hours followed by a quench to room temperature. The product was then transferred directly to a glovebox without air exposure. Other old (circa 1980) potassium layered oxide synthesis methods used sealed vessels for heating with KO_2 [128]. KO_2 is not easily available in Canada now due to export restrictions from the United States. These were placed upon it because it is regarded as an explosives precursor. The synthesis used herein had to be created using the potassium precursors available.

Potassium metal half-cells were constructed in much the same way sodium metal half cells were, with coin cell preparation being carried out in an argon filled glove box. For the negative reference electrode, thin potassium metal disks were used. These disks were punched from thin foil that was cold-rolled from a potassium ingot (chunks in mineral oil, 98% trace metals basis, Sigma Aldrich), since potassium foil is not readily available. The surface of the potassium ingot had to be cleaned prior to use, as the ingots are stored in oil because potassium metal is extremely reactive. A small ingot was then placed in a plastic bag and passed through a foil roller with the desired thickness, to achieve a foil thickness of approximately 0.45 mm. The electrolyte used was 0.5 M KPF_6 (99.5 %, trace metals basis, Sigma Aldrich) dissolved in EC:DEC solvent (Selectilyte, BASF) in a 1:2 volume ratio. Two Celgard 3501 and one BMF (blown microfiber separator, 3M Company) were used as separators.

The Na_xCoO_2 series was made by ball milling approximately five grams of stoichiometric amounts of Na_2CO_3 (BioXtra, ≥ 99.0 %, Sigma Aldrich) and Co_3O_4 (powder, <10 µm, Sigma Aldrich) with approximately 15 grams of half inch steel balls for a half hour in air and then heating in a 10 mL alumina boat under flowing oxygen at 850 ºC for 12 hours. The K_xCoO_2 series was made by grinding stoichiometric amounts of KOH (BioXtra, ≥ 85 % KOH basis, Sigma Aldrich) and Co_3O_4 (powder, <10 µm, Sigma Aldrich) and then heating in a 10 mL alumina boat under flowing oxygen at 600 ºC for 15 hours.

7.3.2 Layered Birnessite $K_{0.3}MnO_2$

The first potassium analogue synthesized was $K_{0.3}MnO_2$. Figure 7.9 show the $K_{0.3}MnO_2$ XRD pattern and refinement. The parameters used for the refinement are given in Table 7.3.

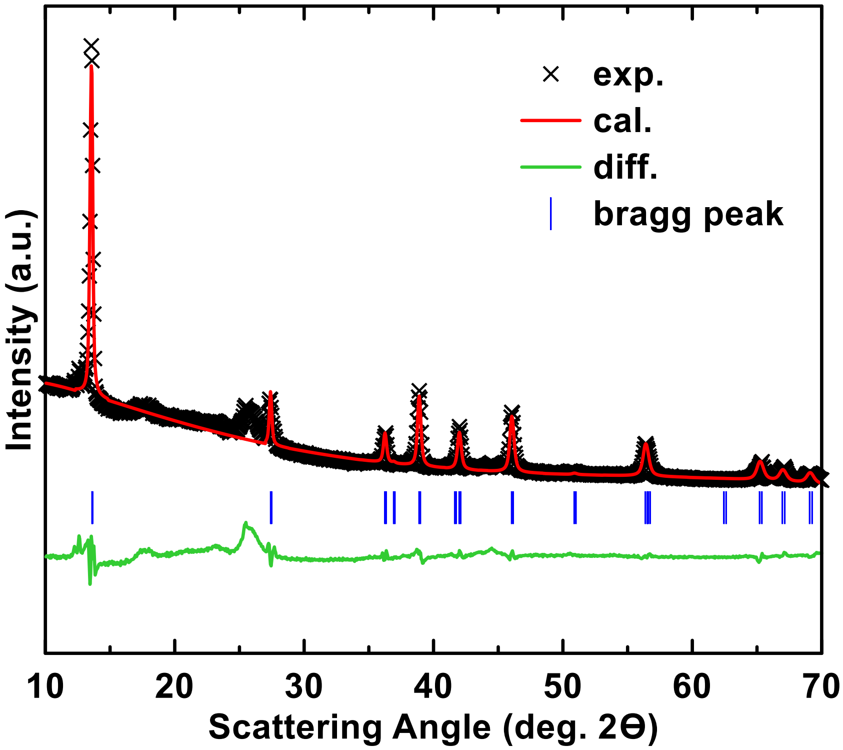

Figure 7.9: XRD pattern and Rietveld refinement of $K_{0.3}MnO_2$, with Bragg peaks indicated.

Table 7.3: Structural parameters obtained from Rietveld refinement of $K_{0.3}MnO_2$ XRD data.

$K_{0.3}MnO_2$ (space group: $P6_3/mmc$)					
atom	site	x	y	z	occupancy
K_f	2b	0	0	0.25	0.0998(8)
K_e	2c	0.66	0.33	0.25	0.2474(6)
Mn	2a	0	0	0	1.00
O	4f	0.33	0.66	0.0752(3)	1.04

Cell parameters	a (Å)	b (Å)	c (Å)	R-factor
	2.859(4)	2.859(4)	13.002(3)	1.72
	α (˚)	β (˚)	γ (˚)	
	90	90	120	

The structure is pure P2-type with a similar *a* lattice constant but much larger *c* lattice constant compared to layered sodium oxides. The increase in the *c* lattice constant is likely due to the larger ionic radius of potassium compared to sodium, as well as the low alkali metal content. A previous report on this material refined the structure as a two-layer orthorhombic phase with space group Ccmm [126]. The XRD pattern had fewer peaks and was thus able to be refined with the P2 structure space group $P6_3/mmc$. ICP experiments gave the potassium manganese ratio at 0.3:1.0, confirming a highly depotassiated layered compound was formed, containing many vacancies.

Figure 7.10 shows the voltage versus capacity profile of $K_{0.3}MnO_2$ in a sodium cell. On the first discharge only about 0.33 sodium can be inserted into the potassium host, giving a capacity of 72 mAh/g. Upon charge sodium and potassium can be removed from the structure to yield a capacity of 140 mAh/g.

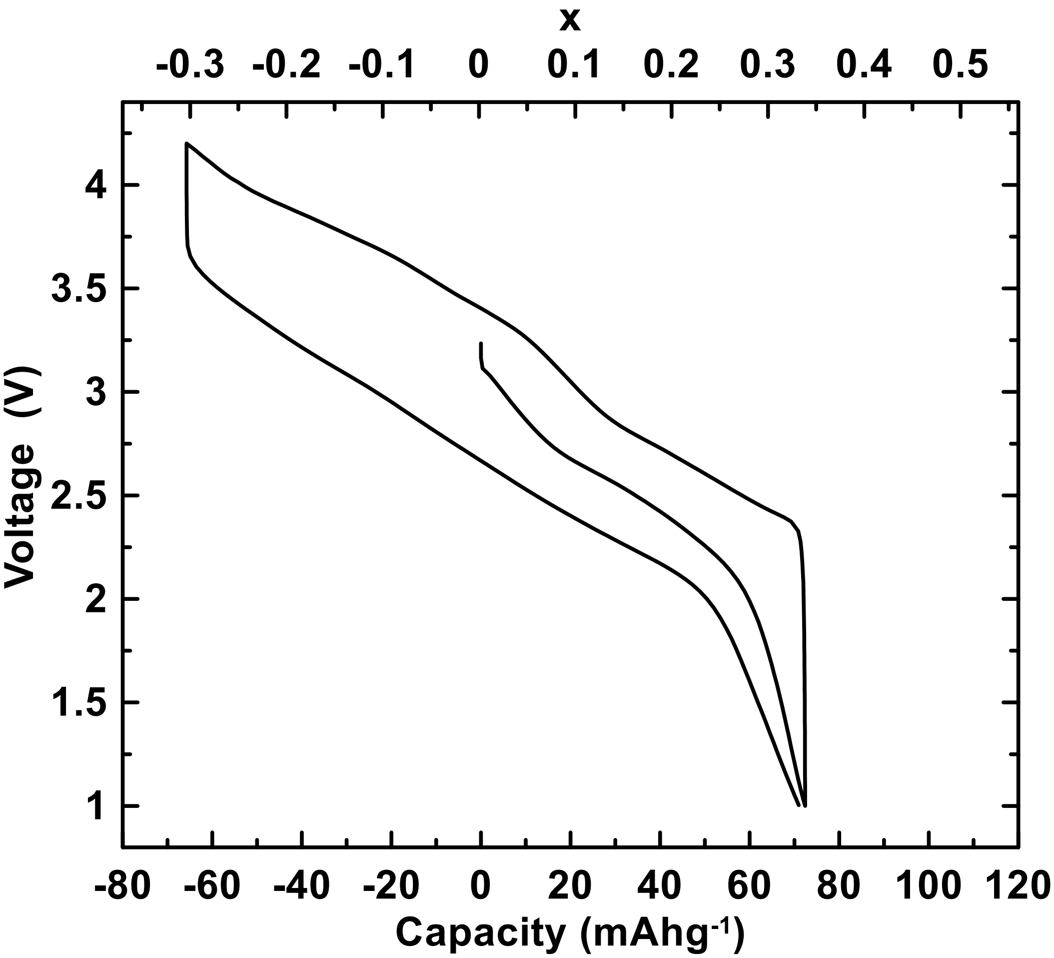

Figure 7.10: Voltage versus capacity profile of P2-$K_{0.3}MnO_2$ vs. a potassium counter/reference electrode.

The average voltage of this material is rather high making it a candidate as a positive electrode material. The objective of this preliminary study was to make a high vacancy layered potassium oxide material and not to worry about voltage. The work that follows incorporated titanium into the potassium layered oxide structure to try to reach lower voltages versus sodium.

7.3.3 $K_{2/3}Cr_{2/3}Ti_{1/3}O_2$

As the $Na_xCr_xTi_{1-x}O_2$ series had the best performing sodium layered oxide negative electrode material the analogous $K_{2/3}Cr_{2/3}Ti_{1/3}O_2$ was made. Figure 7.11 shows the XRD pattern and refinement of $K_{2/3}Cr_{2/3}Ti_{1/3}O_2$. The structure of the material was found to be of P2-type with Rietveld refinements parameters given in Table 7.4.

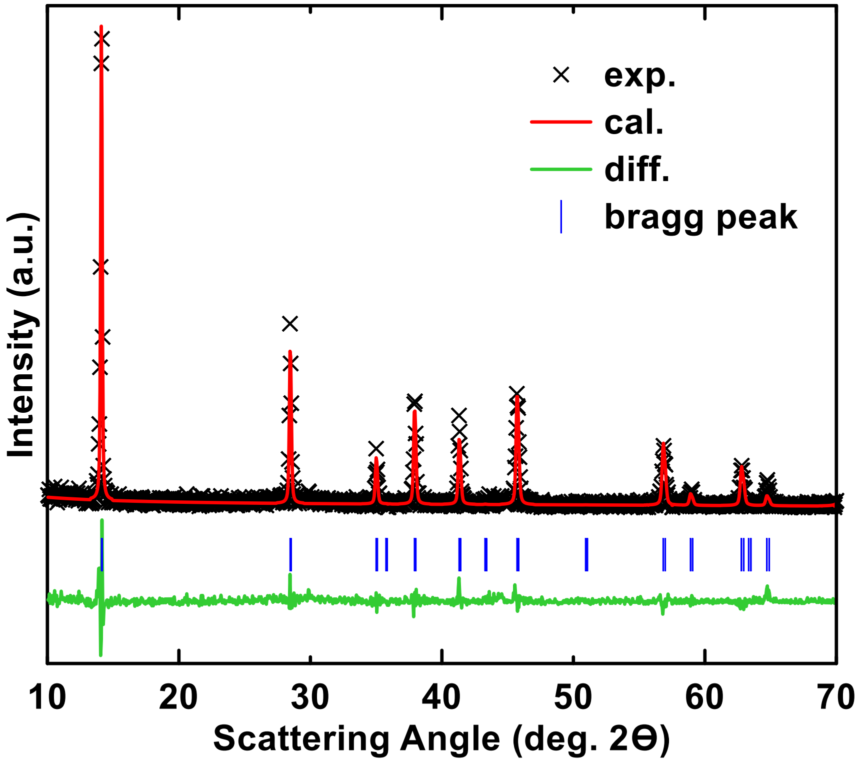

Figure 7.11: XRD pattern and Rietveld refinement of $K_{2/3}Cr_{2/3}Ti_{1/3}O_2$, with Bragg peaks indicated.

Table 7.4: Structural parameters obtained from Rietveld refinement of $K_{2/3}Cr_{2/3}Ti_{1/3}O_2$ XRD data.

$K_{2/3}Cr_{2/3}Ti_{1/3}O_2$ (space group: $P6_3/mmc$)					
atom	site	x	y	z	occupancy
K_f	2b	0	0	0.25	0.2328(8)
K_e	2c	0.33	0.67	0.75	0.4006(3)
Cr	2a	0	0	0	0.66
Ti	2a	0	0	0	0.33
O	4f	0.33	0.67	0.0823(9)	1.00
Cell parameters	a (Å)	b (Å)	c (Å)	R-factor	
	2.957(5)	2.957(5)	12.531(5)	4.27	
	α (˚)	β (˚)	γ (˚)		
	90	90	120		

After pure phase P2- $K_{2/3}Cr_{2/3}Ti_{1/3}O_2$ was synthesized other materials were made with lower potassium concentrations. The goal of these efforts was to make a material with as many vacancies as possible for application as high capacity sodium-ion negative electrode materials. Figure 7.12 shows XRD patterns for the $K_xCr_xTi_{1-x}O_2$ materials where $1/3 \leq x \leq 2/3$.

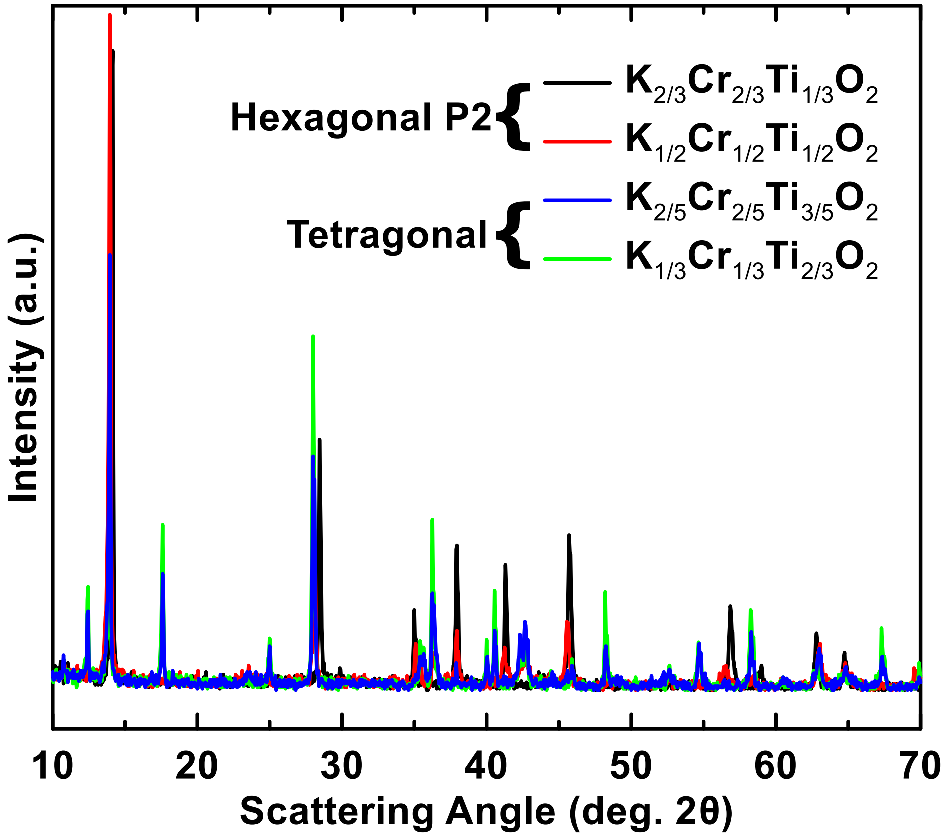

Figure 7.12: XRD patterns of $K_xCr_xTi_{1-x}O_2$ samples where $x = 2/3$, 1/2, 2/5 and 1/3 shown by the black, red, blue and green plots, respectively.

When $x = 0.66$ and 0.5 the structure is purely hexagonal P2. Below $x = 0.5$ a different phase appears. When $x = 0.4$ and 0.33 the structure is tetragonal. The tetragonal phase is not a layered structure. This result implies that the layered vacancy limit for the $K_xCr_xTi_{1-x}O_2$ series is 0.5. This is a 0.1 improvement upon the analogous sodium series.

Electrochemical tests of $K_{2/3}Cr_{2/3}Ti_{1/3}O_2$ were conducted in both sodium and potassium half-cells. Figure 7.13 shows the voltage versus capacity profile of $K_{2/3}Cr_{2/3}Ti_{1/3}O_2$ in a sodium half-cell.

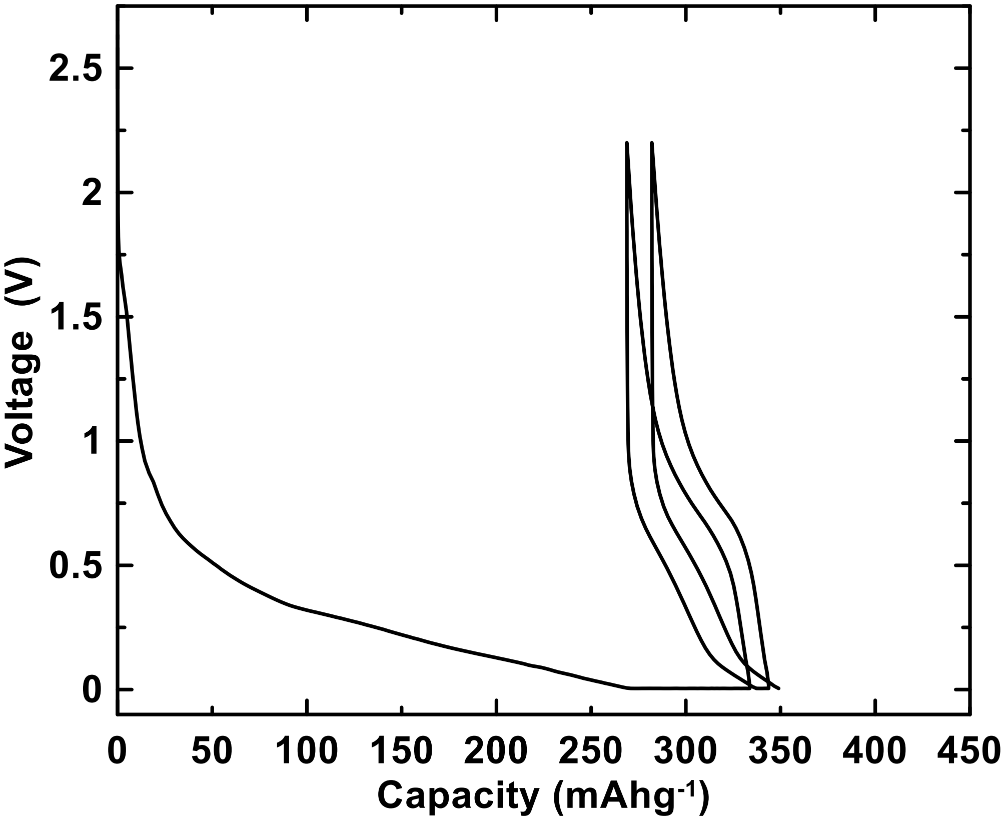

Figure 7.13: Voltage versus capacity profile of $K_{2/3}Cr_{2/3}Ti_{1/3}O_2$ cycled vs. a sodium counter/reference electrode from 0.005 – 2.2 V.

The low voltage behavior of $K_{2/3}Cr_{2/3}Ti_{1/3}O_2$ in sodium cells is very poor. An extremely large irreversible capacity is observed during the first discharge cycle. There is a somewhat reversible capacity that is consistent with the number of vacancies in the structure and a voltage that is indicative of the titanium redox couple. However, the capacity drops off rapidly on subsequent cycles and a large voltage hysteresis is observed.

Figure 7.14 shows the voltage versus capacity profile of $K_{2/3}Cr_{2/3}Ti_{1/3}O_2$ now in a potassium cell. The behavior is quite similar to that of the sodium cell with a large first discharge cycle irreversible capacity and voltage hysteresis.

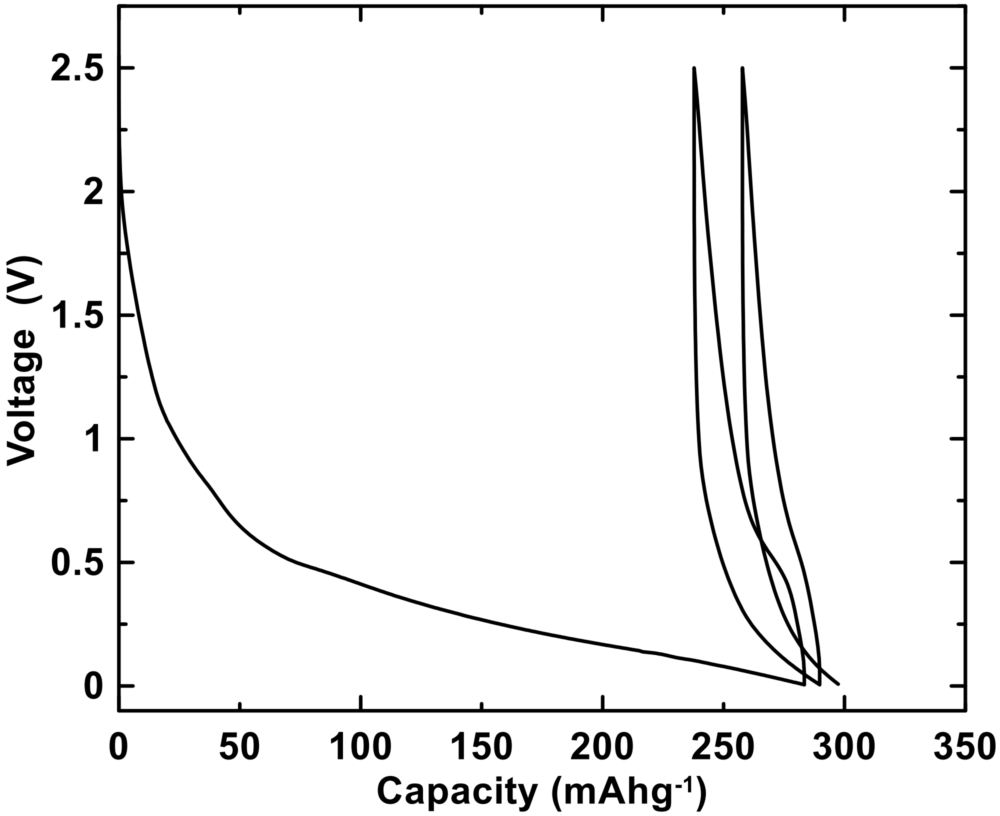

Figure 7.14: Voltage versus capacity profile of $K_{2/3}Cr_{2/3}Ti_{1/3}O_2$ cycled vs. a potassium counter/reference electrode from 0.005 – 2.5 V.

Since $K_{2/3}Cr_{2/3}Ti_{1/3}O_2$ has chromium in its transition metal layer it could also be employed as a positive electrode material in potassium cells. Figure 7.15 shows the voltage versus capacity profile of $K_{2/3}Cr_{2/3}Ti_{1/3}O_2$ charged up to voltages as high as 4.3 V.

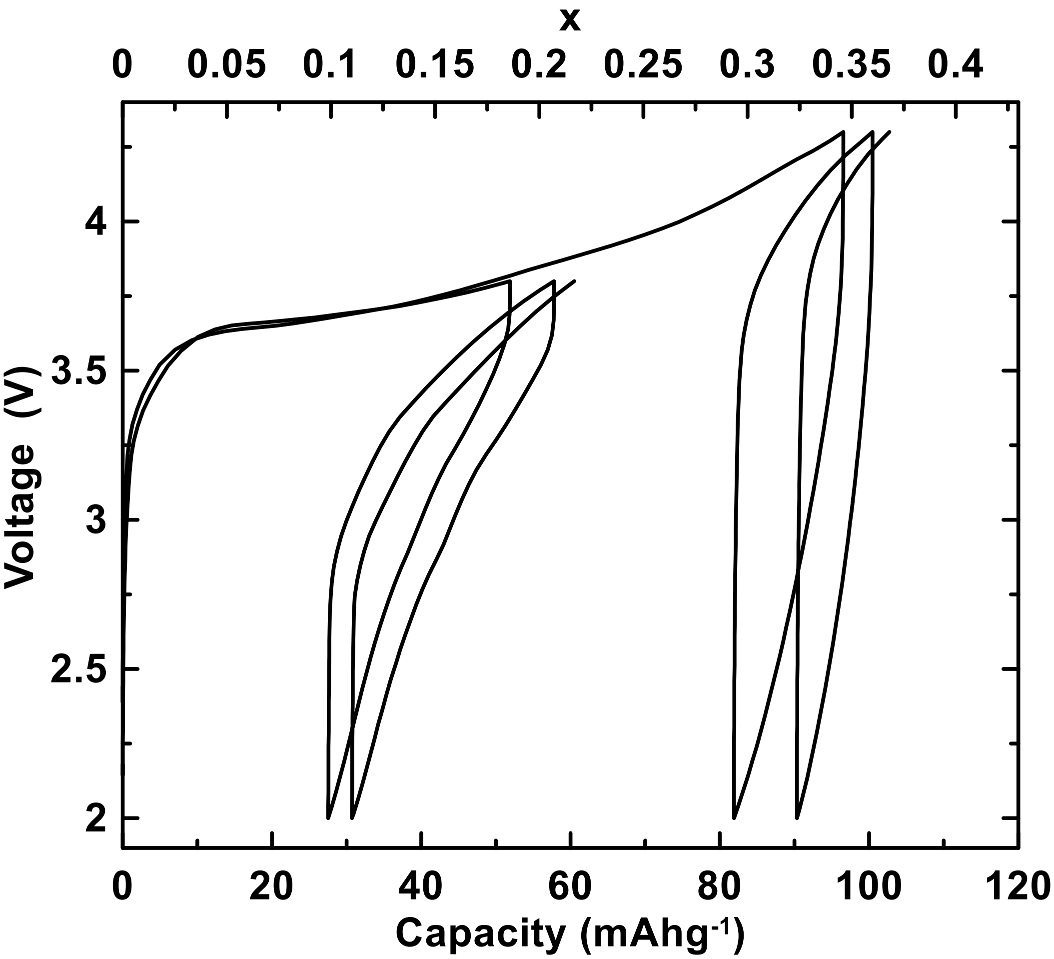

Figure 7.15: Voltage versus capacity profile of $K_{2/3}Cr_{2/3}Ti_{1/3}O_2$ cycled vs. a potassium counter/reference electrode at different high voltage cut off potentials.

The material performs poorly as a positive electrode material with a large irreversible capacity during the first cycle. When charged to 3.8 V only 30 mAh/g of reversible capacity is achieved. To get a higher capacity typically a positive electrode material can be charged to a higher voltage to remove more of the alkali metal. Here, when $K_{2/3}Cr_{2/3}Ti_{1/3}O_2$ is charged to 4.3 V the reversible capacity actually decreases. This is likely due to the irreversible migration of chromium (III) into the potassium layer at high voltages [40].

7.3.4 A_xCoO_2

A 0.10 improvement in the number of vacancies was achieved for the $K_xCr_xTi_{1-x}O_2$ series versus the $Na_xCr_xTi_{1-x}O_2$ series. To verify if this is representative of the family of potassium layered oxides further synthesis of potassium layered oxides was done. The A_xCoO_2 series was chosen where A = Na and K and x was varied. The cobalt series is a good candidate because high vacancy materials have been reported in the literature with cobalt being stable in either the +3 (full alkali metal layer) or +4 (when vacancies are present) oxidation state [97]. Cobalt is easily oxidized to +4 during synthesis in an air or oxygen atmosphere.

Figure 7.16 shows the XRD patterns of the alkali cobalt oxides with differing amounts of alkali metal. $Na_{0.6}CoO_2$ is single phase P2, however when the sodium content is lowered to 0.55 or 0.45 a second impurity phase of Co_3O_4 appears. $K_{0.6}CoO_2$ and $K_{0.5}CoO_2$ are also single phase P2. It is not until the potassium content is lowered to 0.45 or below that the Co_3O_4 phase appears. This result once again shows the vacancy limit between the potassium and sodium series of layered metal oxides. It appears that in going from sodium to potassium 0.1 more vacancies can be obtained within the layered oxide framework.

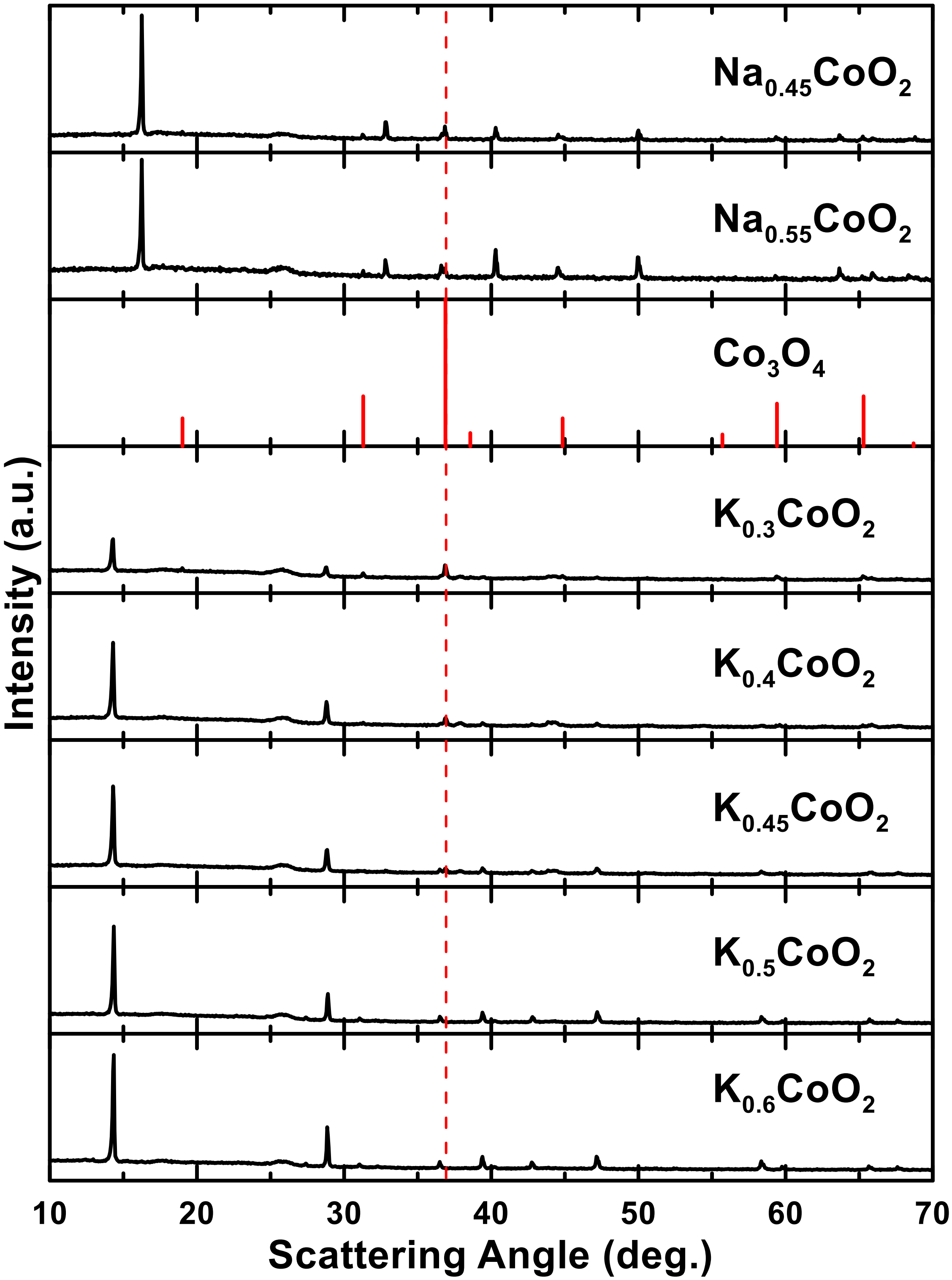

Figure 7.16: XRD patterns of sodium and potassium cobalt oxides with differing amounts of alkali metal to illustrate the vacancy limit of the layered phase. A reference pattern for Co_3O_4 is also indicated by the red lines as it was found to be the second phase that appears.

7.4 Conclusions

The desirable characteristics of $Na_xM_yTi_{1-y}O_2$ materials as negative electrodes in NIBs have been highlighted. These include low average voltage, small hysteresis, good cyclability and high crystallographic density. One area where they lack is their relative lower capacity, which is dictated by the sodium vacancy limit. Two methods were employed to increase the vacancy limit in the alkali metal layer, namely sulfide and potassium analogues.

Sulfide analogues were synthesized and allowed for more vacancies in the layered structure due to the lower bond iconicity compared to oxides. However, $Na_{2/3}Cr_{2/3}Ti_{1/3}S_2$ showed that sulfides had impractical voltages for implementation as negative electrodes in NIBs, with plateaus at approximately 1.7 and 2.8 V. This is likely due to the sulfur taking part in the redox process. Early work on sulfides such as TiS_2 took place decades ago and showed that generally as a group sulfides do indeed display lower voltages than their oxide counterparts with more vacancies [122]. This work demonstrates that mixed metal sulfides do not perform better, in terms of energy density, as negative electrode materials in NIBs than mixed metal oxides such as $Na_xM_yTi_{1-y}O_2$. The increase in vacancies does not offset the higher voltage and poor cyclability of these materials compared to $Na_xM_yTi_{1-y}O_2$ materials.

Going from sodium to potassium layered metal oxides, 0.1 more vacancies can be obtained within the layered framework. This is thought to be due to both the larger ionic radii and smaller electronic charge density of potassium. A 0.1 vacancy increase is observed for both the $A_xCr_xTi_{1-x}O_2$ and A_xCoO_2 series. In the author's opinion, this increase is not significant enough for one to switch over to potassium analogues to achieve higher capacity layered oxide negative electrodes, especially when the poor electrochemistry in sodium cells is taken into account. It may be desirable to try other metal combinations within the metal layer to confirm these results, as these are just two examples where the vacancy limit was improved by only 0.1. The reader may recall that the when manganese is solely in the metal layer 0.7 vacancies are achievable in potassium manganese oxide. Examples of high vacancy potassium materials for comparison are lacking in the literature.

CHAPTER 8 POTASSIUM-ION BATTERIES

8.1 Introduction

One can also go beyond sodium-ion batteries, just as sodium-ion batteries are considered beyond lithium-ion batteries. Potassium-ion batteries have been proposed as alternatives to both lithium and sodium-ion batteries. Potassium raw materials would be lower cost than that of lithium due to their abundance and wider distribution. Like sodium, potassium will not alloy with aluminum at low voltage and thus more expensive copper can be exchanged for aluminum as a negative electrode current collector.

Perhaps where potassium shows a significant advantage over both sodium and lithium is the lower potential in PC based solvents, -2.79, -2.56 and -2.88 for Li, Na and K, respectively [27]. This is advantageous because in a full cell the energy density in Wh is determined by multiplying the capacity in Ah by the average cell voltage. Another area where potassium has an advantage over both lithium and sodium is its lower charge density which could result in higher mobility and transport numbers of potassium ions compared to the lithium and sodium alkali metals [20].

Of course, potassium has a larger ionic radius and higher atomic weight which will result in lower gravimetric and volumetric energy densities but this would be negligible in traditional positive electrode materials such as $ACoO_2$ where only a very small ratio of volume and weight is attributed to the alkali metal. Another challenge is the high reactivity of potassium metal and low melting point (64 ºC), which is probably why potassium-ion batteries have not been investigated in great detail. Great care must be taken when constructing potassium half-cells and more importantly during disposal of potassium metal after cells are spent.

In the author's opinion, the greatest advantage for potassium-ion batteries over sodium-ion batteries is its ability to intercalate in graphite [20,129]. Graphite has been an almost magical negative electrode material for lithium-ion batteries and researchers continue to try and improve it by adding more and more high capacity silicon to the graphite electrode [54]. The fact that sodium does not intercalate into graphite to any appreciable extent is what gave rise to the great need for negative electrode materials for sodium-ion batteries and the $Na_xM_yTi_{1-y}O_2$ materials investigated in this thesis. High reversibility of potassium intercalation into graphite in non-aqueous electrolytes has been demonstrated. A reversible capacity of ~250 mAh/g is attainable from the formation of a stage one KC_8 compound at low voltage.

8.2 Constructing Potassium Half-cells versus Graphite

The initial studies of potassium-ion batteries for this work started with the evaluation of graphite as a negative electrode material. The cell making process had to be optimized in order to fabricate potassium half-cells that would cycle for more than a few cycles versus potassium metal, as they were found to be different than that of lithium and sodium half-cells. Figure 8.1 shows the difference between freshly rolled and punched potassium and sodium metal (a). The reactivity of potassium metal is apparent in (b) as the metal has become gummed up with reduction products and the separators have been discolored. The potassium half-cell depicted was only cycled two times before being opened for inspection. This cells shows increased reactivity compared to sodium half-cells. This cell after only two cycles looks like sodium cells after over 50 cycles in terms of reactivity and buildup of electrolyte decomposition products at the metal surface [107]. It is apparent that only initial voltage versus capacity behavior and not cycling performance can be evaluated in potassium half-cells due to impedance growth at the potassium foil electrode. Ideally full cells would be tested which would forego the use of potassium metal, however, individual electrode characteristics must be understood first before proceeding.

Figure 8.1: (a) Potassium (left) and sodium (right) punched metal foil prior to cell assembly. (b) Potassium graphite half-cell opened after two cycles showing the reactivity of the potassium metal (right).

Lithium half-cells can cycle with only Celgard separator between the two electrodes, however when one goes to sodium half-cells BMF is required to get adequate cycling behavior. BMF simultaneously increases the distance between electrodes and provides a more even stack pressure to limit the growth of sodium dendrites. This approach also works for potassium half-cells, but not to the same extent. An additional Celgard separator (two in total) is also needed and the thickness of potassium foil (0.45 mm) must be increased to get stable cycling over 50 cycles. This slows the growth of dendrites and accumulation of reduction products at the potassium reference electrode. The potassium metal ingots (chunks in mineral oil, 98% trace metals basis, Sigma Aldrich) must be rolled and brushed (to remove the outer oxide layer) just as sodium metal is, though the potassium is much easier to roll as it is much softer and malleable metal than sodium. In fact, the small potassium ingot in a plastic bag is only passed through a rolling mill once at the desired foil thickness as measured by a feeler gauge, unlike sodium where the thickness is decreased incrementally until the desired thickness is reached.

Electrolyte for potassium-ion cells needed to be considered too. Typically for non-aqueous cells, a potassium salt would be dissolved in an organic solvent mixture of alkyl carbonates. Typical salt concentrations are one molar, however, one molar KPF_6 would not dissolve completely in most alkyl carbonates such as PC. For this reason, 0.5 M KPF_6 was used for all potassium-ion cells in this work.

Figure 8.2 shows a voltage versus capacity graph of graphite versus potassium metal. Stable cycling with appropriate capacities are only achieved when utilizing the optimized cell making procedures described above. An example of a non-optimized cell made early on in this work is shown by the red curve in Figure 8.2. Very little reversible capacity is observed for this cell and it dies after only a few cycles. However, the optimized cell shown by the black curve in Figure 8.2 yields a capacity of over 250 mAh/g and stable cycling is shown in Figure 8.3.

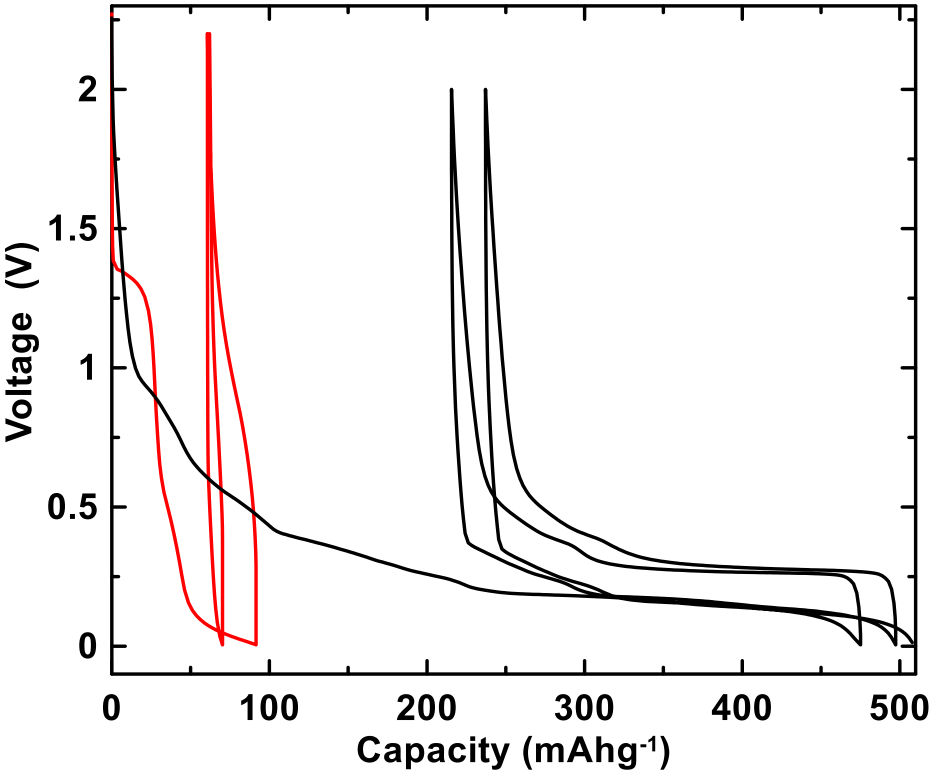

Figure 8.2: Voltage versus capacity profile for graphite and potassium metal. An example of a cell made early on and late in this work are shown in red and black, respectively.

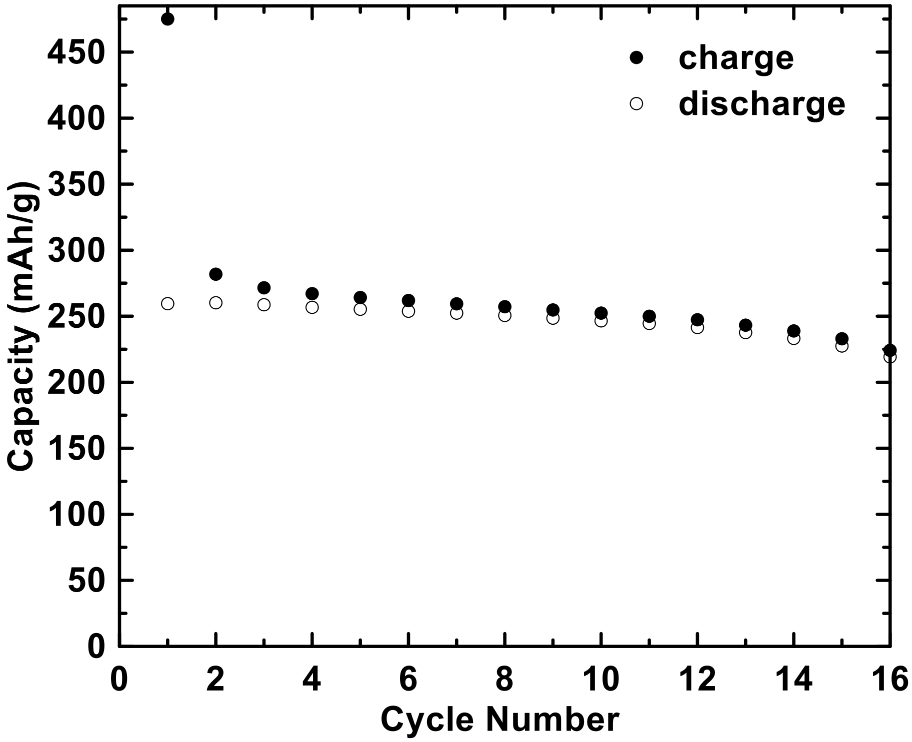

Figure 8.3: Capacity versus cycle number for graphite cycled versus potassium metal, with open and closed circles denoting discharge and charge capacity, respectively.

8.3 K_xCoO_2

A potassium-ion battery review article that came out in late 2016 highlights the work done on potassium batteries thus far [130]. It emphasizes the importance of finding new materials as well as opportunities and challenges facing potassium-ion batteries. Perhaps the largest obstacle is finding suitable positive electrode materials, as graphite has shown great performance as a negative electrode material. The most studied insertion material for potassium positive electrode materials is Prussian blue, however it suffers from low volumetric energy density [131]. The most likely place to start looking for higher energy density potassium insertion positive electrode materials is the K_xMO_2 class of materials. Some of the first reported and best performing positive electrodes for sodium and lithium-ion batteries both were indeed A_xCoO_2 materials. This is where it was decided to start an investigation for potassium-ion battery positive electrode materials, namely the analogous K_xCoO_2.

8.3.1 Experimental

K_xCoO_2 was obtained by mixing approximately five grams of KOH (BioXtra, ≥ 85 % KOH basis, Sigma Aldrich) and Co_3O_4 (powder, <10 μm, Sigma Aldrich) via a half hour of ball milling under argon with approximately 15 grams of half inch steel balls, followed by heating in an oxygen atmosphere at 600 °C for 15 hours. An amount of postassium that is 20 % in excess of stoichiometry was added due to the volatility of potassium at elevated temperatures.

Electrodes comprising K_xCoO_2, carbon black and PVDF binder in a 80:10:10 weight ratio were cast using NMP as a solvent and dried at 120°C. Electrodes were cycled in 2325 coin type cells at a rate of C/10 (assuming a 100 mAh/g capacity) using potassium metal counter/reference electrodes and 0.5M KPF_6 in EC:DEC 1:2 electrolyte.

8.3.2 Results and Discussion

ICP analysis determined that $x = 0.62$ in the K_xCoO_2 formula. Figure 8.4 shows an SEM image of the as prepared $K_{0.62}CoO_2$ material.

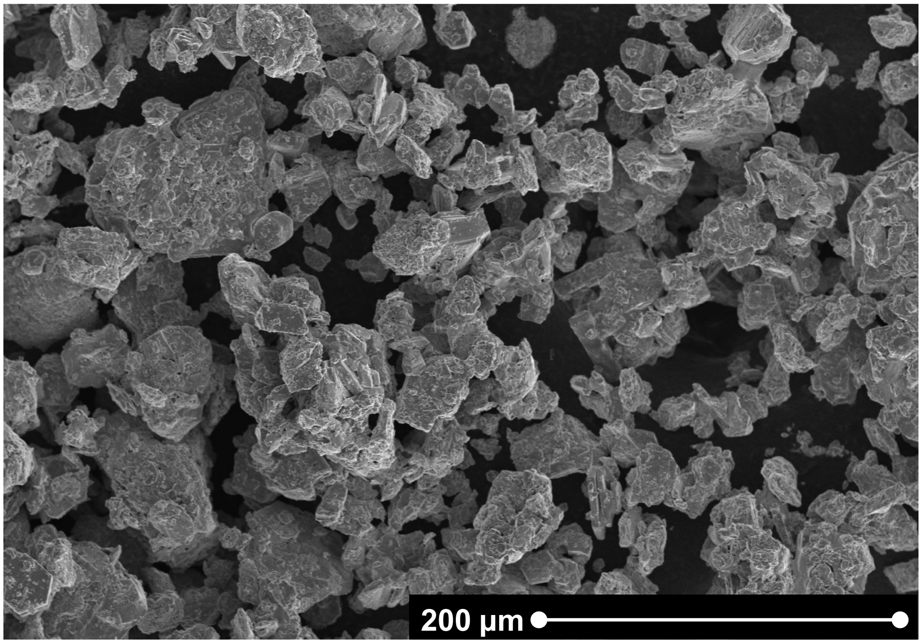

Figure 8.4: SEM image of the as prepared $K_{0.62}CoO_2$ material.

Figure 8.5 shows the XRD pattern and refinement of $K_{0.62}CoO_2$ along with the parameters used in the fit shown in Table 8.1. The structure was determined to be of P2-type.

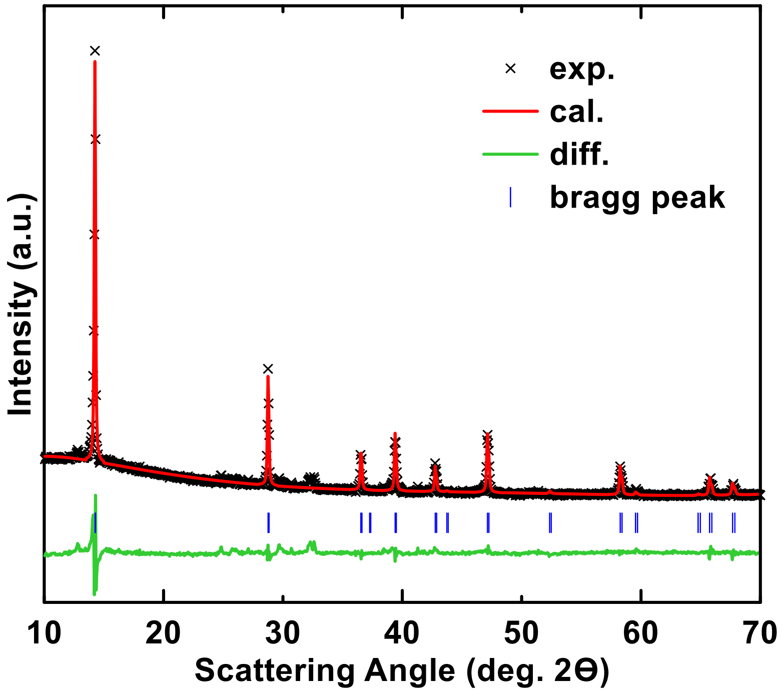

Figure 8.5: XRD pattern and Rietveld refinement of $K_{0.62}CoO_2$, with Bragg peaks indicated.

Table 8.1: Structural parameters obtained from Rietveld refinement of $K_{0.62}CoO_2$ XRD data.

$K_{0.62}CoO_2$ (space group: $P6_3/mmc$)					
atom	site	x	y	z	occupancy
K_f	2b	0	0	0.25	0.1956(1)
K_e	2c	0.66	0.33	0.25	0.3853(1)
Co	2a	0	0	0	1.00
O	4f	0.33	0.66	0.0669(3)	1.00
Cell parameters	a (Å)	b (Å)	c (Å)	R-factor	
	2.841(6)	2.841(6)	12.357(2)	2.36	
	α (°)	β (°)	γ (°)		
	90	90	120		

Figure 8.6 shows the NPD pattern and refinement of $K_{0.62}CoO_2$ with the parameters used in the fit shown in Table 8.2. No new peaks appeared in the neutron data indicating that potassium and transition metal ordering were not present in this material.

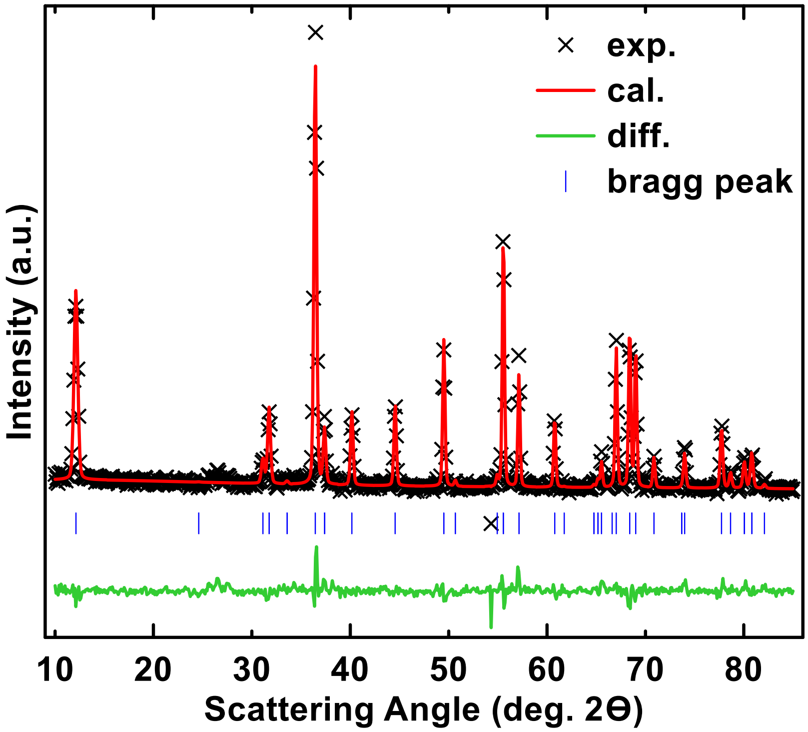

Figure 8.6: NPD pattern and Rietveld refinement of $K_{0.62}CoO_2$, with Bragg peaks indicated.

Table 8.2: Structural parameters obtained from Rietveld refinement of $K_{0.62}CoO_2$ NPD data.

$K_{0.62}CoO_2$ (space group: $P6_3/mmc$)					
atom	site	x	y	z	occupancy
K_f	2b	0	0	0.25	0.1531(7)
K_e	2c	0.66	0.33	0.25	0.2340(9)
Co	2a	0	0	0	1.00
O	4f	0.33	0.66	0.0783(3)	1.00
Cell parameters	a (Å)	b (Å)	c (Å)	R-factor	
	2.839(4)	2.839(4)	12.364(0)	3.44	
	α (˚)	β (˚)	γ (˚)		
	90	90	120		

Figure 8.7 shows the voltage versus capacity profile of $K_{0.62}CoO_2$ cycled over differing voltage ranges. Hysteresis and poor capacity retention was observed when $K_{0.62}CoO_2$ was either charged above 4.0 V or discharged below 1.7 V.

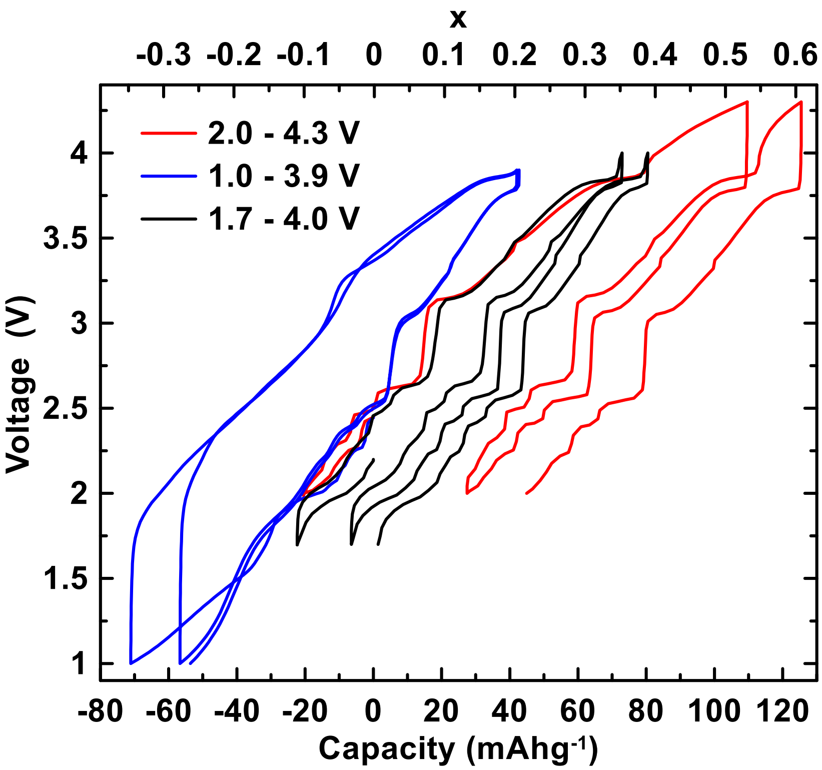

Figure 8.7: Voltage versus capacity profiles of P2-$K_{0.62}CoO_2$ for 1.7 – 4.0 V, 1.0 – 3.9 V and 2.0 – 4.3 V voltage windows which are shown in red, blue and black, respectively.

Figure 8.8 shows the voltage versus capacity profile of $K_{0.62}CoO_2$ in the voltage range 1.7 to 4.0 V. The black and red curves show the first and twelfth cycles, respectively. The cell walks to the right as cycling proceeds due to the difference between the charge and discharge capacities. The cell delivers about 80 mAh/g of reversible capacity at an average discharge voltage of 3.2 V. The capacity corresponds to an x range of 0.32 to 0.72 in K_xCoO_2. This also happens to be the P2 composition range in layered sodium metal oxides. From this and other studies it is thought that potassium does not adopt octahedral coordination in these materials due to its larger ionic radius. It prefers the smaller packing density of a prismatic environment and cycles reversibly in an electrochemical cell within the P2 stability region.

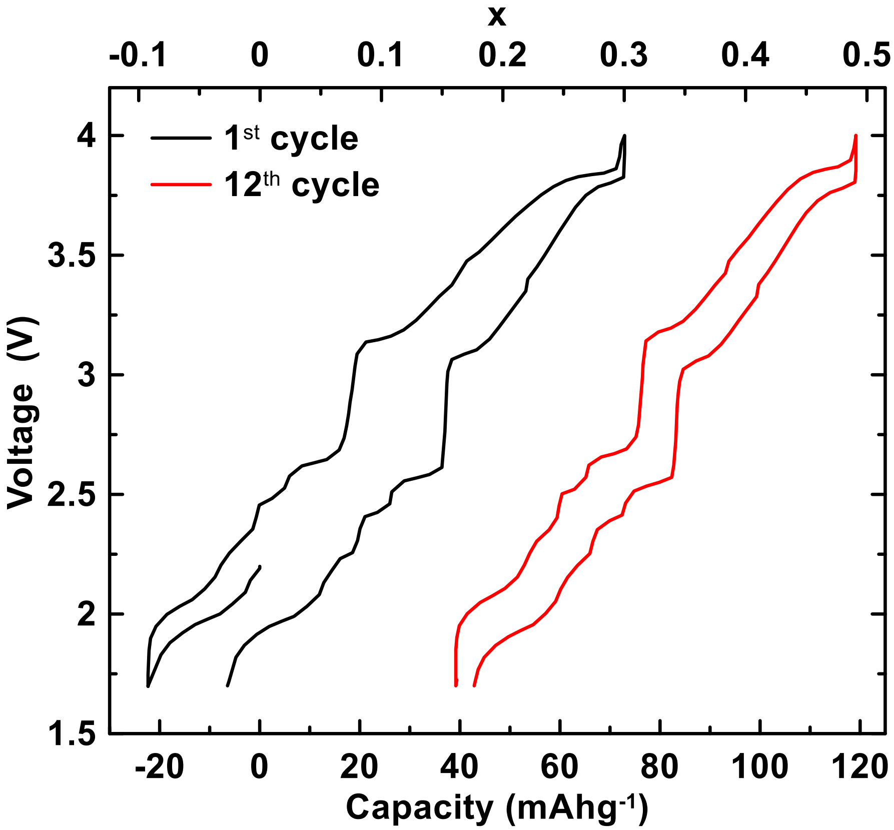

Figure 8.8: Voltage versus capacity profile for the P2-$K_{0.62}CoO_2$ material from 1.7 – 4.0 V with the first and twelfth cycles shown in black and red, respectively. The upper x-axis shows the change of *x* in K_xCoO_2.

Figure 8.9 shows the capacity versus cycle number over 50 cycles for $K_{0.62}CoO_2$ in the voltage range of 1.7 to 4.0 V. The cell does not display linear fade over 50 cycles. There is an inflection point around cycle 25 where the fade becomes greater. This is likely due to impedance growth at the unstable potassium reference electrode. Further cell design improvements are desirable so that potassium half-cells can cycle for a greater number of cycles before failure.

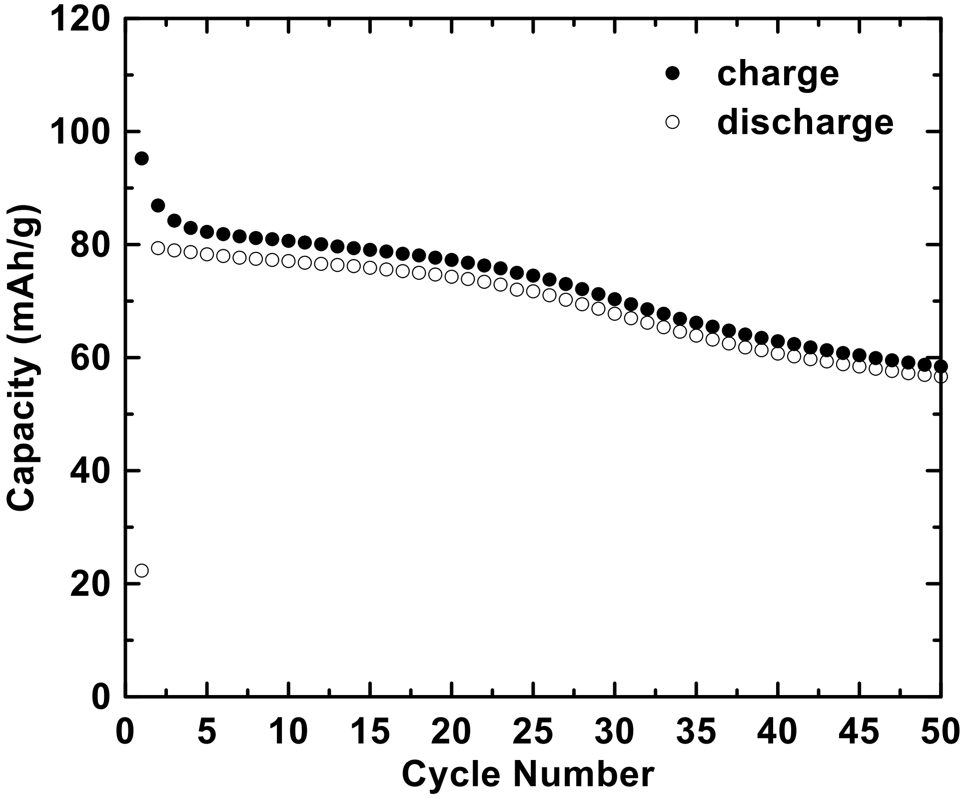

Figure 8.9: Capacity versus cycle number for the P2-$K_{0.62}CoO_2$ material cycled from 1.7 – 4.0 V, with open and closed circles denoting discharge and charge capacity, respectively.

Figure 8.10 shows the differential capacity curve for $K_{0.62}CoO_2$ with black, red and blue curves depicting cycle 1, 2 and 12, respectively. Eight distinct peaks are observed on both charge and discharge. These peaks are reversible over the 12 cycles shown with only slight shifting occurring. Upon charge the peaks shift to higher voltages, while on discharge the peaks shift to lower voltages. This is likely a consequence of the impedance growth at the potassium reference electrode which results in increased voltage hysteresis as cycling proceeds.

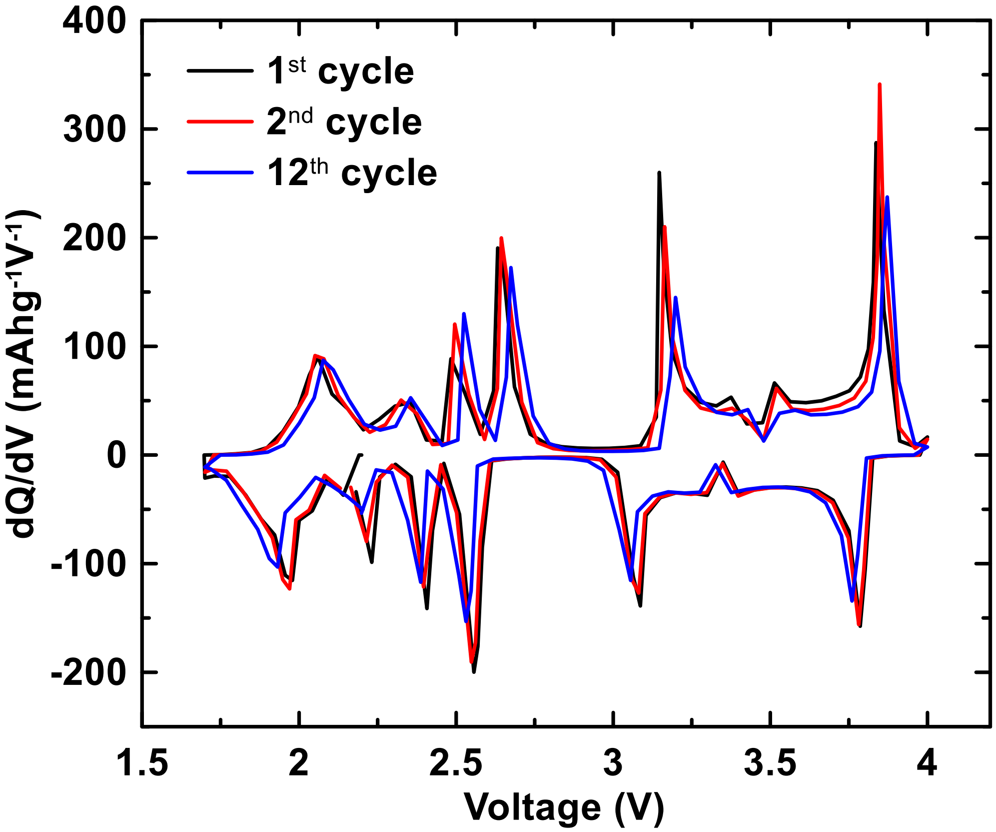

Figure 8.10: Differential capacity curves of P2-$K_{0.62}CoO_2$ cycled from 1.7 – 4.0 V, with the first, second and twelfth cycles shown in black, red and blue, respectively.

The many peaks observed in the differential capacity plot are not typical of commercial lithium-ion battery materials, where usually only one peak is observed. The appearance of many plateaus in the voltage curve, and in turn many peaks in the differential capacity curve, is well understood. These correspond to either alkali metal ordering or phase transitions, such as MO_2 slab gliding, during cycling. The alkali metal ordering becomes more prevalent as the ionic radius of the alkali increases. As potassium is a very large ion it is expected to display more ordering transitions. Indeed, in the literature this behavior has been attributed to potassium ion ordering within the potassium layer as potassium is inserted and removed during cycling [132]. It was also found that the P2 structure is maintained over this large voltage and potassium composition range.

8.3.1 Conclusions

Preliminary potassium half cells were constructed and optimized in order to cycle versus a reactive potassium metal counter/reference electrode. This was done initially with graphite and potassium metal. A thicker separator between the electrodes and an even pressure was needed in the cell stack in order to minimize potassium dendrite growth and obtain tens of cycles.

$K_{0.62}CoO_2$ was found to reversibly intercalate potassium over 50 cycles in coin cells versus potassium metal. This is one of the few examples of a positive electrode material for potassium-ion batteries, besides Prussian blue, $Fe_4[Fe(CN)_6]_3 \cdot xH_2O$. Prussian blue has a very different structure (cubic) than the layered potassium metal oxides and thus meaningful comparisons are difficult to make. $K_{0.62}CoO_2$ has a first charge capacity of 90 mAh/g during cycling between 1.7 and 4.0 V was observed with an average discharge voltage of 3.2 V, which correlates to an energy density of about 1200 Wh/L. This shows that layered oxide materials have promise as positive electrodes for potassium-ion batteries. Further studies of KMO_2 layered oxides are needed with inexpensive and non-toxic transition metals.

CHAPTER 9 CONCLUSIONS AND FUTURE WORK

9.1 Conclusions

Studies of $A_xM_yTi_{1-y}O_2$ materials functioning as negative electrodes in lithium-ion batteries are virtually non-existent. This is because the layered alkali metal titanates display extremely different chemistry in lithium and sodium cells. Sodium transition metal oxides yield lower voltages, tolerate more vacancies and are more stable at low voltages than their lithium counterparts. New high energy density electrodes were studied that exploited these differences. Simple LIB analogues have dominated NIB research thus far. However, the $Na_xM_yTi_{1-y}O_2$ series are innovative materials that do away with copy cat chemistry.

A detailed review of the layered sodium metal titanate materials was given in Section 7.1, Layered $Na_xM_yTi_{1-y}O_2$ Materials Outlook. To conclude, the materials studied herein show great promise as negative electrode materials for sodium-ion batteries. They have a larger volumetric energy density than the current state-of-the-art NIB negative electrode material hard carbon (620 Wh/L when cycled above 50 mV for hard carbon versus 1500 Wh/L for $Na_{0.6}Cr_{0.6}Ti_{0.4}O_2$). They utilize the Ti^{4+}/Ti^{3+} low voltage redox couple. Chapter 4 and Chapter 5 gave two specific examples of these types of series, namely chromium (III) and vanadium (III), respectively. Structural studies of these materials showed that they adopt the O3 structure type when no or relatively few vacancies are present and the P2 structure type when many vacancies are present. Below a certain vacancy limit another non-layered phase appeared that was electrochemically inactive. The large vacancy limit appears to be 0.4, regardless of the transition metal in the $Na_xM_yTi_{1-y}O_2$ formula.

The electrochemical performance of these materials in sodium cells was the focus of this work. They display smooth voltage profiles which was due to a lack of sodium and charge ordering. The voltage hysteresis can be somewhat tuned depending on the metal substituting for titanium, with chromium (III) displaying the least hysteresis to date. This low hysteresis was indicative of an intercalation reaction. Furthermore, *in situ* XRD studies showed that regardless of transition metal substitution the structure does indeed remain layered with extremely little volume change (< 2%) during electrochemical cycling. This structural stability during cycling was evident in capacity versus cycle number plots where many cycles were achieved with little capacity fade. $Na_{0.6}Cr_{0.6}Ti_{0.4}O_2$ was shown to be the best performing $Na_xM_yTi_{1-y}O_2$ type negative electrode material to date in NIBs. It yields a gravimetric capacity of 120 mAh/g and only 0.1 V of hysteresis, which is 30 mAh/g more capacity and half of the hysteresis of the most other $Na_xM_yTi_{1-y}O_2$ materials.

In Chapter 6 two important $Na_xM_yTi_{1-y}O_2$ compositions were studied. An important advantage of SIB over LIB is their sustainability. $Na_{2/3}Mn_{1/3}Ti_{2/3}O_2$ is a beautiful example of a material derived from abundant, non-toxic, low cost and sustainable elements. An important point here is that the performance is not sacrificed when switching to a more sustainable transition metal like manganese in this material. Studies of $Na_{2/3}Ni_{1/3}Mn_{1/3}Ti_{1/3}O_2$ showed that it is likely essential that no structural ordering occur within the layers of these materials for optimal performance. Even though this material has sufficient vacancies in the sodium layer and a corresponding amount of titanium for titanium redox its electrochemical performance was shown to suffer due to transition metal ordering. No example exists to date where an ordered $Na_xM_yTi_{1-y}O_2$

material yields high capacity at low voltage for application as a negative electrode in NIBs.

A key goal of this work was to increase the number of vacancies in the layered structure as the capacity of these materials was found to directly correlate to the number of vacancies. As intercalation materials, it is unlikely that a capacity over 250 mAh/g will be achieved, as this corresponds to no sodium or vice versa 1.0 vacancies within the layered structure. The structural studies of $Na_xM_yTi_{1-y}O_2$ materials showed that 0.4 vacancies were attainable using solid state synthesis methods with a maximum capacity of 120 mAh/g. In Chapter 7 two separate strategies were employed to increase the number of vacancies within the layered framework. The first strategy was sulfide analogues, such as $Na_xM_yTi_{1-y}S_2$. Metal disulfides can actually exist with no alkali in the layered framework while remaining a layered structure, unlike oxides. Unfortunately, this study found that the capacities of these materials occurred at inappropriately high voltages, likely due to the sulfur redox instead of the titanium redox couple.

The second strategy used was synthesizing potassium analogues. It was found that the larger ionic radius of potassium was able to increase the number of vacancies by 0.1 when compared to the smaller sodium. Single phase K_xMO_2 materials where $x = 0.5$ with two separate metal layer compositions were made, namely $K_{0.5}CoO_2$ and $K_{0.5}Cr_{0.5}Ti_{0.5}O_2$. This only slight improvement was not enough to switch to potassium analogues especially when the materials showed poor electrochemistry when cycled in sodium cells.

The synthesis of potassium analogues led to the investigation of potassium-ion batteries. Potassium, like sodium, is another low cost and abundant alkali compared to lithium. Chapter 8 showed preliminary results of reversible potassium insertion in graphite (250 mAh/g) and $K_{0.62}CoO_2$ (80 mAh/g). Coin cell construction and electrolyte formulation had to be developed in order to get tens of cycles in potassium metal cells, as potassium metal is much more reactive than either lithium or sodium. There are relatively few reports on KIB materials for comparison.

9.2 Future Work

There are still a vast number of metal titanate materials yet to be explored, as well as other metal redox couples that might also display low voltages versus sodium metal. Other $Na_xM_yTi_{1-y}O_2$ examples could include, but are not limited to, M= Y^{3+}, Zn^{2+}, Cu^{2+}, Co^{3+}, Mn^{3+}, Al^{3+}, Mg^{2+}, Ca^{2+}. Notice that although Mn^{2+} and Co^{2+} have been studied, different oxidation states of these metals are possible and could have drastically different electrochemistry. Examples of higher metal redox couples, besides titanium, that show low voltage sodium intercalation have been demonstrated. Two such examples are $Na_{2/3}Ni^{2+}_{2/3}Te^{6+}_{1/3}O_2$ and $Na_{2/3}Ni^{2+}_{5/9}Sb^{5+}_{4/9}O_2$ [133,134]. Other possibilities could be M= V^{5+}, Zr^{4+}, Y^{3+}, W^{6+}, Mo^{6+}, Bi^{5+}, Sn^{4+}, Pb^{4+}. This makes the possible metal combinations in the layered sodium metal oxides virtually endless.

Chapter 4 and Chapter 5 demonstrated the differences of these materials when different metals are substituted for titanium. New properties arise in terms of the number of possible vacancies (which determines capacity), air stability, voltage, cycling behavior (hysteresis and irreversible capacity) and surface products due to sodium loss at the bulk during solid state synthesis. Other new metal combinations, besides first row transition metals, could affect these properties in a beneficial way.

Also, in Chapter 4 a material was observed that appeared to exist at two separate voltages. The material was $Na_xCr_{0.75}Ti_{0.25}O_2$ where x = 0.75 or 1. Further studies are needed to support these findings. Neutron diffraction experiments showed that no ordering is present in these materials. ICP can give us the elemental composition of the materials and this needs to be done for the pristine powders, charged $NaCr_{0.75}Ti_{0.25}O_2$ and discharged $Na_{0.75}Cr_{0.75}Ti_{0.25}O_2$. It has been shown that $Na_xCr_{0.75}Ti_{0.25}O_2$ stays in the O3 structure when cycling anywhere between 5 mV and 3.5 V. *In situ* and *ex situ* XRD needs to be done at the correct points on the capacity curves in order to get O3 XRD patterns that give lattice constants that corroborate the same structures are occurring at different voltages.

A diverse array of methods is available to synthesize solids compounds and materials. The high temperature solid state method was used to synthesize the $Na_xM_yTi_{1-y}O_2$ materials and analogues. Different synthesis routes could include the sol gel and hydrothermal methods. For the sol gel method, the synthesis times and temperatures are often decreased. The hydrothermal method would be carried out in an autoclave where lower temperatures but higher pressures are employed. The hydrothermal method might allow unusual metal oxidation states to be stabilized. In general, both of these methods employ lower temperatures for synthesis compared to the solid state method. This is advantageous as lower temperatures could allow access to different phases, such as higher vacancy materials that are not as stable as their fully sodiated counterparts, as shown by DSC experiments herein.

Perhaps in order to achieve this high number of vacancies greater understanding of vacancies in general is required. At this time it is known that vacancies can occur in any of the layers as Schottky or Frenkel defects, this includes the alkali metal, transition metal and oxygen layers [114,135–139]. It is important to know where the vacancies are occurring in the sodium metal titanates and if possible tailor the vacancies to the sodium layer. Careful measurements using XRD, ICP-OES, pycnometer and TEM could be useful in this regard.

The potassium analogue study was by no means exhaustive in terms of different transition metals used in the metal layer. Other metals could yield higher vacancies within the layered structure. Thus, almost limitless metal combinations from the periodic table are possible. These new materials could not only serve as negative electrode materials for NIBs, but deserve study as electrode materials for KIBs. Much more work is needed to understand the practicality of KIBs, beyond graphite and simple K_xMO_2 and into other structural classes of materials. Also, potassium is not the last alkali metal in group I of the periodic table. Other layered large alkali metal oxides would be of interest for future studies, where the alkali is rubidium or caesium.

During the early stages of this work a large format conflat cell was designed and made. This is basically a large two electrode electrochemical cell, with dimensions of 12 x 4 x 3 inches, that allows for larger amounts of electrode material to be studied. This is beneficial as large amounts of material are desirable for Mössbauer and *ex situ* XRD measurements (structure refinement). Electrode materials could be cycled to a chosen voltage and then studied using more than one technique as there are larger amounts of material.

Lastly, transition metal migration to the sodium layer upon charging has been discussed. Many of the metals (Ti, V, Cr and Fe) commonly used in NIBs display this. Other potential research could aim at understanding migration of these metals. The migration causes irreversible structural changes to the materials which leads to low capacities. The only reports of migration have been for O3 structures [14,31,35,41]. The P2-$Na_{2/3}V_{2/3}Ti_{1/3}O_2$ material investigated in this work is, to the author's knowledge, the first non-O3 structure to exhibit metal migration. In this case, the transition metal is going from an octahedral environment to a prismatic one, instead of octahedral to octahedral. It is unknown at this time if migration occurs at the same voltage for both structure types, but perhaps the energy barriers for migration are different. Careful investigations could better understand migration and determine the mechanism, so that it might be prevented to allow improved electrode characteristics.

REFERENCES

[1] Canadian Automobile Association. Electric Vehicles http://electricvehicles.caa.ca/electric-vehicles-available-in-canada/ (accessed Apr 10, 2016).

[2] Subburaj, A.S.; Pushpakaran, B.N.; Bayne, S.B. Overview of Grid Connected Renewable Energy Based Battery Projects in USA. *Renew. Sustain. Energy Rev.*, **2015**, *45*, 219–234.

[3] *Linden's Handbook of Batteries*; Linden, D.; Reddy, T.B., Eds.; 4th ed.; McGraw-Hill, **2010**.

[4] Ke, W.; Zhang, S.; Wu, Y.; Zhao, B.; Wang, S.; Hao, J. Assessing The Future Vehicle Fleet Electrification: The Impacts on Regional and Urban Air Quality. *Environ.Sci. Technol.*, **2017**, *51*, 1007–1016.

[5] Oliveira, L.; Messagie, M.; Rangaraju, S.; Sanfelix, J.; Hernandez Rivas, M.; Van Mierlo, J. Key Issues of Lithium-Ion Batteries - From Resource Depletion to Environmental Performance Indicators. *J. Clean. Prod.*, **2015**, *108*, 354–362.

[6] Tahil, W. The Trouble with Lithium 2: Under the Microscope. *Meridian International Research*, **2008**, 1–54.

[7] China Lithium Carbonate Industry Outlook for 2016 http://www.goldendragoncapital.com/china-lithium-carbonate-outlook/ (accessed May 20, 2017).

[8] Alekseenko, V.; Alekseenko, A. The Abundances of Chemical Elements in Urban Soils. *J. Geochemical Explor.*, **2014**, *147*, 245–249.

[9] Yabuuchi, N.; Kubota, K.; Dahbi, M.; Komaba, S. Research Development on Sodium-Ion Batteries. *Chem. Rev.*, **2014**, *114*, 11636–11682.

[10] Kundu, D.; Talaie, E.; Duffort, V.; Nazar, L.F. The Emerging Chemistry of Sodium Ion Batteries for Electrochemical Energy Storage. *Angew. Chem. Int. Ed.*, **2015**, 3431–3448.

[11] Slater, M.D.; Kim, D.; Lee, E.; Johnson, C.S. Sodium-Ion Batteries. *Adv. Funct. Mater.*, **2013**, *23*, 947–958.

[12] Han, M.H.; Gonzalo, E.; Singh, G.; Rojo, T. A Comprehensive Review of Sodium Layered Oxide: Powerful Cathode for Na-Ion Battery. *Energy Environ. Sci.*, **2014**, *8*, 81–102.

[13] Ong, S.P.; Chevrier, V.L.; Hautier, G.; Jain, A.; Moore, C.; Kim, S.; Ma, X.; Ceder, G. Voltage, Stability and Diffusion Barrier Differences Between Sodium-Ion and Lithium-Ion Intercalation Materials. *Energy Environ. Sci.*, **2011**, *4*, 3680–3688.

[14] Yabuuchi, N.; Yoshida, H.; Komaba, S. Crystal Structures and Electrode Performance of Alpha-$NaFeO_2$ for Rechargeable Sodium Batteries. *Electrochem. Commun.*, **2012**, *80*, 716–719.

[15] Chevrier, V.L.; Ceder, G. Challenges for Na-Ion Negative Electrodes. *J. Electrochem. Soc.*, **2011**, *158*, A1011–A1014.

[16] Doeff, M.M.; Ma, Y.; Visco, S.J.; Jonghe, L.C. De. Electrochemical Insertion of Sodium into Carbon. *J. Electrochem. Soc.*, **1993**, *140*, 169–170.

[17] Xu, C.; Chen, Y.; Shi, S.; Li, J.; Kang, F.; Su, D. Secondary Batteries With Multivalent Ions for Energy Storage. *Sci. Rep.*, **2015**, *5*, 14120.

[18] Wang, R.Y.; Shyam, B.; Stone, K.H.; Weker, J.N.; Pasta, M.; Lee, H.W.; Toney, M.F.; Cui, Y. Reversible Multivalent (Monovalent, Divalent, Trivalent) Ion Insertion in Open Framework Materials. *Adv. Energy Mater.*, **2015**, *5*, 1–10.

[19] Rong, Z.; Malik, R.; Canepa, P.; Sai Gautam, G.; Liu, M.; Jain, A.; Persson, K.; Ceder, G. Materials Design Rules for Multivalent Ion Mobility in Intercalation Structures. *Chem. Mater.*, **2015**, *27*, 6016–6021.

[20] Komaba, S.; Hasegawa, T.; Dahbi, M.; Kubota, K. Potassium Intercalation Into Graphite to Realize High-Voltage/High-Power Potassium-Ion Batteries and Potassium-Ion Capacitors. *Electrochem. Commun.*, **2015**, *60*, 172–175.

[21] Jayaprakash, N.; Das, S.K.; Archer, L.A. The Rechargeable Aluminum-Ion Battery. *Chem. Commun.*, **2011**, *47*, 12610–12612.

[22] Saha, P.; Datta, M.K.; Velikokhatnyi, O.I.; Manivannan, A.; Alman, D.; Kumta, P.N. Rechargeable Magnesium Battery: Current Status and Key Challenges for the Future. *Prog. Mater. Sci.*, **2014**, *66*, 1–86.

[23] Lipson, A.L.; Pan, B.; Lapidus, S.H.; Liao, C.; Vaughey, J.T.; Ingram, B.J. Rechargeable Ca-Ion Batteries: A New Energy Storage System. *Chem. Mater.*, **2015**, *27*, 8442–8447.

[24] Tran, T.T.; Obrovac, M.N. Alloy Negative Electrodes for High Energy Density Metal-Ion Cells. *J. Electrochem. Soc.*, **2011**, *158*, A1411–A1416.

[25] Ua, J.A.; Jow, T.R.; Shacklette, L.W. Rechargeable Cell Based on a Conductive Polymer/Metal Alloy Composite Electrode. *J. Electrochem. Soc.*, **1989**, *136*, 1–6.

[26] Shannon, R.D. Revised Effective Ionic Radii and Systematic Studies of Interatomic Distances in Halides and Chaleogenides. *Acta Cryst.*, **1976**, *A32*, 752–767.

[27] Marcus, Y. Thermodynamic Functions of Transfer of Single Ions from Water to Nonaqueous and Mixed Solvents PART 4 : Standard Potentials of Selected Electrodes. *Pure Appl. Chem.*, **1985**, *57*, 1129–1132.

[28] Dahbi, M.; Yabuuchi, N.; Kubota, K.; Tokiwa, K.; Komaba, S. Negative Electrodes for Na-Ion Batteries. *Phys. Chem. Chem. Phys.*, **2014**, *16*, 15007–15028.

[29] Bommier, C.; Ji, X. Recent Development on Anodes for Na-Ion Batteries. *Isr.J. Chem.*, **2015**, *55*, 468–507.

[30] Klein, F.; Jache, B.; Bhide, A.; Adelhelm, P. Conversion Reactions for Sodium-Ion Batteries. *Phys. Chem. Chem. Phys.*, **2013**, *15*, 15876–15887.

[31] Maazaz, A.; Delmas, C.; Hagenmuller, P. A Study of the Na_xTiO_2 System by Electrochemical Deintercalation. *J. Incl. Phenom.*, **1983**, *1*, 45–51.

[32] Wu, D.; Li, X.; Xu, B.; Twu, N.; Liu, L.; Ceder, G. $NaTiO_2$: A Layered Anode Material for Sodium-Ion Batteries. *Energy Environ. Sci.*, **2014**, *8*, 195–202.

[33] Oh, S.-M.; Myung, S.-T.; Hassoun, J.; Scrosati, B.; Sun, Y.-K. Reversible $NaFePO_4$ Electrode for Sodium Secondary Batteries. *Electrochem. commun.*, **2012**, *22*, 149–152.

[34] Delmas, C.; Braconnier, J.-J.; Fouassier, C.; Hagenmuller, P. Electrochemical Intercalation of Sodium in $NaCoO_2$ Bronzes. *Solid State Ion.*, **1981**, *3*, 165–169.

[35] Didier, C.; Guignard, M.; Denage, C.; Szajwaj, O.; Ito, S.; Saadoune, I.; Darriet, J.; Delmas, C. Electrochemical Na-Deintercalation from $NaVO_2$. *Electrochem. Solid St.*, **2011**, *14*, A75–A78.

[36] Didier, C.; Guignard, M.; Darriet, J.; Delmas, C. $O'3-Na_xVO_2$ System. *Inorg. Chem.*, **2012**, *51*, 11007–11016.

[37] Hamani, D.; Ati, M.; Tarascon, J.-M.; Rozier, P. Na_xVO_2 as Possible Electrode for Na-Ion Batteries. *Electrochem. Commun.*, **2011**, *13*, 938–941.

[38] Braconnier, J.J.; Delmas, C.; Hagenmuller, P. Etude Par Desintercalation Electrochemique Des Systemes Na_xCrO_2 et Na_xNiO_2. *Mat. Res. Bull.*, **1982**, *17*, 993–1000.

[39] Komaba, S.; Takei, C.; Nakayama, T.; Ogata, A.; Yabuuchi, N. Electrochemical Intercalation Activity of Layered $NaCrO_2$ vs. $LiCrO_2$. *Electrochem. Commun.*, **2010**, *12*, 355–358.

[40] Komaba, S.; Nakayama, T.; Ogata, A.; Shimizu, T.; Takei, C.; Takada, S.; Hokura, A.; Nakai, I. Electrochemically Reversible Sodium Intercalation of Layered $NaNi_{0.5}Mn_{0.5}O_2$ and $NaCrO_2$. *ECS Trans.*, **2009**, *16*, 43–55.

[41] Kubota, K.; Ikeuchi, I.; Nakayama, T.; Takei, C.; Yabuuchi, N.; Shiiba, H.; Nakayama, M.; Komaba, S. New Insight into Structural Evolution in Layered $NaCrO_2$ during Electrochemical Sodium Extraction. *J. Phys. Chem. C*, **2015**, *119*, 166–175.

[42] Mendiboure, A.; Delmas, C.; Hagenmuller, P. Electrochemical Intercalation and Deintercalation of Na_xMnO_2 Bronzes. *J. Solid State Chem.*, **1985**, *57*, 323–331.

[43] Ma, X.; Chen, H.; Ceder, G. Electrochemical Properties of Monoclinic $NaMnO_2$. *J. Electrochem. Soc.*, **2011**, *158*, A1307–A1312.

[44] Zhao, J.; Zhao, L.; Dimov, N.; Okada, S.; Nishida, T. Electrochemical and Thermal Properties of $NaFeO_2$ Cathode for Na-Ion Batteries. *J. Electrochem. Soc.*, **2013**, *160*, A3077–A3081.

[45] Vassilaras, P.; Ma, X.; Li, X.; Ceder, G. Electrochemical Properties of Monoclinic $NaNiO_2$. *J. Electrochem. Soc.*, **2012**, *160*, A207–A211.

[46] Arai, H.; Okada, S.; Sakurai, Y.; Yamaki, J. Electrochemical and Structural Study of Li_2CuO_2, $LiCuO_2$ and $NaCuO_2$. *Solid State Ion.*, **1998**, *106*, 45–53.

[47] Ono, Y.; Yui, Y.; Hayashi, M.; Hayashi, K.; Asakura, K.; Kobayashi, R.; Kitabayashi, H. Electrochemical Properties and Structural Changes of NaCuO2 for Sodium Secondary Batteries. In *224th ECS Meeting*; **2013**; p. 370.

[48] Kim, S.-W.; Seo, D.-H.; Ma, X.; Ceder, G.; Kang, K. Electrode Materials for Rechargeable Sodium-Ion Batteries: Potential Alternatives to Current Lithium-Ion Batteries. *Adv. Energy Mater.*, **2012**, *2*, 710–721.

[49] Saadoune, I.; Maazaz, A.; Menetrier, M.; Delmas, C. On the $Na_xNi_{0.6}Co_{0.4}O_2$ System: Physical and Electrochemical Studies. *J. Solid State Chem.*, **1996**, *117*, 111–117.

[50] Lu, Z.; Dahn, J.R. In Situ X-Ray Diffraction Study of P2-$Na_{2/3}[Ni_{1/3}Mn_{2/3}]O_2$. *J. Electrochem. Soc.*, **2001**, *148*, A1225–A1229.

[51] Li, X.; Wu, D.; Zhou, Y.N.; Liu, L.; Yang, X.Q.; Ceder, G. O3-Type $Na(Mn_{0.25}Fe_{0.25}Co_{0.25}Ni_{0.25})O_2$: A Quaternary Layered Cathode Compound for Rechargeable Na Ion Batteries. *Electrochem. Commun.*, **2014**, *49*, 51–54.

[52] Yoshida, H.; Yabuuchi, N.; Kubota, K.; Ikeuchi, I.; Garsuch, A.; Schulz-Dobrick, M.; Komaba, S. P2-Type $Na_{2/3}Ni_{1/3}Mn_{2/3-x}Ti_xO_2$ as a New Positive Electrode for Higher Energy Na-Ion Batteries. *Chem. Commun.*, **2014**, *50*, 3677–3680.

[53] Yabuuchi, N.; Komaba, S. Recent Research Progress on Iron- and Manganese-Based Positive Electrode Materials for Rechargeable Sodium Batteries. *Sci. Tech. Adv. Mater.*, **2014**, *15*, 043501–043529.

[54] Obrovac, M.N.; Chevrier, V.L. Alloy Negative Electrodes for Li-Ion Batteries. *Chem. Rev.*, **2014**, *114*, 11444–114502.

[55] Jache, B.; Adelhelm, P. Use of Graphite as a Highly Reversible Electrode with Superior Cycle Life for Sodium-Ion Batteries by Making Use of Co-Intercalation Phenomena. *Angew. Chem. Int. Ed.*, **2014**, *53*, 10169–10173.

[56] Ponrouch, A.; Dedryvère, R.; Monti, D.; Demet, A.E.; Ateba Mba, J.M.; Croguennec, L.; Masquelier, C.; Johansson, P.; Palacín, M.R. Towards High Energy Density Sodium Ion Batteries through Electrolyte Optimization. *Energy Environ. Sci.*, **2013**, *6*, 2361–2369.

[57] Ellis, L.D.; Hatchard, T.D.; Obrovac, M.N. Reversible Insertion of Sodium in Tin. *J. Electrochem. Soc.*, **2012**, *159*, A1801–A1805.

[58] Stevens, D.A.; Dahn, J.R. High Capacity Anode Materials for Rechargeable Sodium-Ion Batteries. *J. Electrochem. Soc.*, **2000**, *147*, 1271–1273.

[59] Thomas, P.; Billaud, D.; Nancy, I.; Vandoeu, B.P. Electrochemical Insertion of Sodium into Hard Carbons. *Electrochim. Acta*, **2002**, *47*, 3303–3307.

[60] Komaba, S.; Murata, W.; Ishikawa, T.; Yabuuchi, N.; Ozeki, T.; Nakayama, T.; Ogata, A.; Gotoh, K.; Fujiwara, K. Electrochemical Na Insertion and Solid Electrolyte Interphase for Hard-Carbon Electrodes and Application to Na-Ion Batteries. *Adv. Funct. Mater.*, **2011**, *21*, 3859–3867.

[61] Alcantara, R.; Jaraba, M.; Lavela, P.; Tirado, J.L. $NiCo_2O_4$ Spinel : First Report on a Transition Metal Oxide for the Negative Electrode of Sodium-Ion Batteries. *Chem. Mater.*, **2002**, *14*, 2847–2848.

[62] Xiao, L.; Cao, Y.; Xiao, J.; Wang, W.; Kovarik, L.; Nie, Z.; Liu, J. High Capacity, Reversible Alloying Reactions in SnSb/C Nanocomposites for Na-Ion Battery Applications. *Chem. Commun.*, **2012**, *48*, 3321–3323.

[63] Yabuuchi, N.; Matsuura, Y.; Ishikawa, T.; Kuze, S.; Son, J.-Y.; Cui, Y.-T.; Oji, H.; Komaba, S. Phosphorus Electrodes in Sodium Cells: Small Volume Expansion by Sodiation and the Surface-Stabilization Mechanism in Aprotic Solvent. *ChemElectroChem*, **2014**, *1*, 580–589.

[64] Zanini, M.; Shaw, J.L.; Tennehouse, G.J. Behavior of the Na_xTiS_2 as an Electrode Material. *Bull. Am. Phys. Soc.*, **1979**, *25*, 201–201.

[65] Delams, C.; Cherkaoui, F.; Nadiri, A.; Hagenmuller, P. A Nasicon-Type Phase as Intercalation Electrode: $NaTi_2(PO_4)_3$. *Mat. Res. Bull.*, **1987**, *22*, 631–639.

[66] Delmas, C.; Nadiri, A. The NASICON-Type Titanium Phosphates $ATi_2(PO_4)_3$ (A=Li, Na) as Electrode Materials. *Solid State Ion.*, **1988**, *28*, 419–423.

[67] Senguttuvan, P.; Rousse, G.; Seznec, V.; Tarascon, J.-M.; Palacín, M.R. $Na_2Ti_3O_7$: The Lowest Voltage Ever Reported Oxide Insertion Electrode Material for Sodium Ion Batteries. *Chem. Mater.*, **2011**, *23*, 7–10.

[68] Doeff, M.M.; Cabana, J.; Shirpour, M. Titanate Anodes for Sodium Ion Batteries. *J. Inorg. Organomat. Polym.*, **2013**, *24*, 5–14.

[69] Xiong, H.; Slater, M.D.; Balasubramanian, M.; Johnson, C.S.; Rajh, T. Amorphous TiO_2 Nanotube Anode for Rechargeable Sodium Ion Batteries. *J. Phys. Chem. Lett.*, **2011**, *2*, 2560–2565.

[70] Wang, Y.; Yu, X.; Xu, S.; Bai, J.; Xiao, R.; Hu, Y.-S.S.; Li, H.; Yang, X.-Q.Q.; Chen, L.; Huang, X. A Zero-Strain Layered Metal Oxide as the Negative Electrode for Long-Life Sodium-Ion Batteries. *Nat. Commun.*, **2013**, *4*, 1–7.

[71] Ellis, B.L.; Nazar, L.F. Sodium and Sodium-Ion Energy Storage Batteries. *Curr. Opin. Solid State Mater. Sci.*, **2012**, *16*, 168–177.

[72] Barker, J.; Heap, R.J.; Roche, N.; Tan, C.; Liu, Y.; Sheffield, S. Low Cost Na-ion Battery Technology http://www.faradion.co.uk/products/sodium-technology/ (accessed Feb 11, 2017).

[73] Simon, P.; Tarascon, J.-M. A Promising New Prototype of Battery. *French National Press Release*, **2015**, 1–3.

[74] Verma, P.; Maire, P.; Novák, P. A Review of the Features and Analyses of the Solid Electrolyte Interphase in Li-Ion Batteries. *Electrochim. Acta*, **2010**, *55*, 6332–6341.

[75] Komaba, S.; Ishikawa, T.; Yabuuchi, N.; Murata, W.; Ito, A.; Ohsawa, Y. Fluorinated Ethylene Carbonate as Electrolyte Additive for Rechargable Na Batteries. *ACS Appl. Mater. Interfaces*, **2011**, *3*, 4165–4168.

[76] Ponrouch, A.; Monti, D.; Boschin, A.; Steen, B.; Johansson, P.; Palacín, M.R. Non-Aqueous Electrolytes for Sodium-Ion Batteries. *J. Mater. Chem. A*, **2014**, *3*, 22–42.

[77] Nose, M.; Nakayama, H.; Nobuhara, K.; Yamaguchi, H.; Nakanishi, S.; Iba, H. $Na_4Co_3(PO_4)_2P_2O_7$: A Novel Storage Material for Sodium-Ion Batteries. *J. Power Sources*, **2013**, *234*, 175–179.

[78] Mather, G.C.; Dussarrat, C.; Etourneau, J.; West, A.R. A Review of Cation-Ordered Rock Salt Superstructure Oxides. *J. Mater. Chem.*, **2000**, *10*, 2219–2230.

[79] Delmas, C.; Fouassier, C.; Hagenmuller, P. Structural Classification and Properties of the Layered Oxides. *Physica*, **1980**, *99B*, 81–85.

[80] West, A.R. *Solid State Chemistry and Its Applications*; 2nd ed.; Wiley: Sussex, UK, **2014**.

[81] Shao-Horn, Y.; Levasseur, S.; Weill, F.; Delmas, C. Probing Lithium and Vacancy Ordering in O3 Layered Li_xCoO_2 ($x \approx 0.5$). *J. Electrochem. Soc.*, **2003**, *150*, A366–A373.

[82] Buscaglia, V.; Milanese, C. Diffusion-Controlled Solid-State Reactions of Spherical Particles, a General Model for Multiphase Binary Systems. *J. Phys. Chem. B*, **2005**, *109*, 18475–18482.

[83] Cullity, B.D. *Elements of X-Ray Diffraction*; 1st ed.; Addison-Wesley Publishing Company Inc.: Reading, Massachusetts, **1956**.

[84] Economou, E.N. *The Physics of Solids*; Springer-Verlag: Heidelberg; Berlin, **2010**.

[85] Hunter, B. Rietica- A Visual Rietveld Program. In *International Union of Crystallography Commision on Powder Diffraction Newsletter No. 20*; **1998**.

[86] Momma, K.; Izumi, F. VESTA : A Three-Dimensional Visualization System for Electronic and Structural Analysis. *J. Appl. Crystallogr.*, **2008**, *41*, 653–658.

[87] Dinnebier, R.E.; Billinge, S.J.L. *Powder Diffraction: Theory and Practice*; The Royal Society of Chemistry: Cambridge, UK, **2008**.

[88] Dreyer, W.; Jamnik, J.; Guhlke, C.; Huth, R.; Moskon, J.; Gaberscek, M. The Thermodynamic Origin of Hysteresis in Insertion Batteries. *Nat. Mater.*, **2010**, *9*, 448–453.

[89] Dreyer, W.; Guhlke, C.; Herrmann, M. Hysteresis and Phase Transition in Many-Particle Storage Systems. *Contin. Mech. Thermodyn.*, **2011**, *23*, 211–231.

[90] Huang, J.P.; Yuan, D.D.; Zhang, H.Z.; Cao, Y.L.; Li, G.R.; Yang, H.X.; Gao, X.P. Electrochemical Sodium Storage of TiO_2(B) Nanotubes for Sodium Ion Batteries. *RSC Adv.*, **2013**, *3*, 12593–12597.

[91] Fielden, R.; Obrovac, M.N. Low Voltage Sodium Intercalation in $Na_xNi_{x/2}Ti_{1-x/2}O_2$ ($0.5 \leq X \leq 1.0$). *J. Electrochem. Soc.*, **2014**, *161*, A1158–A1163.

[92] Shanmugam, R.; Lai, W. $Na_{2/3}Ni_{1/3}Ti_{2/3}O_2$: "Bi-Functional" Electrode Materials for Na-Ion Batteries. *ECS Electrochem. Lett.*, **2014**, *3*, A23–A25.

[93] Yu, H.; Ren, Y.; Xiao, D.; Guo, S.; Zhu, Y.; Qian, Y.; Gu, L.; Zhou, H. An Ultrastable Anode for Long-Life Room-Temperature Sodium-Ion Batteries. *Angew. Chem. Int. Ed.*, **2014**, *53*, 8963–8969.

[94] Wang, Y.; Xiao, R.; Hu, Y.-S.; Avdeev, M.; Chen, L. P2-$Na_{0.6}[Cr_{0.6}Ti_{0.4}]O_2$ Cation-Disordered Electrode for High-Rate Symmetric Rechargeable Sodium-Ion Batteries. *Nat. Commun.*, **2015**, *6*, 6954–6963.

[95] Tsuchiya, Y.; Takanashi, K.; Nishinobo, T.; Hokura, A.; Yonemura, M.; Matsukawa, T.; Ishigaki, T.; Yamanaka, K.; Ohta, T.; Yabuuchi, N. Layered $Na_xCr_xTi_{1-x}O_2$ as Bi-Functional Electrode Materials for Rechargeable Sodium Batteries. *Chem. Mater.*, **2016**, 1–11.

[96] Yu, M.; Avdeev, V.B.; Nalbandyan, V.B.; Medvedev, B.S. Hexagonal Sodium Titanium Chromite: A New High-Conductivity Solid Electrolyte. *Inorg. Mater.*, **1997**, *33*, 500–503.

[97] Berthelot, R.; Carlier, D.; Delmas, C. Electrochemical Investigation of the P2–Na_xCoO_2 Phase Diagram. *Nat. Mater.*, **2011**, *10*, 74–80.

[98] Duffort, V.; Talaie, E.; Black, R.; Nazar, L.F. Uptake of CO_2 in Layered P2-$Na_{0.67}Mn_{0.5}Fe_{0.5}O_2$: Insertion of Carbonate Anions. *Chem. Mater.*, **2015**, *27*, 2515–2524.

[99] Buchholz, D.; Chagas, L.G.; Vaalma, C.; Wu, L.; Passerini, S. Water Sensitivity of Layered P2/P3-$Na_xNi_{0.22}Co_{0.11}Mn_{0.66}O_2$ Cathode Material. *J. Mater. Chem. A*, **2014**, *2*, 13415–13421.

[100] Cabana, J.; Monconduit, L.; Larcher, D.; Palacín, M.R. Beyond Intercalation-Based Li-Ion Batteries: The State of the Art and Challenges of Electrode Materials Reacting through Conversion Reactions. *Adv. Mater.*, **2010**, *22*, E170–E192.

[101] Hagenmuller, P. Predictive Character of Solid State Chemistry : Relation between Structure, Chemical Bonding and Physical Properties of Solids. *Chem. Sci.*, **1983**, *92*, 1–26.

[102] Zheng, L.; Obrovac, M.N. Investigation of O3-Type $Na_{0.9}Ni_{0.45}Mn_xTi_{0.55-x}O_2$ ($0 \leq X \leq 0.55$) as Positive Electrode Materials for Sodium-Ion Batteries. *Electrochim. Acta*, **2017**, *233*, 284–291.

[103] Sathiya, M.; Hemalatha, K.; Ramesha, K.; Tarascon, J.-M.; Prakash, A.S. Synthesis, Structure, and Electrochemical Properties of Layered Sodium Insertion Cathode Material: $NaNi_{1/3}Mn_{1/3}Co_{1/3}O_2$. *Chem. Mater.*, **2012**, *24*, 1846–1853.

[104] Reddy, B.V.R.; Gopukumar, S. Na_xCoO_2 Cathode Material: Synthesized by Inverse Micro- Emulsion Method for Sodium Ion Batteries. *ECS Trans.*, **2013**, *53*, 49–58.

[105] Li, J.; Camardese, J.; Glazier, S.; Dahn, J.R. Structural and Electrochemical Study of the Li − Mn − Ni Oxide System within the Layered Single Phase Region. *Chem. Mater.*, **2014**, *26*, 7059–7066.

[106] Thorne, J.S.; Chowdhury, S.; Dunlap, R.A.; Obrovac, M.N. Structure and Electrochemistry of $Na_xFe_xTi_{1-x}O_2$ ($1.0 \geq X \geq 0.75$) for Na-Ion Battery Positive Electrodes. *J. Electrochem. Soc.*, **2014**, *161*, A1801–A1805.

[107] Hatchard, T.D.; Obrovac, M.N. Evaluation of Electrolyte Salts and Solvents for Na-Ion Batteries in Symmetric Cells. *J. Electrochem. Soc.*, **2014**, *161*, A1748–A1752.

[108] Fielden, R.; Cole, L.; Obrovac, M.N. Low Voltage Sodium Intercalation in $Na_xV_xTi_{1-x}O_2$ ($2/3 \leq X \leq 1$). *J. Electrochem. Soc.*, **2017**, *164*, A490–A497.

[109] Kubota, K.; Yabuuchi, N.; Yoshida, H.; Dahbi, M.; Komaba, S. Layered Oxides as Positive Electrode Materials for Na-Ion Batteries. *MRS Bull.*, **2014**, *39*, 416–422.

[110] Lu, Z.; Donaberger, R.A.; Dahn, J.R. Superlattice Ordering of Mn, Ni, and Co in Layered Alkali Transition Metal Oxides with P2, P3, and O3 Structures. *Chem. Mater.*, **2000**, *12*, 3583–3590.

[111] Medarde, M.; Mena, M.; Gavilano, J.L.; Pomjakushina, E.; Sugiyama, J.; Kamazawa, K.; Pomjakushin, V.Y.; Sheptyakov, D.; Batlogg, B.; Ott, H.R.; Mansson, M.; Juranyi, F. 1D to 2D Na^+ Ion Diffusion Inherently Linked to Structural Transitions in $Na_{0.7}CoO_2$. *Ph. Rev. Lett.*, **2013**, *110*, 266401.

[112] Guignard, M.; Carlier, D.; Didier, C.; Suchomel, M.R.; Elka, E.; Bordet, P.; Decourt, R.; Darriet, J.; Delmas, C. Vanadium Clustering/Declustering in P2−$Na_{1/2}VO_2$ Layered Oxide. *Chem. Mater.*, **2014**, *26*, 1538–1548.

[113] Li, X.; Ma, X.; Su, D.; Liu, L.; Chisnell, R.; Ong, S.P.; Chen, H.; Toumar, A.; Idrobo, J.; Lei, Y.; Bai, J.; Wang, F.; Lynn, J.W.; Lee, Y.S.; Ceder, G. Direct Visualization of the Jahn-Teller Effect Coupled to Na Ordering in $Na_{5/8}MnO_2$. *Nat. Mater.*, **2014**, *13*, 586–592.

[114] Toumar, A.J.; Ong, S.P.; Richards, W.D.; Dacek, S.; Ceder, G. Vacancy Ordering in O3-Type Layered Metal Oxide Sodium-Ion Battery Cathodes. *Phys. Rev. Appl.*, **2015**, *4*, 0640021–0640029.

[115] Zhao, C.; Wang, Q.; Lu, Y.; Hu, Y. Review on Anionic Redox for High-Capacity Lithium- and Sodium-Ion Batteries. *J. Phys. D Appl. Phys.*, **2017**, *50*, 183001–183023.

[116] Zhang, S.; Liu, Y.; Zhang, N.; Zhao, K.; Yang, J.; He, S. O3-Type $NaNi_{0.33}Li_{0.11}Ti_{0.56}O_2$-Based Electrode for Symmetric Sodium Ion Cell. *J. Power Sources*, **2016**, *329*, 1–7.

[117] Guo, S.; Liu, P.; Sun, Y.; Zhu, K.; Yi, J.; Chen, M.; Ishida, M.; Zhou, H. A High-Voltage and Ultralong-Life Sodium Full Cell for Stationary Energy Storage. *Angew. Chem. Int. Ed.*, **2015**, *54*, 11701–11705.

[118] Delmas, C.; Fouassier, C.; Hagenmuller, P. Stabilite Relative Des Environments Octaedrique et Prismatique Triangulaire Dans Les Oxydes Lamellaires Alcalins A_xMO_2 ($X \leq 1$). *Mater. Res. Bull.*, **1976**, *11*, 1483–1488.

[119] Guo, S.; Yu, H.; Liu, P.; Ren, Y.; Zhang, T.; Chen, M.; Ishida, M.; Zhou, H. High-Performance Symmetric Sodium-Ion Batteries Using a New, Bipolar O3-Type Material, $Na_{0.8}Ni_{0.4}Ti_{0.6}O_2$. *Energy Environ. Sci.*, **2015**, *8*, 1237–1244.

[120] Rouxel, J. Sur Un Diagramme Ionicite-Structure Pour Les Composes Intercalaires Alcalins Des Sulfures Lamellaires. *J. Solid State Chem.*, **1976**, *17*, 223–229.

[121] Dahn, J.R.; Haering, R.R. Lithium Intercalation in TiS_2. *Mat. Res. Bull.*, **1979**, *14*, 1259–1262.

[122] Newmann, G.H.; Klemann, L.P. Ambient Temperature Cycling of an Na-TiS2 Cell. *J. Electrochem. Soc.*, **1980**, *127*, 2097–2099.

[123] Lee, E.; Sahgong, S.; Johnson, C.S.; Kim, Y. Comparative Electrochemical Sodium Insertion/Extraction Behavior in Layered Na_xVS_2 and Na_xTiS_2. *Electrochim. Acta*, **2014**, *143*, 272–277.

[124] Ghaloun, O.A.; Chevalier, P.; Trichet, L.; Rouxel, J. Structural, Electrical, Magnetic and NMR Study of the $Na_xCr_xTi_{1-x}S_2$ System. *Solid State Ion.*, **1981**, *2*, 231–235.

[125] Delmas, C. Battery Materials: Operating Through Oxygen. *Nat. Chem.*, **2016**, *8*, 641–643.

[126] Vaalma, C.; Giffin, G. a.; Buchholz, D.; Passerini, S. Non-Aqueous K-Ion Battery Based on Layered $K_{0.3}MnO_2$ and Hard Carbon/Carbon Black. *J. Electrochem. Soc.*, **2016**, *163*, A1295–A1299.

[127] Bityutskii, P.N.; Khitrova, V.I. Structure of Potassium, Rubidium, and Cesium Nickelates of Composition Me_xNiO_2. *Sov. Ph. Cristal.*, **1969**, *14*, 122–126.

[128] Delmas, C.; Fouassier, C.; Hagenmuller, P. Les Bronzes de Cobalt K_xCoO_2 (x<1). *J. Solid State Chem.*, **1975**, *13*, 165–171.

[129] Zhao, J.; Zou, X.; Zhu, Y.; Xu, Y.; Wang, C. Electrochemical Intercalation of Potassium into Graphite. *Adv. Funct. Mater.*, **2016**, *26*, 8103–8110.

[130] Eftekhari, A.; Jian, Z.; Ji, X. Potassium Secondary Batteries. *ACS Appl. Mater. Interfaces*, **2016**, *9*, 4404–4419.

[131] Eftekhari, A. Potassium Secondary Cell Based on Prussian Blue Cathode. *J. Power Sources*, **2004**, *126*, 221–228.

[132] Hironaka, Y.; Kubota, K.; Komaba, S. P2- and P3-K_xCoO_2 as Electrochemical Potassium Intercalation Host. *Chem. Commun.*, **2017**, *53*, 3693–3696.

[133] Gupta, A.; Buddie Mullins, C.; Goodenough, J.B. $Na_2Ni_2TeO_6$: Evaluation as a Cathode for Sodium Battery. *J. Power Sources*, **2013**, *243*, 817–821.

[134] Ma, J.; Bo, S.-H.; Wu, L.; Zhu, Y.; Grey, C.P.; Khalifah, P.G. Ordered and Disordered Polymorphs of $Na(Ni_{2/3}Sb_{1/3})O_2$: Honeycomb-Ordered Cathodes for Na-Ion Batteries. *Chem. Mater.*, **2015**, *27*, 2387–2399.

[135] Xu, Y.; Zhou, M.; Wang, X.; Wang, C.; Liang, L.; Grote, F.; Wu, M.; Mi, Y.; Lei, Y. Enhancement of Sodium Ion Battery Performance Enabled by Oxygen Vacancies. *Angew. Chem. Int. Ed.*, **2015**, *54*, 8768–8771.

[136] Galceran, M.; Roddatis, V.; Zúñiga, F.J.; Pérez-Mato, J.M.; Acebedo, B.; Arenal, R.; Peral, I.; Rojo, T.; Casas-Cabanas, M. Na–Vacancy and Charge Ordering in $Na_{2/3}FePO_4$. *Chem. Mater.*, **2014**, *26*, 3289–3294.

[137] Qian, D.; Xu, B.; Chi, M.; Meng, Y.S. Uncovering the Roles of Oxygen Vacancies in Cation Migration in Lithium Excess Layered Oxides. *Phys. Chem. Chem. Phys.*, **2014**, *16*, 14665–14668.

[138] McCalla, E.; Rowe, A.W.; Camardese, J.; Dahn, J.R. The Role of Metal Site Vacancies in Promoting Li−Mn−Ni−O Layered Solid Solutions. *Chem. Mater.*, **2013**, *25*, 2716–2721.

[139] Shunmugasundaram, R.; Senthil Arumugam, R.; Harris, K.J.; Goward, G.R.; Dahn, J.R. A Search for Low-Irreversible Capacity and High-Reversible Capacity Positive Electrode Materials in the Li–Ni–Mn–Co Pseudoquaternary System. *Chem. Mater.*, **2016**, *28*, 55–66.

APPENDIX

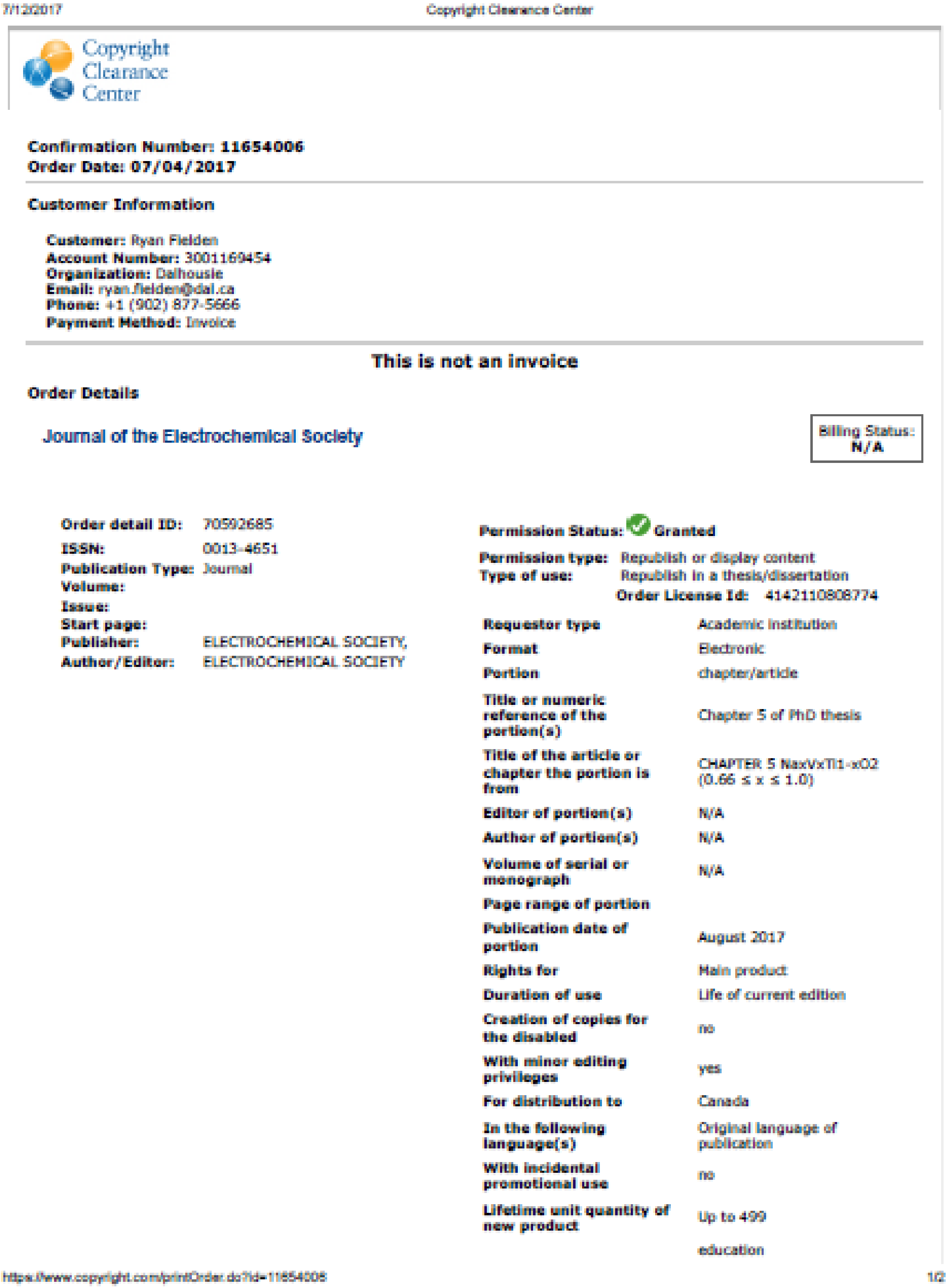

7/12/2017 Copyright Clearance Center

Copyright Clearance Center

Confirmation Number: 11654006
Order Date: 07/04/2017

Customer Information

Customer: Ryan Fielden
Account Number: 3001169454
Organization: Dalhousie
Email: ryan.fielden@dal.ca
Phone: +1 (902) 877-5666
Payment Method: Invoice

This is not an invoice

Order Details

Journal of the Electrochemical Society

Billing Status:
N/A

Order detail ID:	70592685
ISSN:	0013-4651
Publication Type:	Journal
Volume:	
Issue:	
Start page:	
Publisher:	ELECTROCHEMICAL SOCIETY,
Author/Editor:	ELECTROCHEMICAL SOCIETY

Permission Status: ✓ **Granted**

Permission type: Republish or display content
Type of use: Republish in a thesis/dissertation
Order License Id: 4142110808774

Requestor type	Academic institution
Format	Electronic
Portion	chapter/article
Title or numeric reference of the portion(s)	Chapter 5 of PhD thesis
Title of the article or chapter the portion is from	CHAPTER 5 NaxVxTi1-xO2 (0.66 ≤ x ≤ 1.0)
Editor of portion(s)	N/A
Author of portion(s)	N/A
Volume of serial or monograph	N/A
Page range of portion	
Publication date of portion	August 2017
Rights for	Main product
Duration of use	Life of current edition
Creation of copies for the disabled	no
With minor editing privileges	yes
For distribution to	Canada
In the following language(s)	Original language of publication
With incidental promotional use	no
Lifetime unit quantity of new product	Up to 499
	education

https://www.copyright.com/printOrder.do?id=11654006 1/2